

Cell-based Therapy for Pulmonary Injury

Sally Yunsun Kim

A thesis submitted to fulfil requirements

for the degree of

Doctor of Philosophy

Faculty of Pharmacy

The University of Sydney

2018

Statement of Originality

This thesis is submitted to the Faculty of Pharmacy, The University of Sydney, in fulfilment of the requirement for the degree of Doctor of Philosophy.

This is to certify that to the best of my knowledge, the content of this thesis is my own work. This thesis has not been submitted for any degree or other purposes.

I certify that the intellectual content of this thesis is the product of my own work and that all the assistance received in preparing this thesis and sources have been acknowledged.



Sally Yunsun Kim

April 2018

Contents

Acknowledgements	viii
List of Publications	ix
Authorship Attribution Statement	x
Abbreviations	xii
1 General Introduction	1
1.1 Inhalation injury	2
1.2 Smoke inhalation injury	3
1.2.1 Sources of smoke inhalation injuries	3
1.2.2 Complications of smoke inhalation injury and simulation in animal models	4
1.2.3 Current management of smoke inhalation injury have limitations	6
1.3 Stem cell-based therapy for lung injury	7
1.3.1 The innate repair capacity of the lung	7
1.3.2 Stem cell-based therapy for accelerating tissue regeneration in lung injury	7
1.4 Study design, hypothesis & aims	8
1.4.1 Hypothesis	8
1.4.2 Aims and summary of experiments	8
1.5 References	9
2 Direct delivery of stem cells to the airway for uniform distribution of cells demonstrates potential technology for the treatment of lung injury	
2.1 Overview	14
2.1.1 Graphical abstract	14
2.1.2 Highlights and keywords	14
2.1.3 Abstract	15
2.2 Introduction	16
2.3 Materials and Methods	19
2.3.1 Cell culture and maintenance	19
2.3.2 Preparation of substrates	19
2.3.3 Determination of substrate stiffness using atomic force microscopy	19
2.3.4 Cell spraying process and measurement of particle size	20
2.3.5 Cell viability and apoptosis assays	20

2.3.6	Assessment of cell morphology	21
2.3.7	Development and characterisation of decellularised <i>ex vivo</i> lung model	21
2.3.8	Assessing cell distribution in the <i>ex vivo</i> lung models by histology	22
2.3.9	Assessing cell distribution by bioluminescence imaging	23
2.3.10	Statistical analysis	24
2.4	Results and Discussion	24
2.4.1	Atomisation of human amniotic mesenchymal stromal cells (hAMSCs) was superior using the LMA device compared with a PennCentury device	24
2.4.2	Substrates with different stiffness were designed to compare the mechanical stresses that cells are exposed to when ‘‘landing’’	26
2.4.3	The atomisation of the hAMSCs maintained a high viability of the cells	27
2.4.4	Sprayed cells cultured on collagen I-coated plate yielded higher cell proliferation ...	27
2.4.5	Cells delivered using LMA device demonstrate more uniform distribution across the whole lung	33
2.5	Conclusions	35
2.6	Supplementary Information	36
2.6.1	Caspase-3/7 apoptosis assay	36
2.6.2	The incorporation of collagen coating	37
2.6.3	Live imaging of cells on decellularised matrix	38
2.7	References	39
3	Gelatin hydroxyphenyl propionic acid (GHPA) hydrogel for direct pulmonary delivery of decidual mesenchymal stromal cells	
3.1	Overview	45
3.1.1	Graphical abstract	45
3.1.2	Highlights and keywords	45
3.1.3	Abstract	46
3.2	Introduction	47
3.2.1	Decidual mesenchymal stromal cells are the ideal cell type suitable for the microenvironment of lung injury	47
3.2.2	Benefits of using a bioactive hydrogel delivery system	48
3.3	Materials and Methods	49
3.3.1	Synthesis of GHPA	49
3.3.2	Fabrication of GHPA hydrogel	49

3.3.3	Cell culture and maintenance	49
3.3.4	The use of an in-house hypoxia probe to compare resistance to hypoxic stress	50
3.3.5	Morphology of lung epithelial cell line (BEAS-2B) and decidual mesenchymal stromal cell line (DMSC23) on top of GHPA hydrogel	50
3.3.6	Cell viability of DMSC23 encapsulated inside GHPA hydrogel	51
3.3.7	Cell metabolic activity assay for DMSC23 encapsulated inside GHPA hydrogel	51
3.3.8	Measurement of mechanical properties of the hydrogel alone and with DMSC23 ...	52
3.3.9	Atomisation of DMSC23 in GHPA hydrogel and particle size measurement	52
3.3.10	Statistical analysis	52
3.4	Results and Discussion	53
3.4.1	Decidual mesenchymal stromal cell line (DMSC23) are more resistant to hypoxia compared to chorionic mesenchymal stromal cell line (CMSC29)	53
3.4.2	BEAS-2B and DMSC23 proliferate well on GHPA hydrogel	54
3.4.3	Cells encapsulated in GHPA hydrogel proliferate well and have high viability	54
3.4.4	Degradation of GHPA hydrogel and modification in hydrogel stiffness is detected using nanoindentation and advanced sensing measurement	55
3.4.5	Sprayed DMSC23-GHPA has similar cell viability to non-sprayed cells in hydrogel..	57
3.5	Conclusions	58
3.6	References	60
4	Extracellular vesicles (EVs) for the treatment of lung injury	
4.1	Overview	64
4.1.1	Graphical abstract	64
4.1.2	Highlights and keywords	64
4.1.3	Abstract	65
4.2	Introduction	66
4.2.1	Cell-free strategies for tissue regeneration	66
4.2.2	Roles of EVs in regenerative medicine	66
4.2.3	EVs in lung regeneration	67
4.3	Materials and Methods	69
4.3.1	Cell culture and maintenance	69
4.3.2	Isolation of EVs by ultracentrifugation	70
4.3.3	Measurement of size and concentration of EVs	70
4.3.4	Analysis of size and morphology of EVs	71

4.3.5	Analysis of EV molecular composition using atomic force microscope infrared spectroscopy (AFM-IR)	72
4.3.6	RNA isolation from EVs	72
4.3.7	OpenArray® for miRNA profiling of EVs	73
4.3.8	Atomisation of EVs and measurement of particle size	73
4.3.9	Assessment of cell migration and invasion upon EV treatment	73
4.3.10	Analysis of cellular responses to EV treatment after LPS injury	74
4.3.11	Measurement of cytokine release in response to LPS injury after EV treatment	74
4.3.12	Statistical analysis	75
4.4	Results and Discussion	75
4.4.1	Comparison of EV size and concentration	75
4.4.2	Comparison of EVs size and concentration before and after freeze-thaw	78
4.4.3	Analysis of EV molecular composition using AFM-IR	78
4.4.4	DMSC23 EVs and CMSC29 EVs are sprayable using LMA MAD780 device	80
4.4.5	DMSC23 EVs and CMSC29 EVs increase lung epithelial cell migration	81
4.4.6	DMSC23 EVs reduce cellular stress and inflammatory response caused by LPS	82
4.4.7	The therapeutic potential of DMSC23 EVs and CMSC29 EVs are attributed to the miRNA composition	83
4.5	Conclusion	85
4.6	Supplementary Figure	86
4.7	References	87
5	Resolving heterogeneity of extracellular vesicles using single-vesicle, nanoscale characterisation with high-resolution resonance enhanced atomic force microscope infrared spectroscopy (AFM-IR)	
5.1	Overview	93
5.1.1	Graphical abstract	93
5.1.2	Highlights and keywords	93
5.1.3	Abstract	94
5.2	Introduction	95
5.3	Materials and Methods	98
5.3.1	Cell culture for EV isolation	98
5.3.2	EV isolation and preparation for AFM-IR	98
5.3.3	Measurement of molecular composition of EVs using AFM-IR	99

5.4 Results and Discussion	99
5.4.1 AFM-IR enables purity assessment of the EV sample	99
5.4.2 AFM-IR enables probing multiple points on single vesicles	101
5.4.3 High resolution mapping of single vesicles using AFM-IR enables identification of differences between EVs from two types of placenta stem cells	103
5.5 Conclusions	105
5.6 References	107
6 The development of an <i>in vivo</i> smoke inhalation injury model	
6.1 Overview	110
6.1.1 Graphical abstract	110
6.1.2 Highlights and keywords	110
6.1.3 Abstract	111
6.2 Introduction	112
6.2.1 Small animal models of smoke inhalation injury	112
6.2.2 An overview of currently used smoke inhalation injury models	114
6.2.3 The development of a smoke inhalation injury model in mice	116
6.3 Materials and Methods	118
6.3.1 Designing a smoke inhalation chamber	118
6.3.2 Smoke inhalation injury regimen in mice	119
6.3.3 Histology of lung slices	120
6.4 Results and Discussion	120
6.5 Limitations and disadvantages	122
6.6 Conclusions and future work	123
6.7 References	124
7 Summary, outcomes and future directions	
7.1 Research significance	127
7.1.1 Summary	127
7.1.2 Key findings and conclusions	127
7.1.3 New development of research tools and methodologies arising from this thesis	128
7.2 Personal development as a researcher	129
7.2.1 Research field and skills acquired	129
7.2.2 Research highlights and collaborations	129
7.2.3 Research output and achievements	130

7.3 Perspectives and future directions	131
7.3.1 Limitations and future directions arising from this thesis	131
7.3.2 My next research	132
7.3.3 Future plans for my research career	132

Appendices

Appendix A. Protocol for EV characterisation using AFM-IR	134
Appendix B. Development of a ratiometric probe to assess cellular stress to hypoxia	157
Appendix C. Greater cellular stiffness in fibroblasts from patients with pulmonary fibrosis	163
Appendix D. Conference Presentations	182
Appendix E. List of Awards and Achievements	183

Acknowledgements

Firstly, I would like to thank my supervisor Associate Professor Wojciech Chrzanowski for unprecedented support throughout my research journey in both scientific and career-building aspects, as well as emotional support for life outside the lab. The encouragement and guidance I received over the years led me to be motivated throughout and enjoy the journey. I also thank my associate supervisor Professor Hak-Kim Chan for ongoing advice on the pulmonary delivery aspects and for being an influential Christian at work.

I thank Dr Gina Kusuma, Dr Bill Kalionis and his research group at the Royal Women's Hospital for setting the bar high for collaborative research and providing high quality training and ongoing advice for placenta stem cells and extracellular vesicles.

I acknowledge Professor Daniel Weiss and his research group for hosting me for four months of extensive training and ongoing advice on developing *ex vivo* lung models. I thank Dr Yiwei Wang, Dr Yuen Cheng and the team at ANZAC Research Institute for their generous support in establishing the *in vivo* and *ex vivo* models and providing training in histology and advanced imaging work. I thank Dr Elizabeth New, Kylie Yang, Professor Ki Dong Park, Professor Dong-Wook Han, Seung Bae Ryu, Associate Professor Janette Burgess and Dr Jade Jaffar for providing opportunities to demonstrate exceptional collaborative research.

I acknowledge Dr Donna Lai and Dr Sheng Hua for the provision and training in molecular biology work. I thank Naveena Gokoolparsadh for her training and help in sample preparations for imaging. I thank also Associate Professor Anandwardhan Hardikar, Dr Mugdha Joglekar and Wilson Wong for their generous support and help in microRNA profiling.

Thanks to my colleagues, especially Dipesh Khanal for AFM-IR work, Priyanka Tharkar for qEV work as well as Christina Limantoro, Kamini Divakarla and the ADDG colleagues for their emotional and friendly support. I would also like to acknowledge Isabel Bjørge and other colleagues who visited our lab for collaboration.

A huge, special thanks to my fiancé Kevin, my parents, sister and other family members, friends, colleagues and mentors who supported me in prayer, that I couldn't have done without. Most importantly, praise God for the journey through which I grew and gained invaluable skills.

List of Publications

Publications arising from this thesis:

1. **Kim, S.Y.**, Khanal, D., Tharkar, P., Kalionis, B., Chrzanowski, W. None of us is the same as all of us: resolving heterogeneity of extracellular vesicles using single-vesicle, nanoscale characterization with high-resolution resonance enhanced atomic force microscope infrared spectroscopy (AFM-IR). *Nanoscale Horizons* **2018** (advance article). (**Chapter 5**)
2. Bjørge, I.M.*, **Kim, S.Y.***, Mano, J.F., Kalionis, B., Chrzanowski, W. Extracellular vesicles, exosomes and shedding vesicles in regenerative medicine – a new paradigm for tissue repair. *Biomaterials Science* **2018**, 6:60-78. *Equal contribution. (**Introduction of Chapter 4**)
3. Reczyńska, K.*, Tharkar, P.*, **Kim, S.Y.***, Wang, Y., Pamuła, E., Chan, H.K., Chrzanowski, W. Animal models of smoke inhalation injury and related acute and chronic lung diseases. *Advanced Drug Delivery Reviews* **2018**, 123:107-134. *Equal contribution. (**Partly included in Chapter 1**)
4. **Kim, S.Y.**, Burgess, J., Wang, Y., Weiss, D., Chan, H.K., Chrzanowski, W. Aerosolized human amniotic mesenchymal stromal cells for targeted treatment of lung injury. *Journal of Aerosol Medicine and Pulmonary Drug Delivery* **2016**, 29(6):514-524. (**Chapter 2**)

Publications I contributed to during my thesis:

5. Yang, K., Leslie, K.G., **Kim, S.Y.**, Kalionis, B., Chrzanowski, W., Jolliffe, K.A., New, E.J. Tailoring the properties of a hypoxia-responsive 1,8-naphthalimide for imaging applications. *Organic and Biomolecular Chemistry* **2018**, 16:619-624. (**Partly included in Chapter 3; Appendix B**)
6. Jaffar, J., Yang, S.H., **Kim, S.Y.**, Kim, H.Y., Faiz, A., Chrzanowski, W., Burgess, J.K. Greater cellular stiffness in fibroblasts from patients with idiopathic pulmonary fibrosis. *American Journal of Physiology – Lung Cellular and Molecular Physiology* **2018**, in press. (**Appendix C**)

Manuscripts in preparation for publication:

7. **Kim, S.Y.**, Khanal, D., Kalionis, B., Chrzanowski, W. High-fidelity probing of the heterogeneity of extracellular vesicles by resonance enhanced atomic force microscopy infrared spectroscopy (AFM-IR). (**a protocol paper; Appendix A**)

Authorship Attribution Statement

Chapter 1 of this thesis is published as Reczyńska, K.*, Tharkar, P.* and Kim, S.Y.* *et al.* Animal models of smoke inhalation injury and related acute and chronic lung diseases. *Advanced Drug Delivery Reviews* 2018, 123:107-134 (*equal contribution). I performed extensive literature review, structured the contents and drafted the introduction and human smoke inhalation injury section, which is the part used for this thesis. I revised all sections of the manuscript and assisted with parts of the small and large animal model sections.

Chapter 2 of this thesis is published as Kim, S.Y. *et al.* Aerosolized human amniotic mesenchymal stromal cells for targeted treatment of lung injury. *Journal of Aerosol Medicine and Pulmonary Drug Delivery* 2016, 29(6):514-524. I co-designed the study and performed the experiments. I drafted and revised the manuscript.

Chapter 3 of this thesis includes a section from Yang, K., Leslie, K.G., and Kim, S.Y., *et al.* Tailoring the properties of a hypoxia-responsive 1,8-naphthalimide for imaging applications. *Organic and Biomolecular Chemistry* 2018, 16:619-624. I prepared the cells for testing the probes and drafted the cell culture related methods and results sections. I revised the manuscript.

The introduction of Chapter 4 was taken from Bjørge, I.M.*, and Kim, S.Y.* *et al.* Extracellular vesicles, exosomes and shedding vesicles in regenerative medicine – a new paradigm for tissue repair. *Biomaterials Science* 2018, 6:60-78. (*equal contribution). I performed extensive literature review, structured the contents, drafted and revised the review.

Chapter 5 of this thesis is published as Kim, S.Y., *et al.* None of us is the same as all of us: resolving heterogeneity of extracellular vesicles using single-vesicle, nanoscale characterization with high-resolution resonance enhanced atomic force microscope infrared spectroscopy (AFM-IR). *Nanoscale Horizons* 2018 (advance article). I co-designed the study and performed part of the experiments. I drafted and revised the manuscript.

Attesting the Authorship Attribution Statement

In addition to the statements above, in cases where I am not the corresponding author of a published item, permission to include the published material has been granted by the corresponding author.



Sally Yunsun Kim

19/04/2018

As supervisor for the candidature upon which this thesis is based, I can confirm that the authorship attribution statements above are correct.



Wojciech Chrzanowski

19/04/2018

Abbreviations

AFM	Atomic force microscopy
AFM-IR	Atomic force microscope infrared spectroscopy
ALI	Acute lung injury
ARDS	Acute respiratory distress syndrome
BALF	Bronchioalveolar lavage fluid
BEAS-2B	Immortalised human bronchial epithelial cell line
CaCl ₂	Calcium chloride
cDNA	Complementary deoxyribonucleic acid
CFU	Colony-forming unit
CMSC29	Chorionic mesenchymal stromal cell line
CO ₂	Carbon dioxide
COHb	Carboxyhemoglobin
COPD	Chronic obstructive pulmonary disease
DMEM	Dulbecco's Modified Eagle Medium
DMSC23	Decidual mesenchymal stromal cell line
DNA	Deoxyribonucleic acid
DNase	Deoxyribonuclease
ELISA	Enzyme-linked immunosorbent assay
ESCRT	Endosomal sorting complexes required for transport
EVs	Extracellular vesicles
FBS	Fetal bovine serum
GHPA	Gelatin-hydroxyphenyl propionic acid
H&E	Hematoxylin and eosin
H ₂ O ₂	Hydrogen peroxide
hAMSCs	Human amniotic mesenchymal stromal cells
HBSS(-)	Hanks' Balanced Salt Solution without calcium/magnesium
HRP	Horseradish peroxidase
IL	Interleukin
IR	Infrared
IRAK	Interleukin-1 receptor-associated kinase
KGF	Keratinocyte growth factor
kPa	Kilopascal

LPS	Lipopolysaccharide
MEM	Minimum essential media
MgSO ₄	Magnesium
mRNA	Messenger RNA (ribonucleic acid)
miR- or miRNA	microRNA
MSCs	Mesenchymal stem/stromal cells
NaCl	Sodium chloride
NO	Nitric oxide
NOS	Nitric oxide synthase
NpHy3	Nitronaphthalimide hypoxia probe
NTA	Nanoparticle tracking analysis
Pa	Pascal
PBS	Phosphate buffered saline
PCR	Polymerase chain reaction
Pen/Strep	Penicillin Streptomycin mixture
PFC	Perfluorochemical
PLL	Poly-L-lysine
qPCR	Quantitative polymerase chain reaction (also known as Real-Time PCR)
RT	Reverse Transcriptase
SDC	Sodium deoxycholate
SEC	Size-exclusion chromatography
SEM	Scanning electron microscopy
SERT	Serotonin transporter
STAT	Signal transducer and activator of transcription
THP-1	Human monocytic cell line
TNF- α	Tumor necrosis factor alpha
TRAF	TNF receptor associated factor
TRPS	Tunable resistive pulse sensing
UV	Ultraviolet

1.1 Inhalation injury

Inhalation injury as a result of the respiratory absorption of smoke or chemical products is a leading cause of death in thermally injured patients¹. Inhalation injury can lead to long-term pulmonary dysfunction with increased incidence of respiratory complications such as pneumonia or acute respiratory distress syndrome². Previous reports suggest that the severity of fire-induced inhalation injury is directly correlated with the surface area of burns². Approximately 60% of burn injured patients with a total surface area of burns over 70% present with inhalation injuries. The mortality rate of burn patients was reported to increase by a maximum 20% and 60% respectively with inhalation injury alone and with pneumonia³.

Inhalation injuries are classified into 1) upper airway injuries; 2) lower airway and parenchymal injuries and 3) metabolic asphyxiation (Fig. 1.2). Upper airway injuries are primarily caused by thermal injury to the mouth, oropharynx and larynx, while lower and parenchymal injuries are due to chemical and particulate constituents of smoke. Metabolic asphyxiation is induced by smoke constituents, such as carbon monoxide and cyanide, that impairs oxygen delivery to tissues⁴. Damages to the respiratory tract and lung trigger a robust inflammatory response with downstream effects of bronchoconstriction, increased vascular permeability, and vasodilation⁵. In addition, inhalation injuries may further potentiate local cellular damage and increase bronchial blood flow, resulting in the activation of polymorphonuclear leukocytes and cytokines to the lung⁶.

To study smoke inhalation and acute lung injury, initial high-throughput testing can be performed using *in vitro* systems. Depending on the research question, appropriate cells are selected and cultured in strictly controlled conditions (e.g. lung mimicking scaffolds, bioreactors, medium composition, temperature, humidity, air-liquid interface) for a given period of time⁷⁻⁹. Tested compounds are added to the

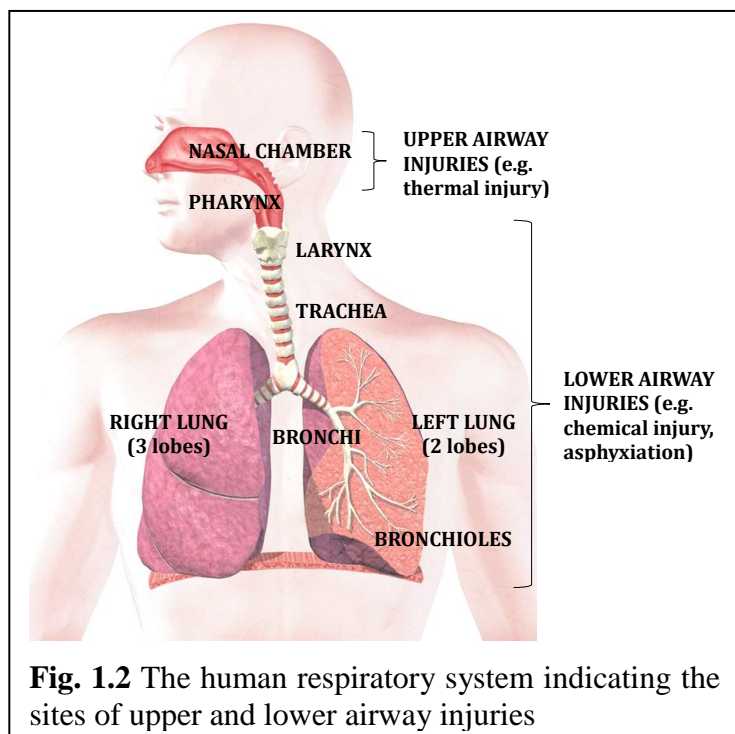


Fig. 1.2 The human respiratory system indicating the sites of upper and lower airway injuries

cultures and biological responses are monitored. Single cell cultures are commonly used to screen the toxicity of substances, but are also used to understand complex ideas and to answer complex mechanisms such as the differentiation of stem cells to repair lung structures¹⁰⁻¹². Although it is possible to create more complex systems *via* co-cultures^{13, 14}, three-dimensional cultures^{15, 16}, or by the application of mechanical or electrical stimuli¹⁷, *in vitro* models are limited in their ability to fully mimic the clinical responses post inhalation injury.

To address the limitations of *in vitro* systems, animal models have been widely used in research studies and have proven to be a useful tool for discovering therapeutic drugs and examining new therapeutic approaches¹⁸. From the currently available animal models, no system is capable of representing all the prominent features of human lung injuries. However, animal models are still highly essential to uncover pathological mechanisms, and understand the molecular and cellular aspects that characterise human lung injuries. Animal models offer the opportunity for researchers to manipulate some environmental variables to support new drug development, vaccine testing and the molecular interactions associated with the pathogenesis of many diseases¹⁹. The last part of this thesis presents a preliminary work on the development of an in-house smoking chamber for an *in vivo* model of smoke inhalation injury which can be utilised in future studies of smoke inhalation and acute lung injuries.

1.2 Smoke inhalation injury

1.2.1 Sources of smoke inhalation injuries

In fire incidents, the presence of particulate matter (e.g. soot), the magnitude of the exposure and individual factors such as pre-existing lung conditions, alter the severity of injury. Since the degree of inhalation injury depends on the material being burnt and gas components being inhaled²⁰, these factors need to be considered when establishing animal injury models.

The lower airway damage from smoke inhalation is attributed to toxic gases exerting asphyxiation, systemic toxicity, or causing direct damage on respiratory tissue. The common combustion products in residential fires due to burning of mineral fibres include carbon monoxide, hydrogen chloride, benzene, acrolein, hydrogen cyanide, sulphur dioxide and nitrogen dioxide, listed from highest to lowest concentration²¹. Smoke generated by cellulose, commonly found in wood, paper and cotton, contains acrolein and aldehydes, while polypropylene and acrylics, commonly found in carpeting, upholstery materials and textiles, also decompose to produce acrolein²². Polyvinyl chloride and polyester found also in upholstery materials and clothings, respectively, produce hydrogen chloride when decomposed.

Melamine resins in household and kitchen goods contribute to the production of hydrogen cyanide, ammonia and formaldehyde.

Carbon monoxide is released from incomplete combustion of carbon-containing fuels, such as gas, oil, wood and also from burning polystyrene, polyurethane²¹. Hydrogen cyanide gas is emitted from thermal decomposition of nitrogen-containing polymers and combustion of products containing carbon and nitrogen commonly from the burning of foam rubber, wool, plastics, and other synthetic materials²³. **The hypoxic fire environment, together with these asphyxiants displace oxygen at the alveolar level causing cellular hypoxia**²⁰. When carbon monoxide perfuses across the alveolar barrier, it binds to haemoglobin to form carboxyhemoglobin, with 210 times greater affinity than oxygen²⁴. Carbon monoxide binds to cytochrome oxidase at the mitochondrial level, impairing oxygen supply to mitochondria. Hydrogen cyanide inhibits electron transport and cellular respiration and also binds to cytochrome oxidase²³. Carbon monoxide and hydrogen cyanide poisoning are the main causes of immediate death in patients with smoke inhalation injuries.

Other sources of burns and inhalation injuries include modern warfare. Explosions in terrorist attacks or battlefields produce unique injury patterns in the lung. The injury patterns vary widely depending on the composition of the bomb and the amount of materials involved²⁵. The initial impact on the lung for primary blast injury include over-pressurisation which is the most fatal, while other casualties have lung injuries due to the inhalation of toxic gases. Toxic chemicals used in manufacturing chemical weapons can be classified into low lethality (e.g. chlorine, phosgene, hydrogen cyanide, cyanogen chloride) or high lethality (e.g. tabun, sarin, sulfur mustard, lewisite)²⁶. In addition, the World Health Organisation reported 4.3 million people per year die prematurely due to households cooking with solid fuels (e.g. wood, crop wastes, charcoal)²⁷. The repeated inhalation of black carbon (soot) particles and methane emitted by inefficient stove combustion leads to pneumonia, chronic obstructive pulmonary disease (COPD) and lung cancer, responsible for around 40% of those premature deaths, following cardiovascular diseases²⁷.

1.2.2 Complications of smoke inhalation injury and simulation in animal models

Clinically observed early complications of smoke inhalation injury include pneumonia and airway obstruction, while delayed complications include sepsis, tracheal stenosis, bronchiolitis obliterans, acute lung injury (ALI) and acute respiratory distress syndrome (ARDS). The inflammatory response activated by the thermal injury, together with impaired surfactant

production, decreased functions of ciliated cells and pulmonary macrophages, predispose patients to develop respiratory tract infections²⁸. The incidence of pneumonia increases with the severity of inhalation injury and the majority are diagnosed within the first week of inhalation injury²⁹. Airway damage and inflammation following smoke inhalation triggers the formation of obstructive airway casts made up of cellular debris, mucin and fibrin deposition³⁰. The resulting ventilation and perfusion mismatch, together with increased nitric oxide production causing impaired hypoxic vasoconstriction, lead to impaired oxygenation and ventilation and thus the development of ALI. In ALI, the arterial oxygen/inspired oxygen fraction less than 300 mmHg, whereas in ARDS the fraction is less than 200 mmHg^{31,32}. In the treatment of inhalation injury, intubation increases the risk of ventilator-associated pneumonia and subsequent ARDS³³. In a study conducted at the US Army Institute of Surgical Research burn centre, the prevalence of acute respiratory distress syndrome in military burn patients was as high as 32.6% and after diagnosis with severe ARDS, mortality rate is as high as 43.8%³⁴. Since these complications are important determinants of mortality in humans, it is important to consider them in animal models. Simulating these complications in animals are challenging due to the shorter duration of experiments and the delayed onset of some complications. Nevertheless, several studies have developed regimens to incorporate these complications in order to more accurately model the injury in animals.

A mouse model of ALI is well established in combination of burn and smoke inhalation injury, with animals meeting the criteria for diagnosis within 48 h³². Since nitric oxide has a critical role in the pathogenesis of ALI and ARDS, the nitric oxide synthase levels are measured in mice lung tissues to examine the response to different injury regimens. Similarly, the levels of lung myeloperoxidase, an enzyme that is released by neutrophils, is an indicator of the extent of injury in mice models as the patients suffering from ALI or ARDS clinically have a dramatic increase in pulmonary neutrophils. However, there are no bronchial mucus glands in mice in contrast to humans and thus the amount of mucus in the obstructive material is limited³². On the other hand, the formation of airway casts in ovine model is similar to that of the humans, composed of shed bronchial epithelial cells, fibrin, mucus and infiltrated neutrophils. There is more similarity in large animal models to simulate pneumonia due to the possibility of adopting mechanical ventilation. To simulate ALI in sheep model after smoke inhalation, live *Pseudomonas aeruginosa* ($2-5 \times 10^{11}$ CFU) in 30 ml saline solution is instilled into three lung lobes using a bronchoscope^{35,36}. Then sheep are mechanically ventilated with oxygen for 24 h before harvesting lung for injury assessment³⁵.

There are limited number of studies that investigate the long-term effects of smoke inhalation injuries. The first rat model which monitored the long-term effects of smoke inhalation demonstrated significant collagen deposition and fibrosis in lungs 28 days after wood smoke inhalation injury in rats³⁷. Further long-term studies would better mimic the complications observed in clinics after smoke inhalation injury.

1.2.3 Current management of smoke inhalation injury have limitations

The current management of smoke inhalation injury is thoroughly reviewed by many experts. Unfortunately, it has been identified that “the treatment of inhalation injury has not kept pace with improvements in the care of cutaneous burns”³⁸. Mortality data for smoke inhalation is disconcerting, given that at least 30% of burn patients with smoke inhalation injury die. Of all fire related fatalities 80-90% are attributed to smoke inhalation³⁹. Smoke inhalation is observed in 49% of explosion victims as well as rescue workers at the explosion site⁴⁰. The management of smoke inhalation injury requires improvement since the current treatment regimens are merely supportive and symptom relieving.

Asphyxiants such as carbon monoxide and cyanide are leading cause of poisoning deaths in fire incidents yet there are specific antidotes available: high-dose oxygen and hydroxycobalamin, respectively²³. Patients with carbon monoxide and cyanide poisoning often present with non-specific symptoms including headache, nausea, fatigue, irritability, confusion, vertigo, and flu-like symptoms, while more serious poisonings present with delirium, ataxia, dyspnoea, cardiovascular emergencies, seizures, coma and death²³. The administration of 100% oxygen is often the initial treatment as soon as inhalation injury is suspected, in order to reduce systemic toxicity / carboxyhemoglobin (COHb) levels as soon as possible⁴¹.

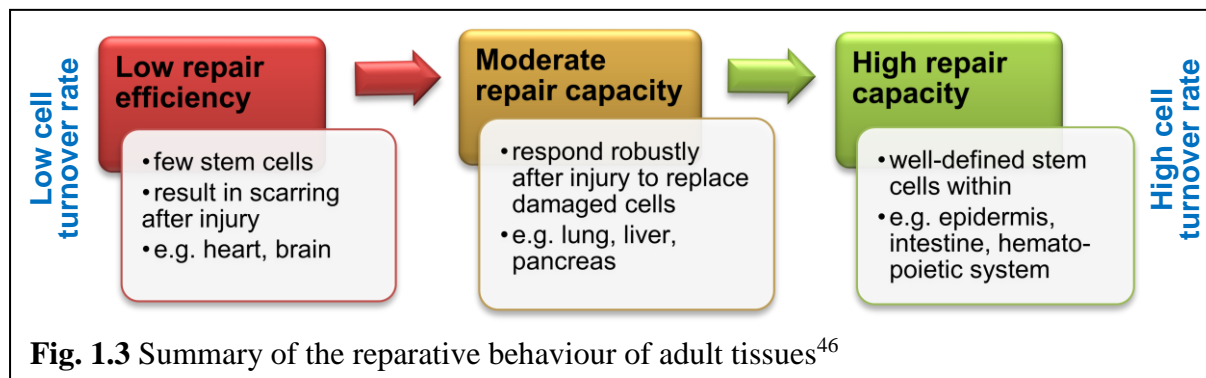
Immediate endotracheal intubation by the most experienced clinician in airway management is required in the case of acute upper airway obstruction, reduced level of consciousness, cardiac arrest and hypoventilation^{42, 43}. The removal of excess secretions, mucus and fibrin cast in the tracheal bronchial tree, which is essential to lower the risks of bronchial obstruction and pneumonia⁴². The techniques used to achieve this include bronchial hygiene therapy, chest physiotherapy, nasotracheal suctioning and therapeutic bronchoscopy. These procedures are continued for approximately a week in hospitals yet these are merely supportive procedures⁴². Mechanical ventilation is used when deemed necessary. The pharmacological adjuncts available include bronchodilators for bronchial muscle relaxation and stimulation of mucociliary clearance, epinephrine for vasoconstriction, bronchodilation and loosening

secretions, N-acetylcysteine combined with heparin to reduce mucus, fibrin casts and free radical damage and anti-inflammatory agents to mitigate the host inflammatory response²⁰. None of these treatment regimens are designed to actively support tissue regeneration after injury, thus regenerative medicine is a promising approach to ultimately improve treatment outcomes of patients with inhalation injury.

1.3 Stem cell-based therapy for lung injury

1.3.1 The innate repair capacity of the lung

The lung exhibits a low steady state cell turnover, particularly in the airways⁴⁴. Since less than 5% of lung epithelial cells proliferate at any given point in time⁴⁵, local self-renewal capacity is rarely needed under normal circumstances⁴⁴. However, the lung is considered to have a moderate repair capacity upon airway epithelial injury (Fig. 1.3), with capabilities to replace damaged cells quite robustly after injury⁴⁶. Therefore, numerous studies investigate the mechanisms and pathways that promote innate repair and renewal capacity of the lung⁴⁷⁻⁵⁰. On the other hand, there has been advances in stem cell therapy approaches to further accelerate the repair capacity in the lung. Mesenchymal stem/stromal cells (MSCs) have demonstrated high potential through pre-clinical studies in the last decade⁵¹⁻⁵³ and was used for this project.



1.3.2 Stem cell-based therapy for accelerating tissue regeneration in lung injury

Stem cell treatment, in particular using MSCs, alleviates lung injuries *via* anti-inflammation and immunomodulatory mechanisms as well as transfer of mitochondria as confirmed in numerous studies^{52, 54-56}. *Escherichia coli* endotoxin (lipopolysaccharide)-induced lung injury in animal models is a widely accepted model of ALI as it yields the clinical manifestations of ALI^{54, 57, 58}. The paracrine effects of MSCs are considered to be primarily responsible for the regenerative potential and increasing interest has focused on extracellular vesicles (EVs) and the bioactive molecules they release^{59, 60}. EVs regulate intercellular communication, which is necessary for multicellular organisms to maintain their vital functions. EVs are a cell-free alternative to current stem cell therapies with advantages of lower immunogenic response and

preservation of biochemical activity upon storage⁶¹⁻⁶³. The tantalising potential of stem cell-derived EVs for accelerating tissue regeneration is presented in Chapter 4.

1.4 Study design, hypothesis & aims

Despite ongoing advances in stem cell therapies, the improved treatment regimen of direct stem cell delivery to the airway has not been thoroughly investigated. Furthermore, although it is established that the mechanism of repair is *via* paracrine signals, there are limited methods to characterise these signals. Therefore, this study was designed to address these critical gaps.

1.4.1 Hypotheses

- Direct and targeted delivery of stem cells to the lung *via* inhalation facilitates functional tissue regeneration after smoke inhalation injury.
- The stem cells encapsulated in an *in-situ* cross-linking bioactive hydrogel platform survive well after being sprayed for direct airway delivery.
- Extracellular vesicles secreted by stem cells carry specialised signals to deliver the benefits of stem cell therapy.

1.4.2 Aims and summary of experiments conducted

Aim	Experiments / techniques
1. To demonstrate the feasibility to deliver stem cells <i>via</i> atomisation for direct delivery to the lung using a three-dimensional <i>ex vivo</i> lung model. (Chapter 2)	<ul style="list-style-type: none"> ▪ Cell viability, morphology apoptosis ▪ Cell atomisation ▪ Particle size measurement ▪ Measurement of substrate stiffness (AFM) ▪ <i>Ex vivo</i> assessment of cell distribution
2. To verify the ideal type of stem cell and synthesise a delivery platform with suitable properties for application in lung regeneration after injury. (Chapter 3)	<ul style="list-style-type: none"> ▪ Measure cells' resistance to hypoxic stress ▪ Hydrogel fabrication ▪ Cell viability, morphology in hydrogel ▪ Confocal microscopy imaging ▪ Atomisation of cells in hydrogel platform
3. To identify the potential mechanism of repair for DMSC23 and interrogate the mechanism of action through extensive characterisation of extracellular vesicles. (Chapter 4 & 5)	<ul style="list-style-type: none"> ▪ Isolation of EVs by ultracentrifugation ▪ EV characterisation by size, morphology and concentration ▪ Analysis of molecular composition and structure (AFM-IR, microRNA profiling) ▪ Functional analyses to assess the therapeutic potential of EVs
4. To generate an in-house smoke inhalation chamber and establish an <i>in vivo</i> smoke inhalation model using mice. (Chapter 6)	<ul style="list-style-type: none"> ▪ Designing a smoke inhalation chamber ▪ Establishing smoke inhalation injury model in mice ▪ Assessment of lung injury (histology)

1.5 References

1. de Carvalho, F.O., Silva, É.R., Felipe, F.A., Teixeira, L.G.B., Zago, L.B.S., Nunes, P.S., Shanmugam, S., Serafini, M.R., and Araújo, A.A.d.S., Natural and synthetic products used for the treatment of smoke inhalation: a patent review. *Expert Opinion on Therapeutic Patents* 2017(just-accepted).
2. Shirani, K.Z., Pruitt Jr, B.A., and Mason Jr, A.D., The influence of inhalation injury and pneumonia on burn mortality. *Annals of surgery* 1987, **205**(1):82.
3. Tanizaki, S., Assessing inhalation injury in the emergency room. *Open access emergency medicine: OAEM* 2015, **7**:31.
4. Association, A.B., Airway management and smoke inhalation injury, in *Advanced Burn Life Support Manual*. 2004, American Burn Association: Chicago. p. 16-20.
5. Kraneveld, A. and Nijkamp, F., Tachykinins and neuro-immune interactions in asthma. *International immunopharmacology* 2001, **1**(9):1629-1650.
6. Murakami, K. and Traber, D.L., Pathophysiological basis of smoke inhalation injury. *Physiology* 2003, **18**(3):125-129.
7. Sakagami, M., In vivo, in vitro and ex vivo models to assess pulmonary absorption and disposition of inhaled therapeutics for systemic delivery. *Adv Drug Deliv Rev* 2006, **58**(9-10):1030-60.
8. Sporty, J.L., Horáľková, L., and Ehrhardt, C., In vitro cell culture models for the assessment of pulmonary drug disposition. *Expert opinion on drug metabolism & toxicology* 2008, **4**(4):333-345.
9. Forbes, B., Human airway epithelial cell lines for in vitro drug transport and metabolism studies. *Pharmaceutical science & technology today* 2000, **3**(1):18-27.
10. Mendez, J.J., Ghaedi, M., Steinbacher, D., and Niklason, L.E., Epithelial cell differentiation of human mesenchymal stromal cells in decellularized lung scaffolds. *Tissue Engineering Part A* 2014, **20**(11-12):1735-1746.
11. Hogan, B.L., Barkauskas, C.E., Chapman, H.A., Epstein, J.A., Jain, R., Hsia, C.C., Niklason, L., Calle, E., Le, A., and Randell, S.H., Repair and regeneration of the respiratory system: complexity, plasticity, and mechanisms of lung stem cell function. *Cell stem cell* 2014, **15**(2):123-138.
12. Mendez, J.J., Ghaedi, M., Steinbacher, D., and Niklason, L.E., Epithelial Cell Differentiation of Human Mesenchymal Stromal Cells in Decellularized Lung Scaffolds. *Tissue Engineering. Part A* 2014, **20**(11-12):1735-1746.
13. Hermanns, M.I., Unger, R.E., Kehe, K., Peters, K., and Kirkpatrick, C.J., Lung epithelial cell lines in coculture with human pulmonary microvascular endothelial cells: development of an alveolo-capillary barrier in vitro. *Laboratory investigation* 2004, **84**(6):736-752.
14. Benam, K.H., Villenave, R., Lucchesi, C., Varone, A., Hubeau, C., Lee, H.-H., Alves, S.E., Salmon, M., Ferrante, T.C., and Weaver, J.C., Small airway-on-a-chip enables

- analysis of human lung inflammation and drug responses in vitro. *Nature methods* 2016, **13**(2):151-157.
15. Amann, A., Zwierzina, M., Gamerith, G., Bitsche, M., Huber, J.M., Vogel, G.F., Blumer, M., Koeck, S., Pechriggl, E.J., and Kelm, J.M., Development of an innovative 3D cell culture system to study tumour-stroma interactions in non-small cell lung cancer cells. *PloS one* 2014, **9**(3):e92511.
 16. Rutter, A.V., Chippendale, T.W., Yang, Y., Španěl, P., Smith, D., and Sulé-Suso, J., Quantification by SIFT-MS of acetaldehyde released by lung cells in a 3D model. *Analyst* 2013, **138**(1):91-95.
 17. Wirtz, H.R. and Dobbs, L.G., Calcium mobilization and exocytosis after one mechanical stretch of lung epithelial cells. *Science* 1990, **250**(4985):1266-1270.
 18. David, P., Dunsford, D., Lu, J., and Moochhala, S., Animal models of smoke inhalation induced injuries. *Frontiers in bioscience (Landmark edition)* 2009, **14**:4618-4630.
 19. Bonfield, T.L., In Vivo Models of Lung Disease, Lung Diseases - Selected State of the Art Reviews, ed. Dr. Elvisegran Malcolm Irusen (Ed.). 2012.
 20. Walker, P.F., Buehner, M.F., Wood, L.A., Boyer, N.L., Driscoll, I.R., Lundy, J.B., Cancio, L.C., and Chung, K.K., Diagnosis and management of inhalation injury: an updated review. *Critical Care* 2015, **19**(1):351.
 21. Savolainen, H. and Kirchner, N., Toxicological Mechanisms Of Fire Smoke. *The Internet Journal of Rescue and Disaster Medicine* 1997, **1**(1).
 22. Prien, T. and Traber, D.L., Toxic smoke compounds and inhalation injury—a review. *Burns* 1988, **14**(6):451-460.
 23. Albright, J.M., Davis, C.S., Bird, M.D., Ramirez, L., Kim, H., Burnham, E.L., Gamelli, R.L., and Kovacs, E.J., The acute pulmonary inflammatory response to the graded severity of smoke inhalation injury. *Crit Care Med* 2012, **40**(4):1113-21.
 24. Stephens, J. and El-Shammaa, E., Carbon monoxide and cyanide poisoning in smoke inhalation victims. *Trauma Reports* 2015(January).
 25. Atiyeh, B.S., Gunn, S.W.A., and Hayek, S.N., Military and Civilian Burn Injuries During Armed Conflicts. *Annals of Burns and Fire Disasters* 2007, **20**(4):203-215.
 26. Parrish, J.S. and Bradshaw, D.A., Toxic inhalational injury: gas, vapor and vesicant exposure. *Respir Care Clin N Am* 2004, **10**(1):43-58.
 27. Organisation, W.H. *Household air pollution and health*. Fact sheet No 292 2016 February 2016 23/06/2017]; Available from: <http://www.who.int/mediacentre/factsheets/fs292/en/>.
 28. Dries, D.J. and Endorf, F.W., Inhalation injury: epidemiology, pathology, treatment strategies. *Scand J Trauma Resusc Emerg Med*. 2013, **21**.
 29. Klein, K., Schense, J., Kronen, P.W., Fouche, N., Makara, M., Kämpf, K., Steffen, T., and von Rechenberg, B., Feasibility Study of a Standardized Novel Animal Model for Cervical Vertebral Augmentation in Sheep Using a PTH Derivate Bioactive Material. *Veterinary Sciences* 2014, **1**(2):96-120.

30. Miller, A.C., Elamin, E.M., and Suffredini, A.F., Inhaled Anticoagulation Regimens for the Treatment of Smoke Inhalation-Associated Acute Lung Injury: A Systematic Review. *Critical care medicine* 2014, **42**(2):413-419.
31. Kimmel, E.C. and Still, K.R., Acute Lung Injury, Acute Respiratory Distress Syndrome and Inhalation Injury: An Overview. *Drug and Chemical Toxicology* 1999, **22**(1):91-128.
32. Mizutani, A., Enkhbaatar, P., Esechie, A., Traber, L.D., Cox, R.A., Hawkins, H.K., Deyo, D.J., Murakami, K., Noguchi, T., and Traber, D.L., Pulmonary changes in a mouse model of combined burn and smoke inhalation-induced injury. *J Appl Physiol (1985)* 2008, **105**(2):678-84.
33. Burmeister, D.M., McIntyre, M.K., Beely, B., Jordan, B., Walker Iii, K.P., Aden, J.K., Batchinsky, A., Chung, K.K., Cancio, L.C., and Christy, R.J., A model of recovery from inhalation injury and cutaneous burn in ambulatory swine. *Burns*.
34. Belenkiy, S.M., Buel, A.R., Cannon, J.W., Sine, C.R., Aden, J.K., Henderson, J.L., Liu, N.T., Lundy, J.B., Renz, E.M., Batchinsky, A.I., Cancio, L.C., and Chung, K.K., Acute respiratory distress syndrome in wartime military burns: application of the Berlin criteria. *J Trauma Acute Care Surg* 2014, **76**(3):821-7.
35. Murakami, K., McGuire, R., Cox, R.A., Jodoin, J.M., Bjertnaes, L.J., Katahira, J., Traber, L.D., Schmalstieg, F.C., Hawkins, H.K., and Herndon, D.N., Heparin nebulization attenuates acute lung injury in sepsis following smoke inhalation in sheep. *Shock* 2002, **18**(3):236-241.
36. Maybauer, M.O., Maybauer, D.M., Fraser, J.F., Traber, L.D., Westphal, M., Enkhbaatar, P., Cox, R.A., Huda, R., Hawkins, H.K., Morita, N., Murakami, K., Mizutani, A., Herndon, D.N., and Traber, D.L., Recombinant human activated protein C improves pulmonary function in ovine acute lung injury resulting from smoke inhalation and sepsis. *Critical Care Medicine* 2006, **34**(9):2432-2438.
37. Zhu, F., Qiu, X., Wang, J., Jin, Y., Sun, Y., Lv, T., and Xia, Z., A rat model of smoke inhalation injury. *Inhalation Toxicology* 2012, **24**(6):356-364.
38. Woodson, L.C., Diagnosis and grading of inhalation injury. *J Burn Care Res* 2009, **30**(1):143-5.
39. Toon, M.H., Maybauer, M.O., Greenwood, J.E., Maybauer, D.M., and Fraser, J.F., Management of acute smoke inhalation injury. *Crit Care Resusc* 2010, **12**(1):53-61.
40. *Rapid Assessment of Injuries Among Survivors of the Terrorist Attack on the World Trade Center - New York City, September 2001*. Morbidity and Mortality Weekly Report 2002 [27/02/2016].
41. Rehberg, S., Maybauer, M.O., Enkhbaatar, P., Maybauer, D.M., Yamamoto, Y., and Traber, D.L., Pathophysiology, management and treatment of smoke inhalation injury. *Expert review of respiratory medicine* 2009, **3**(3):283-297.
42. Mlcak, R.P., Suman, O.E., and Herndon, D.N., Respiratory management of inhalation injury. *Burns* 2007, **33**(1):2-13.
43. Gill, P. and Martin, R.V., Smoke inhalation injury. *BJA Education* 2015, **15**(3):143-148.

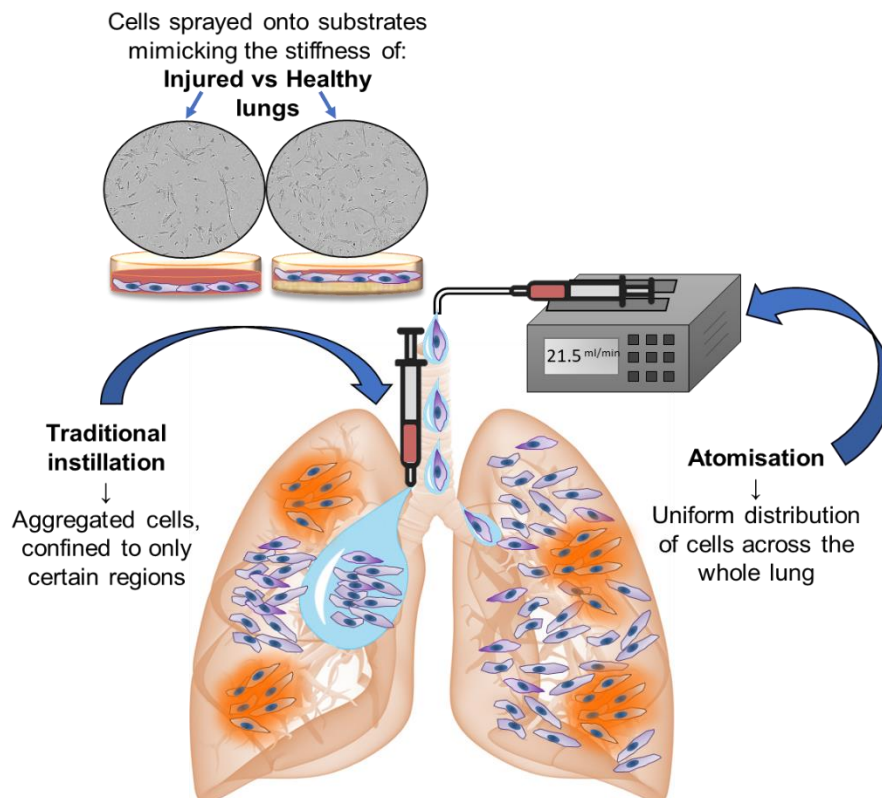
44. Yahaya, B., Understanding Cellular Mechanisms Underlying Airway Epithelial Repair: Selecting the Most Appropriate Animal Models. *The Scientific World Journal* 2012, **2012**:12.
45. Boers, J.E., Den Brok, J., Koudstaal, J., Arends, J.W., and Thunnissen, F., Number and proliferation of neuroendocrine cells in normal human airway epithelium. *American journal of respiratory and critical care medicine* 1996, **154**(3):758-763.
46. Hogan, B.L.M., Barkauskas, C.E., Chapman, H.A., Epstein, J.A., Jain, R., Hsia, C.C.W., Niklason, L., Calle, E., Le, A., Randell, S.H., Rock, J., Snitow, M., Krummel, M., Stripp, B.R., Vu, T., White, E.S., Whitsett, J.A., and Morrissey, E.E., Repair and regeneration of the respiratory system: complexity, plasticity, and mechanisms of lung stem cell function. *Cell stem cell* 2014, **15**(2):123-138.
47. Lynch, T.J., Anderson, P.J., Xie, W., Crooke, A.K., Liu, X., Tyler, S.R., Luo, M., Kusner, D.M., Zhang, Y., Neff, T., Burnette, D.C., Walters, K.S., Goodheart, M.J., Parekh, K.R., and Engelhardt, J.F., WNT SIGNALING REGULATES AIRWAY EPITHELIAL STEM CELLS IN ADULT MURINE SUBMUCOSAL GLANDS. *Stem cells (Dayton, Ohio)* 2016, **34**(11):2758-2771.
48. Dean, C.H. and Lloyd, C.M., Lung Alveolar Repair: Not All Cells Are Equal. *Trends in Molecular Medicine* 2017, **23**(10):871-873.
49. Poobalasingam, T., Yates, L.L., Walker, S.A., Pereira, M., Gross, N.Y., Ali, A., Kolatsi-Joannou, M., Jarvelin, M.-R., Pekkanen, J., Papakrivopoulou, E., Long, D.A., Griffiths, M., Wagner, D., Königshoff, M., Hind, M., Minelli, C., Lloyd, C.M., and Dean, C.H., Heterozygous *Vangl2^{Looptail}* mice reveal novel roles for the planar cell polarity pathway in adult lung homeostasis and repair. *Disease Models & Mechanisms* 2017, **10**(4):409-423.
50. Desai, T.J., Brownfield, D.G., and Krasnow, M.A., Alveolar progenitor and stem cells in lung development, renewal and cancer. *Nature* 2014, **507**(7491):190-4.
51. Geiger, S., Hirsch, D., and Hermann, F.G., Cell therapy for lung disease. *European Respiratory Review* 2017, **26**(144).
52. McIntyre, L.A., Moher, D., Fergusson, D.A., Sullivan, K.J., Mei, S.H.J., Lalu, M., Marshall, J., McLeod, M., Griffin, G., Grimshaw, J., Turgeon, A., Avey, M.T., Rudnicki, M.A., Jazi, M., Fishman, J., Stewart, D.J., and Canadian Critical Care Translational Biology, G., Efficacy of Mesenchymal Stromal Cell Therapy for Acute Lung Injury in Preclinical Animal Models: A Systematic Review. *PLOS ONE* 2016, **11**(1):e0147170.
53. Matthay, M.A., Goolaerts, A., Howard, J.P., and Lee, J.W., Mesenchymal stem cells for acute lung injury: Preclinical evidence. *Critical care medicine* 2010, **38**(10 Suppl):S569-S573.
54. Xu, J., Qu, J., Cao, L., Sai, Y., Chen, C., He, L., and Yu, L., Mesenchymal stem cell-based angiopoietin-1 gene therapy for acute lung injury induced by lipopolysaccharide in mice. *J Pathol* 2008, **214**(4):472-81.
55. Moodley, Y., Sturm, M., Shaw, K., Shimbori, C., Tan, D.B.A., Kolb, M., and Graham, R., Human mesenchymal stem cells attenuate early damage in a ventilated pig model of acute lung injury. *Stem Cell Research* 2016, **17**(1):25-31.

56. Weiss, D.J., Current Status of Stem Cells and Regenerative Medicine in Lung Biology and Diseases. *Stem cells (Dayton, Ohio)* 2014, **32**(1):16-25.
57. Xin, X., Yan, L., Guangfa, Z., Yan, H., Keng, L., and Chunting, W., Mesenchymal Stem Cells Promoted Lung Wound Repair through Hox A9 during Endotoxemia-Induced Acute Lung Injury. *Stem Cells International* 2017, **2017**:8.
58. Zhu, H., Xiong, Y., Xia, Y., Zhang, R., Tian, D., Wang, T., Dai, J., Wang, L., Yao, H., Jiang, H., Yang, K., Liu, E., Shi, Y., Fu, Z., Gao, L., and Zou, L., Therapeutic Effects of Human Umbilical Cord-Derived Mesenchymal Stem Cells in Acute Lung Injury Mice. *Scientific Reports* 2017, **7**:39889.
59. Gneccchi, M., He, H., Liang, O.D., Melo, L.G., Morello, F., Mu, H., Noiseux, N., Zhang, L., Pratt, R.E., Ingwall, J.S., and Dzau, V.J., Paracrine action accounts for marked protection of ischemic heart by Akt-modified mesenchymal stem cells. *Nat Med* 2005, **11**(4):367-8.
60. Sdrimas, K. and Kourembanas, S., MSC Microvesicles for the Treatment of Lung Disease: A New Paradigm for Cell-Free Therapy. *Antioxidants & Redox Signaling* 2014, **21**(13):1905-1915.
61. Konala, V.B., Mamidi, M.K., Bhonde, R., Das, A.K., Pochampally, R., and Pal, R., The current landscape of the mesenchymal stromal cell secretome: A new paradigm for cell-free regeneration. *Cytotherapy* 2016, **18**(1):13-24.
62. Sun, L., Xu, R., Sun, X., Duan, Y., Han, Y., Zhao, Y., Qian, H., Zhu, W., and Xu, W., Safety evaluation of exosomes derived from human umbilical cord mesenchymal stromal cell. *Cytotherapy* 2016, **18**(3):413-22.
63. Wu, Y., Deng, W., and Klinke Ii, D.J., Exosomes: improved methods to characterize their morphology, RNA content, and surface protein biomarkers. *Analyst* 2015, **140**(19):6631-6642.

2 Direct delivery of stem cells to the airway for uniform distribution of cells demonstrates potential technology for the treatment of lung injury

2.1 Overview

2.1.1 Graphical abstract



2.1.2 Highlights and keywords

- Cell atomisation is an innovative technology developed for pulmonary delivery.
- Direct delivery of mesenchymal stromal cells (MSCs) has potential for novel application in cell therapy for lung regeneration.
- MSCs survive well even after being sprayed onto substrates with high stiffness.
- Co-delivery of MSCs with collagen I directly to the lung may improve cell survival.
- This work sets the ground for future application in pulmonary regenerative medicine.

Keywords: Mesenchymal stromal cells, pulmonary delivery, cell atomisation, cell delivery, collagen, atomic force microscopy

Published in:

Mary Ann Liebert, Inc. publishers

Journal of Aerosol Medicine and Pulmonary Drug Delivery, Vol. 29, No. 6 | Original Research

Atomized Human Amniotic Mesenchymal Stromal Cells for Direct Delivery to the Airway for Treatment of Lung Injury

Kim Sally Yunsun, Burgess Janette K., Wang Yiwei, Kable Eleanor P.W., Weiss Daniel J., Chan Hak-Kim, and Chrzanowski Wojciech

Published Online: 1 Dec 2016 | <https://doi.org/10.1089/jamp.2016.1289>

2.1.3 Abstract

Current treatment regimens for inhalation injury are mainly supportive and rely on self-regeneration processes for recovery. Cell therapy with mesenchymal stromal cells (MSCs) is increasingly investigated for the treatment of inhalation injury. Human amniotic mesenchymal stromal cells (hAMSCs) have potential use in inflammatory and fibrotic conditions of the lung. This study aimed to demonstrate that hAMSCs can be atomised with high viability, for the purpose of achieving a more uniform distribution of cells throughout the lung. Another aim for this study was to set ground for future application to healthy and diseased lungs by demonstrating that hAMSCs were able to survive after being sprayed onto substrates with different stiffness.

Two methods of atomisation were evaluated and the LMA MAD780 device was selected for atomising hAMSCs for optimised delivery. In order to mimic the stiffness of healthy and diseased lungs, gelatin gel (10% w/v) and tissue culture plastic were used as preliminary models. Poly-L-lysine (PLL) and collagen I coatings were used as substrates on which the hAMSCs were cultured after being sprayed.

The feasibility of atomising hAMSCs was demonstrated with high cell viability ($81 \pm 3.1\%$ and $79 \pm 11.6\%$ for cells sprayed to plastic and gelatin, respectively, compared to $85 \pm 4.8\%$ for control/non-sprayed cells) unaffected by the different stiffness of substrates. The presence of the collagen I coating on which the sprayed cells were cultured yielded higher cell proliferation compared to both PLL and no coating. The morphology of sprayed cells was minimally compromised and demonstrated that hAMSCs are able to survive well after being sprayed to substrates with different stiffness, especially in the presence of collagen I. When the technology was used for other cell lines on an *ex vivo* rat lung model, the aerosolisation technology was demonstrated to be superior in obtaining uniform distribution of cells compared to the non-aerosol, traditional instillation of cells. Further studies may advance the effectiveness of cell therapy for lung regeneration.

2.2 Introduction

Cell-based therapy using MSCs is a rapidly advancing field of research for lung injury and lung diseases¹⁻³. Self-renewal and injury repair in the lungs are mostly achieved by the endogenous lung stem and progenitor cells upon activation during injury^{2,3}. However, there is an inherently limited regenerative capacity in the lung due to a low rate of cell turnover in some parts. Therefore, MSCs are being studied for promoting reparative and regenerative processes such as promoting angiogenesis, stimulating actions of endogenous progenitor cells, reducing fibrosis, and having anti-inflammatory and immunomodulatory effects³⁻⁵. Systemically administered MSCs have the ability to interact with injured cells at sites of tissue damage due to the expression of relevant cell surface proteins such as integrins and cell adhesion molecules on the MSCs^{6,7}.

A systematic review on smoke inhalation-associated acute lung injury reported that more than 70% of the patients with inhalation injury in a regional burn centre were diagnosed with respiratory failure and 20% with acute respiratory distress syndrome⁸. Current treatment for inhalation injury is mainly supportive, with oxygen and fluid therapies¹, medications to address the coexisting conditions such as bronchospasm and infections^{8, 9}, and heparin and N-acetylcysteine to prevent small airway obstructions^{9, 10}. These treatment regimens ultimately rely on self-regeneration processes for tissue recovery from the injury. However, inflammation caused by inhalation injury may become uncontrolled over time and cause ongoing lung injury¹¹ leading to oedema and fibrosis^{10, 12, 13}. The endogenous MSCs, which are dispatched in the response to injury, support the repair of the damaged tissue. This highlights that cell therapy using MSCs holds promising potential for such injuries, as MSCs may reduce inflammation and facilitate the recovery process through the downregulation of pro-inflammatory factors and the anti-inflammatory cytokines (e.g. IL-4 and IL-10) released by MSCs¹⁴. Furthermore, the growth factors secreted by the MSCs help maintain the functions of the endothelium and epithelium barriers after injury^{1, 12, 14}. However, the ability of MSCs to reach all parts of the lung is limited, particularly when the extracellular matrix and vasculature are damaged, as has been observed for this type of injury. Hence, an adequate supply of MSCs at the site of injury is required. Furthermore, in order to exert effects at the level of the airway epithelium, where most of the immediate injury takes place in smoke inhalation, intratracheal administration of the MSCs directly delivered to the injury site may be beneficial. Therefore, there is a need to optimise the technology to deliver cells directly to airways.

While the optimal source of MSCs for use in lung regeneration is increasingly being discussed, the most commonly investigated adult stem cells are those from bone marrow, adipose and placental tissue¹⁵⁻¹⁷. MSCs from human amniotic membrane (hAMSCs) are progressively of interest as they are easily accessible, available in large quantities and have minimal ethical concerns as they can be obtained from term placentas normally discarded after delivery¹⁸⁻²¹. In a comparison study of different sources of cells utilised in a murine model of sustained lung injury induced by bleomycin, hAMSCs had demonstrated superior anti-inflammatory and immunomodulatory properties compared to bone marrow MSCs and amniotic epithelial cells.²² The pre-clinical data of hAMSCs have provided a basis for the recent development of clinical investigations for the potential treatment of various lung inflammatory and fibrotic conditions, as well as the liver dysfunction associated with cystic fibrosis^{19, 22-25}.

In comparison to the increasing number of studies that investigate the use of MSCs for lung injury, there are limited numbers of studies on the techniques to deliver MSCs to the lung. The intratracheal route for MSCs administration can be as effective as intravenous administration in some lung injury models^{15, 26, 27} and thus intratracheal cell administration is increasingly being studied²⁸⁻³³. These studies have demonstrated the efficiency of direct delivery of cells for potential treatment of various lung diseases. However, there is room for improvement in the intratracheal MSCs delivery technique as most studies use a basic injection method for instillation of cells through the trachea for intratracheal administration of cells. Injection of cells through an intubation tube³² or a catheter³³ or oropharyngeal aspiration^{34, 35} was used yet no studies adopted a spraying technique to deliver cells intratracheally. Recent literature highlights the potential benefits of delivering cells directly to the lung by atomisation as it may promote and enhance the healing processes of various lung diseases^{36, 37}. Since the greatest challenge associated with the atomisation of cells is to maintain their survival, our study focused on this aspect while evaluating for the first time other associated factors such as substrate stiffness and the use of co-factors to enhance cell proliferation.

Several spraying systems have been developed for topical application of MSCs, including the one recently patented to deliver human adipose tissue MSCs to wounds and burns^{38, 39}. In parallel, atomising devices including the PennCenturyTM Microsprayer (model IA-1B) have been previously used to atomise fibroblasts for potential delivery to the lung^{36, 40}. The use of fibroblasts in these studies is not optimal for the treatment of lung injury and regeneration, as those cells are already differentiated and thus may not promote tissue regeneration. Some studies previously used an electrospraying device to atomise cells, including that of Braghirolli

et. al., that atomised MSCs from human deciduous teeth pulp⁴¹. However, this technique was designed for the application in repopulating scaffolds used for tissue engineering and is not applicable for delivering cells to lungs due to its complex design and the high voltage required to spray the cells. Therefore, a new potential atomising device, LMA[®] MADgic[®] MAD780 (LMA device), is proposed in this study and was compared to a PennCenturyTM device.

It should be highlighted that the LMA device we utilised to atomise the cells in our study is currently used as a medical device for airway intubation and there are no previous reports that demonstrate the ability of the LMA device to atomise cells. The mechanism of spraying using the LMA device is a simple spray nozzle similar to that of a common water spray bottle that utilises the pressure of pushing the syringe plunger to disperse the liquid to produce droplets. It requires weaker hydrodynamic stresses during the atomisation process compared to other methods such as nebulisers, which makes the device suitable for use with spraying of cells. This is a repurposing of the device that is clinically accepted for patients who require airway intubations, which highlights the translational value of this research. Furthermore, this adds significance for future application in patients with smoke inhalation injury, as airway intubations are one of the few current treatment options of inhalation injury in some patients at intensive care units.

Taken together, the use of cells that show desired bioactivity and the device that is clinically approved underpins the translational aspect of this research and highlights the high potential of this approach to effectively deliver cells to the airways. Currently, hAMSCs are utilised much less than other MSCs despite their high regenerative potential and the aforementioned benefits whilst this is the first time to report the use of the LMA device for the atomisation of cells. The particle size for optimal delivery of therapeutics (solid materials) to the airways is required to be between 1 and 10 μm , and less than 5 μm for the lower airways⁴². However, the fate of inhaled biological agents during the deposition in the airways is expected to be different and this requires further investigation. This study was designed to demonstrate the feasibility of atomising hAMSCs with high viability, for the purpose to achieve a more uniform distribution of cells throughout the lung. The atomisation of hAMSCs and direct delivery to the lung is an alternative, novel way of delivering cells for the treatment of lung conditions. This method is potentially more targeted and effective than cell injections.

To compare the distribution of cells delivered by atomisation and traditional instillation, we developed an *ex vivo* decellularised rat lung model by modifying a published protocol⁴³. Using

a cell line transfected with luciferase, we visualised the differences in cell distribution using the IVIS[®] imaging system. The effect of co-delivery of cells with perfluorochemical (PFC) liquid was also investigated. PFC is an inert liquid that has been used for several decades to facilitate respiration, due to its benefits of low surface tension and high respiratory gas solubility, known to support adequate oxygenation and carbon dioxide removal in the immature or injured lung⁴⁴. PFC has been previously used for enhancing the treatment of acute lung injury⁴⁵, improving delivery/distribution of gene therapy to the distal lung⁴⁶ and delaying altitude-induced pulmonary complications⁴⁷ in various animal models. The use of PFC in cell therapy has not been previously investigated and thus this is the first report for this application.

This study also included the evaluation of the response of the cells to the substrates which mimic different lung conditions. In this report, we aim to demonstrate that the hAMSCs are able to maintain high viability after being sprayed to substrates with different stiffness. We determined the effects of additional cues for cell attachment and proliferation. Furthermore, using a state-of-the-art *ex vivo* lung model, we assessed the uniformity of cell distribution after delivery by atomisation compared to the traditional instillation method. This study was designed to set the ground for future development and application to healthy and diseased lungs.

2.3 Materials and Methods

2.3.1 Cell culture and maintenance

hAMSCs were purchased from ScienCell (San Diego, CA, USA) and the MSCs Medium along with the supplied growth supplements and 5% fetal bovine serum (FBS) (Bovogen Biologicals, Keilor East, VIC, Australia) were used for the first two passages. Thereafter alpha-MEM (Sigma-Aldrich, Castle Hill, NSW, Australia) with 10% FBS was used with no compromise in cell growth. Cells were maintained at 37°C in 95% air and 5% CO₂ atmosphere and were passaged when approximately 80% confluent. Cells were used at passages 3-5 for all assays.

2.3.2 Preparation of substrates

Gelatin gel (10% w/v) was produced by dissolving gelatin from bovine skin (Type B, Bloom 75) (Sigma-Aldrich, Castle Hill, NSW, Australia) in heated deionised water. The gels were stored at 4°C and sterilised by exposure to UV and rinsing with 70% ethanol. Coatings using collagen I from rat tail (Invitrogen, Thermo Fisher Scientific, Scoresby, VIC, Australia) and poly-L-lysine (PLL) (Sigma-Aldrich, Castle Hill, NSW, Australia) were prepared as per the protocol from the manufacturers.

2.3.3 Determination of substrate stiffness using atomic force microscopy

To probe nanomechanical properties of gelatin gel, non-coated petri dish and collagen or PLL-coated dishes, force probe (MFP-3D-Bio, Santa Barbara, CA, USA) were used. Experiments were conducted using silicon nitride probes (ContGB-G, Budget Sensors, Sofia, Bulgaria). Prior to the indentation of the substrates, sensitivity and spring constant were measured for each probe. Inverse Optical Lever Sensitivity of the probe was measured by single indentation to freshly cleaved mica and calibrating the probe by finding the slope of Deflection vs. ZSensor deflection. Spring constant was measured using the thermal method in air. Next, to calibrate the sensitivity in the cell probing experiment, the sensitivity was measured in liquid (phosphate buffered saline (PBS)) using freshly cleaved mica and the same parameters (force and approach speed) as used for the following cell probing. On average sensitivity was 55 nm/V and the spring constant of the cantilever was ~0.06 N/m.

The stiffness was measured in PBS by indenting the substrate with maximum force 20 nN at the rate of 0.5 Hz and recoding force-deflection (F-D) curves. For each substrate minimum 10 points in different locations were measured. When calculating the stiffness (Young's modulus) of coated and uncoated substrates (non-coated tissue culture plastic, collagen and PLL), the Hertz model was used. Traditionally Hertz's model assumes no adhesion and is developed for ideally elastic materials. The elastic properties and the lack of adhesion of the substrate to the probe tip made this the most appropriate model for this study.

2.3.4 Cell spraying process and measurement of particle size

PennCenturyTM Microsprayer[®] Aerosoliser, model IA-1C (Penn-Century Inc., Wyndmor, PA, USA) was used as a handheld device and LMA[®] MADgic AirwayTM MAD780 (Teleflex Medical Australia, Mascot, NSW, Australia) was used with the syringe fitted onto a PHD 2000 syringe pump (Harvard Apparatus, Holliston, MA, USA) to feed cell suspension at 21.5 ml/min. For measuring the particle size distributions, Spraytec (Malvern Instruments Ltd, Worcestershire, UK) was used with refractive index of 1.0, measured for 4 seconds. Cells (2.5×10^4 cells/ml) were sprayed onto the substrates, collected and transferred to 96-well plates (2,500 cells per well) for subsequent assays.

2.3.5 Cell viability and apoptosis assays

To compare the cell viability and apoptotic profiles after spraying the cells onto the substrates with different stiffness (gelatin gel and tissue culture plastic), Muse[®] Caspase-3/7 Assay Kit (Merck Millipore, Bayswater, VIC, Australia) and Live/Dead Cell Staining Kit II (PromoKine,

Heidelberg, Germany) were used as per manufacturers' protocols. Cells seeded onto tissue culture plastic without being sprayed were used as the control group. Muse[®] Caspase-3/7 Assay Kit was validated using cells treated with hydrogen peroxide 1 mM for 24 h and ultraviolet (UVB) exposure at 275 nm for 30 min and a control sample (1:1 mixture of live and dead cells). Detailed methods of sample preparation for the validation of the apoptosis kit and the apoptosis profiles are included in the supplementary information and Fig. S2.1. DNA quantification using CyQUANT[®] NF Cell Proliferation Assay Kit (Thermo Fisher Scientific, Scoresby, VIC, Australia) and Cell Counting Kit (CCK-8) (Dojindo Molecular Technologies, Inc., Santa Clara, CA, USA) were used for long term cell viability tests as per manufacturers' protocols.

2.3.6 Assessment of cell morphology

Live cell imaging was conducted using IncuCyte ZOOM[®] (Essen BioScience, Ann Arbor, Michigan, USA) for phase contrast images, taken every two hours on 10 x magnification. Selected images were analysed and exported using the IncuCyte ZOOM[®] 2015A GUI software. For immunofluorescence, standard immunostaining procedures were used for actin and nuclei staining. Briefly, cells were fixed with paraformaldehyde 4% for 10 min, blocked using bovine serum albumin 1% for 60 min and stained with Phalloidin CruzFluor[™] 514 for 30 min and DAPI 300 nM for 5 min (All reagents from Thermo Fisher Scientific, Scoresby, VIC, Australia). Immunofluorescence images were taken using the Fluoview FV1000 confocal laser scanning microscope (Olympus Imaging Australia Pty Ltd, Macquarie Park, NSW, Australia).

2.3.7 Development and characterisation of decellularised *ex vivo* lung model

Sprague Dawley rats at 12 weeks old were euthanised using carbon dioxide. Rat lungs were decellularised over 3 days using an optimised sequential instillation of detergents and rinsing through both trachea and the right ventricle, developed after scaling up similar methods developed for mouse lungs^{43, 48}. Briefly, heart-lung blocs were removed following euthanasia and cannulation of trachea. Decellurisation involved flushing of 20 mL of the following reagents through the cannulated trachea and right ventricle, five times each, with lungs allowed to deflate in between flushes: deionised water containing 5 × penicillin / streptomycin (Pen/Strep, Thermo Fisher Scientific) then 0.1% Triton-X 100 containing 5 × Pen/Strep in deionised water on Day 1, deionised water containing 5 × Pen/Strep then 2% sodium deoxycholate (SDC) on Day 2, with 24 h incubation of lungs on a shaker at 4°C, submerged in the final flushed reagent each day. On Day 3, after flushing five times with deionised water containing 5 × Pen/Strep, lungs were flushed and incubated in 1 M sodium chloride (NaCl) and

5 × Pen/Strep in deionised water for 1 h at room temperature. After removing from the NaCl solution, lungs were flushed five times with deionised water containing 5 × Pen/Strep, then flushed and incubated in porcine pancreatic DNase 30 µg/ml, 1.3 mM MgSO₄, 2 mM CaCl₂ and 5 × Pen/Strep in deionised water for 1 h at room temperature. Finally, lungs were flushed five times with 1 × PBS containing 5 × Pen/Strep then stored at 4°C until utilised.

Histology and DNA quantification of decellularised lungs

The extent of decellularisation was confirmed by histology using hematoxylin and eosin (H&E) and Trichrome stains, DNA quantification using gel electrophoresis and NanoDrop™ spectrophotometer, and mass spectrometry. For histology, the ancillary lobes were removed and cannulated *via* the airway, where 4% paraformaldehyde was passed through the tissue sample by gravity then incubated in 4% paraformaldehyde overnight. After flushing with water, samples were embedded in paraffin and 5 µm sections were mounted on glass slides then deparaffinised. Then sections were stained with H&E and Masson's Trichrome were assessed by light microscopy (EVOS, Invitrogen). For DNA quantification using DNeasy® Blood and Tissue kit (Qiagen), approximately 12 mg of the right cranial lobe was removed, cut into small pieces and digested in proteinase K. Following the manufacturer's protocol, DNA was isolated using a column-based method and DNA was eluted in 200 µl buffer for measurement using a NanoDrop™ spectrophotometer. DNA gel electrophoresis was run at 140 volts for 75 min, on a freshly made agarose gel and SYBR® safe DNA gel stain (Thermo Fisher Scientific), with salmon sperm as control.

Sample preparation for mass spectrometry

Approximately 30 mg of dried decellularised lungs were homogenised using lysis buffer, centrifuged at 1200 rpm for 5 min to remove debris and tissue then supernatant containing proteins was collected and boiled for 60-90 s. The concentrations of proteins were measured using NanoDrop™ spectrophotometer and SDS-PAGE was conducted using a standard protocol. Briefly, 15 µl of each sample (homogenised previously in lysis buffer) and duplicates for rats 2, 3 and 5, together with 10 µl SeeBlue® Plus2 pre-stained protein standard (Thermo Fisher Scientific) were placed in each pocket of the gel. Electrophoresis was run at 120 V for 50 min. Gel was stained with Coomassie Blue staining on a shaker at room temperature for 2 h. De-staining to remove background staining was done on a shaker at 4°C overnight. For proteomics, gel was divided into sections A-D (Fig. 2.5D). Section C was selected for proteomics, therefore cut into small pieces and protein was digested for 5 h, then

mass spectrometry was conducted to screen 790 proteins using a standard protocol at the proteomics facility.

2.3.8 Assessing cell distribution in the *ex vivo* lung models by histology

Decellularised lungs reseeded by the traditional instillation method and atomisation method were compared. The assessment of cell distribution in the *ex vivo* lung models required at least 25-75 million cells for filling of the *ex vivo* rat lungs. Since this high number of cells was unable to be achieved using hAMSCs, mouse MSCs derived from bone marrow of adult male C57B1/6 mice were used as a proof of concept for the assessment of cell distribution by histology. Mouse MSCs were prepared for reseeding 25 million cells per left lobe of decellularised rat lung (the right lobes were sutured off). Prior to delivering cells, the PBS containing high concentration of antibiotics was flushed out of the lung by passing through 20 ml complete media 2 to 3 times. For traditional instillation, the cell suspension was transferred into a 10 ml syringe and plunger was extracted to the maximum capacity. The syringe containing the cell suspension was screwed onto the cannula fitted inside the trachea, then the plunger was pulled out to let the cell suspension to fill the lung by gravity. For delivery of cells by atomisation using LMA[®] MAD780, the cannula was taken out from the trachea immediately after filling the lung with complete media then the nozzle of LMA device connected to syringe filled with cell suspension was placed approximately 1 cm above the carina. The cell suspension was pushed with enough force to ensure aerosolisation of the cell suspension. After overnight incubation at 37°C and 5% CO₂, lungs were fixed using 4% paraformaldehyde using the method described above. The sample preparation, staining used for histology and cell distribution assessment by light microscopy were as described above in section 2.3.7, to compare between traditional instillation and atomisation methods.

2.3.9 Assessing cell distribution by bioluminescence imaging

Transfection of cells using luciferase was required for three-dimensional visualisation of the cell distribution in the lungs using the bioluminescence imaging system (IVIS[®] Spectrum, PerkinElmer, Melbourne VIC Australia). Since the transfection efficiency of the mesenchymal stromal cells and proliferation rate after transfection were below the desired limit despite trying multiple methods – 4D-Nucleofector[™] (Lonza, Bella Vista NSW Australia), Lipofectamine (Thermo Fisher Scientific) and FuGENE[®] (Promega, Alexandria NSW Australia) were all successful in obtaining transient transfection but stable selection was not achieved – and we were unable to test whether the transfection was affecting the functionality of the cells, we used

mouse mesothelioma cell lines (AB12) that were previously stably transfected. The morphology and size of AB12 were comparable to the MSCs, therefore, for the purpose of IVIS imaging of cells inside *ex vivo* lungs and proof of concept comparing cell distribution upon delivery by traditional instillation or atomisation, AB12 cells were used.

Luciferase transfection and bioluminescence imaging

Briefly, AB12 cells were transfected using the 4D-Nucleofector™ system (Lonza) according to manufacturer's instructions, pre-set (FF104), with 0.1 µg plasmid DNA (containing PGL4.51 (luc2/CMV/Neo) construct) cocktail. Transfected cells were cultured on 96-well plate and replaced medium at 16 h post-transfection with selection medium containing Geneticin® selective antibiotics (500 µg/ml, Thermo Fisher Scientific). On day 7, the confluent cells were trypsinised and reseeded onto 6-well plates and continued to expand under Geneticin® selection medium. The luciferase activity inside cells were confirmed by adding luciferin substrate (Promega) and measurement on the FLUOstar Optima plate reader (BMG LabTech, Ortenberg, Germany).

For the addition of luciferase-transfected AB12 cells inside the *ex vivo* rat lungs, cells were prepared at 75 million cells per whole lung, resuspended in 5 ml complete media (DMEM with 10% FBS). Cells were delivered by traditional instillation or atomisation methods as described above in section 2.3.8 and immediately the luciferin substrate was added to the cells as per manufacturer's protocol. The dish containing the lungs were transferred to the stage inside the IVIS imaging system and were imaged at 3, 5 and 10 min after the addition of the substrate.

2.3.10 Statistical analysis

All data were produced in triplicates ($n = 3$) and presented as means \pm standard deviation. The differences between the conditions and coatings were analysed using one-way analysis of variance (ANOVA) test, with Tukey's multiple comparisons test, to report statistical significance when p-value was less than 0.05.

2.4 Results and Discussion

2.4.1 Atomisation of human amniotic mesenchymal stromal cells (hAMSCs) was superior using the LMA device compared with a PennCentury device

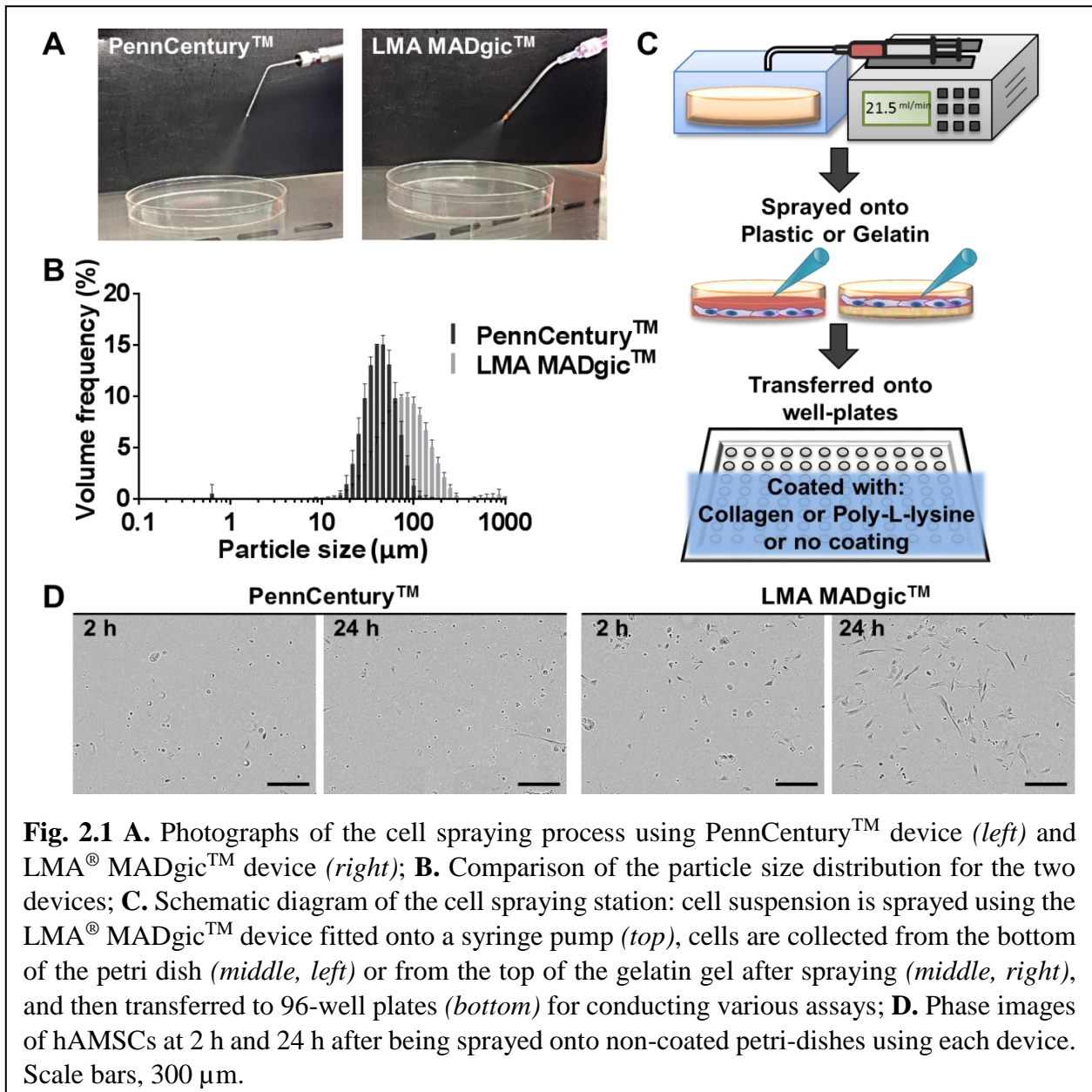
This study demonstrates for the first time that an atomised formulation is possible for hAMSCs for direct delivery to the injured site of the lung using a currently used medical device for airway intubation in clinics. While it has been identified that the ability to maintain cell viability during the spraying process is specific for each cell type, mainly depending on the size of cells

in relation to the nozzle diameter of the atomiser³⁶, it is significant that our research reports that hAMSCs can be atomised with high viability. For future application in patients with smoke inhalation injury, our focus was to deliver cells in an atomised form that would allow uniform distribution and migration of the cells to the critical regions in the trachea and the upper airways, where there are more occurrences of both thermal and chemical injuries in burn victims.

In preliminary studies, hAMSCs (purchased from ScienCell™, San Diego, CA, USA) were sprayed initially using either a PennCentury™ Microsprayer IA-1C or an LMA® MADgic Airway™ MAD780 device (Fig. 2.1A). However, due to the smaller size of the droplets produced by the PennCentury™ Microsprayer, as observed in the particle size distribution (Fig. 2.1B), the device had to be excluded as the droplets were too small to contain an entire cell (hAMSCs are between 17 and 28 µm in diameter (measured when trypsinised/in suspension)). Furthermore, the flow rate of the cell suspension from the handheld PennCentury™ Microsprayer device was limited to the hand strength of the individual users which led to it being uncontrollable and inconsistent. The LMA device yielded higher viability of cells after spraying and the spraying process was better controlled by fitting the syringe of the device onto a syringe pump and using a pre-optimised flow rate of 21.5 ml/min for aerosol production from the LMA device (Fig. 2.1C). This enabled the spraying process to be more consistent between users as the flow rate is controlled and reproducible. Microscopic analyses of cell morphology demonstrated that the cells sprayed using the PennCentury™ Microsprayer were shredded and there was periodic blocking of nozzle during the spraying process (Fig. 2.1D). While it is to be noted that the PennCentury™ devices are designed for animal use (and often considered as the ‘gold standard’) and are no longer commercially available, our study aimed to demonstrate the superiority of the LMA device compared to the PennCentury™ IA-1C device for atomising hAMSCs. The LMA device has other benefits for future research and clinical translation including commercial availability and its current use in medical practice for humans. Hence the LMA device was selected for the subsequent experiments in this study, and its new application for cell therapy was presented.

2.4.2 Substrates with different stiffness were designed to compare the mechanical stresses that cells are exposed to when “landing”

There has been no previous report on the analysis of mechanical stress related to the ‘landing’ of the atomised MSCs on substrates with different stiffness. In the aforementioned studies that atomised fibroblasts^{36, 40}, the viability of cells measured were related to the mechanical stresses the cells were exposed during the atomisation process, without measuring the stiffness of



substrates on which the cells landed. Kardia *et. al.* atomised cells directly into a flask containing liquid medium³⁶ while in the work of Sosnowski *et. al.*, ‘cell survival was analysed solely in the liquid emitted as aerosol’⁴⁰. These approaches do not mimic a potential environment of the lung and do not facilitate studying the effects of different level of mechanical stress to which the cells are exposed to, i.e. the landing of cells on the substrate. This was considered in our study as it may affect the viability and proliferation of the cells after being atomised. These findings may advance this field of research for future translation to *in vivo* studies.

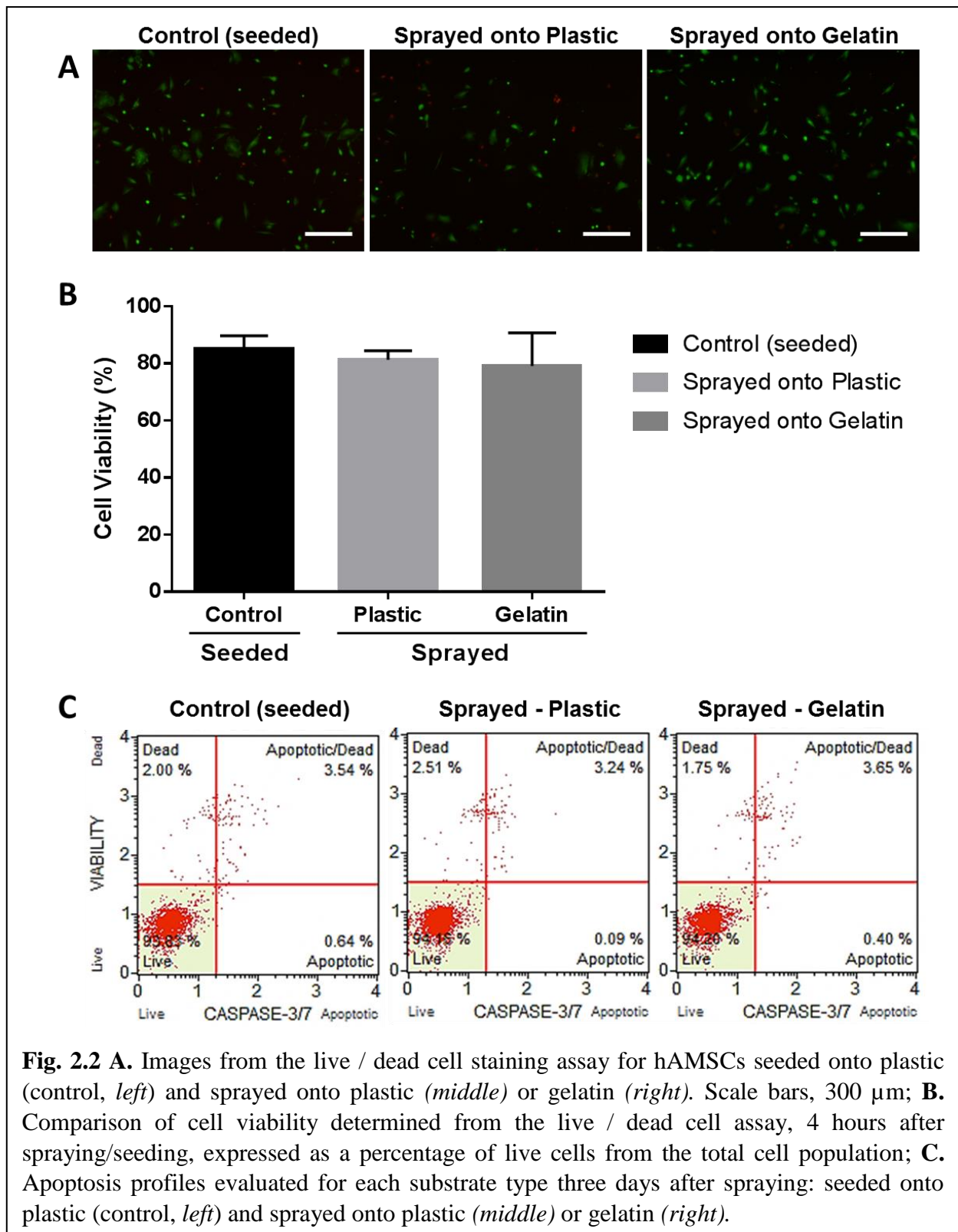
The two major factors that determine the survival of cells after the spraying process were tested in this study – the stiffness of the substrate onto which the cells were sprayed and the cues available for cell attachment and proliferation. Firstly, to examine an impact of mechanical

stress when cells landed on the substrate we considered two materials with distinctively different stiffness: ‘soft’ that mimics healthy lungs (gelatin gel), and extreme opposite ‘hard’ surface that represents hard tissues (tissue culture plastic). The use of different stiffness in this study was for the purpose to highlight that the cells are able to survive after being sprayed onto surfaces of varying stiffness. Preliminary studies demonstrated that the distance from the nozzle of sprayer to the recipient substrate had minimal impact; therefore 5 cm distance was used consistently for all experiments. The gelatin gels used in this study were 10% (w/v) with approximately 1 cm thickness and the stiffness of 8 kPa, which mimic the stiffness of healthy lung tissues. In contrast to the thin gelatin coatings used to help the attachment of cells on tissue culture plates (typically 0.1% (w/v)), our gelatin gel used as a model of healthy lung tissue was not designed for long term culture of cells. The stiffness of gelatin gel and tissue culture plastic were averaged 8 kPa and 1.2 GPa respectively, as determined from nanoindentation using atomic force microscopy (AFM). This stiffness of the gelatin gel corresponds to the rigidity of healthy lung, 2-10 kPa⁴⁹, while the stiffness of tissue culture plastic represents extreme conditions cells may experience – ‘hard’ substrate. The gelatin gel in this study was used solely for the purpose of mimicking the softer substrate at the time of spraying, not for enhancing cell attachment.

2.4.3 The atomisation of the hAMSCs maintained a high viability of the cells

The initial cell viability was quantified at the time of atomisation onto the substrates with different stiffness, immediately after the mechanical stresses experienced by the cells. Then subsequently, in order to observe whether the spraying process (mechanical stress) affected the long-term cell viability, it was necessary that the cells were collected immediately after spraying to be expanded in the same conditions on well plates for other long-term assays (Fig. 2.1C). This approach was required to reduce the effects of stiffness on cell growth.

When a live/dead cell staining assay was performed 4 hours after spraying onto the gelatin or plastic surfaces, the majority of the sprayed hAMSCs were found to be viable (Fig. 2.2A). Cells seeded directly onto the tissue culture plates without being sprayed were used as the control group. The assessment of the viability of cells sprayed onto gelatin and plastic showed that the cells did not have a compromised viability, ($81 \pm 3.1\%$ and $79 \pm 11.6\%$ for cells sprayed to plastic and gelatin, compared to $85 \pm 4.8\%$ for control/non-sprayed cells) confirmed with no statistically significant differences in viability compared to control (Fig. 2.2B).



Prior to investigating the effects of the addition of co-factors such as collagen I or PLL, the impact of the spraying process was investigated using an apoptosis assay. The apoptotic profiles confirmed that the cells sprayed onto gelatin had a similar apoptotic profile compared to the non-sprayed control group (Fig. 2.2C). The cells sprayed onto plastic had a slightly

higher percentage of dead cells but did not show a significantly different apoptotic profile compared to the other groups. The results confirmed that the mechanical stress caused by the atomisation process, regardless of stiffness of substrate, was well tolerated by the hAMSCs. Through these analyses the use of the LMA device, at these atomising parameters, was validated for future application to lungs with varying stiffness, as may result from lung injuries.

In contrast to other pharmaceutical aerosol products, the conventional *in vitro* approaches (impactors) that are used to establish the distribution of particles cannot be used for studying cell delivery. The anticipated distribution of the hAMSCs in the lung cannot be precisely determined from the particle size measurements, as the cells are viable and thus can migrate. Previous *in vivo* studies investigating the migration of MSCs in the lung after intratracheal instillation in various lung disease models demonstrated that MSCs have the capacity to migrate to different regions by responding to different chemoattractants and homing signals^{50, 51}. Therefore, to determine the actual distribution of the hAMSCs delivered *via* atomisation, animal models are required, which was beyond the scope of this study. It was not the scope of this study to use animal models with injury since the objectives were in the fundamental science of ensuring the cell viability during the atomisation process and identifying the conditions in which the cells could survive after being atomised (using varied stiffness of substrate and functionalisation). However, the distribution of the cell suspension in lungs, as produced in this study, is more uniform compared to the conventional intratracheal instillation without atomisation as discussed in 2.4.5.

2.4.4 Sprayed cells cultured on collagen I-coated plate yielded higher cell proliferation

After establishing that hAMSCs could be sprayed with high viability, the impact of the two commonly used coatings – collagen I and PLL – was investigated. This study tested whether the presence of PLL or collagen enhanced the attachment and proliferation of cells. There are no previous reports that measured proliferation of cells on substrates that were functionalised with different biomolecules after exposing the cells to the mechanical stress of atomisation. Previous studies used non-coated plastic substrates that do not mimic cellular environments in any way. The purpose of functionalisation with biomolecules was to assess whether there was an advantage to delivering them together with the cells as they could overcome the mechanical stress of atomisation and landing on a substrate with high stiffness. This part of the study was necessary also to determine whether the atomisation of cells disrupts their ability to proliferate on both collagen I and PLL-coated plates.

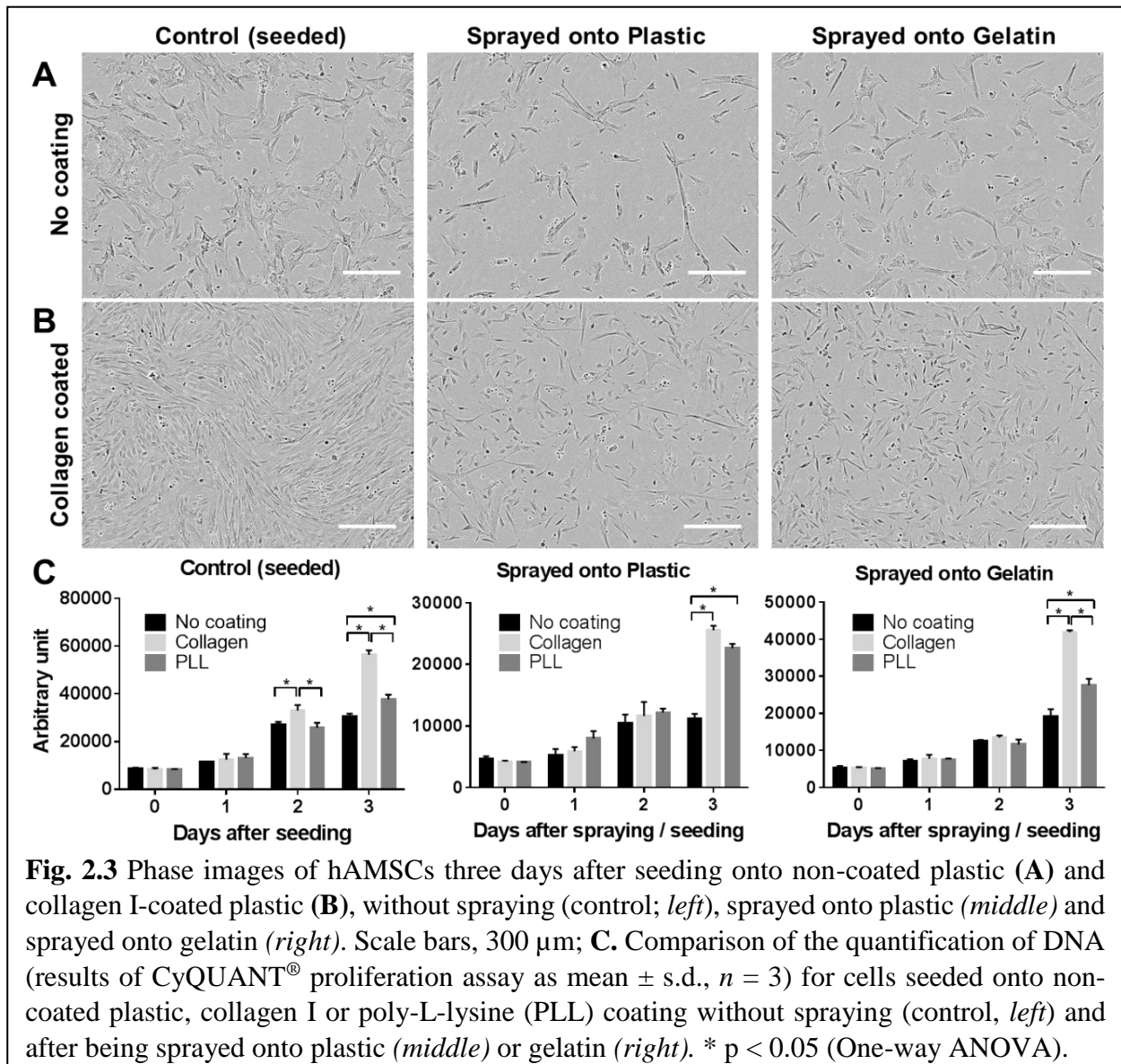
Preliminary studies comparing the growths of cells sprayed directly onto collagen I-coated plate and those sprayed onto non-coated plastic then transferred to collagen I-coated plate found no statistical differences (Fig. S2.2). The long-term cell quantification assays were utilised to investigate how the different coatings (collagen I / PLL / non-coated tissue culture plastic) affected migration and proliferation of the sprayed cells. Both coatings provide chemical cues for cells to attach and then proliferate. The disruption of the proliferation would suggest that cells were impacted by the mechanical stress during the atomisation and landing on different substrates. Collagen I is an extracellular matrix protein that promotes cell adherence *via* interaction with integrins $\alpha_v\beta_1$ and $\alpha_2\beta_1$ ⁵². PLL is a poly-cation which binds to DNA and enhances the electrostatic interaction with the negatively-charged ions on the cell membrane⁵³. Non-coated plastic was used as a control. We hypothesised that the presence of collagen I or PLL incorporated at the cell binding sites *via* pre-treatment or co-delivery with the cells would be beneficial for cell adhesion and growth.

In addition, we have measured the stiffness of these functionalised dishes, which has not been previously demonstrated despite its substantial impact on cell growth. The average stiffness of the collagen I and PLL-coated surfaces were 70.27 ± 23.37 MPa and 170.36 ± 35.50 MPa respectively, as determined by nanoindentation on the AFM. These were higher than gelatin gel and lower than non-coated tissue culture plastic (averaged 8 kPa and 1.2 GPa as mentioned above). It is important to highlight that both collagen and PLL coatings are thin (monolayers – a few nanometers) thus nanoindentation results are affected by the substrate stiffness due to the indentation depth which is greater than 10% of the coating thickness. As a rule of thumb, to reduce the influence of substrate on the measurement of the coating stiffness, the indentation depth should not exceed 10% of the coating thickness⁵⁴. To measure the stiffness of collagen I and PLL coatings only, the depth of the indentations should be in the Å range, which coincides with the noise level of the AFM and thus the data would not be reliable. However, the experimental conditions used here are commonly accepted.

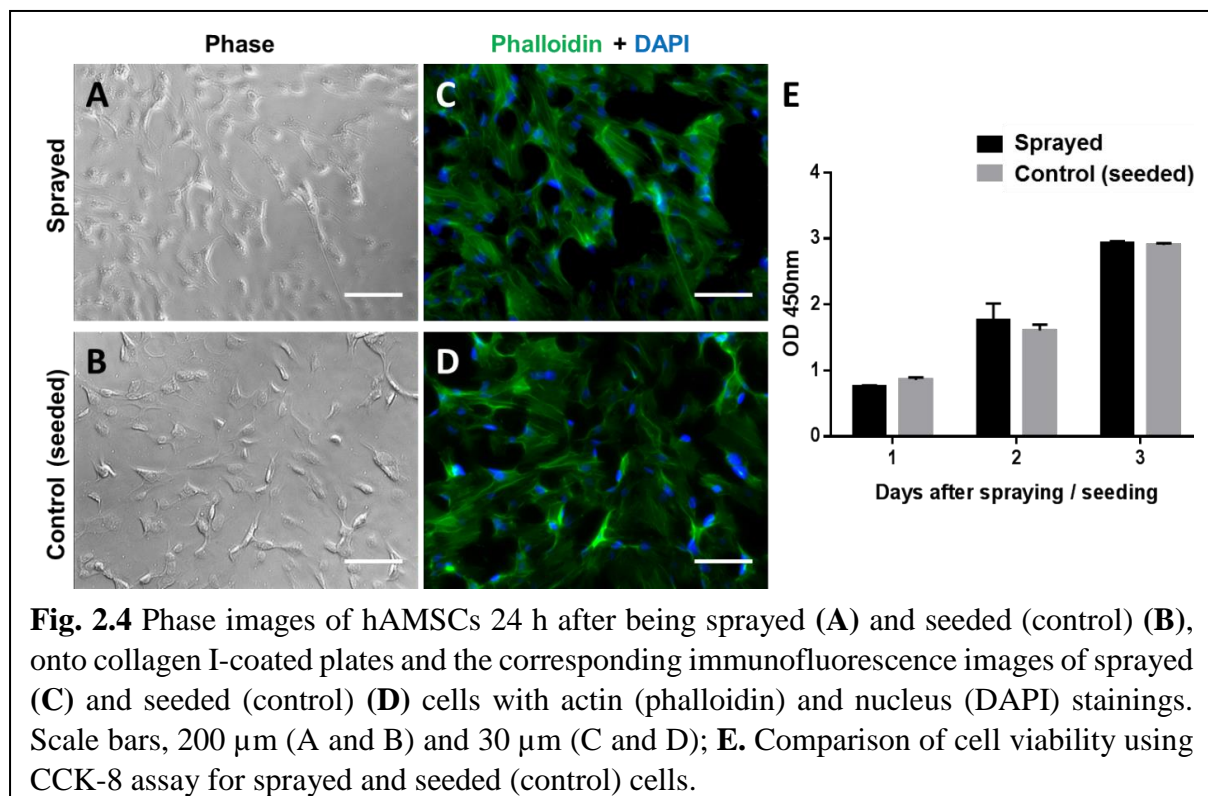
It was noted that when cells were sprayed, there were slightly (but not statistically significant) lower numbers of cells counted initially compared to the non-sprayed control group, possibly due to some cells being retained in the nozzle or not every cell being collected after being atomised. Nevertheless, the sprayed hAMSCs proliferated well despite the lower starting number of cells, especially when cultured on collagen I or PLL-coated surfaces. The live/dead cell staining assay conducted shortly after the cells attached (4 hours after being sprayed/seeding) did not show that collagen I or PLL, onto which the cells were transferred

and seeded after spraying, had a short-term impact on the percentage of live cells (data not shown). The effect of these coatings was more distinguished after 24 hours of culture.

The morphology of sprayed cells seeded onto non-coated plastic was similar to the cells seeded without spraying (control group) (Fig. 2.3A). When the cells were seeded onto collagen I-coated plastic, the control group reached confluence by day 3 (Fig. 2.3B, left). The sprayed cells took longer to reach confluence compared to control, as influenced by the lower initial cell number due to the spraying process. However, they proliferated and reached confluence after 4-5 days, demonstrating that the cells exposed to the mechanical stress of the spraying process were able to recover and proliferate normally. Comparing the cell numbers on day 3 (measured indirectly by DNA quantification using CyQUANT NF[®]), the cells sprayed onto gelatin then seeded onto collagen coated plastic had the highest end total number of cells amongst the sprayed cells (Fig. 2.3C).



Collagen I is known to facilitate cell attachment as well as proliferation^{52, 55-57}. Similarly, in our study, the effect of collagen I coating compared to non-coated plastic and PLL coating was investigated in each group (control, sprayed onto plastic or sprayed onto gelatin). Collagen I coating yielded a higher number of cells, as evident from day 2 onwards in the control group, and on day 3 for the sprayed groups (Fig. 2.3C). Collagen I is a fundamental component in the lung structure and function⁴². In our study, collagen I was demonstrated to enhance cell proliferation, regardless of whether the cells were sprayed or seeded without spraying (control). With the aid of the collagen I coating, the morphology of the sprayed cells (Fig. 2.4A,C) were similar to the morphology of the cells in the control group (Fig. 2.4B,D). The visualisation of actin through phalloidin staining revealed that the sprayed cells had a well-developed network of actin fibres with filopodia stretched in all directions (non-polarised). It was evident that the cytoskeletal structure of the sprayed cells was not compromised, and was similar to the control group. This confirmed that the cell viability was maintained even after spraying, and the cells were able to proliferate normally in the presence of collagen I. As determined from the CCK-8 assay conducted with optimised starting cell number for control and sprayed groups, the indirectly-measured cell viability of the sprayed cells was similar to that of the control group, with no significant differences (Fig. 2.4E). These findings suggest that the presence of collagen I on the substrate is helpful for the sprayed cells to attach and proliferate, yet requires further extensive investigation.



This novel and important part of the research has set the ground for future investigations, since the results suggest the need to co-deliver additional adhesive molecules in situations where the natural lung environment is compromised. After further assessment and optimisation, the co-delivery of collagen I together with the hAMSCs using the LMA device is expected to promote cell localisation and regeneration when delivered to the injured sites in the airways.

2.4.5 Cells delivered using LMA device demonstrate more uniform distribution across the whole lung

An *ex vivo* lung model using decellularised rat lungs were established for the purpose of assessing the effectiveness of the aerosolisation technology to deliver cells to the whole lung with uniform distribution. Firstly, all decellularised lungs were assessed to ensure that no cellular materials were left from the original organ, after the final DNase-step (Fig. 2.5A). From the histological assessment, no visually detectable cells were found and normal morphology of the extracellular matrices were confirmed (Fig. 2.5B). There were no detectable DNA in the decellularised lungs as visualised using agarose gel electrophoresis (Fig. 2.5C). Further assessment using NanoDrop™ spectrophotometer confirmed that all the decellularised rat lungs met the criteria of less than 50 ng of DNA per microgram of tissue. The main protein components of the extracellular matrix of the lung were preserved – collagen (COL6A5), myosin (MYH6-11), filamin A (FLNA) and laminin (LAMA5) – with similar expression levels across the nine samples and duplicates (Fig. 2.5D). One exception was that lung 9 showed significantly higher expression of myosin (MYH1-4), which requires further investigation to identify the reason for this difference. Normal cell attachment, movement and migration on the decellularised lung is demonstrated by the live imaging of Hoechst-stained mouse lung epithelial cells (C10) monitored over 2 h using a multiphoton microscope (Fig. S2.3).

The purpose of developing an atomisation technology for delivery of stem cells is to potentially use the LMA device to deliver hAMSCs directly to the lung so that it can improve the distribution of the cells in the airway. An important benefit of more uniformly distributed cells is that a larger area of the injured site is covered for therapeutic effects. Broader dispersion and more uniform distribution throughout the lung were previously reported for ink and insulin delivered to the lungs of rats using the PennCentury™ microsyrayer device^{58, 59}. Delivering cells by atomisation have further benefits as it creates ideal opportunities for cells to migrate to more distant sites of injury in the deeper lung. These cells that have the capacity to migrate and home to sites of injury and inflammation⁶⁰ may yield significant improvements in cell-based therapies for lung diseases.

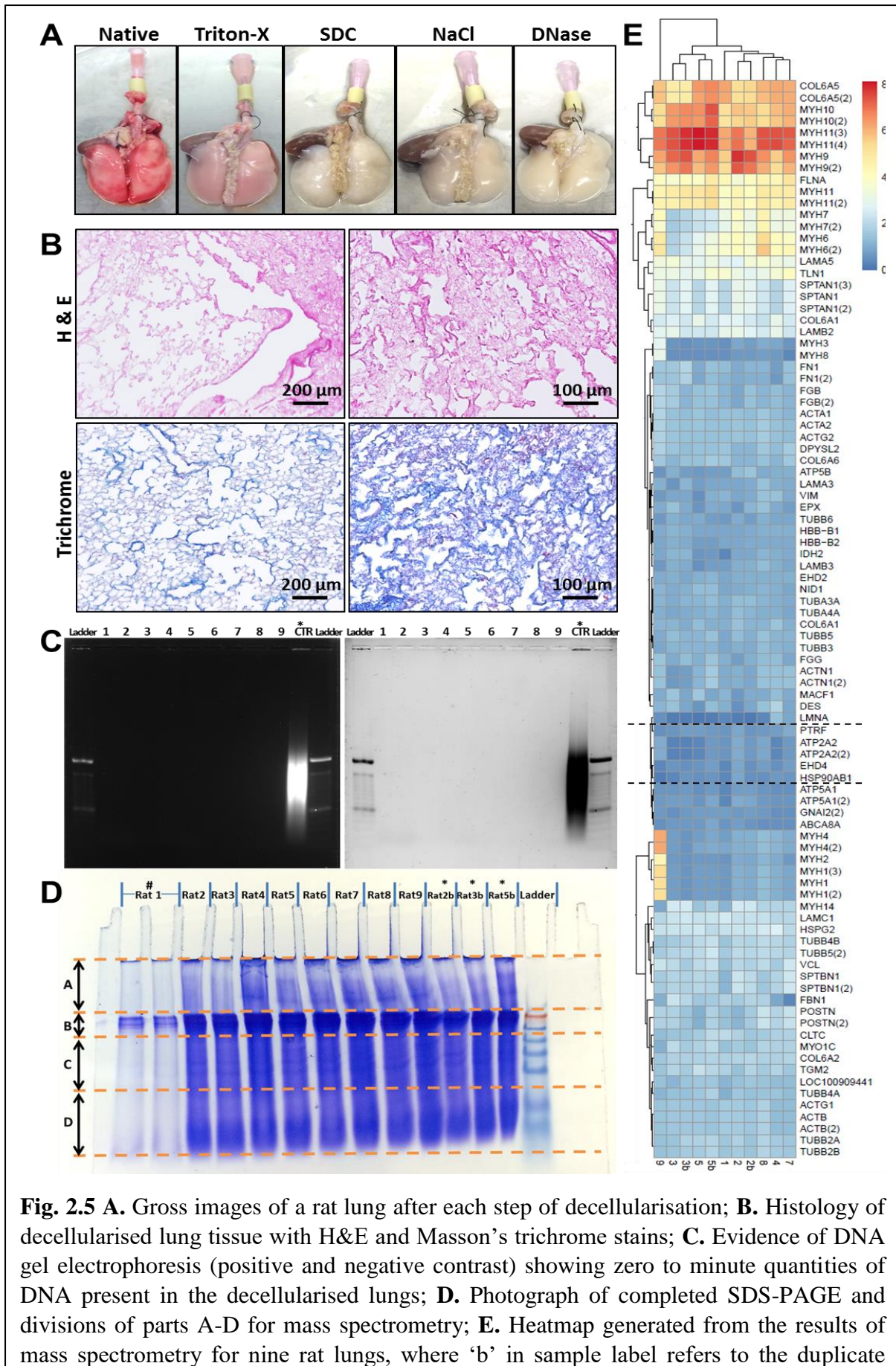
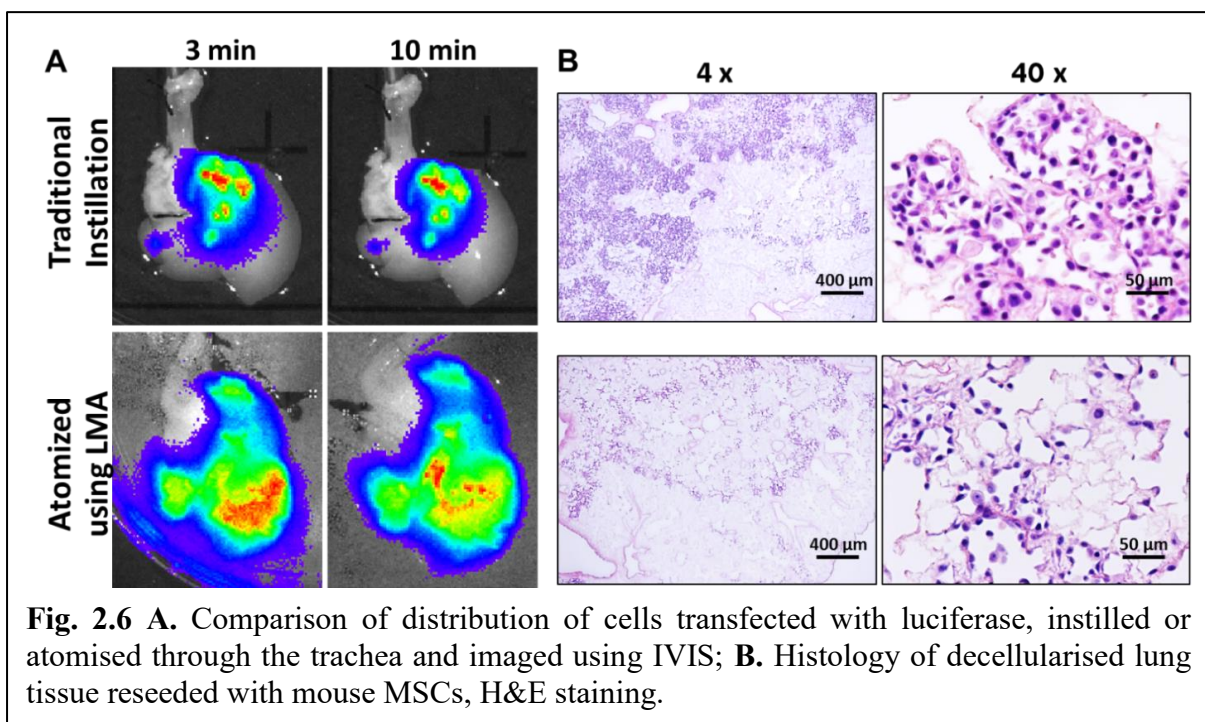


Fig. 2.5 **A.** Gross images of a rat lung after each step of decellularisation; **B.** Histology of decellularised lung tissue with H&E and Masson’s trichrome stains; **C.** Evidence of DNA gel electrophoresis (positive and negative contrast) showing zero to minute quantities of DNA present in the decellularised lungs; **D.** Photograph of completed SDS-PAGE and divisions of parts A-D for mass spectrometry; **E.** Heatmap generated from the results of mass spectrometry for nine rat lungs, where ‘b’ in sample label refers to the duplicate

In this study, AB12 cells pre-transfected with luciferase and mouse MSCs were used for the purpose of assessing cell distribution in the *ex vivo* lung models by bioluminescence imaging and histology, respectively (as explained in 2.3.8 and 2.3.9). When cells were delivered by traditional instillation (i.e. cell suspension injected through the cannulated trachea), cells deposited only in a confined, limited area of the lung, while the cells delivered by atomisation were uniformly distributed in the whole lung, as can be seen by bioluminescence images highlighting the parts of the lung occupied with cells (Fig. 2.6A). Histological analyses reveal that cells delivered by traditional instillation are aggregated and present only in limited regions of the lung, whereas the cells delivered by atomisation were more evenly distributed across the whole lung (Fig. 2.6B). From higher magnification images of cells, it can be seen that cells delivered by atomisation also retain similar morphology to those instilled, with cells incorporated and attached to the lung matrix. This demonstrates that the atomisation process using LMA device is not detrimental to cells and the atomisation technology can be utilised to deliver cells more effectively to lungs.



2.5 Conclusions

The feasibility to atomise hAMSCs was demonstrated in this study. Cell atomisation was achieved using two commercial devices, PennCentury™ Microsprayer® Aerosolizer, model IA-1C and LMA® MADgic Airway™ MAD780. The LMA device was found to be superior in maintaining cell morphology and viability even after the mechanical stress of the spraying

process and therefore was used for further assays. The significant findings from this study are listed below:

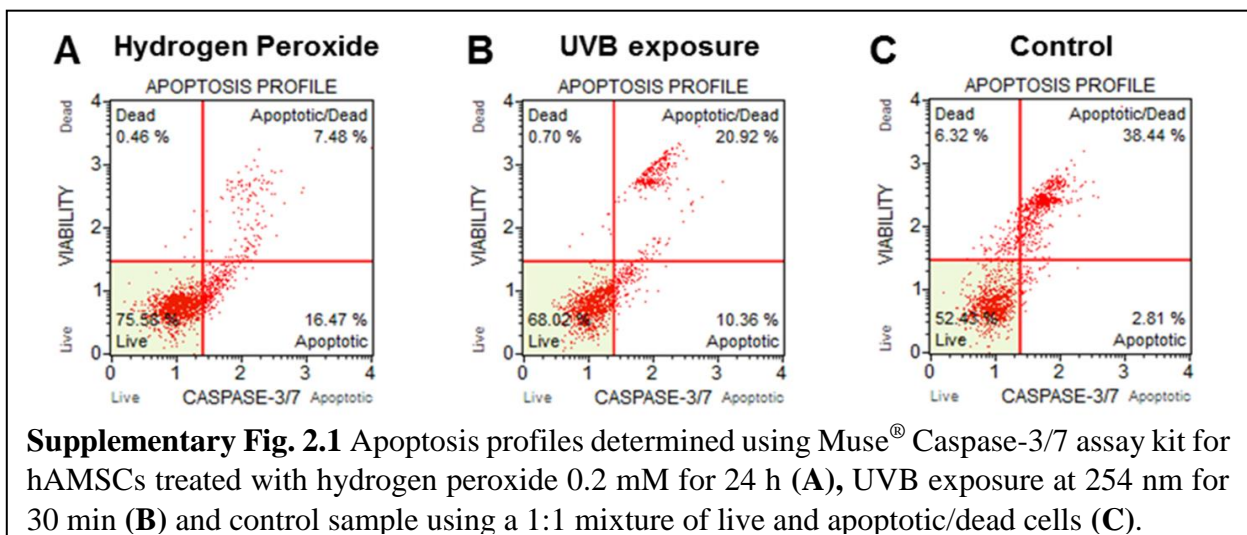
- The atomised hAMSCs maintained high viability on the substrates with varying stiffness which mimic different lung conditions.
- The atomisation of human MSCs was successfully validated for the first time on a three-dimensional *ex vivo* decellularised lung model, which demonstrated a more uniform cell distribution compared to the traditional instillation technique.
- The cell atomisation technology developed in this study is a promising tool for direct delivery of stem cells to the lung as it can potentially be targeted to the deeper injured areas for superior therapeutical benefits.

In the light of cell therapy after lung injury, there were some important findings that require further investigation, including that the sprayed cells had improved proliferation with the presence of collagen I on the substrate. The use of collagen I as an additive for the pre-treatment of the substrate prior to cell delivery is suggested for the purpose of supporting cell adhesion and growth. Further studies and applications of this cell atomisation delivery system for the lung, using *in vivo* animal models, would advance the field of cell therapy for lung regeneration.

2.6 Supplementary Information

2.6.1 Caspase-3/7 apoptosis assay

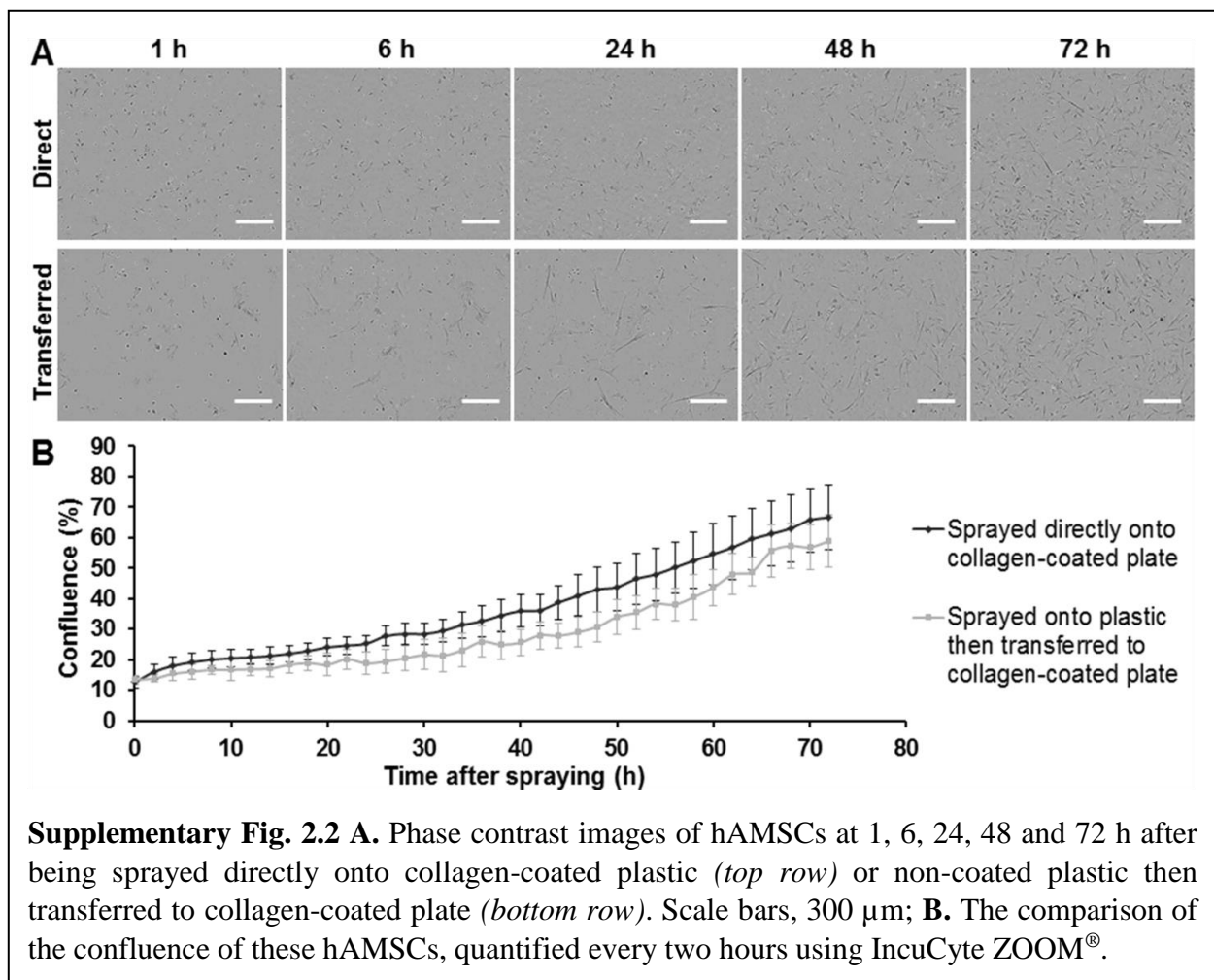
The validation of Muse® Caspase-3/7 Assay Kit was conducted for the purpose of testing that the kit was appropriate in detecting apoptotic and dead hAMSCs. A positive control (cells seeded onto non-coated tissue culture plastic) is included in Fig. 2C of this manuscript therefore is not included in this supplementary information. Prior to inducing apoptosis, cell cycles were



synchronised by starvation of serum overnight. Apoptosis of hAMSCs was induced by incubation in serum-free media containing hydrogen peroxide 1 mM for 24 h at 37°C and 5% CO₂ or UVB exposure at 275 nm for 30 min at room temperature. Following UVB exposure, the cells were incubated in normal culture conditions for 6 h prior to conducting the apoptosis assay. Since hAMSCs are adherent cells, the control sample (50/50 mixture of live and apoptotic/dead cells) was prepared by combining live (attached) cells and apoptotic/dead (detached) cells in 1:1 proportion; apoptotic/dead cells were collected from the detached cells during media renewal in normal culture conditions. The proportion of live and dead cells was confirmed using a trypan blue assay prior to the apoptosis assay.

2.6.2 The incorporation of collagen coating

To assess whether there are differences in cell growth for the cells sprayed directly onto collagen-coated plastic and those transferred to collagen-coated plate after being sprayed onto non-coated plastic, IncuCyte ZOOM[®] was used (as described in the Materials and Methods section) to monitor cell morphology and quantify confluence. There were no significant



differences demonstrated in the morphology and proliferation of cells sprayed directly or those collected after spraying then transferred onto a collagen-coated plate (Fig. S2.2).

2.6.3 Live imaging of cells on decellularised matrix

To ensure that the decellularised lung is suitable for normal cell attachment and proliferation, lungs were thinly sliced using a sharp blade and mouse lung epithelial cells (C10) were seeded on slices were monitored. Briefly, C10 cells were labelled using Hoechst 2 µg/ml for 30 min at room temperature in the dark then gently seeded 200,000 cells onto each lung slice. After 3 h incubation at 37°C and 5% CO₂, cells inside a micro-incubation platform (Warner Instruments Inc, Hamden, CT, USA) were imaged live, every 5 min over 2 h using a multiphoton microscope (Olympus BX51WI fitted with Bio-Rad Radiance2100TM Direct Detection System), for assessing movement and migration. Images were acquired with Zeiss Laser Sharp 2000 software (Fig. S2.3, available to view through the following link: <https://youtu.be/ZWak4lRY2vM>).

2.7 References

1. Lee, J.W., Fang, X., Krasnodembskaya, A., Howard, J.P., and Matthay, M.A., Concise Review: Mesenchymal Stem Cells for Acute Lung Injury: Role of Paracrine Soluble Factors. *Stem Cells* 2011, **29**(6):913-919.
2. Lau, A.N., Goodwin, M., Kim, C.F., and Weiss, D.J., Stem cells and regenerative medicine in lung biology and diseases. *Molecular Therapy* 2012, **20**(6):1116-1130.
3. Lim, R., Tan, J.L., and Wallace, E.M., Cell therapies for lung disease, in *Gene and Cell Therapy: Therapeutic Mechanisms and Strategies*, N.S. Templeton, Editor. 2015, CRC Press: Taylor & Francis Group. p. 1157-1170.
4. Zhu, F., Wang, J., Qiu, X., Li, J., and Xia, Z., Smoke inhalation injury repaired by a bone marrow-derived mesenchymal stem cell paracrine mechanism: Angiogenesis involving the Notch signaling pathway. *Journal of Trauma and Acute Care Surgery* 2015, **78**(3):565-572.
5. Garcia, O. and Warburton, D., Amniotic fluid stem cell therapy for lung disease, in *Perinatal Stem Cells*, A. Atala and S.V. Murphy, Editors. 2014, Springer: New York. p. 59-65.
6. Wei, X., Yang, X., Han, Z.-p., Qu, F.-f., Shao, L., and Shi, Y.-f., Mesenchymal stem cells: a new trend for cell therapy. *Acta Pharmacologica Sinica* 2013, **34**(6):747-754.
7. Docheva, D., Popov, C., Mutschler, W., and Schieker, M., Human mesenchymal stem cells in contact with their environment: surface characteristics and the integrin system. *Journal of Cellular and Molecular Medicine* 2007, **11**(1):21-38.
8. Miller, A.C., Elamin, E.M., and Suffredini, A.F., Inhaled Anticoagulation Regimens for the Treatment of Smoke Inhalation-Associated Acute Lung Injury: A Systematic Review. *Critical care medicine* 2014, **42**(2):413-419.
9. Sharma, A. and Lunawat, A., Role of heparin and N-acetylcystein in prevention of acute respiratory distress syndrome in suspected inhalation injury in burn. *Indian Journal of Basic and Applied Medical Research* 2015, **4**(3):337-343.
10. Dries, D. and Endorf, F., Inhalation injury: epidemiology, pathology, treatment strategies. *Scandinavian Journal of Trauma, Resuscitation and Emergency Medicine* 2013, **21**(1):31.
11. Xu, F., Hu, Y., Zhou, J., and Wang, X., Mesenchymal stem cells in acute lung injury: are they ready for translational medicine? *J Cell Mol Med* 2013, **17**(8):927-35.
12. Johnson, E.R. and Matthay, M.A., Acute Lung Injury: Epidemiology, Pathogenesis, and Treatment. *Journal of Aerosol Medicine and Pulmonary Drug Delivery* 2010, **23**(4):243-252.

13. Chen, X., Liu, Q., Wang, D., Feng, S., Zhao, Y., Shi, Y., and Liu, Q., Protective Effects of Hydrogen-Rich Saline on Rats with Smoke Inhalation Injury. *Oxidative Medicine and Cellular Longevity* 2015, **2015**:106836.
14. Matthay, M.A., Goolaerts, A., Howard, J.P., and Lee, J.W., Mesenchymal stem cells for acute lung injury: Preclinical evidence. *Critical care medicine* 2010, **38**(10 Suppl):S569-S573.
15. Antunes, M.A., Abreu, S.C., Cruz, F.F., Teixeira, A.C., Lopes-Pacheco, M., Bandeira, E., Olsen, P.C., Diaz, B.L., Takyia, C.M., Freitas, I.P.R.G., Rocha, N.N., Capelozzi, V.L., Xisto, D.G., Weiss, D.J., Morales, M.M., and Rocco, P.R.M., Effects of different mesenchymal stromal cell sources and delivery routes in experimental emphysema. *Respiratory Research* 2014, **15**(1):118.
16. Hao, Q., Zhu, Y.G., Monsel, A., Gennai, S., Lee, T., Xu, F., and Lee, J.W., Study of Bone Marrow and Embryonic Stem Cell-Derived Human Mesenchymal Stem Cells for Treatment of Escherichia coli Endotoxin-Induced Acute Lung Injury in Mice. *Stem Cells Transl Med* 2015, **4**(7):832-40.
17. Ismail, S.N., Polak, J.M., and Mantalaris, A., Lung Stem Cell Bioprocessing: Fundamentals of Producing Lung Cells, Section 3: Cell Expansion and Sources, in *Cell Therapy for Lung Disease*, J.M. Polak, Editor. 2010, Imperial College Press. p. 173-177.
18. Alviano, F., Fossati, V., Marchionni, C., Arpinati, M., Bonsi, L., Franchina, M., Lanzoni, G., Cantoni, S., Cavallini, C., Bianchi, F., Tazzari, P., Pasquinelli, G., Foroni, L., Ventura, C., Grossi, A., and Bagnara, G., Term amniotic membrane is a high throughput source for multipotent mesenchymal stem cells with the ability to differentiate into endothelial cells in vitro. *BMC Developmental Biology* 2007, **7**(1):11.
19. Paracchini, V., Carbone, A., Colombo, F., Castellani, S., Mazzucchelli, S., Di Gioia, S., Degiorgio, D., Seia, M., Porretti, L., Colombo, C., and Conese, M., Amniotic Mesenchymal Stem Cells: A New Source for Hepatocyte-Like Cells and Induction of CFTR Expression by Coculture with Cystic Fibrosis Airway Epithelial Cells. *Journal of Biomedicine and Biotechnology* 2012, **2012**:15.
20. Wallace, E.M., Cargnoni, A., Lim, R., Hodge, A., and Sievert, W., The use of placenta-derived cells in inflammatory and fibrotic disorders, in *in press*. 2015.
21. Caruso, M., Evangelista, M., and Parolini, O., Human Term Placental Cells: Phenotype, Properties and New Avenues in Regenerative Medicine. *International Journal of Molecular and Cellular Medicine* 2012, **1**(2):64-74.
22. Moodley, Y., Vaghjiani, V., Chan, J., Baltic, S., Ryan, M., Tchongue, J., Samuel, C.S., Murthi, P., Parolini, O., and Manuelpillai, U., Anti-Inflammatory Effects of Adult Stem Cells in Sustained Lung Injury: A Comparative Study. *PLoS ONE* 2013, **8**(8):e69299.

23. Cargnoni, A., Gibelli, L., Tosini, A., Signoroni, P.B., Nassuato, C., Arienti, D., Lombardi, G., Albertini, A., Wengler, G.S., and Parolini, O., Transplantation of Allogeneic and Xenogeneic Placenta-Derived Cells Reduces Bleomycin-Induced Lung Fibrosis. *Cell Transplantation* 2009, **18**(4):405-422.
24. Silini, A., Parolini, O., Huppertz, B., and Lang, I., Soluble factors of amnion-derived cells in treatment of inflammatory and fibrotic pathologies. *Curr Stem Cell Res Ther* 2013, **8**(1):6-14.
25. Cargnoni, A., Piccinelli, E.C., Ressel, L., Rossi, D., Magatti, M., Toschi, I., Cesari, V., Albertini, M., Mazzola, S., and Parolini, O., Conditioned medium from amniotic membrane-derived cells prevents lung fibrosis and preserves blood gas exchanges in bleomycin-injured mice-specificity of the effects and insights into possible mechanisms. *Cytotherapy* 2014, **16**(1):17-32.
26. Carraro, G., Perin, L., Sedrakyan, S., Giuliani, S., Tiozzo, C., Lee, J., Turcatel, G., De Langhe, S.P., Driscoll, B., Bellusci, S., Minoo, P., Atala, A., De Filippo, R.E., and Warburton, D., Human Amniotic Fluid Stem Cells Can Integrate and Differentiate into Epithelial Lung Lineages. *Stem cells (Dayton, Ohio)* 2008, **26**(11):2902-2911.
27. Curley, G.F., Ansari, B., Hayes, M., Devaney, J., Masterson, C., Ryan, A., Barry, F., O'Brien, T., Toole, D.O., and Laffey, J.G., Effects of Intratracheal Mesenchymal Stromal Cell Therapy during Recovery and Resolution after Ventilator-induced Lung Injury. *Anesthesiology* 2013, **118**(4):924-932.
28. Leblond, A.-L., Naud, P., Forest, V., Gourden, C., Sagan, C., Romefort, B., Mathieu, E., Delorme, B., Collin, C., Pagès, J.-C., Sensebé, L., Pitard, B., and Lemarchand, P., Developing cell therapy techniques for respiratory disease: intratracheal delivery of genetically engineered stem cells in a murine model of airway injury. *Human Gene Therapy* 2009, **20**(11):1329-1343.
29. Serrano-Mollar, A., Nacher, M., Gay-Jordi, G., Closa, D., Xaubet, A., and Bulbena, O., Intratracheal transplantation of alveolar type II cells reverses bleomycin-induced lung fibrosis. *Am J Respir Crit Care Med* 2007, **176**(12):1261-8.
30. van Haaften, T., Byrne, R., Bonnet, S., Rochefort, G.Y., Akabutu, J., Bouchentouf, M., Rey-Parra, G.J., Galipeau, J., Haromy, A., Eaton, F., Chen, M., Hashimoto, K., Abley, D., Korbitt, G., Archer, S.L., and Thebaud, B., Airway delivery of mesenchymal stem cells prevents arrested alveolar growth in neonatal lung injury in rats. *Am J Respir Crit Care Med* 2009, **180**(11):1131-42.
31. Kim, E.S., Chang, Y.S., Choi, S.J., Kim, J.K., Yoo, H.S., Ahn, S.Y., Sung, D.K., Kim, S.Y., Park, Y.R., and Park, W.S., Intratracheal transplantation of human umbilical cord blood-derived mesenchymal stem cells attenuates Escherichia coli-induced acute lung injury in mice. *Respir Res* 2011, **12**:108.

32. Tibboel, J., Keijzer, R., Reiss, I., de Jongste, J.C., and Post, M., Intravenous and Intratracheal Mesenchymal Stromal Cell Injection in a Mouse Model of Pulmonary Emphysema. *COPD: Journal of Chronic Obstructive Pulmonary Disease* 2013, **11**(3):310-318.
33. Gui, L., Qian, H., Rocco, K.A., Grecu, L., and Niklason, L.E., Efficient intratracheal delivery of airway epithelial cells in mice and pigs. *Am J Physiol Lung Cell Mol Physiol* 2015, **308**(2):L221-8.
34. Zhang, S., Danchuk, S.D., Imhof, K.M.P., Semon, J.A., Scruggs, B.A., Bonvillain, R.W., Strong, A.L., Gimble, J.M., Betancourt, A.M., Sullivan, D.E., and Bunnell, B.A., Comparison of the therapeutic effects of human and mouse adipose-derived stem cells in a murine model of lipopolysaccharide-induced acute lung injury. *Stem Cell Research & Therapy* 2013, **4**(1):13-13.
35. Danchuk, S., Ylostalo, J.H., Hossain, F., Sorge, R., Ramsey, A., Bonvillain, R.W., Lasky, J.A., Bunnell, B.A., Welsh, D.A., Prockop, D.J., and Sullivan, D.E., Human multipotent stromal cells attenuate lipopolysaccharide-induced acute lung injury in mice via secretion of tumor necrosis factor- α -induced protein 6. *Stem Cell Research & Therapy* 2011, **2**(3):1-15.
36. Kardia, E., Yusoff, N.M., Zakaria, Z., and Yahaya, B., Aerosol-based delivery of fibroblast cells for treatment of lung diseases. *J Aerosol Med Pulm Drug Deliv* 2014, **27**(1):30-4.
37. Ghadiri, M., Young, P.M., and Traini, D., Cell-based therapies for the treatment of idiopathic pulmonary fibrosis (IPF) disease. *Expert Opinion on Biological Therapy* 2016, **16**(3):375-387.
38. Falanga, V., Iwamoto, S., Chartier, M., Yufit, T., Butmarc, J., Kouttab, N., Shraye, D., and Carson, P., Autologous bone marrow-derived cultured mesenchymal stem cells delivered in a fibrin spray accelerate healing in murine and human cutaneous wounds. *Tissue Eng* 2007, **13**(6):1299-312.
39. Ebensperger, R., *Spray formulation of mesenchymal stem cells for the treatment of chronic wounds*. 2014, Google Patents.
40. Sosnowski, T., Kurowska, A., Butruk, B., and Jablczynska, K., Spraying of cell colloids in medical atomizers. *AIDIC Conference Series* 2013, **11**:371-380.
41. Braghirolli, D.I., Zamboni, F., Chagastelles, P.C., Moura, D.J., Saffi, J., Henriques, J.A., Pilger, D.A., and Pranke, P., Bio-electrospraying of human mesenchymal stem cells: An alternative for tissue engineering. *Biomicrofluidics* 2013, **7**(4):44130.

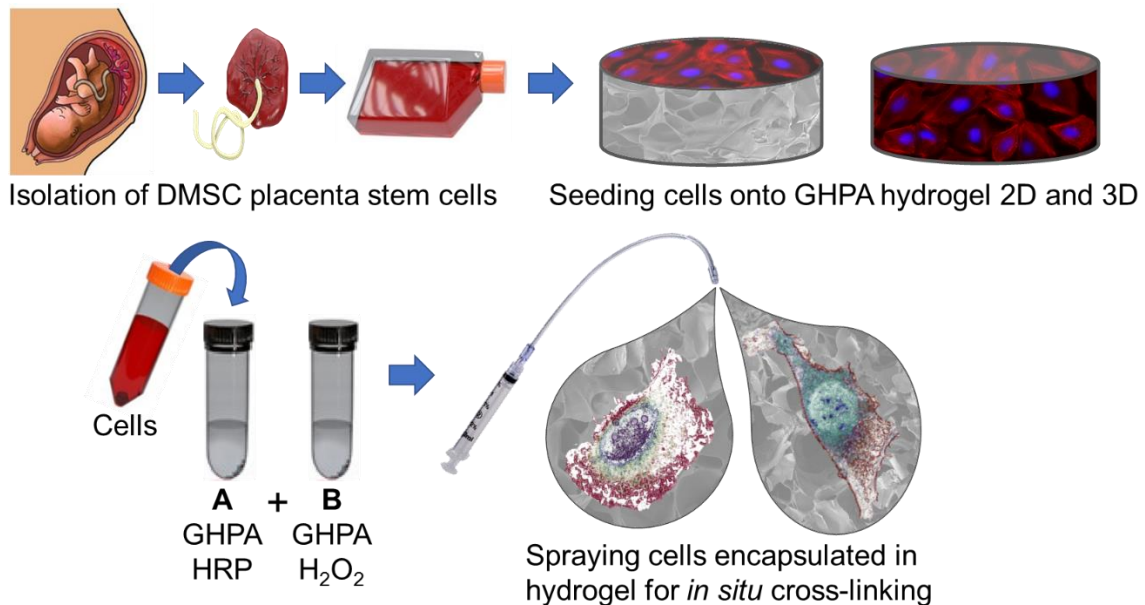
42. Kim, S.Y., Wong, A.H., Abou Neel, E.A., Chrzanowski, W., and Chan, H.K., The future perspectives of natural materials for pulmonary drug delivery and lung tissue engineering. *Expert Opin Drug Deliv* 2015, **12**(6):869-87.
43. Daly, A.B., Wallis, J.M., Borg, Z.D., Bonvillain, R.W., Deng, B., Ballif, B.A., Jaworski, D.M., Allen, G.B., and Weiss, D.J., Initial binding and recellularization of decellularized mouse lung scaffolds with bone marrow-derived mesenchymal stromal cells. *Tissue Eng Part A* 2012, **18**(1-2):1-16.
44. Shaffer, T.H., Wolfson, M.R., Greenspan, J.S., Rubenstein, S.D., and Stern, R.G., Perfluorochemical liquid as a respiratory medium. *Artif Cells Blood Substit Immobil Biotechnol* 1994, **22**(2):315-26.
45. Jeng, M.-J., Yang, S.-S., Wolfson, M.R., and Shaffer, T.H., Perfluorochemical (PFC) Combinations for Acute Lung Injury: An In Vitro and In Vivo Study in Juvenile Rabbits. *Pediatric Research* 2003, **53**:81.
46. Kazzaz, J.A., Strayer, M.S., Wu, J., Malone, D.J., Koo, H.-c., Shaffer, T.H., Davis, J.M., Strayer, D.S., and Wolfson, M.R., Perfluorochemical Liquid-Adenovirus Suspensions Enhance Gene Delivery to the Distal Lung. *Pulmonary Medicine* 2011, **2011**:10.
47. Wolfson, M.R., Wu, J., Baker, S.T., Gill, C., Johnson, J., Poole, L., and Shaffer, T.H., Aerosolized Perfluorochemical Rescue Against Acute Altitude-Induced Pulmonary Compromise. *The FASEB Journal* 2016, **30**(1_supplement):1007.3-1007.3.
48. Wallis, J.M., Borg, Z.D., Daly, A.B., Deng, B., Ballif, B.A., Allen, G.B., Jaworski, D.M., and Weiss, D.J., Comparative assessment of detergent-based protocols for mouse lung decellularization and re-cellularization. *Tissue Eng Part C Methods* 2012, **18**(6):420-32.
49. Haghi, M., Traini, D., Wood, L.G., Oliver, B., Young, P.M., and Chrzanowski, W., A 'soft spot' for drug transport: modulation of cell stiffness using fatty acids and its impact on drug transport in lung model. *Journal of Materials Chemistry B* 2015, **3**(13):2583-2589.
50. Xin, H., Sun, R., Kanehira, M., Takahata, T., Itoh, J., Mizuguchi, H., and Saijo, Y., Intratracheal Delivery of CX3CL1-Expressing Mesenchymal Stem Cells to Multiple Lung Tumors. *Molecular Medicine* 2009, **15**(9-10):321-327.
51. Cai, S.-x., Liu, A.-r., Chen, S., He, H.-l., Chen, Q.-h., Xu, J.-y., Pan, C., Yang, Y., Guo, F.-m., Huang, Y.-z., Liu, L., and Qiu, H.-b., Activation of Wnt/ β -catenin signalling promotes mesenchymal stem cells to repair injured alveolar epithelium induced by lipopolysaccharide in mice. *Stem Cell Research & Therapy* 2015, **6**(1):1-11.
52. Freyer, A.M., Johnson, S.R., and Hall, I.P., Effects of growth factors and extracellular matrix on survival of human airway smooth muscle cells. *Am J Respir Cell Mol Biol* 2001, **25**(5):569-76.

53. Mazia, D., Schatten, G., and Sale, W., Adhesion of cells to surfaces coated with polylysine. Applications to electron microscopy. *J Cell Biol* 1975, **66**(1):198-200.
54. Fischer-Cripps, A., Nanoindentation Test Standards, in *Nanoindentation*. 2011, Springer: New York. p. 181-198.
55. Gonzalez-Lopez, A. and Albaiceta, G., Repair after acute lung injury: molecular mechanisms and therapeutic opportunities. *Critical Care* 2012, **16**(2):209.
56. Hirst, S.J., Twort, C.H., and Lee, T.H., Differential effects of extracellular matrix proteins on human airway smooth muscle cell proliferation and phenotype. *Am J Respir Cell Mol Biol* 2000, **23**(3):335-44.
57. Dekkers, B.G.J., Schaafsma, D., Nelemans, S.A., Zaagsma, J., and Meurs, H., Extracellular matrix proteins differentially regulate airway smooth muscle phenotype and function. *American Journal of Physiology - Lung Cellular and Molecular Physiology* 2007, **292**(6):L1405-L1413.
58. Hasegawa-Baba, Y., Kubota, H., Takata, A., and Miyagawa, M., Intratracheal Instillation Methods and the Distribution of Administered Material in the Lung of the Rat. *Journal of Toxicologic Pathology* 2014, **27**(3-4):197-204.
59. Garcia-Contreras, L., Morçöl, T., Bell, S.J.D., and Hickey, A.J., Evaluation of novel particles as pulmonary delivery systems for insulin in rats. *AAPS PharmSci* 2003, **5**(2):10-20.
60. Rustad, K.C. and Gurtner, G.C., Mesenchymal Stem Cells Home to Sites of Injury and Inflammation. *Advances in Wound Care* 2012, **1**(4):147-152.

3 Gelatin hydroxyphenyl propionic acid (GHPA) hydrogel for direct pulmonary delivery of decidual mesenchymal stromal cells

3.1 Overview

3.1.1 Graphical abstract



3.1.2 Highlights and keywords

- A ratiometric hypoxia probe synthesised in-house was used to demonstrate the robustness of decidual mesenchymal stromal cells in hypoxic conditions.
- Both lung epithelial cell line and decidual mesenchymal stromal cells proliferated well after being seeded onto GHPA hydrogel, demonstrating cytocompatibility.
- GHPA hydrogel has stiffness mimicking that of healthy lungs and therefore has the potential to correctly guide stem cell differentiation to lung epithelial cells.
- A first of its kind ‘sprayable hydrogel’ has been developed as a potential delivery platform for direct stem cell delivery to the lung.
- Sprayed cells in hydrogel demonstrate high viability and normal cell morphology.

Keywords: sprayable hydrogel, cell encapsulation, placenta stem cells, hypoxia-resistant cells, stem cell delivery, pulmonary delivery

Manuscript is being prepared to be submitted to:



3.1.3 Abstract

Poor cell retention in the injury site and limited cell survival in the hostile microenvironment of the injured lung represent the challenges in stem cell therapy for lung injury. In this study, sprayable, in-situ cross-linkable GHPA hydrogel to encapsulate decidual mesenchymal stem cell line (DMSC23) has been developed to achieve the goals of improved retention and survival of the delivered cells. The ability of the hydrogel to encapsulate lung epithelial cells (BEAS-2B) and support their proliferation was evaluated. The cytocompatibility of the GHPA hydrogel for both BEAS-2B and DMSC23 was demonstrated using live/dead viability assays.

The stiffness profiles of hydrogel alone and hydrogel encapsulating DMSC23 were measured using both nanoscale and macroscale techniques, by nanoindentation and viscoelasticity measurement using micrometric vibration. Increased stiffness observed in the hydrogel with cells represented cell proliferation and matrix remodelling while the decreased stiffness observed in the hydrogel only group demonstrated degradability of the hydrogel over time.

The feasibility of spraying GHPA hydrogel was evaluated and the cell viability of DMSC23 sprayed in hydrogel was found comparable to those encapsulated in hydrogel without being sprayed.

The outcomes of this study suggest that GHPA hydrogel is a suitable platform for the delivery of DMSC23 directly to the airway by atomisation. This is an innovative approach that will have significant impact on the cell delivery and pulmonary regenerative medicine field, for enhancing the exogenous cells to survive and proliferate well by following the cues of the co-delivered bioactive molecules for optimal tissue repair.

3.2 Introduction

3.2.1 Decidual mesenchymal stromal cells are the ideal cell type suitable for the microenvironment of lung injury

In the last two decades, there has been a huge progress in the search for alternative source of stem cells that retain the multipotent properties of embryonic stem cells yet without ethical dilemma¹⁻⁴. Thus, mesenchymal stem/stromal cells (MSCs) from fetal origin such as amniotic fluid, amniotic membrane, placenta, umbilical cord Wharton's jelly and umbilical cord blood have been in the limelight for their use in regenerative medicine⁵⁻⁷. These are advantageous for their therapeutic applications as MSCs are known to have low immunogenicity as they naturally possess low expression of major histocompatibility complex (MHC) class I antigens and lack in MHC class II antigens⁸. MSCs also secrete paracrine factors that regulate the immune system by inhibiting T cell activation and also enhancing the secretion of anti-inflammatory cytokines⁹, which are favourable for numerous therapeutical applications.

Although amniotic fluid and amniotic membrane MSCs have been characterised well in a number of studies for application in regenerative medicine^{2, 4, 10}, there are major limitations in isolation and obtaining sufficient amount of samples, especially for amniotic fluid MSCs as they are isolated from small samples obtained from amniocentesis¹¹. In contrast, the human placenta offers an abundant source of human placental MSCs and they have been recognised to have a high potential for therapeutic applications^{12, 13}. Placenta-derived MSCs were demonstrated to have superior immunomodulatory effects compared to the umbilical cord MSCs from the same donor¹⁴. Human placental MSCs have been demonstrated to have potential therapeutic repair capability in a number of injury models including bleomycin-induced pulmonary fibrosis¹⁵, myocardial infarction¹⁶, spina bifida¹⁷, and ischemia^{18, 19}.

The placenta stem cells used in this study were fetal and maternal MSCs, namely chorionic MSCs (CMSCs) and decidual MSCs (DMSCs), isolated from *chorionic villi* (fetal side) and *decidua basalis* (maternal side) of human placenta²⁰. CMSCs have been demonstrated to possess embryonic stem cell markers OCT-4, NANOG, SSEA-3 and TRA-1-60²¹. DMSCs have previously been demonstrated to be resistant to hypoxic stress using ALDH expression²⁰. To improve reproducibility of experiments and for the ease of culturing cells, fetal and maternal CMSC29 and DMSC23 cell lines have been established demonstrated to retain the similar MSC properties to the primary cells¹².

The aim of the first part of this study was to demonstrate DMSC23 as a superior placenta stem cell line compared to CMSC29 for potential use in lung injury, which is likely to be a hostile

microenvironment with hypoxic conditions. The robustness of DMSC23 to hypoxic stress was validated using an innovative an ratiometric probe synthesised in-house to measure the level of cellular hypoxic stress²².

3.2.2 Benefits of using a bioactive hydrogel delivery system

Although the principal mechanism underlying current cell therapies is mainly due to their paracrine signals, the retention and survival of transplanted cells continues to be the goals in improving therapeutic outcomes as short-term paracrine signals at the injured site are insufficient²³. The retention of biomaterial encapsulating the cells has been suggested to impact cell retention at the delivered site²⁴. The use of an *in-situ* gelling hydrogel platform for cell delivery for tissue regeneration has been identified as a promising approach for maximising therapeutic effects of the stem cells²⁵. Here, a relatively fast gelation is required to promote homogenous cell distribution at the delivered site, yet slow enough to prevent gelation within the delivery device²⁶. The use of hydrogel cell delivery matrix is beneficial for improving cell viability, as it provides the platform to nourish the transplanted cells in the microenvironment lacking vasculature and niche²⁷. Numerous studies reported the use of a hydrogel platform for improving retention and longevity of stem cells or other bioactive factors after delivery to the eye²⁸, heart^{23, 29, 30}, muscle^{31, 32}, cartilage³³ and bone³⁴. It is known that substrate stiffness heavily influences the fate of stem cells on differentiation, with softer materials leading to soft tissue lineages while stiffer materials promote hard tissue lineages²⁶. A recent study also demonstrates strategies to design hydrogels to enhance the secretory profile of growth factors, chemokines, and cytokines from the stem cells to improve the angiogenic potential³⁵.

Gelatin is an ideal material source for hydrogel fabrication due to its excellent biocompatibility and biodegradability with the absence of immune/antigenicity³⁶. Modification of gelatin to enable hydrogel formation by the use of photocrosslinkable methacrylamide (GelMA) has received an extensive interest for tissue engineering applications in the last few years³⁷. There are numerous advantages in the GelMA system including tunable properties of the hydrogel to meet the needs of individual applications and easy visualisation of cell behaviour due to the transparent material^{37, 38}. However, this system requires a UV light source (360-480 nm) for the photocrosslinking process³⁷ which can be inconvenient and require optimisation to minimise potential UV-damage in the encapsulated cells. A more recently developed *in-situ* cross-linkable gelatin hydrogel fabricated by the conjugation hydroxyphenyl propionic acid to the free amines of gelatin resulting in gelatin-hydroxyphenyl propionic acid (GHPA) hydrogel overcomes the limitations of fast enzymatic degradation of gelatin alone³⁹. This conjugated

gelatin enabled fast and convenient crosslinking process mediated by hydrogen peroxide (H_2O_2) and horseradish peroxidase (HRP)^{39, 40}. This GHPA hydrogel system has tunable mechanical properties controlled by altering the concentration of H_2O_2 and HRP³⁹⁻⁴¹ and thus it is a versatile platform to deliver cells to numerous organs. A chemically crosslinked gelatin-based scaffolds have been demonstrated to possess enhanced mucoadhesive properties⁴², which is highly desired for a delivery system to injured lung that has increased mucus secretion. In this study, GHPA hydrogel, an *in-situ* forming gelatin-based tissue adhesive⁴⁰, was engineered for the delivery of stem cells to the lung by atomisation, which is an innovative and fundamental approach to improving therapeutic outcomes, presenting a versatile system for other applications for pulmonary regenerative medicine.

3.3 Materials and Methods

3.3.1 Synthesis of GHPA

The synthesis of GHPA has already been reported in detail by the collaborators who provided the material⁴⁰. Briefly, gelatin was dissolved in 40°C deionised water for 1 h. Hydroxyphenyl propionic acid (HPA) was dissolved in water and dimethylformamide (DMF) (volume ratio of 3:2) then activated with 1-ethyl-3-(3-dimethylaminopropyl)-carbodiimide (EDC) and N-hydroxysuccinimide (NHS). The activated HPA solution was then added to the pre-heated gelatin solution and stirred at 40°C for 24 h. The resulting solution was transferred into a dialysis bag (MWCO. 3.5 kDa), dialysed in deionised water for 3 days then subsequently in sodium chloride, water/ethanol and distilled water. The solution was then filtered for purification and lyophilised to obtain the GHPA conjugates.

3.3.2 Fabrication of GHPA hydrogel

GHPA 55.6 mg was dissolved in 1 ml pre-warmed phosphate-buffered saline (PBS), filtered using 0.22 μ m syringe filter, then divided into part A and B, 500 μ l each. A stock of HRP (Sigma-Aldrich, Castle Hill NSW Australia) was diluted to 0.025 mg/ml and H_2O_2 (Junsei Chemical Co., Tokyo, Japan) was diluted to 0.102% in PBS and filter-sterilised. The diluted solutions of HRP 50 μ l was added to part A and 50 μ l H_2O_2 was added to part B. The solutions were warmed at 37°C immediately before incorporating part A to the cell pellet and combining part A (with cells) and B together.

3.3.3 Cell culture and maintenance

Immortalised human bronchial epithelial cell line (BEAS-2B) and transduced foetal maternal mesenchymal stromal cell line (DMSC23)^{12, 20} were used for hydrogel encapsulation.

Chorionic mesenchymal stromal cell line (CMSC29) was used as control when describing the rationale for the choice of DMSC23 cell line in this study. BEAS-2B were cultured in Dulbecco's Modified Eagle Medium (DMEM) supplemented with 10% foetal bovine serum (FBS, French origin, Scientifix, Cheltenham, VIC, Australia) and 1% penicillin-streptomycin 5000 U/ml (PenStrep[®], Thermo Fisher Scientific, North Ryde, NSW, Australia). DMSC23 was cultured in Mesencult[™] proliferation kit (STEMCELL Technologies, Tullamarine, VIC, Australia) and CMSC29 were cultured in AmnioMAX[™] (Invitrogen[™], Thermo Fisher Scientific). Hanks' Balanced Salt Solution (HBSS(-), Sigma-Aldrich) was used for washing DMSC23 and CMSC29, while phosphate buffer saline without Ca²⁺ and Mg²⁺ (PBS, Lonza, Bella Vista, NSW, Australia) was used for BEAS-2B. TrypLE[™] Select Enzyme (Thermo Fisher Scientific) was used as dissociation reagent for all adherent cells. DMSC23 and CMSC29 were used for isolation of EVs at passages P23-28 while BEAS-2B cells were used at P12-16 and P14-20. All cells were maintained at 37°C and 5% CO₂.

3.3.4 The use of an in-house hypoxia probe to compare resistance to hypoxic stress

The aim of this experiment was to demonstrate the robustness of DMSC23 by its resistance to hypoxic stress using an in-house nitronaphthalimide hypoxia (NpHy3) probe. The detailed methods are published in the article co-authored with Yang *et al*²². Briefly, DMSC23 and CMSC29 (control) cell lines were seeded at 4,000 cells per well on a 96-well plate and incubated overnight. Probes were added to cells in FluoroBrite[™] DMEM media and cells were incubated in normoxia (19% O₂) or hypoxia (1% O₂, 94% N₂ and 5% CO₂). Cells were imaged using the IncuCyte[®] live-cell analysis system, fitted with a 440 - 480 nm excitation passband and a 504 - 544 nm emission passband.

3.3.5 Morphology of lung epithelial cell line (BEAS-2B) and decidual mesenchymal stromal cell line (DMSC23) on top of GHPA hydrogel

Initially, the cytocompatibility of the hydrogel was tested by assessing proliferation and morphology of DMSC23 and BEAS-2B (lung epithelial cell line as a control) cultured on top of the hydrogel (two-dimensional) casted in the wells of a 96-well plate (seeded 5,000 cells per well). Cell morphology and proliferation were monitored by live imaging (IncuCyte, 10 × magnification) and detailed analyses of morphology were conducted using the scanning electron microscopy (SEM). For preparing samples for SEM, samples were fixed in 2.5% glutaraldehyde in 0.1 M phosphate buffer (pH 7.2) overnight. The fixed cells were washed three times using 0.1 M phosphate buffer and fixed using a secondary fixative osmium tetroxide

1% for 1 h at room temperature. Osmium tetroxide was removed and samples were washed three times using Milli-Q water, 5 min each. For dehydration, samples were incubated 5 min each in 30%, 50%, 70%, 90%, 95% and 100% ethanol, with each of 70-95% step repeated once and 100% step repeated twice. Samples in 100% ethanol were placed in critical point dryer for 2 h with a gentle cycle (Option 14: 50% stirrer, Auto, CO₂ IN: Speed slow, Filler 1/1, Delay 120s, Exchange: Speed 5, Cycles 14, Gas OUT: Heat slow, Speed slow 100%). Samples were sputter coated with approximately 20 nm thick gold using a K550X sputter coater (Quorum Emitech, Kent, UK). Images were obtained using Zeiss Sigma high definition field emission gun scanning electron microscope (Carl Zeiss AG, Oberkochen, Germany).

3.3.6 Cell viability of DMSC23 encapsulated inside GHPA hydrogel

For incorporation of cells in three-dimensional structure of the hydrogel, 1.5×10^4 cells (for 30 μ l each hydrogel sample) were centrifuged to form a pellet. GHPA part A and B were prepared as described above using 14.46 mg GHPA dissolved in 260 μ l, for final volume of A and B each to be 125 μ l after incorporation of HRP and H₂O₂. The HRP-containing part A was directly added onto the cell pellet, to yield 30 μ l samples containing 1.5×10^4 cells. By pipetting up and down several times, cells were evenly distributed across the hydrogel sample and same volume of part B was added and mixed evenly before quickly casting the sample onto glass-bottom μ -slide 8-well dishes (ibidi USA Inc, Madison, Wisconsin, USA).

At each time point (days 1, 3, 7 and 14), samples were washed with PBS, Calcein-AM and Ethidium homodimer III (EthD-III) dyes were used to fluorescently label the live and dead cells using the Live/Dead Cell Staining Kit II (PromoKine, Heidelberg, Germany) as per the manufacturer's protocols. samples were fixed in 4% formaldehyde fixative solution (Image-iT™, Sigma-Aldrich) for 20 min then gently washed with PBS three times. Immediately following fixation, the live and dead cells were imaged respectively using the 488 nm and 633 nm lasers, in Z-stacks consisting of 40 slices each on Zeiss LSM 510 Meta Spectral confocal microscope (Carl Zeiss AG). The images were merged together using the ImageJ software.

3.3.7 Cell metabolic activity assay for DMSC23 encapsulated inside GHPA hydrogel

At each predetermined time point (days 1, 3 and 7), samples were washed twice with pre-warmed PBS. The metabolic activities of triplicate samples were measured using the alamarBlue® assay (Thermo Fisher Scientific), following the manufacturer's instructions. Victor X multilabel plate reader (PerkinElmer, Melbourne, VIC, Australia) was used to measure the fluorescence intensity at excitation 544 nm / emission 590 nm.

3.3.8 Measurement of mechanical properties of the hydrogel alone and with DMSC23

An atomic force microscope was used to determine nanomechanical properties of the hydrogel alone and with DMSC23 (MFP-3D-Bio, Santa Barbara, CA, USA). Experiments were conducted using silicon nitride probes (ContGB-G; Budget Sensors, Sofia, Bulgaria). The stiffness was measured in PBS by indenting the substrate with maximum force 20 nN at the rate of 0.5 Hz and recording force-deflection (F-D) curves. For each substrate, minimum 10 points in different locations were measured. Young's modulus was calculated. Stiffness map was generated by measuring $20 \times 20 \mu\text{m}$.

For measuring the bulk mechanical properties of the samples, Elastosens Bio² (Rheolution Inc., Montreal, Quebec, Canada) was used. Following calibration of the system, small sample holders (2.7 ml) were placed inside the equipment for 30 min for equilibration. The measurement parameters were configured to measure every 45 sec at room temperature. Hydrogel samples alone and with DMSC23 were casted directly inside the sample holder and stiffness measurement was conducted for 75 min. After completing the measurements, samples were placed back inside the incubator until the future time points, day 7 and 28.

3.3.9 Atomisation of DMSC23 in GHPA hydrogel and particle size measurement

After incorporating cells and HRP into GHPA part A and H₂O₂ into GHPA part B (as detailed above in 3.3.2) and thorough mixing of each parts, part A was taken up into a syringe. Then after incorporating part B into the same syringe, LMA[®] MADgic Airway[™] MAD780 (Teleflex Medical Australia, Mascot, NSW, Australia) was attached to the syringe immediately and the GHPA solution was sprayed onto a glass bottom dish (ibidi Inc.). At each time point (days 1, 3 and 7), samples were washed twice with pre-warmed PBS and live/dead assay was conducted as described above in 3.3.6. The particle size measurement for atomised hydrogel was conducted using a Spraytec (Malvern Instruments Ltd, Worcestershire, UK) used with refractive index of 1.0 and flow rate at 87 L/min, measured for 4 sec.

3.3.10 Statistical analysis

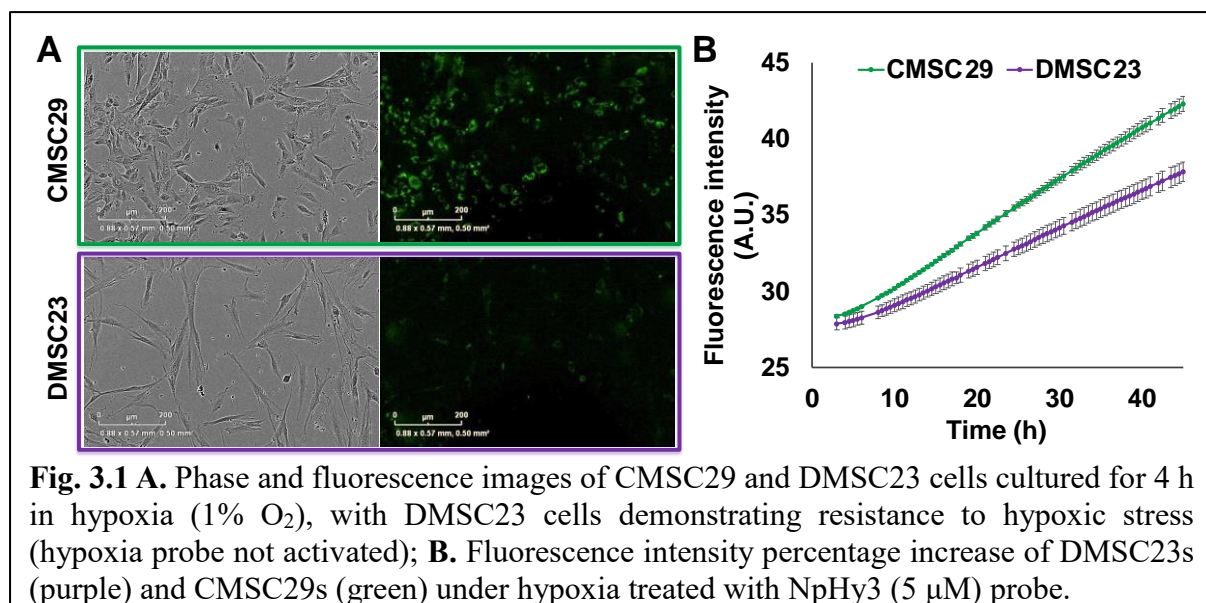
Triplicates were used in each experimental condition being examined. Data were analysed and presented as mean \pm standard deviation. The differences between the experimental and control groups were analysed using one-way analysis of variance (ANOVA) test. A p-value less than 0.05 was reported as having a statistically significant difference.

3.4 Results and Discussion

3.4.1 Decidual mesenchymal stromal cell line (DMSC23) are more resistant to hypoxia compared to chorionic mesenchymal stromal cell line (CMSC29)

Similarly to DMSC primary cells, DMSC23 is naturally resistant to oxidative stress due to the pre-conditioning on the region of placenta where the cells are isolated from^{12, 20}. To compare the resistance of cells to hypoxic injury for DMSC23 and CMSC29, an in-house nitronaphthalimide hypoxia (NpHy3) probe was used, designed to switch on fluorescence in response to hypoxic stress when internalised by cells²². The results confirmed that DMSC23 is more resistant to hypoxic stress, as the intensity of fluorescence of the NpHy3 probe was significantly lower in DMSC23 compared to CMSC29 (Fig. 3.1). A recent study found that hypoxia-preconditioned MSCs ameliorate ischemia/reperfusion-induced lung injury⁴³. This study highlighted the anti-oxidant, anti-inflammatory and anti-apoptotic mechanisms of hypoxic MSCs in ischemia/reperfusion lung injury. Thus, the hypoxia-resistant and naturally pre-conditioned DMSC23 is an ideal cell type for our proposed cell type. If necessary, further pre-conditioning of DMSC23 in hypoxia will be achievable due to its robustness in hypoxic conditions and may further deliver beneficial effects for therapeutic use.

There is increasing evidence that the EVs have an important role in intercellular communications between cells *via* the transfer of their biological content and to a certain degree their molecular contents reflect the properties of cells from which they are secreted^{44, 45}. Thus, DMSC23 EVs were further tested for capability to reduce stress in an established *in vitro* model of acute lung injury using LPS for BEAS-2B lung epithelial cells (as reported in Chapter 4 of this thesis).

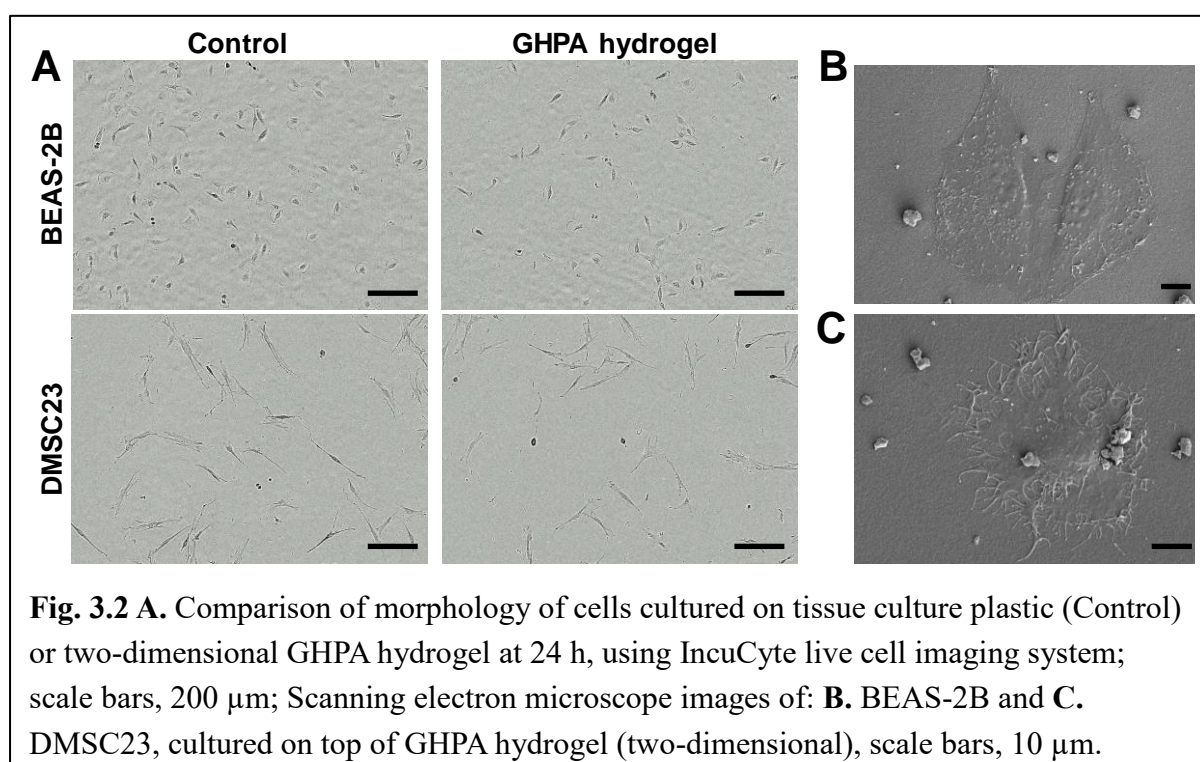


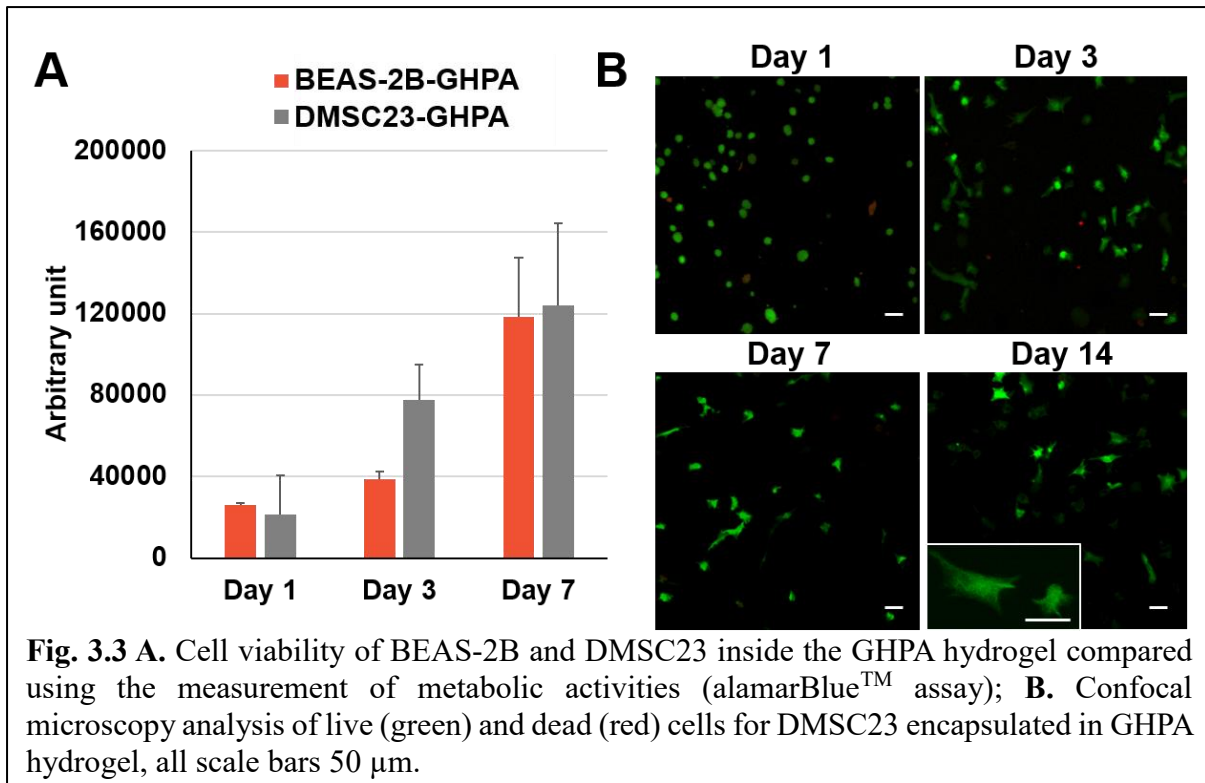
3.4.2 BEAS-2B and DMSC23 proliferate well on GHPA hydrogel

Initially, cells cultured two dimensionally on top of the hydrogel casted in well plates demonstrated satisfactory cellular attachment and normal proliferation as monitored by live cell imaging. At 24 h time point, there were minimal differences between cells cultured on tissue culture plastic (control) and cells cultured on top of GHPA hydrogel for both BEAS-2B and DMSC23 (Fig. 3.2A). The detailed morphology of the cells cultured on top of the GHPA hydrogel at 24 h after cell attachment demonstrated that the cells were spread well, with sufficient adhesion points overall (Fig. 3.2B). Initially, the representative images from each cell type indicated that the hydrogel was more compatible to BEAS-2B compared to the DMSC23, especially as seen from longer incubations (data not presented). However, with repeated experiment and supposedly improved techniques during the hydrogel fabrication, DMSC23 were also demonstrated to survive and proliferate well for long term incubations (Fig. 3.3).

3.4.3 Cells encapsulated in GHPA hydrogel proliferate well and have high viability

After achieving proficiency in the techniques of hydrogel fabrication, the process became faster and more reproducible. Both BEAS-2B and DMSC23 encapsulated three-dimensionally in GHPA hydrogel proliferated well as measured by their metabolic activity (Fig. 3.3A). The proliferation of BEAS-2B was slower than DMSC23 until day 3 then the rate of proliferation increased to yield similar levels as those of DMSC23 by day 7. The cells were successfully





incorporated into the three-dimensional structure of the hydrogel as was observed by z-stack imaging on a confocal microscope. As can be seen on day 1 images of DMSC23 (Fig. 3.3B), the cells were initially rounded and did not adhere to the hydrogel structure. By day 3, the cells were nicely stretched and developed a similar morphology to those observed when cells were cultured two dimensionally on hydrogel and tissue culture plastic (Fig. 3.2A). This demonstrates that the cells take some time (longer than 24 h) to adhere and incorporate themselves into the hydrogel structure, possibly due to several mechanical and biomechanical mechanisms that cells undergo when interacting with the surrounding matrix. However, cells have high viability, as can be seen minimal number of dead (red) cells from the live/dead assay (Fig. 3.3B). The cells survived well until day 21 (data not presented) with similar morphology to those observed on day 14, with stretched morphology that portrays adherence of these cells to the extracellular matrix and the degrading hydrogel matrix. This confirmed that GHPA hydrogel is a suitable platform for DMSC23 encapsulation that enables the proliferation of cells, while retaining high viability within the hydrogel platform.

3.4.4 Degradation of GHPA hydrogel and modification in hydrogel stiffness is detected using nanoindentation and an advanced sensing measurement

The mechanical properties and degradation of the GHPA hydrogel were characterised alone and with encapsulated cells in wet conditions using nanoindentation on the atomic force

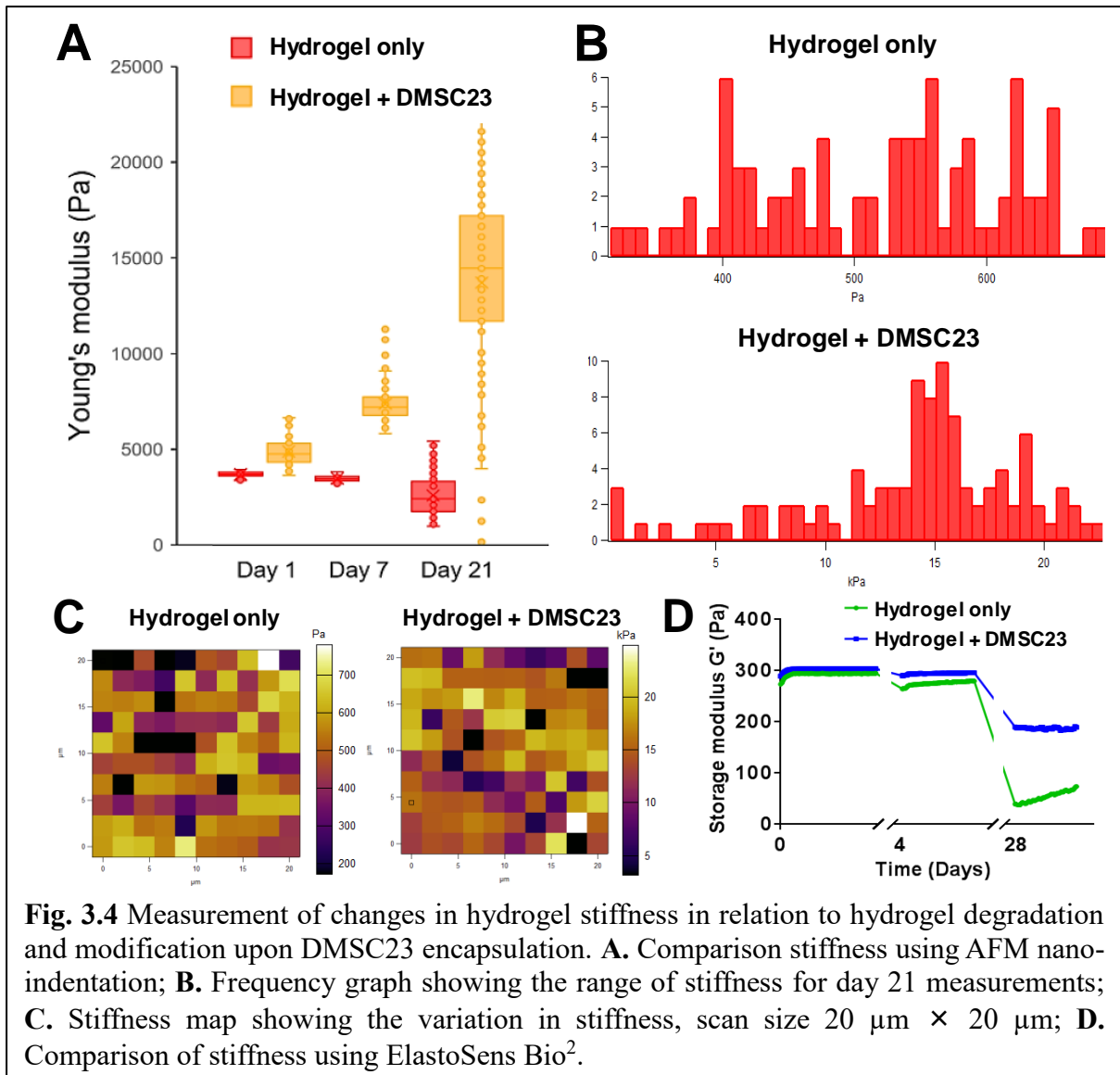


Fig. 3.4 Measurement of changes in hydrogel stiffness in relation to hydrogel degradation and modification upon DMSC23 encapsulation. **A.** Comparison stiffness using AFM nano-indentation; **B.** Frequency graph showing the range of stiffness for day 21 measurements; **C.** Stiffness map showing the variation in stiffness, scan size 20 $\mu\text{m} \times 20 \mu\text{m}$; **D.** Comparison of stiffness using ElastoSens Bio².

microscope (AFM) as well as *via* a contactless mechanical degradation measurement using micrometric vibrations (Elastosens Bio²). Since GHPA hydrogel has tunable physicochemical and mechanical properties, the stiffness of the hydrogel was optimised to be approximately 4 kPa (Day 1, Fig. 3.4A), by altering the concentration of H₂O₂, to match the stiffness of the healthy lung, which is approximately 0.5 – 5 kPa⁴⁶. The nanoindentation method revealed the degradation of the hydrogel over 21 days as observed from the decreased stiffness in the measurements for the hydrogel alone group (Fig. 3.4A). On the other hand, the stiffness of the hydrogel increased when cells embedded within the hydrogel proliferated over time. By day 21, the stiffness of hydrogel alone was within the 400 – 900 Pa range whereas the stiffness of the hydrogel with cells was within the 5 – 20 kPa range (Fig. 3.4B). This can be explained by increased proliferation of cells as cells have higher stiffness profile compared to the degrading hydrogel or it can be part of a dynamic matrix stiffening process due to increased crosslinking

density over time⁴⁷. A study using the same GHPA hydrogel demonstrated a similar relationship wherein the resistance to degradation correlated directly with crosslinking density⁴⁰. When the stiffness map was generated for the day 21 time point, it was evident that both hydrogel alone and hydrogel with DMSC23 had a range of stiffness non-uniformly distributed across the sample (Fig. 3.4C), revealing that the crosslinking was not homogenous throughout the mixture. This may have been due to the crosslinking agents H₂O₂ and HRP not being evenly mixed due to imperfect pipetting techniques and limited time of mixing prior to cross-linking.

The measurement of hydrogel degradation is critical as was recently reported that the stemness properties of encapsulated stem cells are correlated with hydrogel degradability⁴⁸. The increase in cell-mediated degradation and remodelling of their microenvironment was directly correlated to maintenance of stemness and increase in growth of cells⁴⁸. The bulk, averaged measurement of GHPA hydrogel alone and with DMSC23 over three time points, day 1, 4 and 28 revealed that the differences in stiffness is not as evident on day 1 and 4, yet it is more obvious after 28 days (Fig. 3.4D). The results from the measurement of mechanical properties of hydrogel highlight the benefits of combining two different approaches of stiffness measurements, using bulk / averaged measurement (Elastosens Bio²) and nanoindentation (AFM) together. The Elastosens Bio² enables the analysis of the Young viscoelastic modulus. The sample is placed inside the sample holder with a mechanically flexible membrane at the bottom, where an external low frequency-amplitude vibration is transmitted. The sample's dynamic response to the vibrations is measured. On the other hand, the AFM nanoindentation measures the Young's modulus as force is applied to a specific point on the sample by calculating the deflection of the cantilever in relation to its stiffness. Combining the bulk, averaged measurement with Elastosens Bio² together with AFM nanoindentation resulted in a more thorough characterisation profiling of the cell-laden hydrogel, suited to the investigation of the dynamic properties and changes upon a prolonged incubation period. The GHPA hydrogel designed and synthesised in this study was demonstrated to have desirable properties of an ideal hydrogel platform, which include biocompatibility, biodegradability, therapeutic cell interactions, mechanical strength and elastic properties⁴⁹.

3.4.5 Sprayed DMSC23-GHPA has similar cell viability to non-sprayed cells in hydrogel

After confirming the suitability of GHPA hydrogel for encapsulating DMSC23 cells, the components A and B of the hydrogel fabrication parts were combined inside a syringe attached with LMA MAD780 atomisation device for spraying hydrogel. Initially, the feasibility of

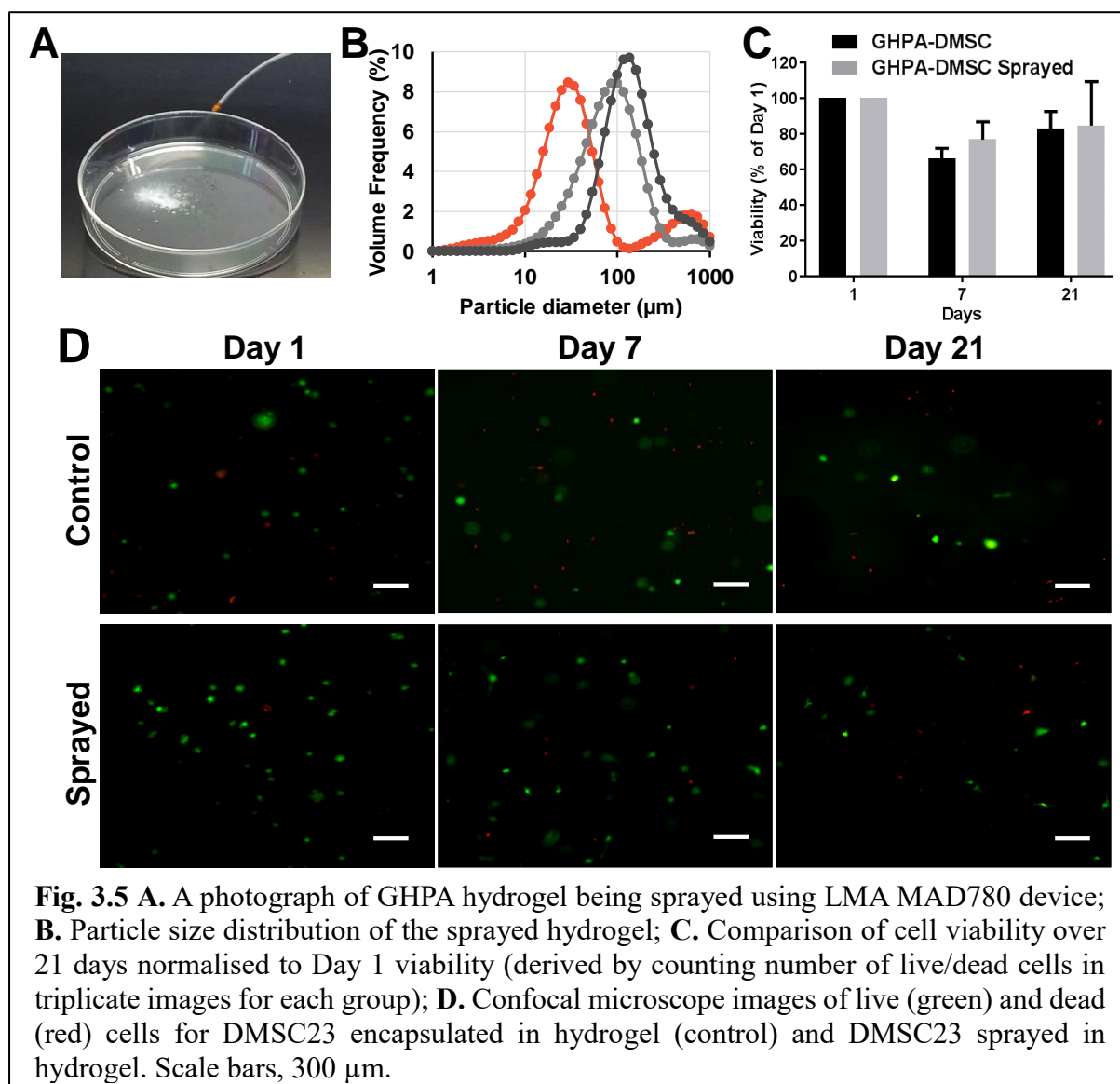


Fig. 3.5 A. A photograph of GHPA hydrogel being sprayed using LMA MAD780 device; B. Particle size distribution of the sprayed hydrogel; C. Comparison of cell viability over 21 days normalised to Day 1 viability (derived by counting number of live/dead cells in triplicate images for each group); D. Confocal microscope images of live (green) and dead (red) cells for DMSC23 encapsulated in hydrogel (control) and DMSC23 sprayed in hydrogel. Scale bars, 300 μm .

spraying the GHPA hydrogel without cells were tested to ensure that the time of cross-linking was longer than the time of spraying the formulation. The feasibility to achieve this and sprayability of GHPA hydrogel was confirmed (Fig. 3.5A,B). The D50 value of particle size distribution (the midpoint diameter of the particle that 50% of the sample is smaller than and 50% of the sample is larger than) of the hydrogel particles varied (28.8 μm , 77.5 μm and 123.4 μm). The variation is likely to be from the limited consistency in pressure pushing the plunger of the syringe in this handheld device and possible cross-linking that was initiate before passing through the nozzle. This variation was more evident also due to the viscosity of the hydrogel formulation, as evident from the data using the same handheld device for spraying extracellular vesicles in less-viscous PBS on the same day did not result in such variation (Fig. 4.4 in Chapter 4 of this thesis). The particle size range observed indicates that these DMSC23 in GHPA

hydrogel is likely to reach and deposit in the trachea and upper airways rather than reaching the lower airways, which is also beneficial for the proposed use in inhalation injury.

The cell viability measured after spraying in the GHPA hydrogel platform showed high viability and proliferation over 21 days with no statistical difference compared to the non-sprayed group (Fig. 3.5C,D). This study demonstrated the feasibility to encapsulate and spray the DMSC23 cells in hydrogel, for direct airway delivery.

3.5 Conclusions

In this study, an *in-situ* crosslinkable gelatin-based hydrogel was formulated for potential airway delivery to the lung. The favourable properties of this GHPA hydrogel include:

- An excellent biocompatibility was demonstrated with DMSC23, which is naturally pre-conditioned to be resistant to hypoxic stress.
- The ability to spray GHPA hydrogel and maintenance of high viability of DMSC23 when sprayed in GHPA hydrogel.
- Biodegradability as measured using two different approaches, nanoindentation and bulk / averaged measurement of the hydrogel alone and with cells encapsulated.

With growing interest on how material microenvironments influence cellular functions, it is critical that further studies are conducted on measuring the function of DMSC23 after encapsulation in GHPA hydrogel. In particular, studies to determine which lineages DMSC23 differentiate into, as guided by the hydrogel, is ongoing and the outcomes are expected to lead to broader application of GHPA hydrogel cell delivery system.

3.6 References

1. Moschidou, D., Mukherjee, S., Blundell, M.P., Drews, K., Jones, G.N., Abdulrazzak, H., Nowakowska, B., Phoolchand, A., Lay, K., Ramasamy, T.S., Cananzi, M., Nettersheim, D., Sullivan, M., Frost, J., Moore, G., Vermeesch, J.R., Fisk, N.M., Thrasher, A.J., Atala, A., Adjaye, J., Schorle, H., De Coppi, P., and Guillot, P.V., Valproic acid confers functional pluripotency to human amniotic fluid stem cells in a transgene-free approach. *Mol Ther* 2012, **20**(10):1953-67.
2. Moschidou, D., Mukherjee, S., Blundell, M.P., Jones, G.N., Atala, A.J., Thrasher, A.J., Fisk, N.M., De Coppi, P., and Guillot, P.V., Human mid-trimester amniotic fluid stem cells cultured under embryonic stem cell conditions with valproic acid acquire pluripotent characteristics. *Stem Cells Dev* 2013, **22**(3):444-58.
3. Rao, R.C., Alternatives to embryonic stem cells and cloning: a brief scientific overview. *Yale J Health Policy Law Ethics* 2009, **9 Suppl**:603-22.
4. Prusa, A.R., Marton, E., Rosner, M., Bernaschek, G., and Hengstschlager, M., Oct-4-expressing cells in human amniotic fluid: a new source for stem cell research? *Hum Reprod* 2003, **18**(7):1489-93.
5. Prasajak, P. and Leraanaksiri, W., Mesenchymal Stem Cells: Current Clinical Applications and Therapeutic Potential in Liver Diseases. *Journal of Bone Marrow Research* 2014, **2**(1):137.
6. Lim, R., Concise Review: Fetal Membranes in Regenerative Medicine: New Tricks from an Old Dog? *Stem Cells Translational Medicine* 2017, **6**(9):1767-1776.
7. Doi, H., Kitajima, Y., Luo, L., Yan, C., Tateishi, S., Ono, Y., Urata, Y., Goto, S., Mori, R., Masuzaki, H., Shimokawa, I., Hirano, A., and Li, T.-S., Potency of umbilical cord blood- and Wharton's jelly-derived mesenchymal stem cells for scarless wound healing. *Scientific Reports* 2016, **6**:18844.
8. Ankrum, J.A., Ong, J.F., and Karp, J.M., Mesenchymal stem cells: immune evasive, not immune privileged. *Nature biotechnology* 2014, **32**(3):252-260.
9. Kyurkchiev, D., Bochev, I., Ivanova-Todorova, E., Mourdjeva, M., Oreshkova, T., Belemezova, K., and Kyurkchiev, S., Secretion of immunoregulatory cytokines by mesenchymal stem cells. *World Journal of Stem Cells* 2014, **6**(5):552-570.
10. Kim, E.Y., Lee, K.-B., and Kim, M.K., The potential of mesenchymal stem cells derived from amniotic membrane and amniotic fluid for neuronal regenerative therapy. *BMB Reports* 2014, **47**(3):135-140.
11. Elias, M., Hoover, J., Nguyen, H., Reyes, S., Lawton, C., and Borlongan, C.V., Stroke therapy: the potential of amniotic fluid-derived stem cells. *Future neurology* 2015, **10**(4):321-326.
12. Qin, S.Q., Kusuma, G.D., Al-Sowayan, B., Pace, R.A., Isenmann, S., Pertile, M.D., Gronthos, S., Abumaree, M.H., Brennecke, S.P., and Kalionis, B., Establishment and characterization of fetal and maternal mesenchymal stem/stromal cell lines from the human term placenta. *Placenta* 2016, **39**:134-46.

13. Zhu, Y., Yang, Y., Zhang, Y., Hao, G., Liu, T., Wang, L., Yang, T., Wang, Q., Zhang, G., Wei, J., and Li, Y., Placental mesenchymal stem cells of fetal and maternal origins demonstrate different therapeutic potentials. *Stem Cell Research & Therapy* 2014, **5**(2):48.
14. Talwadekar, M.D., Kale, V.P., and Limaye, L.S., Placenta-derived mesenchymal stem cells possess better immunoregulatory properties compared to their cord-derived counterparts—a paired sample study. *Scientific Reports* 2015, **5**:15784.
15. Liu, X., Zhu, Y., Liang, X., Han, F., and Wei, J., Effects of Inflammation-Mediated Autophagy of Human Placental Mesenchymal Stem Cells of Fetal Origin on Their Immunomodulatory Properties and Therapeutic Potential in Bleomycin-Induced Pulmonary Fibrosis Models. *Molecular Therapy* 2016, **24**:S71: 182.
16. Passipieri, J.A., Kasai-Brunswick, T.H., Suhett, G., Martins, A.B., Brasil, G.V., Campos, D.B., Rocha, N.N., Ramos, I.P., Mello, D.B., Rodrigues, D.C., Christie, B.B., Silva-Mendes, B.J., Balduino, A., Sá, R.M., Lopes, L.M., Goldenberg, R.C., Campos de Carvalho, A.C., and Carvalho, A.B., Improvement of cardiac function by placenta-derived mesenchymal stem cells does not require permanent engraftment and is independent of the insulin signaling pathway. *Stem Cell Research & Therapy* 2014, **5**(4):102.
17. Wang, A., Brown, E.G., Lankford, L., Keller, B.A., Pivetti, C.D., Sitkin, N.A., Beattie, M.S., Bresnahan, J.C., and Farmer, D.L., Placental mesenchymal stromal cells rescue ambulation in ovine myelomeningocele. *Stem Cells Transl Med* 2015, **4**(6):659-69.
18. Kinzer, M., Hingerl, K., König, J., Reinisch, A., Strunk, D., Huppertz, B., and Lang, I., Mesenchymal stromal cells from the human placenta promote neovascularization in a mouse model in vivo. *Placenta* 2014, **35**(7):517-519.
19. Zhang, B., Adesanya, T.M.A., Zhang, L., Xie, N., Chen, Z., Fu, M., Zhang, J., Zhang, J., Tan, T., Kilic, A., Li, Z., Zhu, H., and Xie, X., Delivery of Placenta-Derived Mesenchymal Stem Cells Ameliorates Ischemia Induced Limb Injury by Immunomodulation. *Cellular Physiology and Biochemistry* 2014, **34**(6):1998-2006.
20. Kusuma, G.D., Abumaree, M.H., Pertile, M.D., Perkins, A.V., Brennecke, S.P., and Kalionis, B., Mesenchymal Stem/Stromal Cells Derived From a Reproductive Tissue Niche Under Oxidative Stress Have High Aldehyde Dehydrogenase Activity. *Stem Cell Rev* 2016, **12**(3):285-97.
21. Nazarov, I., Lee, J.W., Soupene, E., Etemad, S., Knapik, D., Green, W., Bashkirova, E., Fang, X., Matthay, M.A., Kuypers, F.A., and Serikov, V.B., Multipotent Stromal Stem Cells from Human Placenta Demonstrate High Therapeutic Potential. *STEM CELLS Translational Medicine* 2012, **1**(5):359-372.
22. Yang, K., Leslie, K.G., Kim, S.Y., Kalionis, B., Chrzanowski, W., Jolliffe, K.A., and New, E.J., Tailoring the properties of a hypoxia-responsive 1,8-naphthalimide for imaging applications. *Organic & Biomolecular Chemistry* 2018, **16**(4):619-624.
23. Speidel, A.T., Stuckey, D.J., Chow, L.W., Jackson, L.H., Nosedá, M., Abreu Paiva, M., Schneider, M.D., and Stevens, M.M., Multimodal Hydrogel-Based Platform To Deliver and Monitor Cardiac Progenitor/Stem Cell Engraftment. *ACS Cent Sci* 2017, **3**(4):338-348.

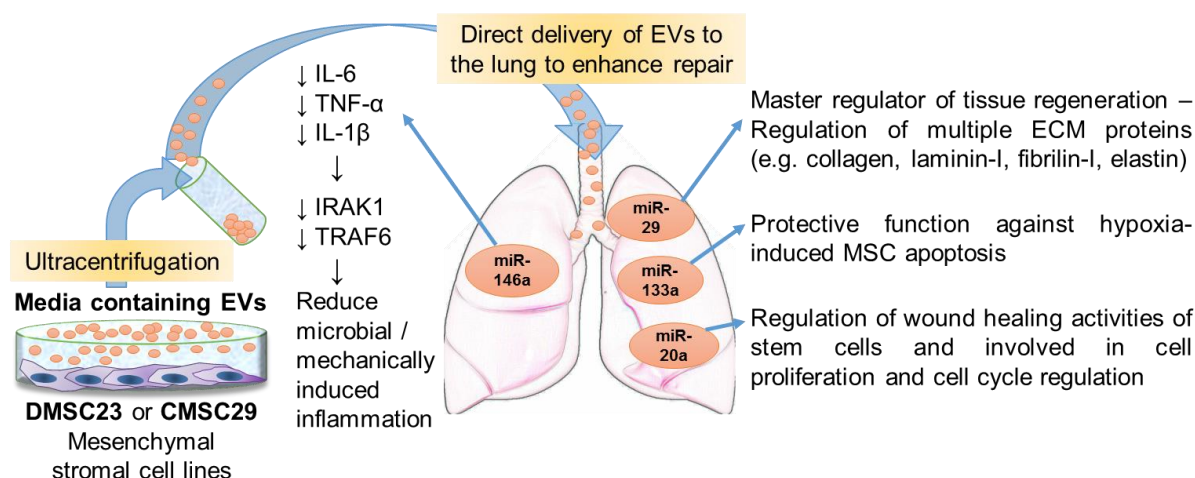
24. Lai, C.Y., Wu, P.J., Roffler, S.R., Lee, S.T., Hwang, S.M., Wang, S.S., Wang, K., and Hsieh, P.C., Clearance kinetics of biomaterials affects stem cell retention and therapeutic efficacy. *Biomacromolecules* 2014, **15**(2):564-73.
25. Zhang, Z., Injectable biomaterials for stem cell delivery and tissue regeneration. *Expert Opinion on Biological Therapy* 2017, **17**(1):49-62.
26. Foster, A.A., Marquardt, L.M., and Heilshorn, S.C., The diverse roles of hydrogel mechanics in injectable stem cell transplantation. *Current Opinion in Chemical Engineering* 2017, **15**:15-23.
27. Zarembinski, T.I., Tew, W.P., and Atzet, S.K., The Use of a Hydrogel Matrix as a Cellular Delivery Vehicle in Future Cell-Based Therapies: Biological and Non-Biological Considerations, in *Regenerative Medicine and Tissue Engineering - Cells and Biomaterials*, D. Eberli, Editor. 2011, InTech.
28. Ke, Y., Wu, Y., Cui, X., Liu, X., Yu, M., Yang, C., and Li, X., Polysaccharide Hydrogel Combined with Mesenchymal Stem Cells Promotes the Healing of Corneal Alkali Burn in Rats. *PLOS ONE* 2015, **10**(3):e0119725.
29. Kurdi, M., Chidiac, R., Hoemann, C., Zouein, F., Zgheib, C., and Booz, G.W., Hydrogels as a platform for stem cell delivery to the heart. *Congest Heart Fail* 2010, **16**(3):132-5.
30. Michal, S., Rotem, Z., Alona, A., Sharon, F., Assaf, S., and Tal, D., Omentum ECM-based hydrogel as a platform for cardiac cell delivery. *Biomedical Materials* 2015, **10**(3):034106.
31. Lev, R. and Seliktar, D., Hydrogel biomaterials and their therapeutic potential for muscle injuries and muscular dystrophies. *Journal of The Royal Society Interface* 2018, **15**(138).
32. Liu, J., Xu, H.H., Zhou, H., Weir, M.D., Chen, Q., and Trotman, C.A., Human umbilical cord stem cell encapsulation in novel macroporous and injectable fibrin for muscle tissue engineering. *Acta Biomater* 2013, **9**(1):4688-97.
33. Rey-Rico, A., Madry, H., and Cucchiari, M., Hydrogel-Based Controlled Delivery Systems for Articular Cartilage Repair. *BioMed Research International* 2016, **2016**:12.
34. Huebsch, N., Lippens, E., Lee, K., Mehta, M., Koshy, S.T., Darnell, M.C., Desai, R.M., Madl, C.M., Xu, M., Zhao, X., Chaudhuri, O., Verbeke, C., Kim, W.S., Alim, K., Mammoto, A., Ingber, D.E., Duda, G.N., and Mooney, D.J., Matrix elasticity of void-forming hydrogels controls transplanted-stem-cell-mediated bone formation. *Nat Mater* 2015, **14**(12):1269-77.
35. Cai, L., Dewi, R.E., Goldstone, A.B., Cohen, J.E., Steele, A.N., Woo, Y.J., and Heilshorn, S.C., Regulating Stem Cell Secretome Using Injectable Hydrogels with In Situ Network Formation. *Adv Healthc Mater* 2016, **5**(21):2758-2764.
36. Gorgieva, S. and Kokol, V., Collagen- vs. Gelatine-Based Biomaterials and Their Biocompatibility: Review and Perspectives, in *Biomaterials Applications for Nanomedicine*, R. Pignatello, Editor. 2011, InTech.

37. Zhao, X., Lang, Q., Yildirim, L., Lin, Z.Y., Cui, W., Annabi, N., Ng, K.W., Dokmeci, M.R., Ghaemmaghami, A.M., and Khademhosseini, A., Photocrosslinkable Gelatin Hydrogel for Epidermal Tissue Engineering. *Adv Healthc Mater* 2016, **5**(1):108-18.
38. Yue, K., Santiago, G.T.-d., Alvarez, M.M., Tamayol, A., Annabi, N., and Khademhosseini, A., Synthesis, properties, and biomedical applications of gelatin methacryloyl (GelMA) hydrogels. *Biomaterials* 2015, **73**:254-271.
39. Lee, S.H., Lee, Y., Chun, Y.W., Crowder, S.W., Young, P.P., Park, K.D., and Sung, H.-J., In Situ Crosslinkable Gelatin Hydrogels for Vasculogenic Induction and Delivery of Mesenchymal Stem Cells. *Advanced functional materials* 2014, **24**(43):6771-6781.
40. Lee, Y., Bae, J.W., Oh, D.H., Park, K.M., Chun, Y.W., Sung, H.-J., and Park, K.D., In situ forming gelatin-based tissue adhesives and their phenolic content-driven properties. *Journal of Materials Chemistry B* 2013, **1**(18):2407-2414.
41. Kim, M.J., Shin, Y.C., Lee, J.H., Jun, S.W., Kim, C.-S., Lee, Y., Park, J.-C., Lee, S.-H., Park, K.D., and Han, D.-W., Multiphoton imaging of myogenic differentiation in gelatin-based hydrogels as tissue engineering scaffolds. *Biomaterials Research* 2016, **20**:2.
42. Liu, C.-W., Chang, L.-C., Lin, K.-J., Yu, T.-J., Tsai, C.-C., Wang, H.-K., and Tsai, T.-R., Preparation and Characterization of Gelatin-Based Mucoadhesive Nanocomposites as Intravesical Gene Delivery Scaffolds. *BioMed Research International* 2014, **2014**:12.
43. Liu, Y.-Y., Chiang, C.-H., Hung, S.-C., Chian, C.-F., Tsai, C.-L., Chen, W.-C., and Zhang, H., Hypoxia-preconditioned mesenchymal stem cells ameliorate ischemia/reperfusion-induced lung injury. *PLOS ONE* 2017, **12**(11):e0187637.
44. Willms, E., Johansson, H.J., Mäger, I., Lee, Y., Blomberg, K.E.M., Sadik, M., Alaarg, A., Smith, C.I.E., Lehtiö, J., El Andaloussi, S., Wood, M.J.A., and Vader, P., Cells release subpopulations of exosomes with distinct molecular and biological properties. *Scientific Reports* 2016, **6**:22519.
45. Østergaard, O., Nielsen, C.T., Iversen, L.V., Jacobsen, S., Tanassi, J.T., and Heegaard, N.H.H., Quantitative Proteome Profiling of Normal Human Circulating Microparticles. *Journal of Proteome Research* 2012, **11**(4):2154-2163.
46. Asano, S., Ito, S., Takahashi, K., Furuya, K., Kondo, M., Sokabe, M., and Hasegawa, Y., Matrix stiffness regulates migration of human lung fibroblasts. *Physiological Reports* 2017, **5**(9):e13281.
47. Shih, H. and Lin, C.-C., Tuning stiffness of cell-laden hydrogel via host-guest interactions. *Journal of Materials Chemistry B* 2016, **4**(29):4969-4974.
48. Madl, C.M., LeSavage, B.L., Dewi, R.E., Dinh, C.B., Stowers, R.S., Khariton, M., Lampe, K.J., Nguyen, D., Chaudhuri, O., Enejder, A., and Heilshorn, S.C., Maintenance of neural progenitor cell stemness in 3D hydrogels requires matrix remodelling. *Nature Materials* 2017, **16**:1233.
49. Tsou, Y.-H., Khoneisser, J., Huang, P.-C., and Xu, X., Hydrogel as a bioactive material to regulate stem cell fate. *Bioactive Materials* 2016, **1**(1):39-55.

4 Extracellular vesicles (EVs) for the treatment of lung injury

4.1 Overview

4.1.1 Graphical abstract



4.1.2 Highlights and keywords

- The therapeutic benefit of stem cells is mainly through paracrine actions of EVs.
- EVs derived from decidual mesenchymal stromal cell line have a potential role to ameliorate the effects of lung injury.
- Direct delivery of EVs to the lung by atomisation is a promising therapeutic approach to drive lung tissue regeneration after injury.
- An innovative approach to characterise EVs using atomic force microscope infrared spectroscopy enables single vesicle characterisation.
- The identification of the most therapeutically relevant EV subtypes using single vesicle characterisation and microRNA profiling will advance this field of EV-based therapies.

Keywords: Extracellular vesicles, microvesicles, exosomes, placenta mesenchymal stromal cells, regenerative potential, lung injury

The introduction section was published in (contributed as equal first-author):

Biomaterials
Science



REVIEW

[View Article Online](#)
[View Journal](#) | [View Issue](#)



Cite this: *Biomater. Sci.*, 2018, 6, 60

Extracellular vesicles, exosomes and shedding vesicles in regenerative medicine – a new paradigm for tissue repair

I. M. Bjørge, ^{†a} S. Y. Kim, ^{†b,c} J. F. Mano, ^a B. Kalionis ^d and W. Chrzanowski ^{*b,c}

[†]Equal contribution.

4.1.3 Abstract

Tissue regeneration by stem cells is driven by the paracrine activity of extracellular vesicles (EVs), which deliver specific cargoes to the recipient cells. Proteins, RNA, cytokines and subsequent gene expression, orchestrate the regeneration process by improving the microenvironment to promote cell survival, controlling inflammation, repairing injury and enhancing the healing process. The action of microRNA is widely accepted as an essential driver of the regenerative process through its impact on multiple downstream biological pathways, and its ability to regulate the host immune response.

This study presents the assessment of placenta-derived mesenchymal stromal cell EVs for regenerative medicine. The EVs from different stem cell lines, chorionic mesenchymal stromal cell line (CMSC29) and decidual mesenchymal stromal cell line (DMSC23), from hypoxic or normoxic conditions, were assessed using a combination of conventional microscopy, nanoparticle tracking analysis, tunable resistive pulse sensing and biological analyses. This study also presents the use of atomic force microscope infrared spectroscopy for the characterisation of EV chemical composition for the first time. This innovative technique enables the study of structural and molecular differences of individual EVs at nanoscale application, as highlighted in the results section. The functional analyses using *in vitro* models of injury demonstrated potential of EVs derived from DMSC23 cell line in reducing cellular stress, which can be developed into pre-clinical studies. This study is fundamental to the overall assessment of CMSC29 and DMSC23 EVs for future application in regenerative treatment of the lung after injury.

4.2 Introduction

4.2.1 Cell-free strategies for tissue regeneration

Tissue engineering strategies often resort to the use of stem cells due to their regenerative and reparative potential. These effects are still not fully comprehended but are generally attributed to the trans-differentiation and cell fusion capacity, paracrine effects, mitochondrial transfer, and finally, the intercellular exchange of extracellular vesicles (EVs) ¹.

Recently, paracrine effects, in particular release and uptake of EVs (which includes exosomes and microvesicles) attracts considerably increasing attention and it was demonstrated that EVs have regenerative potential². Cell-free strategies using conditioned medium^{3, 4} or supplemented with EVs⁵ confirmed the capability of EVs to stimulate tissue regeneration. Cell-free approaches may be advantageous when risk factors associated with stem cell use are considered. These can be intrinsic factors relating to cell origin, tumorigenic potential, differentiation and proliferation capacity, or extrinsic factors concerning cell handling, storage, transport conditions, among others⁶. Furthermore, it is important to consider that stem cell yield decreases with donor age and that age also quantitatively impacts on stem cell functionality⁷. EVs, on the other hand, bypass a series of issues associated with stem cell therapy. Moreover, they can be easily stored, tested according to dosage and potency, and also lead to a cost and time reduction associated with cell expansion or collection from patients².

Stem/progenitor cells transfer EVs containing functional regenerative signals to injured cells and organs⁸. Examples of disease models that have been used to demonstrate EV capabilities in promoting the regeneration of tissues include chronic wound⁹, osteoarthritis¹⁰, myocardial infarction¹¹, chronic kidney disease¹² and lung diseases¹³.

The heterogenous compositions of proteins, lipids, and nucleic acids are selectively packaged into EVs by the secreting cells in response to the microenvironment^{8, 14}. The regenerative effects of EVs have been, at least in part, attributed to the transfer of specific protein and microRNA (miRNA) cargo¹⁵. With increasing interest on identifying the subpopulations of EVs that has maximum therapeutic potential and functionally relevant^{16, 17}, it has been demonstrated that miRNAs are enriched in the biologically active exosome fraction, rather than the microvesicle/shedding vesicle fraction¹⁵. Therefore, this review focuses on the role of exosomes and exosomal-miRNA in tissue regeneration and regenerative medicine.

4.2.2 Roles of EVs in regenerative medicine

Tissue engineering is a promising option for tissue repair and this technology can be combined with stem cell-based therapies since there is evidence that stem cells promote and regulate

tissue regeneration. Current strategies use the cell and/or its by-products secreted into the culture medium, as the active biological agent(s)¹⁸. EVs are by-products that regulate intercellular communication, which is necessary for multicellular organisms to maintain their vital functions. These EVs comprise the following sub-classes; apoptotic bodies, shedding vesicles and exosomes¹⁹.

EVs are a cell-free alternative to current stem cell therapies with advantages of lower immunogenic response and preservation of biochemical activity upon storage²⁰⁻²². Furthermore, employing EVs bypasses important safety concerns associated with the engraftment of viable replicating cells, which have the potential for long term pathological transformation²³. MSC-derived exosomes and shedding vesicles have been investigated for a range of *in vitro* and *in vivo* regenerative medicine applications involving brain²⁴, bone²⁵, lung^{26, 27}, liver^{28, 29}, kidney^{30, 31}, heart³², and colon³³ injuries. The role of miRNA in tissue engineering and regenerative medicine is of interest because miRNAs influence a wide range of cell functions including differentiation and gene expression³⁴⁻³⁷. Exosomal miRNA is thought to be the key factor in intracellular communication and regulation, with a preponderant role in the modulation of biological functions of acceptor cells³⁸⁻⁴⁰.

4.2.3 EVs in lung regeneration

In response to injury and disease, the lung has the ability to activate quiescent stem or progenitor cell lineages within the lung and the epithelial cell lineages may re-enter the cell cycle to repopulate lost cells⁴¹. Attempts to assist tissue regeneration of the lung using exogenous stem cells have discovered that the benefits are through paracrine actions regardless of the route of delivery⁴². The lung is unique in that it allows not only the intravenous route for stem cell delivery but also a more direct delivery route by inhalation⁴³. Gupta *et al* in 2007 carried out one of the first studies to demonstrate that intratracheal delivery of MSCs is as effective as intravenous route in attenuating acute lung injury in mice⁴⁴. Subsequently, many studies investigated the intravenous and intratracheal route of delivery of stem/progenitor cells but to date there is no consensus on the best route^{43, 45-48}. Regardless of the route of delivery, most studies support a paracrine mechanism of action and therefore it is widely accepted that stem cell-derived extracellular vesicles are promising paracrine factors that aid and accelerate lung regeneration. Microvesicles released by human MSCs were recently shown to be as effective as the stem cell type of origin in alleviating lung inflammation caused by severe bacterial pneumonia, and in improving survival in a murine model⁴⁹.

MSC exosomes have also been shown to ameliorate chronic lung diseases including bronchopulmonary dysplasia, as recently reported⁵⁰. In a mouse model of hyperoxia-induced pulmonary hypertension and bronchopulmonary dysplasia, even a single dose of MSC exosomes restored lung architecture and led to significant long-term benefits in the lung function through immunomodulatory effects⁵⁰. The mRNA sequencing of the lung revealed that the proinflammatory M1 state of macrophages were suppressed while the anti-inflammatory M2-like state was augmented.

Numerous studies showed not only specific miRNAs contained in EVs are crucial for lung repair *in vivo*, particularly for influenza⁵¹, and hypoxia-induced pulmonary hypertension²⁶, while specific miRNAs are effective in endotoxin-induced acute lung injury⁵². Tan *et al.* analysed the regulation of miRNAs during early and late stages of repair after influenza infection in a mouse model⁵¹. The miRNAs that play major roles in priming pulmonary tissues for repair and regeneration following influenza were identified, and particularly miR-290, miR-21, let-7 and miR-200 appeared to be highly involved in the regeneration process. Beyond regulating regeneration, miR-21 and let-7 have further benefits such as anti-inflammatory properties. These properties are of significant benefit since many lung conditions that require regeneration have concomitant, uncontrolled inflammation. miR-21 is also present in microvesicles of important stem cell types such as murine embryonic stem cells⁵³ and human bone marrow mesenchymal stem cells⁵⁴.

Lee *et al.* provided strong evidence that exosomes prevented the activation of hypoxic signalling, which underlies pulmonary inflammation and pulmonary hypertension. In a model of hypoxia-induced pulmonary hypertension, mice treated with exosomes derived from umbilical cord-derived MSCs showed suppression of hypoxia-induced pulmonary inflammation and vascular remodelling, in a dose-dependent manner. In that study, exosomes derived from mouse lung fibroblasts were used as a control and showed no protective effect against pulmonary hypertension, when compared with MSC-derived exosomes²⁶. The effect of the exosomes derived from umbilical cord-derived MSCs was attributed to their enriched levels of miR-16 and miR-21. miR-16 reduces SERT expression, which is a critical protein for the resolution of pulmonary oedema⁵⁵. Although let7b miRNA levels were similar in exosomes derived from fibroblasts and MSC-derived exosomes, the latter contained levels of let7b pre-miRNA that were ten times higher. The reduction of IL-6 pro-inflammatory cytokine by the MSC-derived exosomes led to de-activation of the STAT3 gene, which is a key mediator of hypoxic, pro-inflammatory signalling associated with pulmonary hypertension²⁶.

In a mouse model of endotoxin-induced acute lung injury, reduced inflammation and prevention of pulmonary oedema formation in the injured alveoli followed intratracheal administration of human bone marrow MSC-derived microvesicles. A major finding of this study was that the microvesicles contained the mRNA for the keratinocyte growth factor (KGF). KGF was previously shown to restore alveolar fluid clearance in an *ex vivo* model of acute lung injury. Transfer of the mRNA from the microvesicles to the injured alveolar epithelium, and subsequent expression of KGF, was thought to be a key factor in the repair process⁵².

miRNA expression studies in acute lung injury report that overexpression of several miRNAs including miR-146 may be directly related to the host response that regulates macrophage function and inflammatory cytokine expression⁵⁶. An important functional role of miR-146 was the suppression of TNF- α , IL-6, and IL-1 β expression in alveolar macrophages through the inhibition of IRAK-1 and TRAF-6 in a mouse model of ventilator-induced lung injury²⁷. A recent study found miR-146a was critical for the immunomodulatory effects of exosomes derived from human umbilical cord MSCs in a mouse model of sepsis⁵⁷. Another study reported that miR-146a reduces inflammatory gene expression and inhibits endotoxin-induced inflammation in mice⁵⁸. miR-146a reduces microbial and mechanically induced inflammation in lung epithelia through the toll-like receptor signalling pathway⁵⁹. A recent review by Basu and Ludlow highlighted that the selection of RNA for recruitment into exosomes is highly precise and is regulated by proteins such as RNA binding complex ESCRT-II, which is present in the exosomal membrane¹⁸. Interestingly, Song *et al.* showed that miR-146a could be selectively packaged into the exosomes of MSCs by pre-treating the cells with the pro-inflammatory cytokine IL-1 β ⁵⁷.

This study is a leap forward to the previously published work on the direct delivery of mesenchymal stromal cells to the airway by atomisation for the treatment of lung injury⁴³. Here, the extracellular vesicles derived from placenta derived mesenchymal stromal cells were analysed for potential application in the treatment of pulmonary injury.

4.3 Materials and Methods

4.3.1 Cell culture and maintenance

Transduced foetal chorionic and maternal mesenchymal stromal cells, respectively CMSC29 and DMSC23 cell lines^{60, 61}, since cell lines were preferred over primary cells for reproducibility, reducing the occurrence of MSC senescence and ease of maintenance. CMSC29 was cultured in AmnioMAXTM (InvitrogenTM, Thermo Fisher Scientific, North Ryde,

NSW, Australia) and DMSC23 was cultured in Mesencult™ proliferation kit (STEMCELL Technologies, Tullamarine, VIC, Australia). Immortalised human bronchial epithelial cell line (BEAS-2B) and human monocyte cell line (THP-1) were cultured in Dulbecco's Modified Eagle Medium (DMEM) and Roswell Park Memorial Institute medium (RPMI 1640) respectively (Sigma-Aldrich, Castle Hill, NSW, Australia), both supplemented with 10% foetal bovine serum (FBS, French origin, Scientifix, Cheltenham, VIC, Australia) and 1% penicillin-streptomycin 5000 U/ml (PenStrep®, Thermo Fisher Scientific). Hanks' Balanced Salt Solution (HBSS(-), Sigma-Aldrich) was used for washing DMSC23 and CMSC29, while phosphate buffer saline without Ca²⁺ and Mg²⁺ (PBS, Lonza, Bella Vista, NSW, Australia) was used for BEAS-2B. TrypLE™ Select Enzyme (Thermo Fisher Scientific) was used as dissociation reagent for all adherent cells. DMSC23 and CMSC29 were used for isolation of EVs at passages P23-28 while BEAS-2B and THP-1 cells were used at P12-16 and P14-20. All cells were maintained at 37°C and 5% CO₂.

4.3.2 Isolation of EVs by ultracentrifugation

DMSC23 and CMSC29 were cultured until 80% confluence in normal maintenance culture media then cells were washed twice with HBSS(-) then cells were cultured in EV isolation media (serum-free media containing 0.5% bovine serum albumin and 1% PenStrep) for 48 h. After 48 h, EV-containing media was collected and transferred into RNase-free centrifuge tube, kept on ice. To remove cells and debris, media was centrifuged at 500 × g for 5 min then supernatant collected and further centrifuged at 2,000 × g for 10 min. Supernatant was transferred to thick-wall polycarbonate ultracentrifuge tubes (Seton Scientific Inc, Petaluma, CA, USA) and centrifuged at 31,200 rpm (100,000 × g) for 60 min at 4°C using rotor Ti-70 in Optima LE-80K Ultra Centrifuge (Beckman Coulter, Lane Cove West, NSW, Australia). Supernatant was removed and the EV pellet was resuspended in 1 ml RNase-free PBS (Lonza) using RNase-free pipette tips. Then ultracentrifugation was repeated at 31,200 rpm (100,000 × g) for 60 min at 4°C, supernatant was removed. The pellet was resuspended in 200 µl RNase-free PBS, transferred to RNase-free microcentrifuge tubes and stored at -80°C if not used immediately.

4.3.3 Measurement of size and concentration of EVs

Nanoparticle tracking analysis (NTA) and Flow NanoAnalyser (NanoFCM)

EV samples were diluted 1:40 with nuclease-free water, vortexed at a moderate speed for 30 sec then immediately measured on the NanoSight NS300 (Malvern Instruments, ATA Scientific, Taren Point, NSW, Australia). Diluted samples (1 ml) were infused using a syringe

pump with temperature control set at 25°C and particles were imaged with auto-focus camera for 60 sec, repeated to a total of three times per sample. Data was processed using the NTA software using camera level 11 and detection threshold 4, to calculate and compare the mean particle diameter, mode, D50 values and particle concentration. For precise, quantitative analysis of single particles in a sheathed flow, EV samples were diluted in PBS and measured on the Flow NanoAnalyzer (NanoFCM Inc, Xiamen, China).

Tunable Resistive Pulse Sensing (TRPS)

For the measurement of particle size and concentration with higher precision and accuracy, TRPS was used using qNano (IZON Science, Christchurch, New Zealand). Particles were suspended in electrolytes and passed through an engineered pore (NP100) which sends signals for each particle that passes through which then can be converted to size and concentration. All reagents were freshly prepared and filtered (0.22 µm) to avoid contamination.

Protein quantification using Bradford assay

Since the measurement of protein content is a common method of quantifying EVs, the total protein in each EV sample was quantified using the Pierce™ Detergent Compatible Bradford Assay Kit (Thermo Fisher). Firstly, EV samples were lysed by incubating 10 µl sample together with 290 µl of radioimmunoprecipitation assay (RIPA) buffer (Thermo Fisher) inside each well of a 96-well plate. Then after thorough mixing by pipetting, 10 µl from each well was transferred into a new 96-well plate. For BSA standards, 2000 µg/ml stock was diluted ranging from 25 µg/ml to 2.5 µg/ml and added 10 µl to each well. To each well containing sample or BSA standard, 300 µl of Pierce Detergent Compatible Bradford Assay Reagent and pipetted up and down. After 10 min incubation at room temperature in the dark, absorbance at 600 nm was measured using a plate reader (VICTOR X, Perkin Elmer, Melbourne, VIC, Australia).

4.3.4 Analysis of size and morphology of EVs

Scanning electron microscopy

Scanning electron microscopy (SEM) was used to observe the changes in morphology and size of the particles. Samples were sputter coated with approximately 20 nm thick gold using a K550X sputter coater (Quorum Emitech, Kent, UK). Images were obtained using Zeiss Sigma HD field emission gun scanning electron microscope (Carl Zeiss AG, Oberkochen, Germany).

Transmission electron microscopy

The size and morphology of the particles were analysed using transmission electron microscopy (TEM). Samples were mounted on carbon and Formvar coated copper grids for 30

minutes and fixed with 2.5% glutaraldehyde for 30 min. Following 3 times washings in sterile PBS, they were negative stained with 2% w/v ammonium molybdate in water for 5 min. Excess stain was removed by blotting and the samples were further air dried before imaging. JEOL JEM-1400 TEM (Tokyo, JPN) was used to image the samples.

Atomic force microscopy

For observing particle size and imaging 3D surface topography, EV samples were placed onto freshly cleaved mica and dried for atomic force microscopy (AFM) on nanoIR™ AFM-IR instrument (Anasys Instruments, USA). Images were obtained at scan rate of 0.5 – 0.8 Hz using a tapping-mode EX-T125 probe (resonance frequency 200-400 kHz and spring constant 13-77 N/m, Anasys Instruments, USA). The scan sizes used were 5 × 10 μm.

4.3.5 Analysis of EV molecular composition using atomic force microscope infrared spectroscopy (AFM-IR)

An innovative method for interrogating the structure and composition of EVs was developed in this study, using AFM-IR (nanoIR™, Anasys Instruments). A detailed protocol is included in section 5.7. Briefly, 5 μl of each EV sample was placed on a zinc selenide prism to dry overnight at room temperature for AFM-IR spectroscopy. After optimisation of the laser signal, AFM-IR spectra were collected from 1000 to 1800 cm⁻¹ at 1 cm⁻¹ intervals with a scan rate of 0.1 Hz with a co-coverage of 16. A silicon nitride cantilever (EXC450 tips, AppNano, CA, USA) with a nominal spring constant of 0.5 Nm⁻¹ was used for all measurements. The scan sizes used were 10 × 10 μm for probing one point per EV and 1 × 1 μm for probing multiple points on individual EVs. Analysis Studio™ software was used for data analyses. Smoothing of the spectra using the ‘Savitzky-Golay’ function was achieved by using the polynomial function of 2 and 15 numbers of points.

4.3.6 RNA isolation from EVs

Total RNA was isolated from EVs using the TRIzol™ reagent (Invitrogen), following the manufacturer’s protocol with some modifications. Briefly, DMSC23 and CMSC29 were cultured until 75-80% confluent then switched to serum-free MV isolation media and followed the ultracentrifugation protocol for isolating EVs (as described in 4.3.2). After obtaining EV pellet from ultracentrifugation, 300 μl TRIzol was added directly to the EV pellet then transferred to RNase-free microcentrifuge tube. An additional 200 μl TRIzol was added to the ultracentrifuge tube to ensure all the residual pellet is collected, then samples were stored immediately at –80°C until RNA isolation.

4.3.7 OpenArray® for miRNA profiling of EVs

For interrogating the miRNA content in EVs, OpenArray® was conducted, with modified protocol for low sample input. RNA samples were diluted to 10 ng/μl. Reverse Transcriptase (RT) mastermix was prepared using the manufacturer's protocol. 4.5 μl of mastermix was added to each sample, inverted to mix then spun down for incubation on ice for 5 min. For cDNA synthesis, the following program on the thermocycler was used: 40 cycles (16°C for 2 min, 42°C for 1 min, 50°C for 1 sec), 85°C for 5 min, hold at 4°C. To generate preamplified cDNA, PreAmp mastermix was prepared (TaqMan PreAmp Mastermix and custom PreAmp primers (Thermo Fisher Scientific) diluted in nuclease-free water), added to each well and the following program was run on the thermocycler: 95°C for 10 min, 55°C for 2 min, 72°C for 2 min, 16 cycles (95°C for 15 sec, 60°C for 4 min), 99°C for 10 min, hold at 4°C. Preamplified cDNA were diluted 1:20 in 0.1 × TE buffer. 5 μl of diluted preamplified cDNA was transferred to a new 96-well plate and added 5 μl of TaqMan OpenArray real-time PCR mastermix to each well. Plate was sealed and vortexed to mix. After transferring 5 μl of each sample to each well of the 384-well sample plate, the plate was sealed to reduce evaporation, centrifuged at 490 × g for 1 min at 4°C. The relevant run file/s (.tpf) were downloaded from the Thermo Fisher Scientific website. QuantStudio 12K Flex was initialised and the qPCR was run. The RStudio software (version 1.0.153) was used for generation of heatmaps for data analysis.

4.3.8 Atomisation of EVs and measurement of particle size

DMSC23 EVs and CMSC29 EVs were diluted in RNase-free PBS to 5×10^5 particles/ml and kept on ice until use. For measuring the particle size distributions during atomisation of EVs using LMA MAD780 device, Spraytec (Malvern Instruments Ltd, Worcestershire, UK) was used with refractive index of 1.0 and flow rate at 87 L/min, measured for 4 sec.

4.3.9 Assessment of cell migration and invasion upon EV treatment

Cell wound repopulation assay

To investigate the impact of DMSC23 EVs and CMSC29 EVs on epithelial cell migration, the rates of repopulation of a two-dimensional scratch wound on a monolayer of cells were compared. BEAS-2B cells were seeded at 1×10^4 cells/well on 96-well plates and were cultured in normal media until 90% confluent. Then cells were incubated in low serum media (containing 1% FBS) for 24 h prior to scratching a wound on the midline of the culture well using a 96-pin woundmaking tool (IncuCyte® WoundMaker™). After washing with low serum media twice to remove cell debris, then fresh media was added. EVs were supplemented at $5 \times$

10^5 particles per well. Wound images were taken using the IncuCyte[®] live cell imaging system (Essen BioScience, Inc. Ann Arbor, MI, USA) every 2 h for 48 h with $10 \times$ magnification. IncuCyte ZOOM software program was used for quantitative analysis, to measure and calculate the relative density and confluence of the scratch wound at each time point.

Cell invasion and migration assay using impedance measurement

Cell invasion and migration were monitored on xCELLigence[®] Real-Time Cell Analyzer Dual Purpose (RTCA DP) instrument using the 16-well electronic cell invasion and migration plate (CIM-Plate[®] 16). The plate assembly is fitted with a Boyden chamber composed of upper and lower chambers separated by a membrane coated with gold microelectrode sensors that measures the movement of cells from the upper to the lower chamber by detecting the impedance signal. Following the manufacturer's instructions, CIM-Plate[®] 16 was filled with media and equilibrated at 37°C for 1 h, then background impedance values were recorded.

A549 and BEAS-2B cells were passaged a day prior to the experiment, kept in serum-free media (SFM) for 24 h. Cells were trypsinised and made to 4×10^5 cells/ml in SFM. Each plate was seeded with A549 or BEAS-2B in the upper chamber at 40,000 cells per well in 100 μ l serum-free media. DMSC23 EVs and CMSC29 EVs isolated from normal culture conditions were diluted to 6×10^5 particles in 20 μ l SFM (15 particles/cell) and were added to cells immediately after seeding. Plates were left at room temperature for 30 min to allow the cells to settle at the bottom surface of the upper chamber. Then plates were loaded onto the RTCA DP instrument inside the 37°C incubator and impedance was measured every 10 min for 72 h.

4.3.10 Analysis of cellular responses to EV treatment after LPS injury

EVs were diluted in DMEM complete media and transferred to a 24-well plate, with each well containing 1×10^5 particles in 100 μ l media. Control group was given media without EVs. Then BEAS-2B were seeded at 2×10^4 cells per well on 24-well plate, to incubate with EVs 30 min prior to exposing cells to lipopolysaccharide (LPS) injury used at final concentration of 100 ng/ml (*E. Coli* O111:B4, Sigma-Aldrich). After 16 h incubation, cells were collected and followed the manufacturer's instructions for measuring nitric oxide expression and Annexin V expression Muse[™] Nitric Oxide Assay Kit (Merck Millipore, Frenches Forest, NSW, Australia) and Annexin V-FITC Apoptosis Detection Kit (BioTools, Loganholme, QLD, Australia).

4.3.11 Measurement of cytokine release in response to LPS injury after EV treatment

THP-1 cells were seeded at 3×10^5 cells per well (180 μ l of 1.6×10^6 cells/ml). LPS (*E. coli* O111:B4, Sigma-Aldrich) diluted to 1 μ g/ml was added at 20 μ l per well, exposing cells at 100

ng/ml final concentration, incubated on a shaker at 37°C, 5% CO₂ for 4 h. EVs were made to 1.5×10^7 or 7.5×10^6 particles/ml and added 50 µl per well to expose THP-1 cells at high or low (10 or 5 particles/cell) EV doses. EVs from DMSC23 and CMSC29 cultured in normal and hypoxic conditions and the freeze-dried form of DMSC23 (normoxia) EVs were used.

Enzyme-linked immunosorbent assay (ELISA) was conducted using IL-6 and TNF-α ELISA kits (BD Biosciences, North Ryde, NSW, Australia) following the manufacturer's protocols. Briefly, Nunc® MaxiSorp™ plates (Thermo Fisher Scientific) were coated with capture antibodies (100 µl/well; 40 µl in 10 ml for 1×96 -well plate for 1:250 dilution), incubated at 4°C overnight. After 16 h incubation (20 h LPS exposure in total), samples were mixed by pipetting, collected (240 µl) and centrifuged to remove cells. Supernatant (220 µl) was transferred to an empty 96-well plate (sample plate) and checked to ensure no cells are present. IL-6 and TNF-α standards were prepared in assay diluent, following the manufacturer's protocol. Wash buffer diluted from 20 × stock solution was used to wash away unbound capture antibodies, blocked with assay diluent for 1 h and followed the manufacturer's protocol for subsequent washing and incubation steps, using the BD OptEIA™ set (BD Biosciences).

4.3.12 Statistical analysis

At a minimum, triplicates or quadruplicates were used for reliability in each experimental condition being examined. Data were analysed and presented as mean ± standard deviation. The differences between the experimental and control groups were analysed using one-way analysis of variance (ANOVA) test. A p-value less than 0.05 was reported as having a statistically significant difference.

4.4 Results and Discussion

4.4.1 Comparison of EV size and concentration

The morphology of EVs were similarly spherical, regardless of cell type from which the EVs were isolated (CMSC29 or DMSC23), with no morphological differences in EVs isolated from hypoxic or normoxic conditions. Typical size of EVs analysed using the AFM enabled analyses of much smaller EVs in the range between 20 and 100 nm in diameter as well as larger EVs with diameters in the 100 to 300 nm range (Fig. 4.1A,B). While the SEM sample preparation is easier than TEM gives more detail on the surface morphology, only the larger EVs were imaged at acceptable resolution, approximately 150 to 300 nm in diameter (Fig. 4.1D–G). TEM allowed the analyses of smaller vesicles (less than 100 nm) as well as the visualisation the internal structures including the lipid bilayer and the presence of smaller vesicles within the

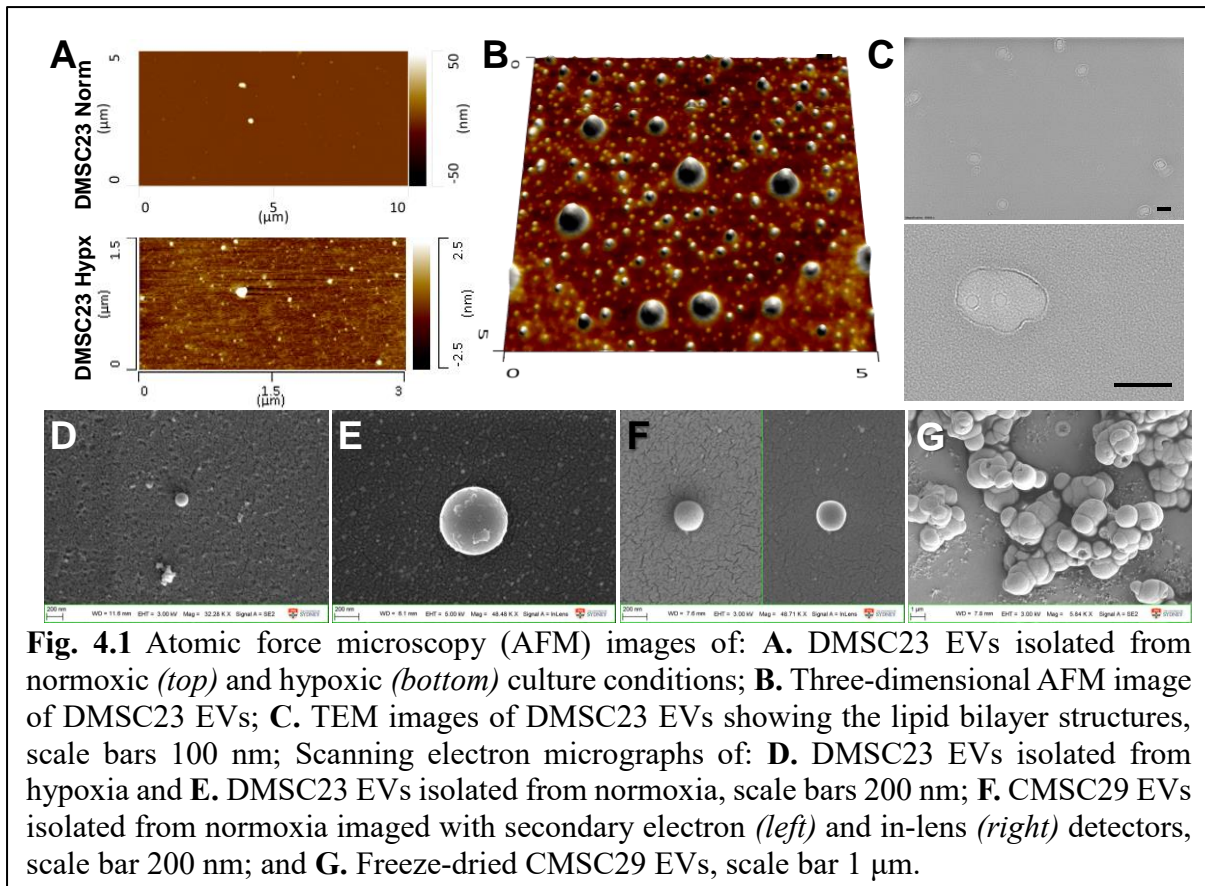


Fig. 4.1 Atomic force microscopy (AFM) images of: **A.** DMSC23 EVs isolated from normoxic (*top*) and hypoxic (*bottom*) culture conditions; **B.** Three-dimensional AFM image of DMSC23 EVs; **C.** TEM images of DMSC23 EVs showing the lipid bilayer structures, scale bars 100 nm; Scanning electron micrographs of: **D.** DMSC23 EVs isolated from hypoxia and **E.** DMSC23 EVs isolated from normoxia, scale bars 200 nm; **F.** CMSC29 EVs isolated from normoxia imaged with secondary electron (*left*) and in-lens (*right*) detectors, scale bar 200 nm; and **G.** Freeze-dried CMSC29 EVs, scale bar 1 μm .

larger vesicles (Fig. 4.1C). The use of InLens signal merged with secondary electron detection produced images with higher contrast and detail (Fig. 4.1E,F).

In contrast, there were varying sizes and concentrations of CMSC29 EVs and DMSC23 EVs depending on the hypoxia or normoxia conditions as measured by nanoparticle tracking analysis (NTA) and tunable resistive pulse sensing (TRPS) techniques. These results are summarised in Table 4.1 and Figure 4.2. The averaged mean and mode sizes identified from NTA (Fig. 4.2A,B) were slightly larger than those measured by TRPS (Fig. 4.2D), which is also evident visually when comparing the shift of the green and blue curves on Fig. 4.2A,B with those of Fig. 4.2D. The mode diameters for DMSC23 EV normoxia measured by NTA and TRPS were 114.6 ± 10.1 nm and 106.0 ± 1.4 nm, while those for DMSC23 EV hypoxia were 120.8 ± 6.0 nm and 91.0 ± 5.7 nm, respectively. Although NTA and TRPS yielded comparable total particle counts overall, NTA detected more particles with larger diameters (>110 nm) while TRPS detected more particles with smaller diameter (<110 nm). Quantitative assessment using NTA and TRPS are heavily influenced by the settings used e.g. camera level and detection threshold for NTA and nanopore size for TRPS^{62,63}. As nanopore NP100 was used in this study, the detectable vesicle size for TRPS was in the range of 50 to 330 nm, limiting its utility for detection of EV particles smaller than 50 nm.

Table 4.1. Summary of averaged particle size and concentration measured using nanoparticle tracking analysis (NTA) and tunable resistive pulse sensing (TRPS) method for CMSC29 EVs and DMSC23 EVs.

Measurement Method / Type	NTA		TRPS		
	Mean (nm)	Mode (nm)	Mean (nm)	Mode (nm)	Conc. (particles/ml)
CMSC29 EV normoxia	106.9 ± 13.0	65.3 ± 39.5	101.5 ± 6.4	75 ± 2.8	1.3 × 10 ¹⁰
CMSC29 EV hypoxia	140.6 ± 4.5	140.0 ± 15.3	102.5 ± 14.8	102.5 ± 30.4	1.4 × 10 ¹⁰
DMSC23 EV normoxia	131.9 ± 0.4	114.6 ± 10.1	112.5 ± 3.5	106.0 ± 1.4	2.2 × 10 ⁹
DMSC23 EV hypoxia	122.1 ± 5.1	120.8 ± 6.0	91.5 ± 0.7	91.0 ± 5.7	3.0 × 10 ⁹

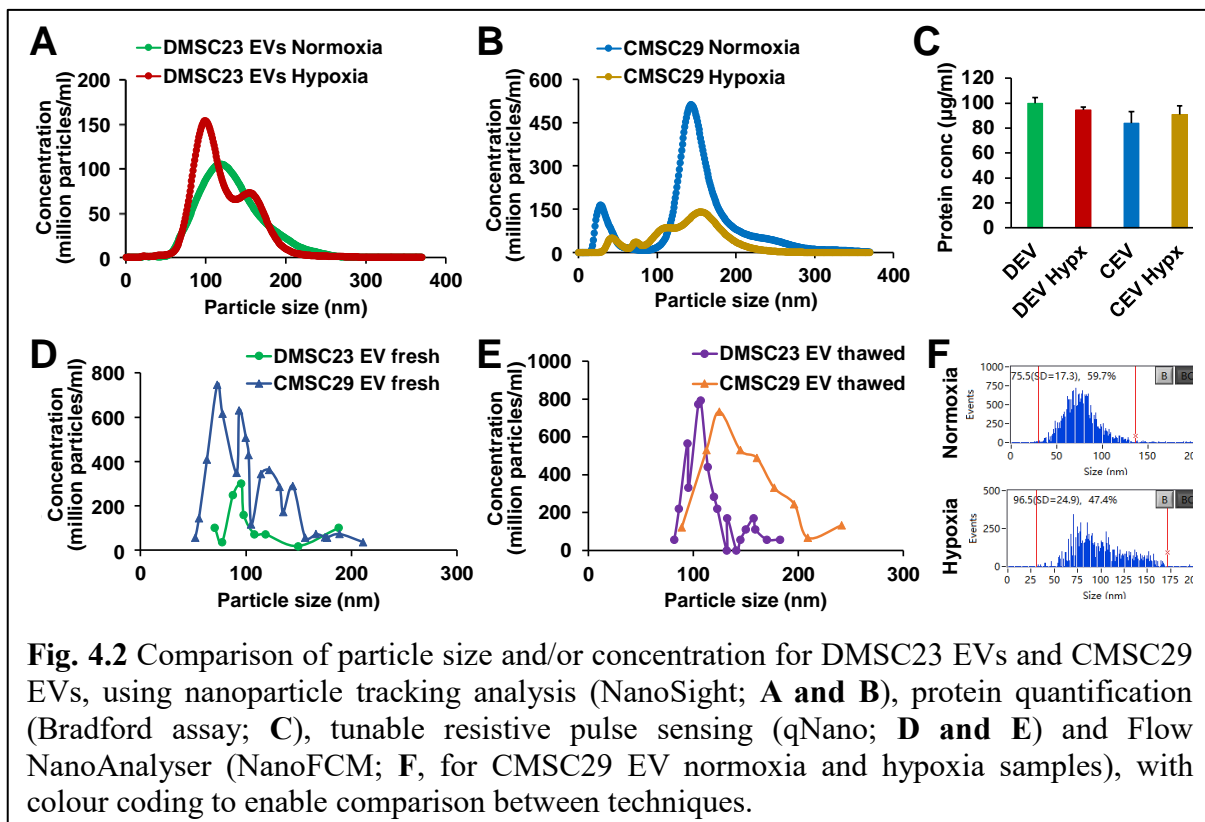


Fig. 4.2 Comparison of particle size and/or concentration for DMSC23 EVs and CMSC29 EVs, using nanoparticle tracking analysis (NanoSight; **A and B**), protein quantification (Bradford assay; **C**), tunable resistive pulse sensing (qNano; **D and E**) and Flow NanoAnalyser (NanoFCM; **F**, for CMSC29 EV normoxia and hypoxia samples), with colour coding to enable comparison between techniques.

The amount of protein is another measure of quantifying EVs. Protein quantification determined by Bradford assay was similar across the samples (Fig. 4.2C), with highest observed in DMSC23 EV isolated from normal conditions ($99.7 \pm 4.8 \mu\text{g/ml}$) while the lowest protein was observed in CMSC29 EV isolated from normal conditions ($84.1 \pm 9.1 \mu\text{g/ml}$).

The two techniques demonstrated comparable size distribution, however one finding common to results from both methods was that the CMSC29 EVs isolated from hypoxic conditions had

higher number of larger particles, which increased both the mean and mode diameter. It is unknown whether the properties of the EV membrane had been altered in the hypoxic condition so that they were more likely to aggregate, which may be a reason for the larger particles detected using NTA and TRPS. However, this is unlikely as the AFM images demonstrated that most of the EV samples were not aggregated. Further studies are required to interrogate the differences between DMSC23 EVs and CMSC29 EVs as well as those derived from hypoxia and normoxia conditions. The differences in molecular composition are found in sections 4.4.3 and 4.4.7.

4.4.2 Comparison of EVs size and concentration before and after freeze-thaw

There are numerous debates about the storage of EVs and whether the repeated freeze and thawing cycles have an impact on the EV properties⁶⁴. In this study, the concentration of DMSC23 EVs and CMSC29 EVs measured before and after freeze-thawing were comparable, however the overall particle size and the standard deviation of the size distribution after thawing were higher (Fig. 4.2E). This change may be attributed to the membrane damage and leakage of vesicular content induced by the freezing process⁶⁵.

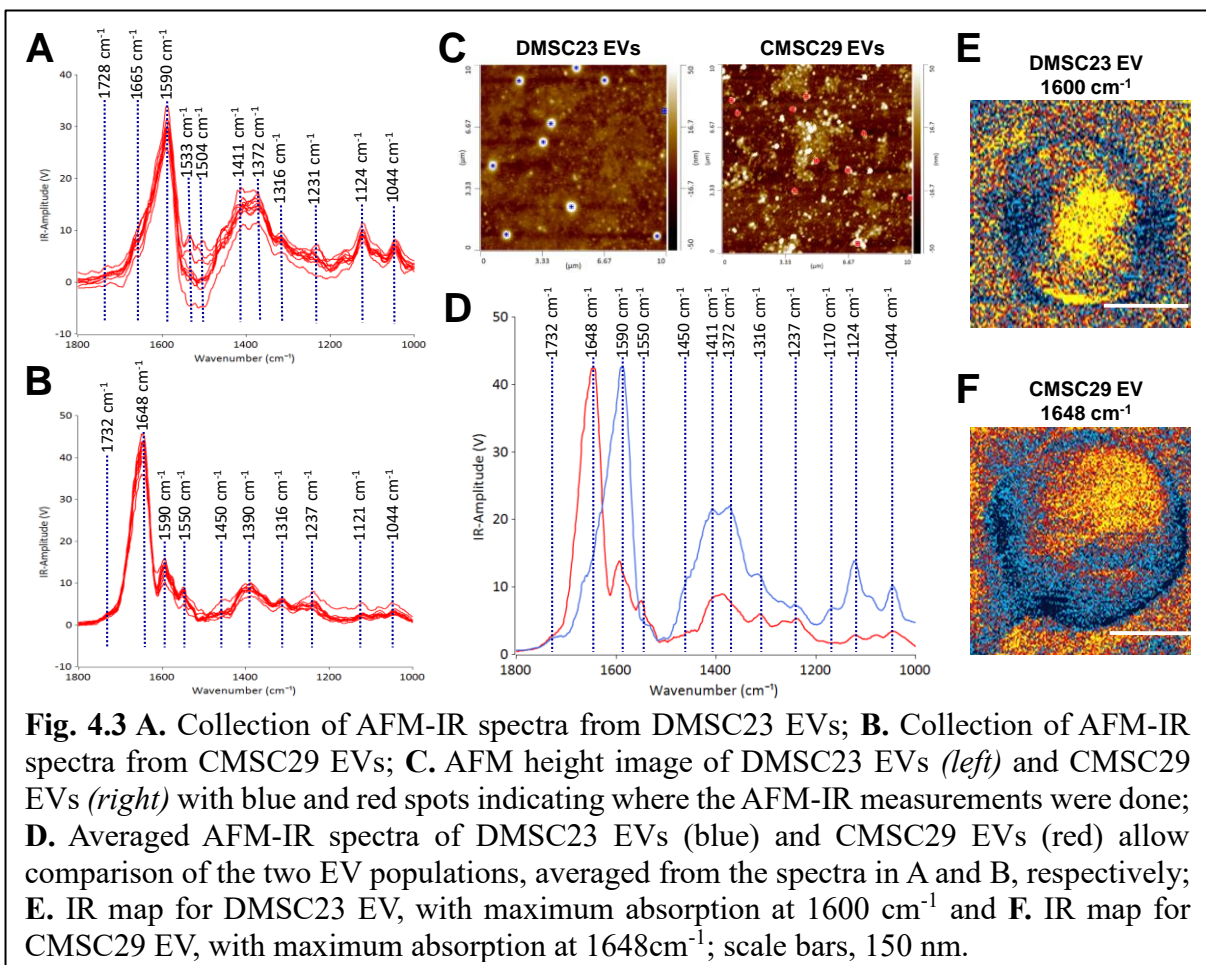
The feasibility of measuring EVs using the Flow NanoAnalyser was demonstrated the preliminary data generated using freeze-thawed CMSC29 EVs, as presented in Fig. 4.2F. The median particle size obtained using NanoFCM corresponded to those obtained from TRPS as normoxia and hypoxia, with mode diameters 75.5 ± 17.3 nm and 96.5 ± 24.9 nm respectively (Fig. 4.2F). However, these median diameters were significantly lower than the mode diameter of CMSC29 EV normoxia determined using TRPS (124.95 nm, Fig. 4.2E). These differences highlight that the combinations of these techniques are required to accurately assess the particle size of EVs, rather than relying on a single method for measuring size and concentration.

4.4.3 Analysis of EV molecular composition using AFM-IR

The differences in the molecular composition of CMSC29 EVs and DMSC23 EVs were interrogated using resonance enhanced AFM-IR. This study demonstrated the first-of-its-kind label-free analysis of EVs by nanoscale infrared biospectroscopy conducted using the state-of-art AFM-IR instrument, which has recently been used for determining conformational changes in intra and extracellular protein structures indicating altered biological function⁶⁶. Initially, the AFM-IR spectra were collected from multiple individual DMSC23 EVs (Fig. 4.3A) and CMSC29 EVs (Fig. 4.3B) which showed a peak within the amide stretching region of peptides (1500 to 1700 cm^{-1}), which corresponds to the bulk protein composition⁶⁷. The Amide I peak

in proteins (1590 to 1700 cm^{-1}) is composed of overlapping bands that belong to different secondary structures of proteins such as α -helix, β -sheet, random coil⁶⁸. Therefore, using AFM-IR, changes to the individual protein components can be resolved. For CMSC29, the Amide I peak was in the typical wavenumber of 1648 cm^{-1} (Fig. 4.3B), which suggests normal conformation of the protein that contains high α -helix structure. While for DMSC23 EVs, the main Amide I peak was broadened and shifted to lower wavenumber with the main peak present at 1590 cm^{-1} (Fig. 4.3A). In addition, the Amide I band peak with a weaker intensity is also seen at a 1665 cm^{-1} . Cumulatively, broadening of the Amide I peak with the shift to lower frequencies and appearance of weak intensity peak at 1665 cm^{-1} indicated changes to the protein conformation in the DMSC23 EV sample.

Changes to Amide I peak could also be attributed to different concentrations and types of nucleic acid which have peaks between 1800 cm^{-1} and 1500 cm^{-1} . To discriminate between changes to the protein conformation and the contribution from nuclei acid the calculation of second derivative from the spectra, is required. This analysis separates individual peaks associated with different components of nucleic acid. In the DMSC23 EV spectra, we observed presence of two well-defined peaks at 1590 cm^{-1} and 1533 cm^{-1} which correspond to adenine



(C=N bond) and guanine (C=N bond)²⁶. Both peaks were detected only at a very low level in CMSC29 EVs (Fig. 4.3B). For both DMSC23 EVs and CMSC29 EVs a low intensity peak at 1730 cm^{-1} that corresponds to purine base (C=O bond) was observed. However, the intensity of this peak varied across the EV populations, which demonstrated heterogeneity of nucleic acid content in the samples. Overall, this study confirmed differences in protein structure and nucleic acid content between both types of EVs, as well as differences in the composition in single EVs between the two populations.

The AFM height images (Fig. 4.3C), and the AFM-IR averaged spectra (Fig. 4.3D) obtained from two different EV populations allow direct comparison of DMSC23 EVs and CMSC29 EVs. The AFM height images were used to select the EVs of the same size for AFM-IR measurement. The peaks at 1411 cm^{-1} and 1372 cm^{-1} had higher intensities in the spectra of DMSC23 EVs, which refer to the phosphatidylcholine head group and thymine, respectively⁶⁷. These data indicate larger amounts of those components in lipids and nucleic acids packaged in DMSC23 EVs compared to CMSC29 EVs. The IR map at the maximum absorption region at 1590-1600 cm^{-1} for DMSC23 EVs (Fig. 4.3E) and at 1648 cm^{-1} for CMSC29 EVs (Fig. 4.3F) demonstrate the capacity of AFM-IR to generate a fingerprint for individual EVs. The AFM-IR analyses of EVs enable subpopulations of EVs to be analysed at the level of individual EVs and also distinguish differences in the composition and structure of various EV populations.

4.4.4 DMSC23 EVs and CMSC29 EVs are sprayable using LMA MAD780 device

Since the airway delivery of therapeutic molecules are preferred over the intravenous route, EVs were sprayed using the LMA MAD780 device previously used to deliver stem cells directly to the airway⁴³. The particle sizes of both DMSC23 EVs and CMSC29 EVs were in the range 15.85 μm to 116.59 μm when sprayed, with maximum percentage frequency at 46.42 μm , with 11.87% and 12.23% of total particle population for DMSC23 EVs and CMSC29 EVs respectively (Fig. 4.4).

These results highlight the comparable particle sizes for both EV populations, however it also indicates that the sprayed particle size is dependent on the nozzle of the atomisation device.

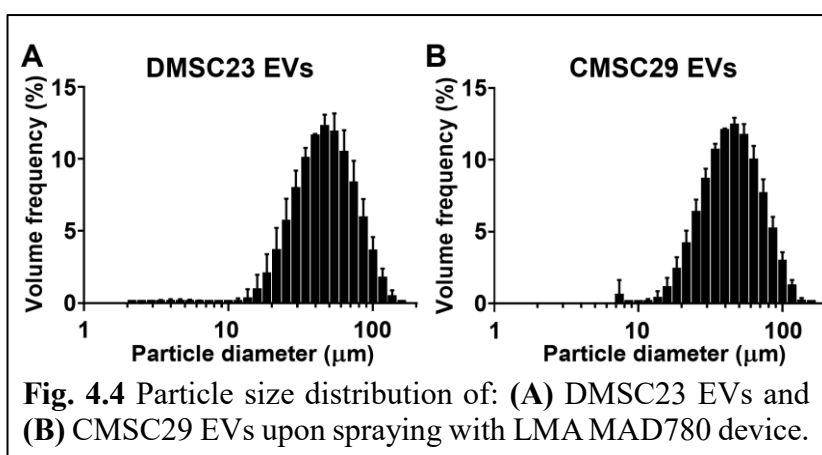
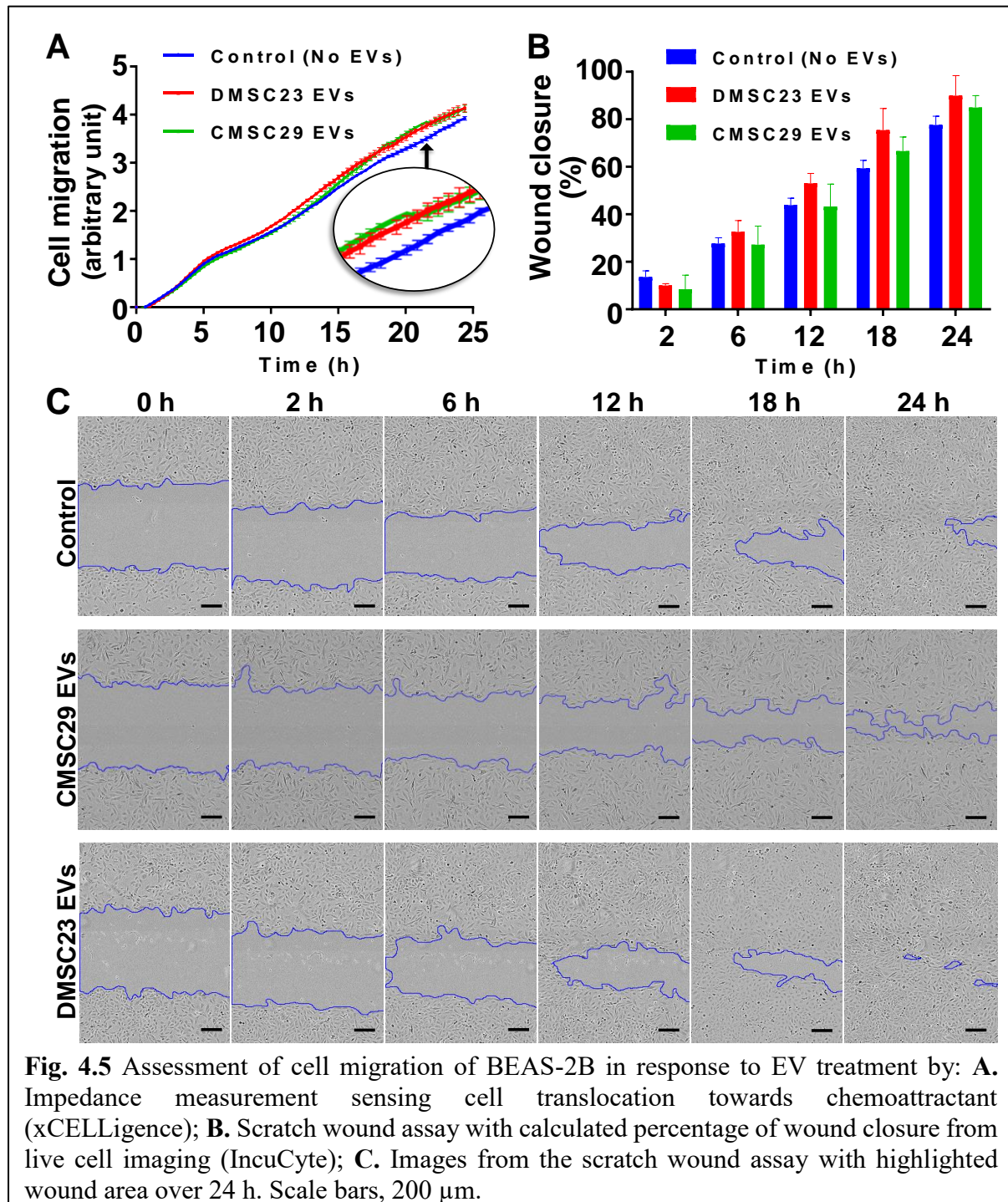


Fig. 4.4 Particle size distribution of: (A) DMSC23 EVs and (B) CMSC29 EVs upon spraying with LMA MAD780 device.

4.4.5 DMSC23 EVs and CMSC29 EVs increase lung epithelial cell migration

The lung epithelial cells (BEAS-2B) treated with DMSC23 and CMSC29 EVs were placed on a chamber with a chemotaxis gradient (FBS) to test whether the EVs increase BEAS-2B migration. From the results of the impedance measurement that measures the translocation of cells as they migrate from the upper chamber to lower chamber (xCELLigence CIM-16), increased number of cells passed through the chamber when treated with EVs (Fig. 4.5). The DMSC23 and CMSC29 EVs both enhanced the migration of BEAS-2B, implying that the



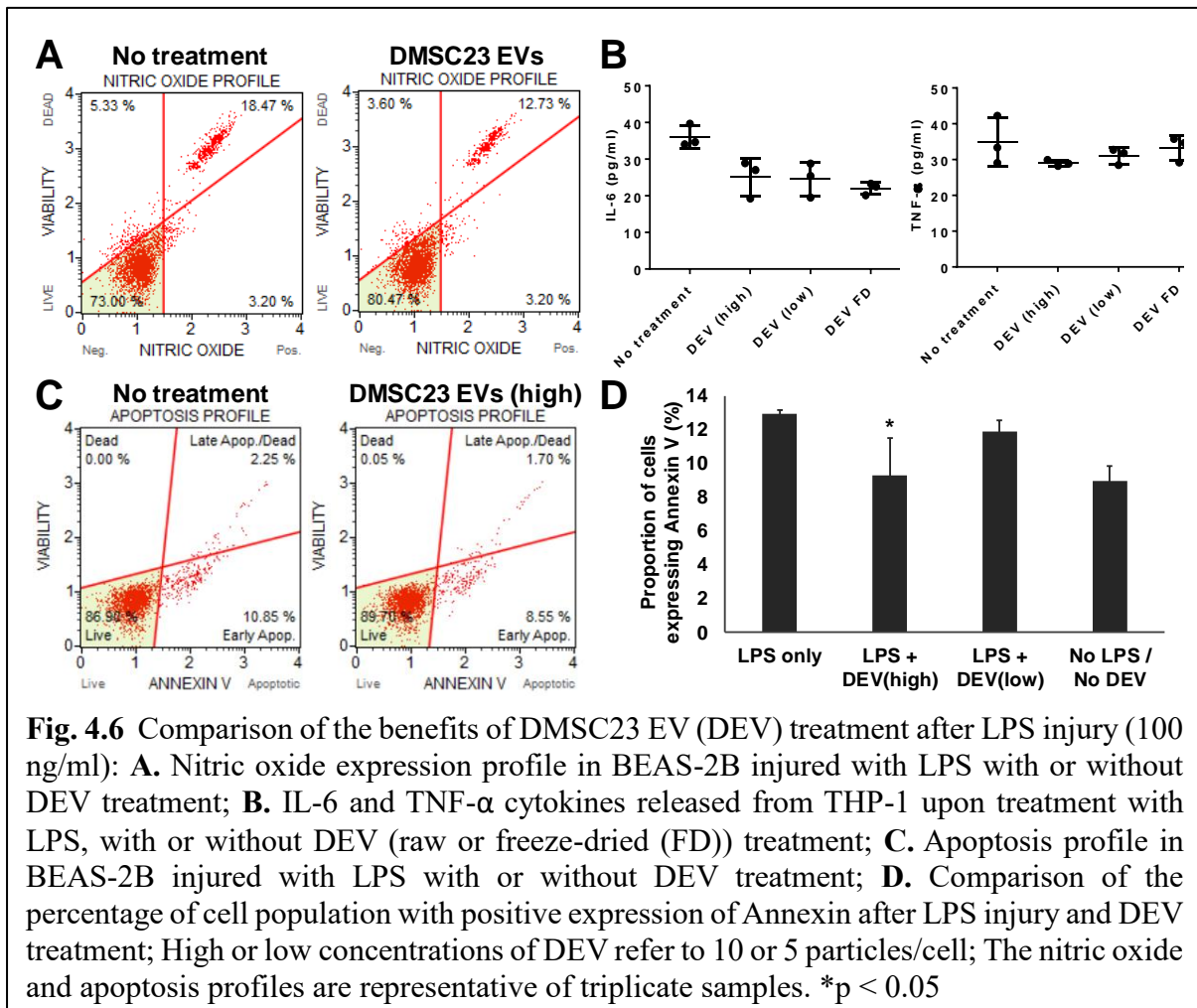
healthy lung epithelial cells with increased mobility will be helpful during the lung injury microenvironment. This was further verified by the wound closure assay. In a simplified wound model using a scratch wound, it was also observed that DMSC23 EVs increase the speed of cells migrating towards the ‘wound’. Cell migration enhancing capability is important in wound healing as it is natural mechanism of wound repair processes in the epithelium. The progenitor cells nearby the injured epithelium migrate and spread to cover the denuded surfaces⁶⁹. Enhanced cell migration by CMSC29 EVs was not as evident in the cell migration assays and thus CMSC29 EVs were excluded from further functional analyses.

4.4.6 DMSC23 EVs reduce cellular stress and inflammatory response caused by LPS

Similarly to DMSC primary cells, DMSC23 is naturally resistant to oxidative stress due to the pre-conditioning on the region of placenta where the cells are isolated from^{60, 61}. It has been well established that DMSC23 are more robust to hypoxic stress compared to CMSC29⁷⁰. With evidence that the EVs carry similar properties to the cells which they are secreted from⁷¹, DMSC23 EVs were further tested for capability to reduce stress in an established *in vitro* model of acute lung injury, using LPS for BEAS-2B lung epithelial cells.

The measurement of nitric oxide and Annexin V expression allows quantification of cellular stress in response to injury. Nitric oxide is a small molecule generated by the enzyme nitric oxide synthase (NOS) in cells, which participates in many biological functions⁷². In the context of cellular stress, nitric oxide is produced in large amounts in response to inflammatory stimuli, as part of a defence mechanism in oxidative toxicity⁷³. The intracellular detection of nitric oxide is important for the detection of apoptotic signal cascades as the cell protects itself from pathological processes including inflammation and apoptosis⁷⁴. The comparison of the nitric oxide profiles after LPS injury demonstrated that the cells treated by EVs have lower nitric oxide expression as can be seen from the reduction in the average percentage of nitric oxide positive cells from 21.7% to 15.9% (Fig. 4.6A). This suggests that the oxidative stress signalling cascade within cells is modified in response to LPS injury after the uptake of DMSC23 EVs.

The immunomodulatory effects of DMSC23 EVs on cytokine release by human monocytic cell line (THP-1) was investigated using ELISA. It was evident that the EVs have a positive impact based on the reduced release of IL-6 and TNF- α pro-inflammatory cytokines, especially for high doses of DMSC23 EVs, at ten EV particles/cell (Fig. 4.6B). While the reduction of TNF- α release in EV-treated groups were not statistically significant, the high standard deviation on the control / no EV treatment possibly due to technical error may be the reason for this and



requires further repetition to validate these results. The efficacy of freeze-dried EVs was also tested, however the production of TNF- α in those cells had no significant difference compared to the control group which had no EV treatment (Fig. 4.6B, right).

For comparing the apoptosis profiles upon LPS injury with or without DMSC23 EV treatment, BEAS-2B expressing Annexin V were analysed (Fig. 4.6C). When BEAS-2B were given high dose of DMSC23 EVs prior to LPS exposure, the number of cells expressed Annexin V reduced from $12.6 \pm 0.5\%$ to $8.6 \pm 2.4\%$, approximately 4% less than in cells without the EV treatment (Fig. 4.6D). Although this difference is statistically significant, the maximum benefit of DMSC23 EVs may be highlighted better through optimisation of parameters such as EV dosage and LPS concentration, which may be investigated in future studies.

4.4.7 The therapeutic potential of DMSC23 EVs and CMSC29 EVs are attributed to the miRNA composition

EVs produced by MSCs reprogram tissue-injured cells by delivering mRNA and/or miRNA to modulate soluble paracrine mediator production, mediate cell de-differentiation and cell-cycle

re-entry, contributing to tissue regeneration⁷⁵. Another important rationale for analysing miRNA profile is that the EVs released from the injured cells may mediate phenotypic transfer of surrounding MSCs to acquire certain features by delivering mRNA and/or miRNA to MSCs⁷⁵. Thus, comparative analysis of the miRNAs carried in EVs and miRNAs contained in the cells excreting those EVs may reveal important mechanism of the therapeutic effects of MSCs and their EVs. We interrogated the miRNA content of CMSC29s and DMSC23s and their EVs isolated from various conditions including hypoxia and normoxia, using an OpenArray™ platform simultaneously enabling analyses of 405 miRNAs. The miRNA important in regulating cellular repair and tissue regeneration were identified from literature (31 miRNAs) for comparison between samples as well as for comparison with the miRNA profile of their cells (Fig. S4.1). A heat map was generated from the DMSC23 EV samples that have positive expression of miRNAs relevant for tissue repair and wound healing (Fig. 4.7). The key miRNAs involved in regeneration of the lung present in DMSC23 EVs were miR-29b, miR-106b, miR-20a, miR-146a, miR-92a, miR-125b and miR-29a (Table 4.2). miR-29a/b are highly expressed in the adult lung and they are regarded as the ‘master regulator of tissue regeneration’. Overall there were more miRNA carried in DMSC23 EVs isolated from normal conditions compared to those from hypoxic conditions (Fig. 4.7A). The DMSC23 EVs had a similar profile to DMSC23 cells, especially with the EVs isolated from normoxic conditions retaining proportionally similar expression of miRNAs in cells (Fig. 4.7A). The EVs had much lower expression of miRNA overall compared to the cells, except for miR-133a, which is involved in the regulatory roles in the airway inflammation. This indicates that the cells selectively package and sends out more miR-133a through encapsulation in EVs than the amount retained inside the cells. These processes can be altered in the future to modify the

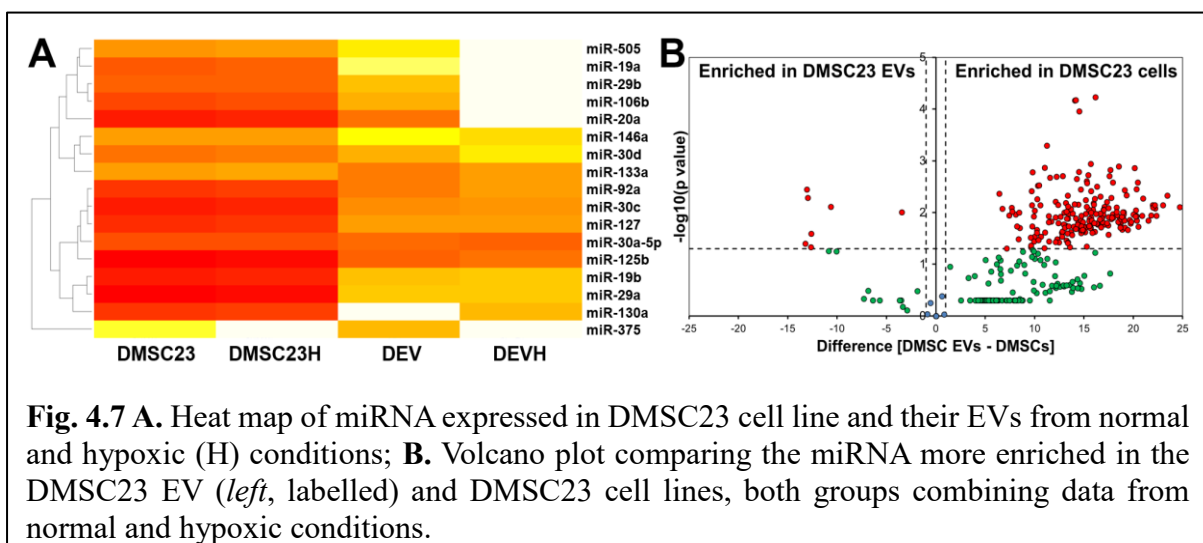


Fig. 4.7 A. Heat map of miRNA expressed in DMSC23 cell line and their EVs from normal and hypoxic (H) conditions; **B.** Volcano plot comparing the miRNA more enriched in the DMSC23 EV (*left*, labelled) and DMSC23 cell lines, both groups combining data from normal and hypoxic conditions.

Table 2. Selected miRNAs in EVs that may be involved in tissue repair and regeneration.

miRNA	Functions	Ref.
miR-505	Highly involved in targeting relevant gene functions in repair	51
miR-19a/b	Involved in organogenesis (highly expressed in fetal lung)	77
miR-29a/b	The ‘master regulator of tissue regeneration’	35
miR-106b	Involved in organogenesis, branching morphogenesis	78
miR-20a	Regulation of wound healing, involved in organogenesis (highly expressed in fetal lung)	75, 79
miR-146a	Reduce inflammation, increase proliferation, migration and angiogenesis of endothelial progenitor cells	80, 81
miR-30d	Important in the late repair phase	51
miR-133a	Regulatory roles in airway inflammation, tumour suppressor	77
miR-92a	Highly expressed in the fetal lung; involved in lung organogenesis	77
miR-30c	Important in the late repair phase	51
miR-127, miR-375	Proliferation and differentiation of lung epithelial cells and branching morphogenesis	82, 83
miR-30a-5p	Tumour suppressor, modulate epithelial-mesenchymal transition	84
miR-125b	Controls inflammation; attenuate inflammation in LPS-induced acute lung injury	77
miR-130a	Involved in lung organogenesis	78

content of miRNA and other biological signals carried inside the EVs for potential therapeutic applications. The results of the miRNA analyses demonstrate the promising potential of EVs for regenerative medicine applications⁷⁶.

4.5 Conclusion

With increasing research on the mechanism behind MSC-driven tissue regeneration, it is widely accepted that the transfer of genetic information between MSCs and injured cells in tissues plays a critical part. The results from this study demonstrate that:

- DMSC23 EVs and CMSC29 EVs have a potential therapeutic application in reducing lung injury and enhancing repair.
- DMSC23 EVs and CMSC29 EVs can be directly delivered to the airways using an atomisation device.
- EVs can be modified to carry a favourable miRNA profile, optimised through the modification of cell culture conditions.

Future studies that use EVs to improve regeneration of the lung after injury should consider:

- Conditioning EVs such that they are enriched in miRNA favourable for tissue repair and regeneration, such as miR-29a, miR-29b and miR-146a.
- Further proteomic analyses and discrimination between subpopulations of EVs that have more favourable cargoes, which will be of great importance for potential preclinical studies.
- Further development of the single vesicle characterisation technique using AFM-IR as presented in this study that will enable the identification of the most therapeutically relevant EV subtypes.
- Taking this innovative approach together with profiling of miRNA and proteins, to advance the field of EV-therapies towards clinical translation.

4.6 Supplementary Figure

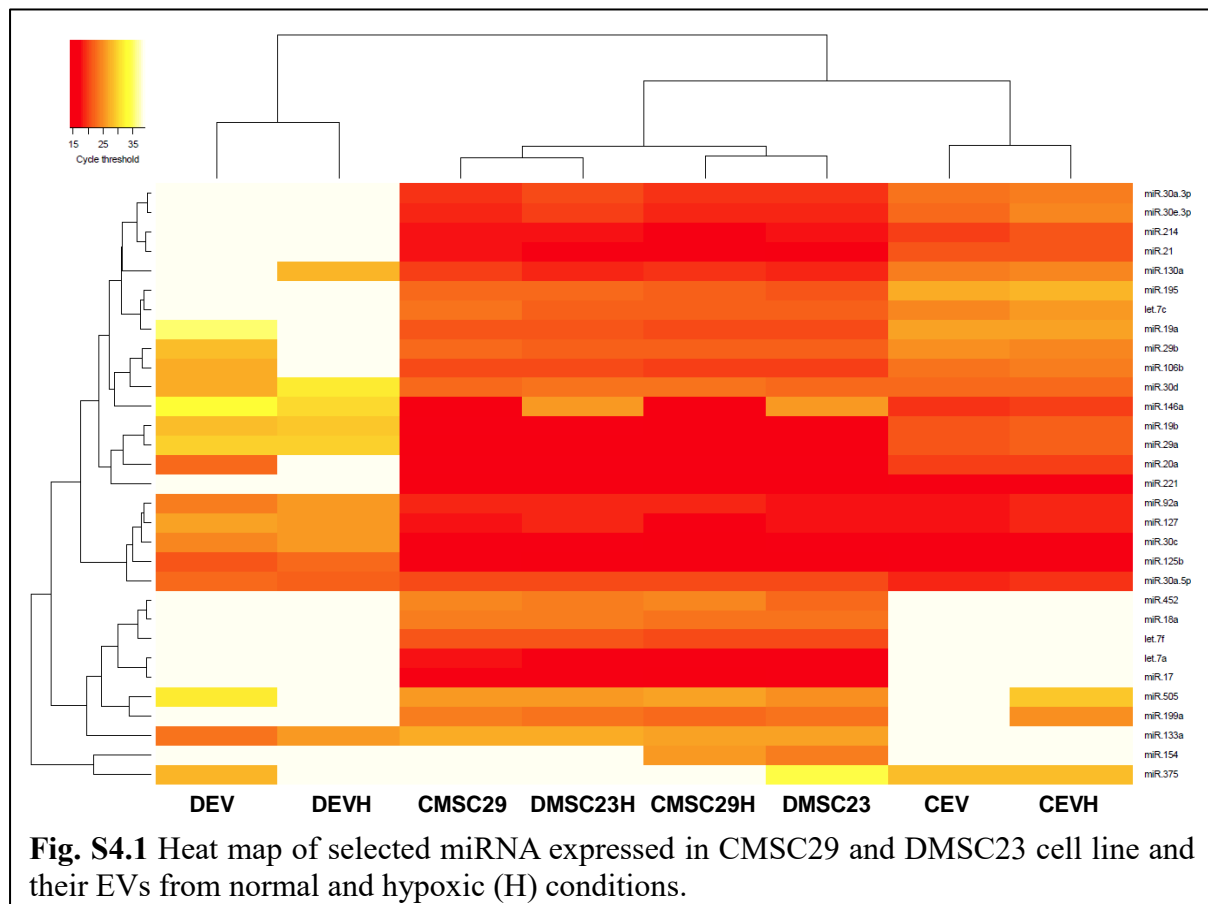


Fig. S4.1 Heat map of selected miRNA expressed in CMSC29 and DMSC23 cell line and their EVs from normal and hypoxic (H) conditions.

4.7 References

1. Liang, X., Ding, Y., Zhang, Y., Tse, H.F., and Lian, Q., Paracrine mechanisms of mesenchymal stem cell-based therapy: current status and perspectives. *Cell Transplant* 2014, **23**(9):1045-59.
2. Vizoso, F.J., Eiro, N., Cid, S., Schneider, J., and Perez-Fernandez, R., Mesenchymal Stem Cell Secretome: Toward Cell-Free Therapeutic Strategies in Regenerative Medicine. *International Journal of Molecular Sciences* 2017, **18**(9):1852.
3. Timmers, L., Lim, S.K., Arslan, F., Armstrong, J.S., Hofer, I.E., Doevendans, P.A., Piek, J.J., El Oakley, R.M., Choo, A., Lee, C.N., Pasterkamp, G., and de Kleijn, D.P., Reduction of myocardial infarct size by human mesenchymal stem cell conditioned medium. *Stem Cell Res* 2007, **1**(2):129-37.
4. Park, S.R., Kim, J.W., Jun, H.S., Roh, J.Y., Lee, H.Y., and Hong, I.S., Stem Cell Secretome and Its Effect on Cellular Mechanisms Relevant to Wound Healing. *Mol Ther* 2018, **26**(2):606-617.
5. Nakamura, Y., Miyaki, S., Ishitobi, H., Matsuyama, S., Nakasa, T., Kamei, N., Akimoto, T., Higashi, Y., and Ochi, M., Mesenchymal-stem-cell-derived exosomes accelerate skeletal muscle regeneration. *FEBS Lett* 2015, **589**(11):1257-65.
6. Herberts, C.A., Kwa, M.S.G., and Hermsen, H.P.H., Risk factors in the development of stem cell therapy. *Journal of Translational Medicine* 2011, **9**:29-29.
7. Fan, M., Chen, W., Liu, W., Du, G.Q., Jiang, S.L., Tian, W.C., Sun, L., Li, R.K., and Tian, H., The effect of age on the efficacy of human mesenchymal stem cell transplantation after a myocardial infarction. *Rejuvenation Res* 2010, **13**(4):429-38.
8. Deregibus, M.C., Iavello, A., Tetta, C., and Camussi, G., Role of Extracellular Vesicles in Tissue/Organ Regeneration, in *Adult Stem Cell Therapies: Alternatives to Plasticity*, M.Z. Ratajczak, Editor. 2014, Springer New York: New York, NY. p. 231-244.
9. Shabbir, A., Cox, A., Rodriguez-Menocal, L., Salgado, M., and Van Badiavas, E., Mesenchymal Stem Cell Exosomes Induce Proliferation and Migration of Normal and Chronic Wound Fibroblasts, and Enhance Angiogenesis In Vitro. *Stem Cells Dev* 2015, **24**(14):1635-47.
10. Zhang, S., Chu, W.C., Lai, R.C., Lim, S.K., Hui, J.H., and Toh, W.S., Exosomes derived from human embryonic mesenchymal stem cells promote osteochondral regeneration. *Osteoarthritis Cartilage* 2016, **24**(12):2135-2140.
11. Khan, M., Nickoloff, E., Abramova, T., Johnson, J., Verma, S.K., Krishnamurthy, P., Mackie, A.R., Vaughan, E., Garikipati, V.N., Benedict, C., Ramirez, V., Lambers, E., Ito, A., Gao, E., Misener, S., Luongo, T., Elrod, J., Qin, G., Houser, S.R., Koch, W.J., and Kishore, R., Embryonic stem cell-derived exosomes promote endogenous repair mechanisms and enhance cardiac function following myocardial infarction. *Circ Res* 2015, **117**(1):52-64.
12. van Koppen, A., Joles, J.A., van Balkom, B.W., Lim, S.K., de Kleijn, D., Giles, R.H., and Verhaar, M.C., Human embryonic mesenchymal stem cell-derived conditioned medium rescues kidney function in rats with established chronic kidney disease. *PLoS One* 2012, **7**(6):e38746.
13. Cruz, F.F. and Rocco, P.R.M., Stem-cell extracellular vesicles and lung repair. *Stem Cell Investigation* 2017, **4**:78.
14. Quesenberry, P.J., Aliotta, J., Deregibus, M.C., and Camussi, G., Role of extracellular RNA-carrying vesicles in cell differentiation and reprogramming. *Stem Cell Research & Therapy* 2015, **6**:153.

15. Collino, F., Pomatto, M., Bruno, S., Lindoso, R.S., Tapparo, M., Sicheng, W., Quesenberry, P., and Camussi, G., Exosome and Microvesicle-Enriched Fractions Isolated from Mesenchymal Stem Cells by Gradient Separation Showed Different Molecular Signatures and Functions on Renal Tubular Epithelial Cells. *Stem Cell Rev* 2017, **13**(2):226-243.
16. Aliotta, J.M., Pereira, M., Wen, S., Dooner, M.S., Del Totto, M., Papa, E., Goldberg, L.R., Baird, G.L., Ventetuolo, C.E., Quesenberry, P.J., and Klinger, J.R., Exosomes induce and reverse monocrotaline-induced pulmonary hypertension in mice. *Cardiovasc Res* 2016, **110**(3):319-30.
17. Xu, R., Greening, D.W., Rai, A., Ji, H., and Simpson, R.J., Highly-purified exosomes and shed microvesicles isolated from the human colon cancer cell line LIM1863 by sequential centrifugal ultrafiltration are biochemically and functionally distinct. *Methods* 2015, **87**:11-25.
18. Basu, J. and Ludlow, J.W., Exosomes for repair, regeneration and rejuvenation. *Expert Opin Biol Ther* 2016, **16**(4):489-506.
19. Vlassov, A.V., Magdaleno, S., Setterquist, R., and Conrad, R., Exosomes: current knowledge of their composition, biological functions, and diagnostic and therapeutic potentials. *Biochim Biophys Acta* 2012, **1820**(7):940-8.
20. Wu, Y., Deng, W., and Klinke, D.J., Exosomes: Improved methods to characterize their morphology, RNA content, and surface protein biomarkers. *The Analyst* 2015, **140**(19):6631-6642.
21. Konala, V.B., Mamidi, M.K., Bhonde, R., Das, A.K., Pochampally, R., and Pal, R., The current landscape of the mesenchymal stromal cell secretome: A new paradigm for cell-free regeneration. *Cytotherapy* 2016, **18**(1):13-24.
22. Sun, L., Xu, R., Sun, X., Duan, Y., Han, Y., Zhao, Y., Qian, H., Zhu, W., and Xu, W., Safety evaluation of exosomes derived from human umbilical cord mesenchymal stromal cell. *Cytotherapy* 2016, **18**(3):413-22.
23. Lai, R.C., Chen, T.S., and Lim, S.K., Mesenchymal stem cell exosome: a novel stem cell-based therapy for cardiovascular disease. *Regen Med* 2011, **6**(4):481-92.
24. Zhang, Y., Chopp, M., Zhang, Z.G., Katakowski, M., Xin, H., Qu, C., Ali, M., Mahmood, A., and Xiong, Y., Systemic administration of cell-free exosomes generated by human bone marrow derived mesenchymal stem cells cultured under 2D and 3D conditions improves functional recovery in rats after traumatic brain injury. *Neurochem Int* 2017, **111**:69-81.
25. Narayanan, R., Huang, C.-C., and Ravindran, S., Hijacking the Cellular Mail: Exosome Mediated Differentiation of Mesenchymal Stem Cells. *Stem Cells International* 2016, **2016**:11.
26. Lee, C., Mitsialis, S.A., Aslam, M., Vitali, S.H., Vergadi, E., Konstantinou, G., Sdrimas, K., Fernandez-Gonzalez, A., and Kourembanas, S., Exosomes mediate the cytoprotective action of mesenchymal stromal cells on hypoxia-induced pulmonary hypertension. *Circulation* 2012, **126**(22):2601-11.
27. Vaporidi, K., Vergadi, E., Kaniaris, E., Hatziapostolou, M., Lagoudaki, E., Georgopoulos, D., Zapol, W.M., Bloch, K.D., and Iliopoulos, D., Pulmonary microRNA profiling in a mouse model of ventilator-induced lung injury. *Am J Physiol Lung Cell Mol Physiol* 2012, **303**(3):L199-207.
28. Li, T., Yan, Y., Wang, B., Qian, H., Zhang, X., Shen, L., Wang, M., Zhou, Y., Zhu, W., Li, W., and Xu, W., Exosomes derived from human umbilical cord mesenchymal stem cells alleviate liver fibrosis. *Stem Cells Dev* 2013, **22**(6):845-54.

29. Tan, C.Y., Lai, R.C., Wong, W., Dan, Y.Y., Lim, S.-K., and Ho, H.K., Mesenchymal stem cell-derived exosomes promote hepatic regeneration in drug-induced liver injury models. *Stem Cell Research & Therapy* 2014, **5**(3):76-76.
30. Gatti, S., Bruno, S., Deregibus, M.C., Sordi, A., Cantaluppi, V., Tetta, C., and Camussi, G., Microvesicles derived from human adult mesenchymal stem cells protect against ischaemia-reperfusion-induced acute and chronic kidney injury. *Nephrol Dial Transplant* 2011, **26**(5):1474-83.
31. Zhou, Y., Xu, H., Xu, W., Wang, B., Wu, H., Tao, Y., Zhang, B., Wang, M., Mao, F., Yan, Y., Gao, S., Gu, H., Zhu, W., and Qian, H., Exosomes released by human umbilical cord mesenchymal stem cells protect against cisplatin-induced renal oxidative stress and apoptosis in vivo and in vitro. *Stem Cell Res Ther* 2013, **4**(2):34.
32. Lai, R.C., Arslan, F., Lee, M.M., Sze, N.S., Choo, A., Chen, T.S., Salto-Tellez, M., Timmers, L., Lee, C.N., El Oakley, R.M., Pasterkamp, G., de Kleijn, D.P., and Lim, S.K., Exosome secreted by MSC reduces myocardial ischemia/reperfusion injury. *Stem Cell Res* 2010, **4**(3):214-22.
33. Yang, J., Liu, X.X., Fan, H., Tang, Q., Shou, Z.X., Zuo, D.M., Zou, Z., Xu, M., Chen, Q.Y., Peng, Y., Deng, S.J., and Liu, Y.J., Extracellular Vesicles Derived from Bone Marrow Mesenchymal Stem Cells Protect against Experimental Colitis via Attenuating Colon Inflammation, Oxidative Stress and Apoptosis. *PLoS One* 2015, **10**(10):e0140551.
34. Peng, B., Chen, Y., and Leong, K.W., MicroRNA delivery for regenerative medicine. *Adv Drug Deliv Rev* 2015, **88**:108-22.
35. Sen, C.K. and Ghatak, S., miRNA control of tissue repair and regeneration. *Am J Pathol* 2015, **185**(10):2629-40.
36. Yao, S., Zhao, W., Ou, Q., Liang, L., Lin, X., and Wang, Y., MicroRNA-214 Suppresses Osteogenic Differentiation of Human Periodontal Ligament Stem Cells by Targeting ATF4. *Stem Cells International* 2017, **2017**:13.
37. Mencía Castaño, I., Curtin, C.M., Duffy, G.P., and O'Brien, F.J., Next generation bone tissue engineering: non-viral miR-133a inhibition using collagen-nanohydroxyapatite scaffolds rapidly enhances osteogenesis. *Scientific Reports* 2016, **6**:27941.
38. Valadi, H., Ekstrom, K., Bossios, A., Sjostrand, M., Lee, J.J., and Lotvall, J.O., Exosome-mediated transfer of mRNAs and microRNAs is a novel mechanism of genetic exchange between cells. *Nat Cell Biol* 2007, **9**(6):654-9.
39. Mittelbrunn, M., Gutiérrez-Vázquez, C., Villarroya-Beltri, C., González, S., Sánchez-Cabo, F., González, M.Á., Bernad, A., and Sánchez-Madrid, F., Unidirectional transfer of microRNA-loaded exosomes from T cells to antigen-presenting cells. *Nature Communications* 2011, **2**:282.
40. Zhang, J., Li, S., Li, L., Li, M., Guo, C., Yao, J., and Mi, S., Exosome and Exosomal MicroRNA: Trafficking, Sorting, and Function. *Genomics, Proteomics & Bioinformatics* 2015, **13**(1):17-24.
41. Kotton, D.N. and Morrissey, E.E., Lung regeneration: mechanisms, applications and emerging stem cell populations. *Nature medicine* 2014, **20**(8):822-832.
42. Ionescu, L., Byrne, R.N., van Haaften, T., Vadivel, A., Alphonse, R.S., Rey-Parra, G.J., Weissmann, G., Hall, A., Eaton, F., and Thébaud, B., Stem cell conditioned medium improves acute lung injury in mice: in vivo evidence for stem cell paracrine action. *American Journal of Physiology - Lung Cellular and Molecular Physiology* 2012, **303**(11):L967-L977.

43. Kim, S.Y., Burgess, J.K., Wang, Y., Kable, E.P., Weiss, D.J., Chan, H.K., and Chrzanowski, W., Atomized Human Amniotic Mesenchymal Stromal Cells for Direct Delivery to the Airway for Treatment of Lung Injury. *J Aerosol Med Pulm Drug Deliv* 2016, **29**(6):514-524.
44. Gupta, N., Su, X., Popov, B., Lee, J.W., Serikov, V., and Matthay, M.A., Intrapulmonary delivery of bone marrow-derived mesenchymal stem cells improves survival and attenuates endotoxin-induced acute lung injury in mice. *J Immunol* 2007, **179**(3):1855-63.
45. Tibboel, J., Keijzer, R., Reiss, I., de Jongste, J.C., and Post, M., Intravenous and Intratracheal Mesenchymal Stromal Cell Injection in a Mouse Model of Pulmonary Emphysema. *COPD* 2014, **11**(3):310-318.
46. Antunes, M.A., Abreu, S.C., Cruz, F.F., Teixeira, A.C., Lopes-Pacheco, M., Bandeira, E., Olsen, P.C., Diaz, B.L., Takyia, C.M., Freitas, I.P., Rocha, N.N., Capelozzi, V.L., Xisto, D.G., Weiss, D.J., Morales, M.M., and Rocco, P.R., Effects of different mesenchymal stromal cell sources and delivery routes in experimental emphysema. *Respiratory Research* 2014, **15**(1):118.
47. Serrano-Mollar, A., Nacher, M., Gay-Jordi, G., Closa, D., Xaubet, A., and Bulbena, O., Intratracheal Transplantation of Alveolar Type II Cells Reverses Bleomycin-induced Lung Fibrosis. *American Journal of Respiratory and Critical Care Medicine* 2007, **176**(12):1261-1268.
48. Sung, D.K., Chang, Y.S., Ahn, S.Y., Sung, S.I., Yoo, H.S., Choi, S.J., Kim, S.Y., and Park, W.S., Optimal Route for Human Umbilical Cord Blood-Derived Mesenchymal Stem Cell Transplantation to Protect Against Neonatal Hyperoxic Lung Injury: Gene Expression Profiles and Histopathology. *PLoS One* 2015, **10**(8):e0135574.
49. Monsel, A., Zhu, Y.-g., Gennai, S., Hao, Q., Hu, S., Rouby, J.-J., Rosenzweig, M., Matthay, M.A., and Lee, J.W., Therapeutic Effects of Human Mesenchymal Stem Cell-derived Microvesicles in Severe Pneumonia in Mice. *American Journal of Respiratory and Critical Care Medicine* 2015, **192**(3):324-336.
50. Willis, G.R., Fernandez-Gonzalez, A., Anastas, J., Vitali, S.H., Liu, X., Ericsson, M., Kwong, A., Mitsialis, S.A., and Kourembanas, S., Mesenchymal Stromal Cell Exosomes Ameliorate Experimental Bronchopulmonary Dysplasia and Restore Lung Function through Macrophage Immunomodulation. *Am J Respir Crit Care Med* 2018, **197**(1):104-116.
51. Tan, K.S., Choi, H., Jiang, X., Yin, L., Seet, J.E., Patzel, V., Engelward, B.P., and Chow, V.T., Micro-RNAs in regenerating lungs: an integrative systems biology analysis of murine influenza pneumonia. *BMC Genomics* 2014, **15**(1):587.
52. Zhu, Y.G., Feng, X.M., Abbott, J., Fang, X.H., Hao, Q., Monsel, A., Qu, J.M., Matthay, M.A., and Lee, J.W., Human mesenchymal stem cell microvesicles for treatment of Escherichia coli endotoxin-induced acute lung injury in mice. *Stem Cells* 2014, **32**(1):116-25.
53. Yuan, A., Farber, E.L., Rapoport, A.L., Tejada, D., Deniskin, R., Akhmedov, N.B., and Farber, D.B., Transfer of microRNAs by embryonic stem cell microvesicles. *PLoS One* 2009, **4**(3):e4722.
54. Collino, F., Deregibus, M.C., Bruno, S., Sterpone, L., Aghemo, G., Viltono, L., Tetta, C., and Camussi, G., Microvesicles derived from adult human bone marrow and tissue specific mesenchymal stem cells shuttle selected pattern of miRNAs. *PLoS One* 2010, **5**(7):e11803.
55. Sessa, R. and Hata, A., Role of microRNAs in lung development and pulmonary diseases. *Pulm Circ* 2013, **3**(2):315-28.
56. Goodwin, A.J., MicroRNA Analysis in Acute Lung Injury, in *Acute Lung Injury and Repair: Scientific Fundamentals and Methods*, L.M. Schnapp and C. Feghali-Bostwick, Editors. 2017, Springer International Publishing: Cham. p. 161-177.

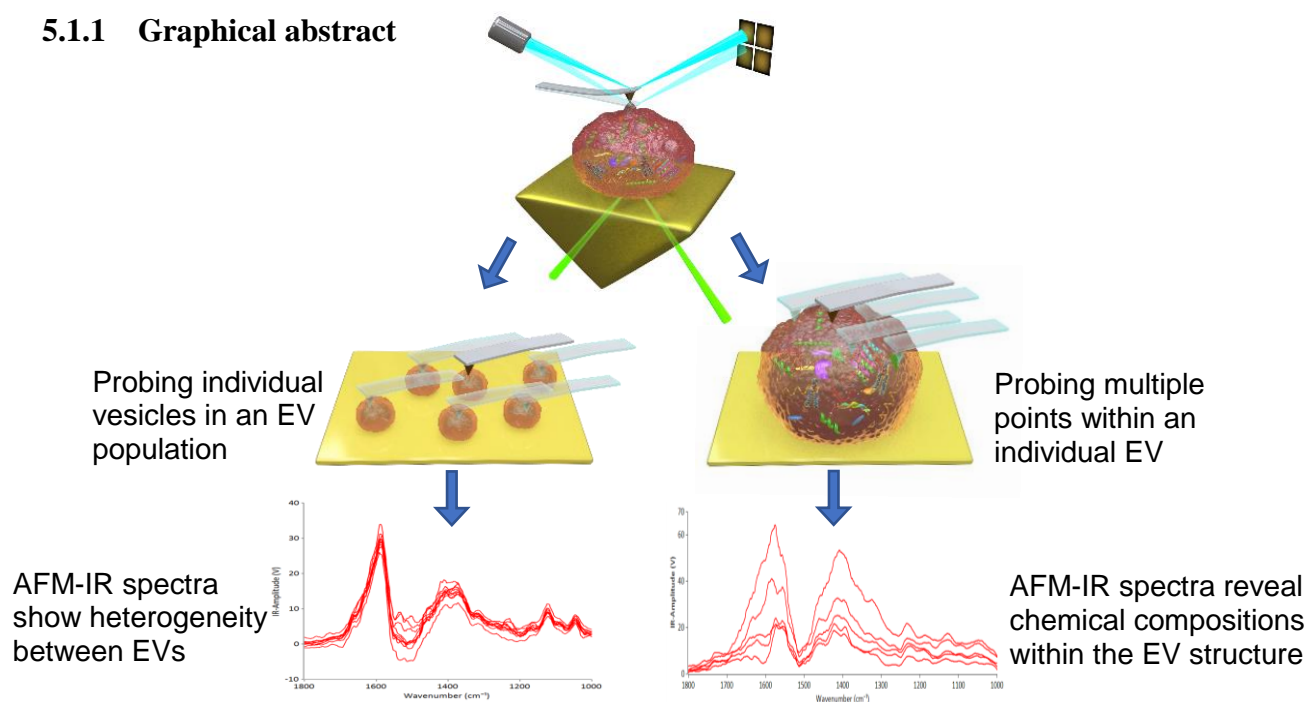
57. Song, Y., Dou, H., Li, X., Zhao, X., Li, Y., Liu, D., Ji, J., Liu, F., Ding, L., Ni, Y., and Hou, Y., Exosomal miR-146a Contributes to the Enhanced Therapeutic Efficacy of Interleukin-1beta-Primed Mesenchymal Stem Cells Against Sepsis. *Stem Cells* 2017, **35**(5):1208-1221.
58. Alexander, M., Hu, R., Runtsch, M.C., Kagele, D.A., Mosbrugger, T.L., Tolmachova, T., Seabra, M.C., Round, J.L., Ward, D.M., and O'Connell, R.M., Exosome-delivered microRNAs modulate the inflammatory response to endotoxin. *Nat Commun* 2015, **6**:7321.
59. Huang, Y., Crawford, M., Higuera-Castro, N., Nana-Sinkam, P., and Ghadiali, S.N., miR-146a regulates mechanotransduction and pressure-induced inflammation in small airway epithelium. *FASEB J* 2012, **26**(8):3351-64.
60. Qin, S.Q., Kusuma, G.D., Al-Sowayan, B., Pace, R.A., Isenmann, S., Pertile, M.D., Gronthos, S., Abumaree, M.H., Brennecke, S.P., and Kalionis, B., Establishment and characterization of fetal and maternal mesenchymal stem/stromal cell lines from the human term placenta. *Placenta* 2016, **39**:134-46.
61. Kusuma, G.D., Abumaree, M.H., Pertile, M.D., Perkins, A.V., Brennecke, S.P., and Kalionis, B., Mesenchymal Stem/Stromal Cells Derived From a Reproductive Tissue Niche Under Oxidative Stress Have High Aldehyde Dehydrogenase Activity. *Stem Cell Rev* 2016, **12**(3):285-97.
62. Maas, S.L.N., de Vrij, J., van der Vlist, E.J., Geragousian, B., van Bloois, L., Mastrobattista, E., Schiffelers, R.M., Wauben, M.H.M., Broekman, M.L.D., and Nolte-'t Hoen, E.N.M., Possibilities and limitations of current technologies for quantification of biological extracellular vesicles and synthetic mimics. *Journal of Controlled Release* 2015, **200**:87-96.
63. Akers, J.C., Ramakrishnan, V., Nolan, J.P., Duggan, E., Fu, C.-C., Hochberg, F.H., Chen, C.C., and Carter, B.S., Comparative Analysis of Technologies for Quantifying Extracellular Vesicles (EVs) in Clinical Cerebrospinal Fluids (CSF). *PLoS ONE* 2016, **11**(2):e0149866.
64. Jeyaram, A. and Jay, S.M., Preservation and Storage Stability of Extracellular Vesicles for Therapeutic Applications. *The AAPS Journal* 2017, **20**(1):1.
65. Bosch, S., de Beaupaire, L., Allard, M., Mosser, M., Heichette, C., Chrétien, D., Jegou, D., and Bach, J.-M., Trehalose prevents aggregation of exosomes and cryodamage. *Scientific Reports* 2016, **6**:36162.
66. Khanal, D., Kondyurin, A., Hau, H., Knowles, J.C., Levinson, O., Ramzan, I., Fu, D., Marcott, C., and Chrzanowski, W., Biospectroscopy of Nanodiamond-Induced Alterations in Conformation of Intra- and Extracellular Proteins: A Nanoscale IR Study. *Analytical Chemistry* 2016, **88**(15):7530-7538.
67. Lee, J., Wen, B., Carter, E.A., Combes, V., Grau, G.E.R., and Lay, P.A., Infrared spectroscopic characterization of monocytic microvesicles (microparticles) released upon lipopolysaccharide stimulation. *The FASEB Journal* 2017, **31**(7):2817-2827.
68. Mihály, J., Deák, R., Szigyártó, I.C., Bóta, A., Beke-Somfai, T., and Varga, Z., Characterization of extracellular vesicles by IR spectroscopy: Fast and simple classification based on amide and CH stretching vibrations. *Biochimica et Biophysica Acta (BBA) - Biomembranes* 2017, **1859**(3):459-466.
69. Crosby, L.M. and Waters, C.M., Epithelial repair mechanisms in the lung. *American Journal of Physiology - Lung Cellular and Molecular Physiology* 2010, **298**(6):L715-L731.
70. Yang, K., Leslie, K.G., Kim, S.Y., Kalionis, B., Chrzanowski, W., Jolliffe, K.A., and New, E.J., Tailoring the properties of a hypoxia-responsive 1,8-naphthalimide for imaging applications. *Organic & Biomolecular Chemistry* 2018, **16**(4):619-624.

71. Xin, H., Li, Y., and Chopp, M., Exosomes/miRNAs as mediating cell-based therapy of stroke. *Frontiers in cellular neuroscience* 2014, **8**:377.
72. Omer, N., Rohilla, A., Rohilla, S., and Kushnoor, A., Nitric Oxide: Role in Human Biology. *International Journal of Pharmaceutical Sciences and Drug Research* 2012, **4**(2):105-109.
73. Bogdan, C., Nitric oxide and the immune response. *Nat Immunol* 2001, **2**(10):907-16.
74. Kim, P.K., Zamora, R., Petrosko, P., and Billiar, T.R., The regulatory role of nitric oxide in apoptosis. *Int Immunopharmacol* 2001, **1**(8):1421-41.
75. Guo, L., Zhao, R.C.H., and Wu, Y., The role of microRNAs in self-renewal and differentiation of mesenchymal stem cells. *Experimental Hematology* 2011, **39**(6):608-616.
76. Bjorge, I.M., Kim, S.Y., Mano, J.F., Kalionis, B., and Chrzanowski, W., Extracellular vesicles, exosomes and shedding vesicles in regenerative medicine - a new paradigm for tissue repair. *Biomaterials Science* 2018, **6**(1):60-78.
77. *MicroRNA in Regenerative Medicine*, ed. C.K. Sen. 2015, USA: Elsevier Inc.
78. Amanda, O.R., Claudia, R.G.S., Alberto, I., Lygia, V.P., and Luciana, R.V., MicroRNAs: Modulators of Cell Identity, and their Applications in Tissue Engineering. *MicroRNA* 2014, **3**(1):45-53.
79. Mogilyansky, E. and Rigoutsos, I., The miR-17/92 cluster: a comprehensive update on its genomics, genetics, functions and increasingly important and numerous roles in health and disease. *Cell Death And Differentiation* 2013, **20**:1603.
80. Alipoor, S.D., Mortaz, E., Garssen, J., Movassaghi, M., Mirsaeidi, M., and Adcock, I.M., Exosomes and Exosomal miRNA in Respiratory Diseases. *Mediators of Inflammation* 2016, **2016**:11.
81. Su, Z.F., Sun, Z.W., Zhang, Y., Wang, S., Yu, Q.G., and Wu, Z.B., Regulatory effects of miR-146a/b on the function of endothelial progenitor cells in acute ischemic stroke in mice. *Kaohsiung J Med Sci* 2017, **33**(8):369-378.
82. Bhaskaran, M., Wang, Y., Zhang, H., Weng, T., Baviskar, P., Guo, Y., Gou, D., and Liu, L., MicroRNA-127 modulates fetal lung development. *Physiological Genomics* 2009, **37**(3):268-278.
83. Wang, Y., Huang, C., Chintagari, N.R., Xi, D., Weng, T., and Liu, L., miR-124 regulates fetal pulmonary epithelial cell maturation. *Am J Physiol Lung Cell Mol Physiol* 2015, **309**(4):L400-13.
84. Zhang, L., Wang, Y., Li, W., Tsonis, P.A., Li, Z., Xie, L., and Huang, Y., MicroRNA-30a Regulation of Epithelial-Mesenchymal Transition in Diabetic Cataracts Through Targeting SNAI1. *Scientific Reports* 2017, **7**(1):1117.

5 Resolving heterogeneity of extracellular vesicles (EVs) using single-vesicle, nanoscale characterisation with high-resolution resonance enhanced atomic force microscope infrared spectroscopy (AFM-IR)

5.1 Overview

5.1.1 Graphical abstract



5.1.2 Highlights and keywords

- Extracellular vesicles (EVs) emerged recently as key messenger molecules that regulate cellular function.
- AFM-IR enables characterisation of EVs at ultra-high resolution to define subtle differences between individual vesicles and their subpopulations.
- We present, for the first time, a study of the molecular structure and composition of individual EVs and populations using AFM-IR.
- This characterisation approach is probe-free and outperforms other methods with unmatched resolution as it characterises at a single vesicle level.

Published in:

Nanoscale Horizons

COMMUNICATION

Check for updates

Cite this: DOI: 10.1039/c8nh00048d

Received 1st March 2018
Accepted 4th April 2018
DOI: 10.1039/c8nh00048d
rsc.li/nanoscale-horizons

None of us is the same as all of us: resolving the heterogeneity of extracellular vesicles using single-vesicle, nanoscale characterisation with resonance enhanced atomic force microscope infrared spectroscopy (AFM-IR)

Sally Yunsun Kim,^a Dipesh Khanal,^a Priyanka Tharkar,^{ab} Bill Kalonits^c and Wojciech Chrzanowski^{a*}



View Article Online
View Journal

The Sydney Morning Herald
NATIONAL HEALTH
There's a postal network running through your veins. Can it heal you?

EurekaAlert! AAAS
The Global Source for Science News

PUBLIC RELEASE: 12-APR-2018

Scientists unlock path to use cell's own nanoparticles as disease biomarkers
Extracellular vesicles can now be identified at the individual level
UNIVERSITY OF SYDNEY

SCIENCE
Message in a body could hold clue to human health

RN Breakfast
Program Home Past Programs Features

Cell nanoparticles could help diagnose and treat cancer

Thursday 12 April 2018 6:55AM (view full episode)

5.1.3 Abstract

Extracellular vesicles (EVs) are highly specialised, nanoscale messengers that deliver biological signals and in doing so mediate intercellular communication. EVs are recognised not only for their therapeutic potential but also for their critical role in early disease diagnosis. EVs emerged recently as key messenger molecules that regulate cellular function. Increasing evidence shows that within populations of EVs, important properties including morphology, membrane composition, and content vary substantially. This heterogeneity arises in response to the nature, state, and environmental condition of the cell source. However, currently there are no effective approaches, which unequivocally discriminate differences between individual EVs, which critically hampers progress in this emerging scientific area. Measuring EV heterogeneity is paramount to our understanding of how EVs influence physiological and pathological functions of their target cells. Moreover, understanding EV heterogeneity is essential for their application as diagnostics and therapeutics.

Despite of significant investments and advances in the field, until now multifaceted characterisation of individual vesicles (of sizes below 200 nm) and EV subpopulations has not been achieved. To address this unmet need, we present, for the first time, a study of the molecular structure and composition of individual EVs and populations using resonance enhanced atomic force microscope infrared spectroscopy (AFM-IR). We demonstrate and validate that AFM-IR enables identification of nanoscale structural compositions using EVs derived from two types of placenta stem cells. The particular strength of this approach is that it is a label-free and ultra-high sensitive technique that has the power to measure individual EV heterogeneity. New insights gained by this nanoscale characterisation method will have profound impact not only on our basic understanding of EV biology but also to disease diagnostics and the emerging area of EV-therapies.

5.2 Introduction

Extracellular vesicles (EVs) are highly specialised biological nanoscale messengers that orchestrate both physiological and pathophysiological processes in recipient cells. EVs are classified based on their cellular origin and biological function, or on their distinct biogenesis pathways. Intense research focuses on understanding EV biogenesis, developing methods for their isolation, purification and characterisation, defining their package of bioactive macromolecules (e.g. protein, lipids, nucleic acids), and understanding how their uptake by recipient cells results in cellular reprogramming. Currently, key global challenges in EV research are:

- establishing heterogeneity of EV populations.
- high resolution detection of differences of molecular structure of individual vesicles.
- validation of isolation and purification protocols.

All these challenges hinge on our ability to probe individual vesicles at a significantly improved resolution than what is currently achieved with conventional protocols.

The study of EVs is fundamental to our understanding of cell signalling in normal and pathological tissues. EVs are also in the limelight because of their potential as biomarkers for cancer, cardiovascular and kidney diseases¹⁻⁴, their promise as ‘natural’ drug delivery systems, but primarily for their intrinsic therapeutic properties. This is most notable in the field of cell-based therapies for regenerative medicine where EVs deliver biological signals that direct a cascade of protective biological responses that ultimately restore cellular function in damaged or diseased tissues⁵⁻⁷. Therefore, to unlock the true potential of EVs for their versatile applications, what is needed is new approach to unequivocally define nanoscale differences at a single EV level. Ironically, currently used methods for EV characterisation are only suitable for bulk EV populations and fall short of pinpointing differences between individual EVs and there are no current methods to discriminate structural and molecular differences of individual vesicles of nanosize range.

Nanoscale understanding of the biological signals packaged by cells into EVs is essential for application in diagnosis and therapy of diseases. However, while there has been advances in characterising intracellular lipid droplets and other organelles, which has no direct correlation to EVs and have different size range, there are no reported methods for analysing individual EV composition within a population of EVs. While conventional spectroscopy techniques may probe larger EVs, e.g. apoptotic bodies, it has not been possible to probe individual EVs e.g.

exosomes (20 – 120 nm). Comparing subpopulations of EVs has only been possible by separating them from the total population of EVs with little control in which portion is being selected for characterisation. The heterogeneity assessment of EV populations has only recently been recognised as of critical importance to advancing the field. We present an innovative approach using resonance enhanced atomic force microscope infrared spectroscopy (AFM-IR) to assess heterogeneity and identify the nanoscale structural composition of EVs. AFM-IR not only provides ultra-high resolution but also overcomes limitations of conventional methods suited to bulk EV populations, which include limited resolution and sensitivity. Since the individual EVs can be probed within a bulk EV sample, this technique is a useful high-resolution screening tool to identify the protein, lipids and nucleic acid content of EVs simultaneously prior to conducting molecular assays to interrogate the exact molecular make-up. Within the context of EVs being highlighted as early biomarkers of a number of diseases and stem cell-derived EVs being developed as therapeutics to replace cell therapies, nanoscale examination of individual EVs using AFM-IR has the potential for profound significance in disease diagnostics and in the emerging area of EV-therapies. Thus, the development of AFM-IR technique for individual EV profiling is pushing the forefront of regenerative medicine closer to the creation of truly bioactive therapies, the demand for which is rapidly increasing.

Our interest is human mesenchymal stromal cells (MSCs), which have stem cell-like properties and are derived from tissues and fluids. MSCs have therapeutic potential for many applications⁸, including enhancing recovery from cellular injuries caused by myocardial infarction^{9, 10}, and they have additional beneficial properties of attenuating inflammation and immune responses¹¹⁻¹³. The therapeutic action of MSCs is primarily through a paracrine mechanism mediated by EVs. EVs secreted by mesenchymal stromal cells have been extensively researched for their regenerative medicine applications⁸.

A major problem that besets all EV research is that current isolation methods produce heterogeneous populations of EVs with respect to their size and structure. These problems arise in part due the nanoscale size of EVs and the paucity of specific markers for isolating and identifying the different classes of EVs. The composition of EVs is another confounding factor. EV composition of bioactive macromolecules in several classes of EVs is the result of selective packaging. The secreting cell uses a regulated mechanism that responds to various stimuli (e.g. growth conditions such as hypoxia⁵, the cellular microenvironment, and pathological changes within the cell of origin¹⁴), which determines the final specific composition of EVs. Thus, the

physical structure and composition of the EV population, and of individual EVs, is heterogeneous. Heterogeneity of EVs is a substantial problem for EV research even where EVs are isolated from a source of uniform cell populations. However, for MSC-based therapeutics a further confounding factor is that MSC-EVs are themselves a heterogeneous population, and this heterogeneity is maintained during *ex vivo* cell expansion. Methods to monitor EVs during MSC cell expansion would therefore be highly beneficial to this area of research.

The absence of available technique to interrogate the heterogeneity of EVs restrict our understanding of EV function¹⁵⁻¹⁷. Conventional technologies to probe individual EVs are limited to determining individual EV particle size, morphology and number. The overall molecular composition of a population of EVs is primarily determined on the entire EV population using protein, lipid or nucleic acids-based analyses. There are no currently available methods for analysing subpopulations of EVs without isolating them, using capture antibodies for example, from the total population of EVs. Moreover, there are no methods for determining individual EV composition within a population. Despite the recent progress in the development of IR-based characterisation methods, many conventional methods have limited resolution and are only suitable for bulk materials without enabling direct comparison of individual EVs within a sample. We present an innovative approach using AFM-IR, to study the structure, composition and dynamics of whole populations, subpopulations and individual EVs at an ultra-high resolution of less than 20 nm.

AFM-IR has recently been used for determining conformational changes in intra and extracellular protein structures, which indicate altered biological function¹⁸, for probing chemical and mechanical nanodomains within nanoparticles¹⁹, and for studying intracellular lipid droplets, vesicles and cytoskeletal filaments of cells at the subcellular level²⁰. However, AFM-IR for complex biological nanoparticles such as EVs has not yet been reported. The advantages of incorporating AFM-IR for EV characterisation are based primarily on ultra-high sensitivity and resolution and represent leap forward in a quest to unequivocally define molecular composition of individual EVs and their subpopulations. These allow the user to profile the composition and structure of single EVs within a population to identify nanoscale heterogeneity, which is critical for assessing the effects of EV isolation and processing methods, or for identifying alterations in protein to lipid ratios. The latter application may potentially add significant value in diagnosis and prognosis of disease in the field of biomarkers. This fast, label-free technique requires only a few microliters of sample for

mapping IR-absorbing species of individual EVs, and is a convenient tool for comparing individual EV composition and structure. With the outstanding resolution of less than 20 nm, we can probe multiple points on individual EVs to interrogate differences in composition and structure within single EVs. Gaining a better understanding of EV composition and heterogeneity will lead to the advances in the precise development of EV therapeutics and biomarkers, as well as to reveal the purity of EV populations.

We demonstrate the feasibility of probing individual EVs and identifying differences in the molecular composition of EV populations in nanoscale resolution. We present the comparison of EV samples isolated using ultrafiltration and after further purification using the additional size-exclusion chromatography (SEC) column. We also present EV samples isolated by conventional ultracentrifugation method and demonstrate AFM-IR to pinpoint differences between EVs derived from two stem cell lines. The nanoscale structural and compositional differences within individual EVs are presented to highlight the importance of defining the differences to potentially maximise the use of EVs in regenerative medicine.

5.3 Materials and Methods

5.3.1 Cell culture for EV isolation

EVs were isolated from a well-characterised, telomerase (hTERT)-transformed human chorionic mesenchymal stromal cell line (CMSC29) and decidual mesenchymal stromal cell line (DMSC23)²¹. CMSC29 and DMSC23 retain many of the important characteristics of the primary mesenchymal stromal/stem cells²¹ while ensuring reproducibility by avoiding the variation between primary mesenchymal stromal cell preparations. CMSC29 and DMSC23 were cultured in AmnioMAX™ (Life Technologies) and Mesencult™ (StemCell Technologies) media respectively, until 80% confluent then cells were washed twice in HBSS(-) (Sigma Aldrich) and incubated in EV isolation media (bovine serum albumin 0.5%, GlutaMAX™ 1%, penicillin 100 U/mL, streptomycin 100 µg/mL (Life Technologies) in AmnioMAX™ basal media) for 48 h. Cells were counted to ensure comparable number of cells and cell viability >90% was confirmed using trypan blue assay prior to the isolation of EVs from the conditioned media. To ensure reproducibility, biological triplicates were used for the isolation of EVs.

5.3.2 EV isolation and preparation for AFM-IR

EVs were isolated from conditioned media by the ultrafiltration method using Amicon® Ultra centrifugal filter (10k MWCO, Merck Millipore), following the manufacturer's protocol²². Enriched EV populations were achieved by passing through the qEV_{single} SEC column (Izon

Science) following the manufacturer's protocol²³, to remove background proteins, lipids, and other contaminating particulates²⁴. For EV isolation by ultracentrifugation, initially cells and debris were removed by centrifuging media at $500 \times g$ for 5 min followed by further centrifugation at $2,000 \times g$ for 10 min. Supernatant was transferred to thick-wall polycarbonate ultracentrifuge tubes (Seton Scientific Inc) and centrifuged at $100,000 \times g$ for 60 min at 4°C using rotor Ti-70 in Optima LE-80K Ultra Centrifuge (Beckman Coulter). Supernatant was removed and the EV pellet was resuspended in 1 ml RNase-free PBS (Lonza) using RNase-free pipette tips. Then ultracentrifugation was repeated at 31,200 rpm ($100,000 \times g$) for 60 min at 4°C , supernatant was removed. The pellet was resuspended in 200 μl RNase-free PBS, Five microliters each of fraction 7 containing EVs, and the original batch of EV sample prior to SEC, were placed on a zinc selenide prism to dry at room temperature for AFM-IR.

5.3.3 Measurement of molecular composition of EVs using AFM-IR spectroscopy

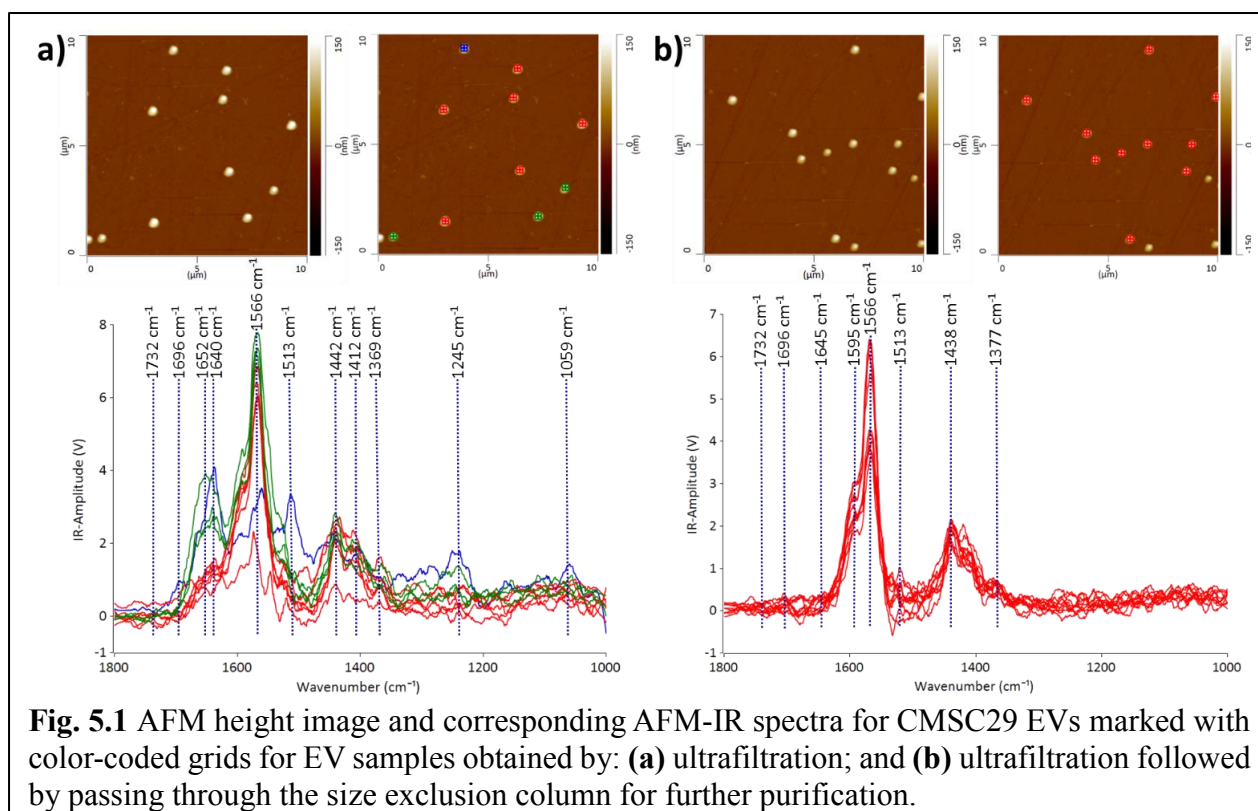
Nanoscale infrared biospectroscopy was conducted using an AFM-IR instrument (nanoIRTM, Anasys Instruments) as per a previously published protocol¹⁸. Briefly, four IR background spectra were collected from 1000 to 1800 cm^{-1} , these were then averaged and normalised for calibration of the signal intensity prior to measurement. The cantilever ringdown signal was optimised at its frequency center of above 75 kHz and frequency window of 50 kHz. After optimisation of the laser signal, AFM-IR spectra were collected from 1000 to 1800 cm^{-1} at 1 cm^{-1} intervals with a scan rate of 0.1 Hz with a coverage of 16. A silicon nitride cantilever (EXC450 tips, AppNano, CA, USA) with a nominal spring constant of 0.5 Nm^{-1} was used for all measurements. The scan sizes used were $10 \times 10 \mu\text{m}$ for probing one point per EV and $1 \times 1 \mu\text{m}$ for probing multiple points on individual EVs. Data analysis was done using the Analysis StudioTM software. Smoothing of the spectra using the 'Savitzky-Golay' function was achieved by using the polynomial function of 2 and 15 numbers of points. All data from AFM-IR are representative of at least triplicate samples and positions.

5.4 Results and Discussion

5.4.1 AFM-IR enables purity assessment of the EV sample

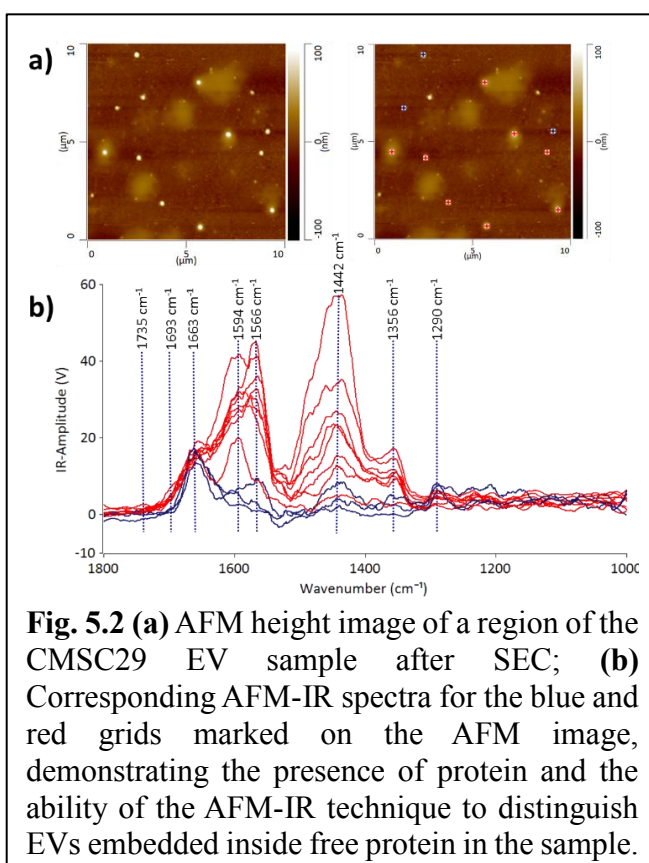
We demonstrate that the AFM-IR technique is capable of probing the heterogeneity of EV populations and interrogating nanoscale structural and compositional differences in individual EVs in two different EV populations; CMSC29 EVs isolated using ultrafiltration and CMSC29 EVs isolated by ultrafiltration followed by additional purification through SEC. Ultrafiltration is a faster method than ultracentrifugation and produces higher yield in the isolation of EVs

from cell culture conditioned media²⁵. However, various methods of EV isolation produce heterogeneous populations of EVs, and identifying this heterogeneity in EV populations is critical in advancing this field of research²⁶. The AFM-IR spectra of EVs give information on the molecular constituents and their structures, enabling identification of heterogeneity in the structure and composition of individual EVs at nanoscale resolution. The IR peaks with the highest intensities at 1566 cm^{-1} and 1595 cm^{-1} are common in both samples before and after passing through SEC (Fig. 5.1). Both peaks indicate the presence of amide II, arising from the N-H bending vibrations of the peptide groups within individual EVs^{27, 28}. The EV samples obtained by ultrafiltration prior to passing through SEC were more heterogenous, as grouped in red, green and blue subgroups according to the similarity of IR peak profile (Fig. 5.1a). The prominent absorption peaks at 1640 cm^{-1} and 1652 cm^{-1} for the EVs marked green or blue in Fig. 5.1a indicate the presence of amide I structure of proteins, originating mainly from C=O stretching vibrations of the protein peptide backbone²⁹. The intensity of these peaks reduced dramatically or were absent in the EV samples after passing through SEC (Fig. 5.1b), demonstrating the effectiveness of SEC in purifying EV populations. The absorption bands at 1438 cm^{-1} and 1442 cm^{-1} are due to CH_2 and CH_3 of protein or the bending (scissoring) vibration of lipid acyl CH_2 groups, found commonly in both EV populations before and after passing through SEC. The peaks at 1412 cm^{-1} are present in both samples at similar intensities, which refer to the phosphatidylcholine head group²⁹. The low intensity peaks at 1369 cm^{-1} and



1377 cm^{-1} represent thymine and this reveals that RNAs are contained inside CMSC29 EVs obtained by ultrafiltration, regardless of further SEC purification step²⁹. The low intensity peaks at 1732 cm^{-1} in both EV populations (Fig. 5.1) are attributed to the ester groups of phospholipids, triglycerides and cholesterol esters³⁰.

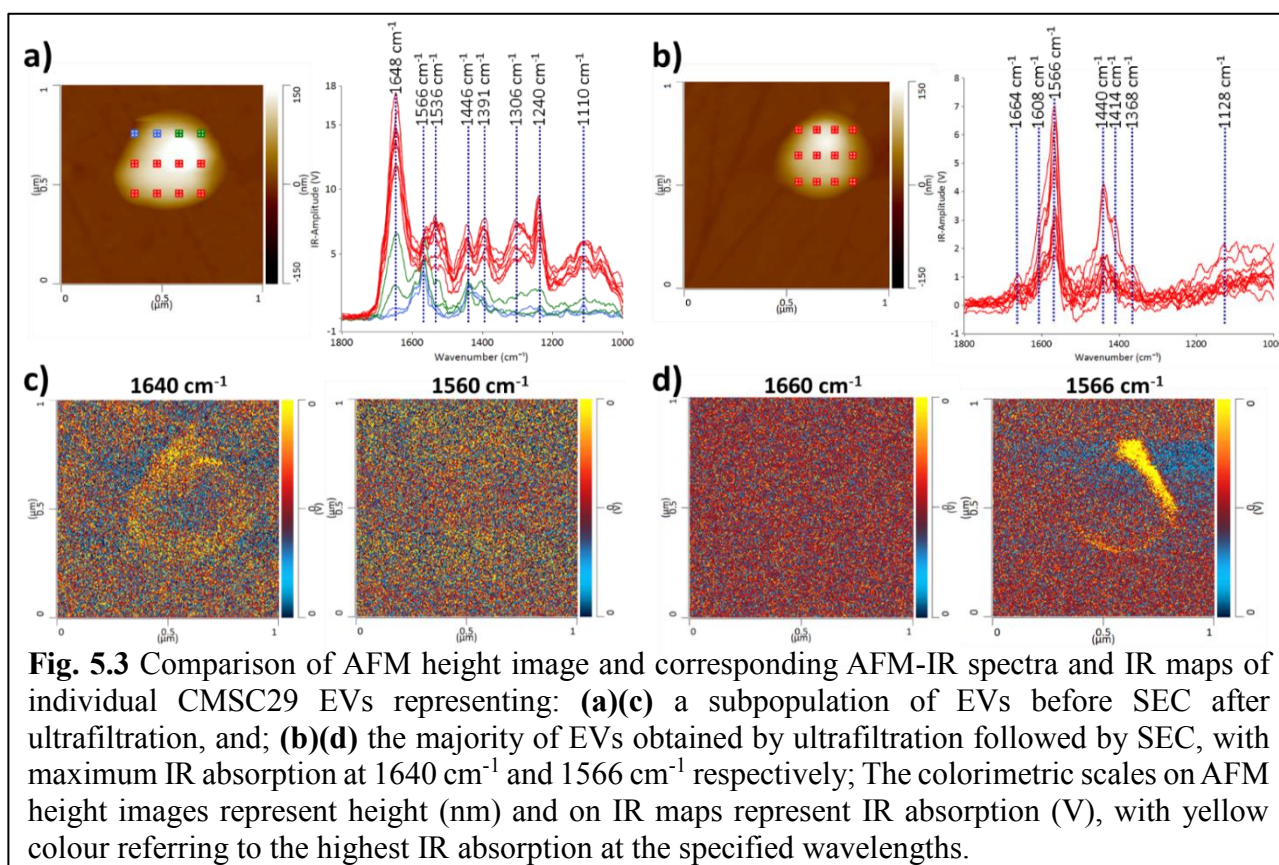
Some protein-rich regions were found within the EV sample in fraction 7 after passing through the SEC column as can be observed in the lighter patchy regions on the AFM height image (Fig. 5.2). The IR profiles of the EVs embedded inside the protein-rich regions (red) have a different IR profile to the individual EVs on their own (blue). This is an evidence that the detection of heterogeneity in EV populations can arise from the surrounding contaminating molecules. With the precise techniques of AFM-IR we can identify that the EVs embedded within the protein structures have stronger intensity peak at 1442 cm^{-1} . This peak is attributed to CH_2 and CH_3 of a protein assignment or the bending (scissoring) vibration of lipid acyl CH_2 groups. This reveals the presence of free proteins and lipids in the EV samples, however it is more likely referring to the presence of protein, since the lipid peak at 1735 cm^{-1} is of low intensity. An important aspect of EV samples for all applications is not merely detecting the presence of contaminating molecules but also to identify the composition of the contamination in order to assess suitability for downstream applications. Thus, we demonstrate that AFM-IR is capable of measuring the purity of EV samples with ultrahigh resolution. AFM-IR also has the power to identify the composition of the contaminating molecules, which is critical for optimising EV purification protocols.



5.4.2 AFM-IR enables probing multiple points on single vesicles

We also present the capability for AFM-IR to probe multiple points on a single EV as an array, for obtaining IR spectra and maps (Fig. 5.3) allowing visualisation and comparison of structural and compositional differences within a single EV. Multipoint analysis (nanoscale mapping) of

single EVs is a particular strength of AFM-IR, and it is not achievable with any other currently used techniques that characterise EVs. Mapping at the nanoscale level is critically important to probe the heterogeneity of individual EVs and their populations. Although it is possible to compare EVs within a single population, in Fig. 5.3 we compare single EVs in the two EV populations consistent with the above examples; CMSC29 EVs isolated using ultrafiltration, before and after SEC. Although the majority of CMSC29 EVs retain the same AFM-IR spectra before and after SEC as observed in Fig. 5.1, we identified that the EV population before SEC is more heterogeneous and there were some minor subpopulations with different AFM-IR profiles. An example of a single EV that represents this minor subpopulation is presented in Fig. 5.3a, for comparison with Fig. 5.3b which represents the majority of other EVs in the same sample before SEC as well as the overall population of EVs after SEC. The peak at 1640-60 cm^{-1} in Fig. 5.3a is characteristic of amide I band in the protein while the peak at 1566 cm^{-1} in Fig. 5.3b is linked to the -N-H bending vibration of amide II band^{27, 29}. The peaks at 1500 to 1700 cm^{-1} in Fig. 5.3a represents a conventional protein band with distinct peaks for amides I and II composed of overlapping bands that belong to the different secondary structures of proteins such as α -helix, β -sheet, random coil^{29, 30}. In contrast, the AFM-IR spectra of CMSC29 EVs after SEC (Fig. 5.3b), which is also representative of the majority of other EVs in the sample before SEC, displays unresolved bands with overlapping amide I and II peaks, as



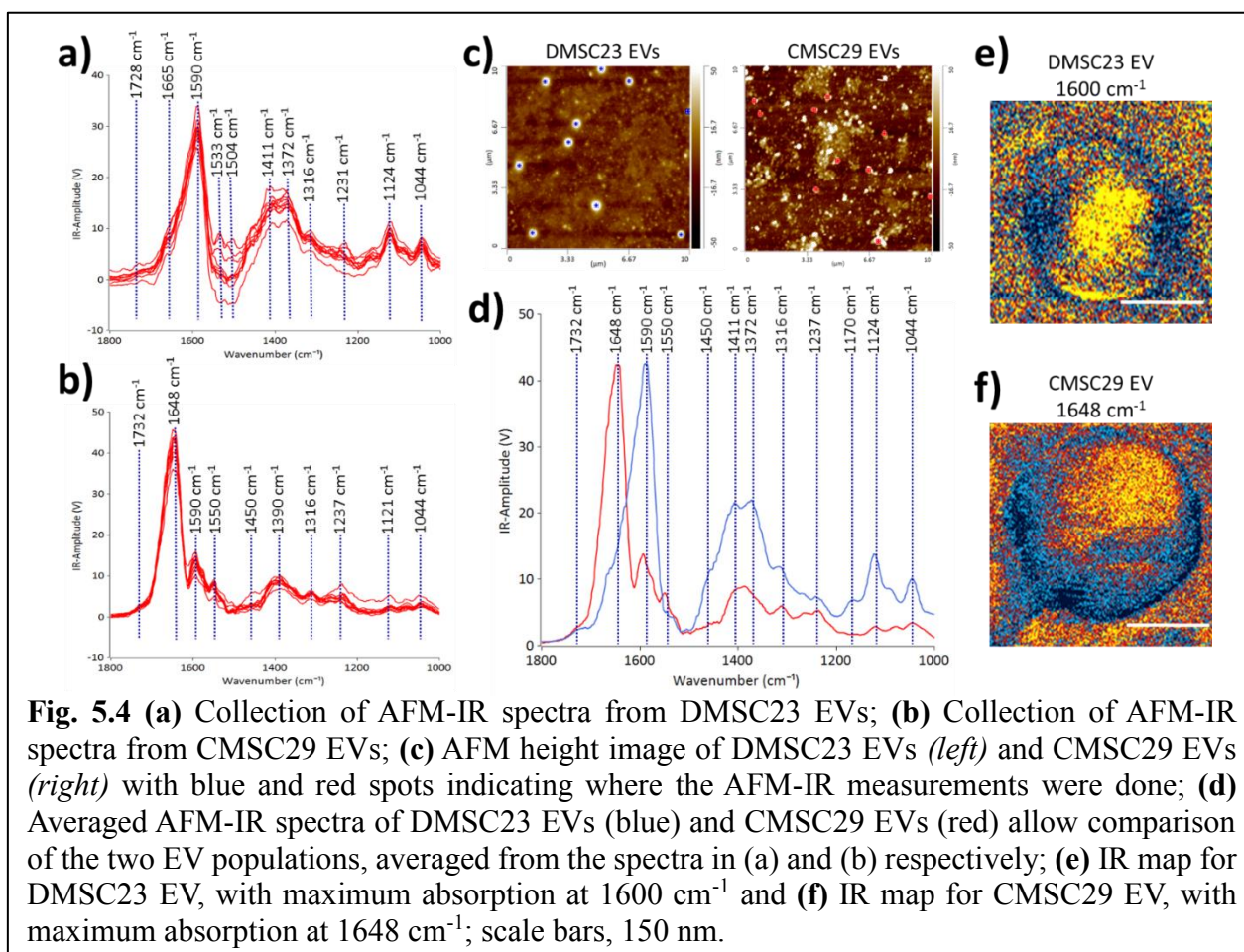
observed in the conventional IR characterisation of microvesicles²⁹. The AFM-IR profile of minor single EV presented in Fig. 5.3a corresponds to the IR profile of the EV marked in blue in Fig. 5.1a representing a minor subpopulation. Thus, we demonstrate that AFM-IR is a sensitive method to identify heterogeneity and is capable to interrogate structural differences between the subpopulations within the same EV sample. As multiple points are probed on a single EV, the area with the highest amide I concentration can be viewed at a nanoscale level.

5.4.3 High resolution mapping of single vesicles using AFM-IR enables identification of differences between EVs from two types of placenta stem cells

Furthermore, AFM-IR allows high resolution mapping of individual EVs (IR-absorbing species). The different IR peaks were clearly identifiable and the regions rich in amide I and II structures were visualised in EVs before and after SEC, as demonstrated by maximum absorption in yellow at 1640 cm^{-1} and 1566 cm^{-1} , respectively (Fig. 5.3c,d). Hence, we demonstrated that AFM-IR is a highly sensitive method to detect nanoscale compositional and structural differences between EV populations and individual EVs within a sample.

To demonstrate the use of AFM-IR in identifying optimal EV formulations for potential EV-therapies, the differences in the molecular composition of CMSC29 EVs and DMSC23 EVs were interrogated. Despite CMSC29 and DMSC23 cell lines are derived from the same source (human placenta), there are clear differences in their EV composition as determined by AFM-IR (Fig. 5.4). The AFM-IR spectra collected from multiple individual DMSC23 EVs (Fig. 5.4a) and CMSC29 EVs (Fig. 5.4b) show a peak within the amide stretching region of peptides (1500 to 1700 cm^{-1}), which corresponds to the bulk protein composition²⁹. The Amide I peak in proteins (1590 to 1700 cm^{-1}) is composed of overlapping bands that belong to different secondary structures of proteins such as α -helix, β -sheet, random coil³⁰. Therefore, using AFM-IR, changes to the individual protein components can be resolved. For CMSC29, the Amide I peak was in the typical wavenumber of 1648 cm^{-1} (Fig. 5.4b), which suggests normal conformation of the protein that contains high α -helix structure. While for DMSC23 EVs, the main Amide I peak was broadened and shifted to lower wavenumber with the main peak present at 1590 cm^{-1} (Fig. 5.4a). In addition, the Amide I band peak with a weaker intensity is also seen at a 1665 cm^{-1} . Cumulatively, broadening of the Amide I peak with the shift to lower frequencies and appearance of weak intensity peak at 1665 cm^{-1} indicated changes to the protein conformation in the DMSC23 EV sample.

AFM-IR also enables a fast screening of the differences in the nucleic acid composition between the samples. In the DMSC23 EV spectra, we observed presence of two well-defined



peaks at 1590 cm^{-1} and 1533 cm^{-1} which correspond to adenine (C=N bond) and guanine (C=N bond)²⁹. Both peaks were detected only at a very low level in CMSC29 EVs (Fig. 5.4b). For both DMSC23 EVs and CMSC29 EVs a low intensity peak at 1730 cm^{-1} that corresponds to purine base (C=O bond) was observed. However, the intensity of this peak varied across the EV populations, which demonstrated heterogeneity of nucleic acid content in the samples. Overall, this study confirmed differences in protein structure and nucleic acid content between both types of EVs, as well as differences in the composition in single EVs between the two populations.

The AFM height images (Fig. 5.4c), and the AFM-IR averaged spectra (Fig. 5.4d) obtained from two different EV populations allow direct comparison of DMSC23 EVs and CMSC29 EVs. The AFM height images were used to select the EVs of the same size for AFM-IR measurement. The peaks at 1411 cm^{-1} and 1372 cm^{-1} had higher intensities in the spectra of DMSC23 EVs, which refer to the phosphatidylcholine head group and thymine, respectively²⁹. These data indicate larger amounts of those components in lipids and nucleic acids packaged in DMSC23 EVs compared to CMSC29 EVs. The IR map at the maximum absorption region at 1590 – 1600 cm^{-1} for DMSC23 EVs (Fig. 5.4e) and at 1648 cm^{-1} for CMSC29 EVs (Fig.

5.4f) demonstrate the capacity of AFM-IR to generate a fingerprint for individual EVs. The AFM-IR analyses of EVs enable subpopulations of EVs to be analysed at the level of individual EVs and also distinguish differences in the composition and structure of various EV populations.

Taken together, there is a potential for AFM-IR to be utilised as highly sensitive, precise and relatively fast measurement of alterations in EV structure and composition to verify EVs purification protocols as well as to establish the fundamental science of EVs and their diagnostic and therapeutic potential.

5.5 Conclusions

One of the critical challenges in the EVs area, which curbs the translation of EVs to clinical applications is the capability to characterise individual vesicles and their heterogeneity. Whilst the ideal scenario would be to have a full profile of RNAs, DNA, proteins and lipids in each individual nanosize vesicle, it is technically unachievable. For molecular biological analyses, large quantities of EVs are required (hundreds of thousands of EVs) and typical yield of the molecules from such preparation does not exceed a few picograms. These quantities are currently the lower detection limit of existing techniques and thus the final result merely represent averaged profile of entire, large vesicle population. These significant technological constraints are unlikely to be resolved in the near future. Therefore, alternative approaches which can determine heterogeneity and composition of individual vesicles are highly sought after.

Indeed, we demonstrated for the first time that AFM-IR technique is capable of probing molecular constituents and structures of individual vesicles. We showed that using this approach we can validate purification protocols and clearly distinguish protein aggregates from vesicles, which is not possible with other approaches due their similar sizes. The data presented in this study suggest AFM-IR can transform existing protocols for interrogating EV composition and structures, and assessing EV purity. Despite this technique does not enable sequencing of RNAs it provides a robust data on protein, DNA and lipid content and their structure that points to the molecular structure of each of the individual vesicles. We demonstrated the strength of the technique to determine differences in structural differences of vesicles from different cells by probing vesicles isolated from two subtypes of placenta stem cells, which characterise with different molecular composition.

We know that variations in IR spectra can be used to identify pathologies, which has been previously demonstrated for microvesicles at micron scale. However, due to the resolution of the conventional techniques, a very high concentration of the sample is required and perhaps only advanced stages of the diseases can be identified. Therefore, our ability to probe individual vesicle is a leap forward in diagnosis and is likely to enable early diseases detection from a few vesicles. This advance may transform the way we diagnose (earlier detection with smaller sample quantity) and treat diseases in particular for diseases which characterize with high mortality: cancer, multiple sclerosis or dementia.

The fact that only few microliters of samples are required is an added benefit for the use of this technique in diagnosis or prognosis of diseases. For therapeutic applications, AFM-IR will allow researchers to not only assess EV purity and identify the contaminating molecules in EV preparations but furthermore can be developed to:

- (i) enable the development of protocols for effective EV preparation,
- (ii) assist fundamental studies of biological principles that govern the production and export of the vesicles via a better understating of packaging and assembly of EVs,
- (iii) identify the most effective EV formulations or optimal EV subtypes that are most therapeutically relevant, manipulated *via* pre-conditioning of secreting cells.

5.6 References

1. Guo, L. and He, B., Extracellular vesicles and their diagnostic and prognostic potential in cancer. *Translational Cancer Research* 2017, **6**(3):599-612.
2. Zhang, W., Zhou, X., Zhang, H., Yao, Q., Liu, Y., and Dong, Z., Extracellular vesicles in diagnosis and therapy of kidney diseases. *American Journal of Physiology - Renal Physiology* 2016, **311**(5):F844-F851.
3. Jansen, F., Nickenig, G., and Werner, N., Extracellular Vesicles in Cardiovascular Disease: Potential Applications in Diagnosis, Prognosis, and Epidemiology. *Circ Res* 2017, **120**(10):1649-1657.
4. Verma, M., Lam, T.K., Hebert, E., and Divi, R.L., Extracellular vesicles: potential applications in cancer diagnosis, prognosis, and epidemiology. *BMC Clinical Pathology* 2015, **15**:6.
5. Shurtleff, M.J., Temoche-Diaz, M.M., Karfilis, K.V., Ri, S., and Schekman, R., Y-box protein 1 is required to sort microRNAs into exosomes in cells and in a cell-free reaction. *Elife* 2016, **5**:e19276.
6. van der Pol, E., Böing, A.N., Harrison, P., Sturk, A., and Nieuwland, R., Classification, Functions, and Clinical Relevance of Extracellular Vesicles. *Pharmacological Reviews* 2012, **64**(3):676-705.
7. Silva, A.M., Teixeira, J.H., Almeida, M.I., Goncalves, R.M., Barbosa, M.A., and Santos, S.G., Extracellular Vesicles: Immunomodulatory messengers in the context of tissue repair/regeneration. *Eur J Pharm Sci* 2017, **98**:86-95.
8. Bjorge, I.M., Kim, S.Y., Mano, J.F., Kalionis, B., and Chrzanowski, W., Extracellular vesicles, exosomes and shedding vesicles in regenerative medicine - a new paradigm for tissue repair. *Biomaterials Science* 2018.
9. Bian, S., Zhang, L., Duan, L., Wang, X., Min, Y., and Yu, H., Extracellular vesicles derived from human bone marrow mesenchymal stem cells promote angiogenesis in a rat myocardial infarction model. *J Mol Med (Berl)* 2014, **92**(4):387-97.
10. Arslan, F., Lai, R.C., Smeets, M.B., Akeroyd, L., Choo, A., Aguor, E.N., Timmers, L., van Rijen, H.V., Doevendans, P.A., Pasterkamp, G., Lim, S.K., and de Kleijn, D.P., Mesenchymal stem cell-derived exosomes increase ATP levels, decrease oxidative stress and activate PI3K/Akt pathway to enhance myocardial viability and prevent adverse remodeling after myocardial ischemia/reperfusion injury. *Stem Cell Res* 2013, **10**(3):301-12.
11. Drommelschmidt, K., Serdar, M., Bendix, I., Herz, J., Bertling, F., Prager, S., Keller, M., Ludwig, A.-K., Duhan, V., Radtke, S., de Miroschedji, K., Horn, P.A., van de Looij, Y., Giebel, B., and Felderhoff-Müser, U., Mesenchymal stem cell-derived extracellular vesicles ameliorate inflammation-induced preterm brain injury. *Brain, Behavior, and Immunity* 2017, **60**:220-232.
12. Lo Sicco, C., Reverberi, D., Balbi, C., Ulivi, V., Principi, E., Pascucci, L., Becherini, P., Bosco, M.C., Varesio, L., Franzin, C., Pozzobon, M., Cancedda, R., and Tasso, R., Mesenchymal Stem Cell-Derived Extracellular Vesicles as Mediators of Anti-Inflammatory Effects: Endorsement of Macrophage Polarization. *Stem Cells Translational Medicine* 2017, **6**(3):1018-1028.

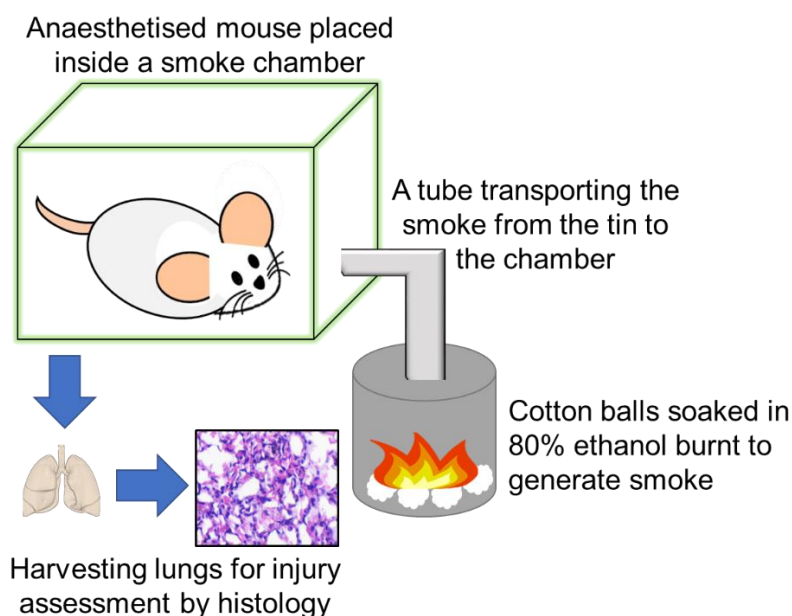
13. Shigemoto-Kuroda, T., Oh, J.Y., Kim, D.-k., Jeong, H.J., Park, S.Y., Lee, H.J., Park, J.W., Kim, T.W., An, S.Y., Prockop, D.J., and Lee, R.H., MSC-derived Extracellular Vesicles Attenuate Immune Responses in Two Autoimmune Murine Models: Type 1 Diabetes and Uveoretinitis. *Stem Cell Reports* 2017, **8**(5):1214-1225.
14. Yuana, Y., Sturk, A., and Nieuwland, R., Extracellular vesicles in physiological and pathological conditions. *Blood Reviews* 2013, **27**(1):31-39.
15. Fatima, F. and Nawaz, M., Nexus between extracellular vesicles, immunomodulation and tissue remodeling: for good or for bad? *Annals of Translational Medicine* 2017, **5**(6):139.
16. Giebel, B., On the function and heterogeneity of extracellular vesicles. *Annals of Translational Medicine* 2017, **5**(6):150.
17. Willms, E., Johansson, H.J., Mäger, I., Lee, Y., Blomberg, K.E.M., Sadik, M., Alaarg, A., Smith, C.I.E., Lehtiö, J., El Andaloussi, S., Wood, M.J.A., and Vader, P., Cells release subpopulations of exosomes with distinct molecular and biological properties. 2016, **6**:22519.
18. Khanal, D., Kondyurin, A., Hau, H., Knowles, J.C., Levinson, O., Ramzan, I., Fu, D., Marcott, C., and Chrzanowski, W., Biospectroscopy of Nanodiamond-Induced Alterations in Conformation of Intra- and Extracellular Proteins: A Nanoscale IR Study. *Analytical Chemistry* 2016, **88**(15):7530-7538.
19. Khanal, D., Zhang, B., Ramzan, I., Marcott, C., Li, Q., and Chrzanowski, W., Probing Chemical and Mechanical Nanodomains in Co-Polymer Nanorods with Correlative Atomic Force Microscopy - Nano-correscopy. *Particle and Particle Systems Characterization* 2018.
20. Quaroni, L., Pogoda, K., Zuber, J.-W., and Kwiatek, W., Mid-Infrared Spectroscopy and Microscopy of Subcellular Structures in Eukaryotic Cells with Atomic Force Microscopy-Infrared Spectroscopy. *arXiv preprint arXiv:1704.01395* 2017.
21. Qin, S.Q., Kusuma, G.D., Al-Sowayan, B., Pace, R.A., Isenmann, S., Pertile, M.D., Gronthos, S., Abumaree, M.H., Brennecke, S.P., and Kalionis, B., Establishment and characterization of fetal and maternal mesenchymal stem/stromal cell lines from the human term placenta. *Placenta* 2016, **39**:134-46.
22. Merck. *Extracellular Vesicle Protocol*. 2017 Accessed on 16/11/2017.
23. Science, I., *qEV Application Note: qEV Size Exclusion Column*. 2016, Izon Science Ltd: Oxford, UK.
24. Böing, A.N., van der Pol, E., Grootemaat, A.E., Coumans, F.A.W., Sturk, A., and Nieuwland, R., Single-step isolation of extracellular vesicles by size-exclusion chromatography. *Journal of Extracellular Vesicles* 2014, **3**:10.3402/jev.v3.23430.
25. Lobb, R.J., Becker, M., Wen Wen, S., Wong, C.S.F., Wiegmans, A.P., Leimgruber, A., and Möller, A., Optimized exosome isolation protocol for cell culture supernatant and human plasma. *Journal of Extracellular Vesicles* 2015, **4**:10.3402/jev.v4.27031.
26. Bobrie, A., Colombo, M., Krumeich, S., Raposo, G., and Thery, C., Diverse subpopulations of vesicles secreted by different intracellular mechanisms are present in exosome preparations obtained by differential ultracentrifugation. *J Extracell Vesicles* 2012, **1**.

27. Guang Choo, E.S., Tang, X., Sheng, Y., Shuter, B., and Xue, J., Controlled loading of superparamagnetic nanoparticles in fluorescent nanogels as effective T2-weighted MRI contrast agents. *Journal of Materials Chemistry* 2011, **21**(7):2310-2319.
28. Lin, S.-Y., Li, M.-J., and Cheng, W.-T., FT-IR and Raman vibrational microspectroscopies used for spectral bdiagnosis of human tissues. *Spectroscopy* 2007, **21**(1).
29. Lee, J., Wen, B., Carter, E.A., Combes, V., Grau, G.E.R., and Lay, P.A., Infrared spectroscopic characterization of monocytic microvesicles (microparticles) released upon lipopolysaccharide stimulation. *Faseb j* 2017, **31**(7):2817-2827.
30. Mihály, J., Deák, R., Szigyártó, I.C., Bóta, A., Beke-Somfai, T., and Varga, Z., Characterization of extracellular vesicles by IR spectroscopy: Fast and simple classification based on amide and CH stretching vibrations. *Biochimica et biophysica acta* 2017, **1859**(3):459-466.

6 The development of an *in vivo* smoke inhalation injury model

6.1 Overview

6.1.1 Graphical abstract



6.1.2 Highlights and keywords

- A smoke inhalation chamber was designed and fabricated in-house for mouse model of smoke inhalation injury.
- A successful injury model was verified by the inflammatory cells in the lungs of smoke-exposed mice.
- Further development of the smoke exposure regimen and assessment of injury would lead to broader use and application of this injury model to other studies.

Keywords: smoke inhalation, mouse model, lung injury, smoke chamber

Parts of the introduction section was published in:



Animal models of smoke inhalation injury and related acute and chronic lung diseases

Katarzyna Reczyńska^{a,b,1}, Priyanka Tharkar^{b,c,1}, Sally Yunsun Kim^{b,c,1}, Yiwei Wang^d, Elżbieta Pamuła^a, Hak-Kim Chan^b, Wojciech Chrzanowski^{b,c,*}

^a AGH University of Science and Technology, Faculty of Materials Science and Ceramics, Department of Biomaterials and Composites, Al. Mickiewicza 30, 30-059 Krakow, Poland

^b The University of Sydney, Faculty of Pharmacy, NSW 2006, Sydney, Australia

^c Australian Institute for Nanoscale Science and Technology, The University of Sydney, NSW 2006, Sydney, Australia

^d Burns Research Group, ANZAC Research Institute, Concord Hospital, The University of Sydney, Concord, NSW 2139, Australia

6.1.3 Abstract

Smoke inhalation injury leads to various acute and chronic lung diseases and thus is the dominant cause of fire-related fatalities. In a search for an effective treatment and validation of therapies, various animal models have been developed in literature. These models have advanced our understanding of the mechanism of smoke inhalation injury, enabling a better understanding of pathogenesis and pathophysiology and development of new therapies. In this study, a unique smoke inhalation chamber was designed and fabricated to induce smoke inhalation injury in mice. Histology analysis revealed that the smoke inhalation injury caused in mice using a 5-min exposure had mimicked the injury observed in literature and included the features of the injury observed in human. Further development of this in-house smoke inhalation chamber is likely of versatile use for other related studies.

In addition to the overview of the newly developed smoke inhalation injury model, this chapter also includes the discussion of the advantages and disadvantages of using mice for modelling smoke inhalation injury. All animal models have their limitations in replicating complex clinical conditions associated with smoke inhalation injury in humans. Therefore, for a correct interpretation of the results and to avoid bias, a precise understanding of similarities and differences of lungs between different animal species and humans is critical.

6.2 Introduction

6.2.1 Small animal models of smoke inhalation injury

Challenges in mimicking human response in small animal models are inevitable due to the vast differences in the lung anatomy (Fig. 6.1A,B) and airway structures (Table 6.1). All animals including mice have the same number of lobes in each lung (four lobes in the right lung and three lobes in the left lung) while the human lung has three lobes in the right lung and two lobes in the left lung. Small animals are more susceptible to inhaled toxicants due to their greater respiratory minute volume and respiratory surface area per unit body weight¹. For example,

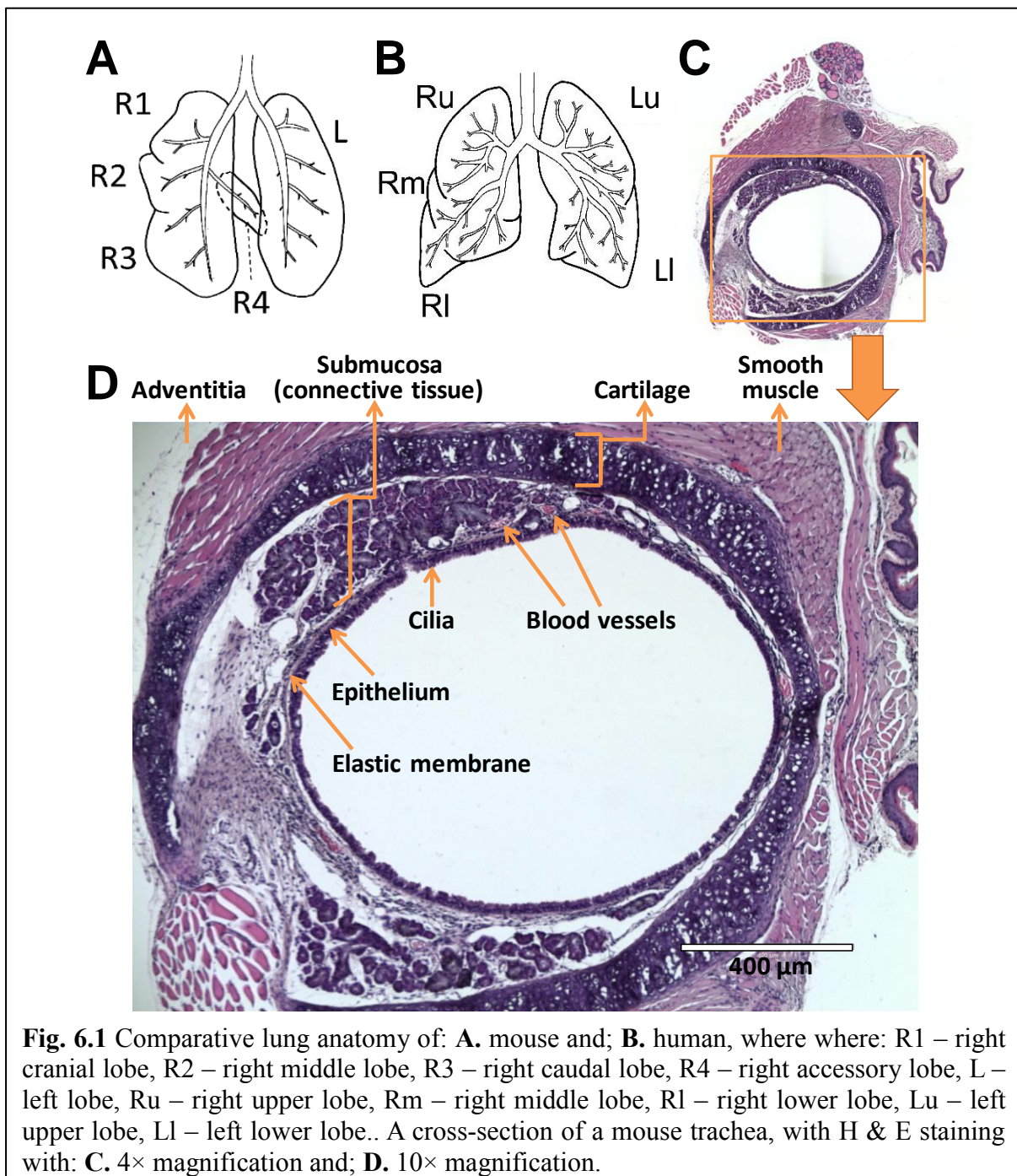


Table 6.1 Comparison of the characteristics of mouse and human lungs: features of pleura, lobation, tracheobronchial branching patterns and properties of distal airways.

	Body mass (kg)	Tidal volume (ml)	Characteristics of pleura and interlobular tissue	Lung segmentation/lobation	Typical number of branches to terminal bronchioles	Bifurcation pattern	Presence of respiratory bronchioles (RB)
Mouse	0.02-0.04	0.15	Thin pleura, with little interlobular tissue ²	5 lobes: 1 lobe in the left lung and 4 lobes in the right lung ^{3,4}	13-17	Monopodial, very sharp and very high throughout the lung ^{3,4}	Absent
Human	70	500	Thick pleura, extensive interlobular connective tissue, almost complete interlobular separation ⁵	Right lung: 3 lobes (upper, middle, lower) Left lung: 2 lobes (upper, lower) ⁶	14-17	Relatively symmetric and dichotomous branching ^{3,6}	Several (3-5) generations of RB ^{3,5}

the diameter of mouse trachea is approximately 1.2 mm, while human trachea is around 16 mm, therefore the surface area available and the contact time for absorption of toxicants in mice epithelia is by far greater compared to that of human. The mouse pleura is thin, unlike the human lung, yet strong enough to be inflated to considerably higher pressures around 30 cm H₂O (Table 6.1). There are distinct features such as large number of non-ciliated, Clara-like cells in the tracheal epithelia that contribute to the differences in the responses to smoke inhalation injury (Fig. 6.1C,D and Fig. 6.2). The epithelial cells are ciliated but not as uniform as in humans (Fig. 6.2). Goblet cells are absent in rodents and thus have a weak metaplastic response compared to larger animals or humans. This is relevant in considering models for smoke inhalation injury of humans through chronic exposure to solid fuel smoke at homes because those individuals are at higher risk of developing COPD⁷⁻⁹ and goblet cell metaplasia is a characteristic feature in the small airways of humans with COPD.

The severity of smoke inhalation injury is related to many factors such as the temperature of smoke, physical and chemical composition of the smoke (gas, particle, and vapor), contact area (depth of breath), and contact time (time exposed to smoke). The smoke can be equilibrated to an ambient temperature to eliminate the influence of thermal injury to the airway. The severity of injury in an impulsively breathing animal is also affected by hyperventilation as a reaction to the carbon monoxide content of the smoke. Therefore, the smoke exposure can be done under general anaesthesia to prevent changes in the depth of breath that directly affect contact area of airway with the smoke¹⁰.

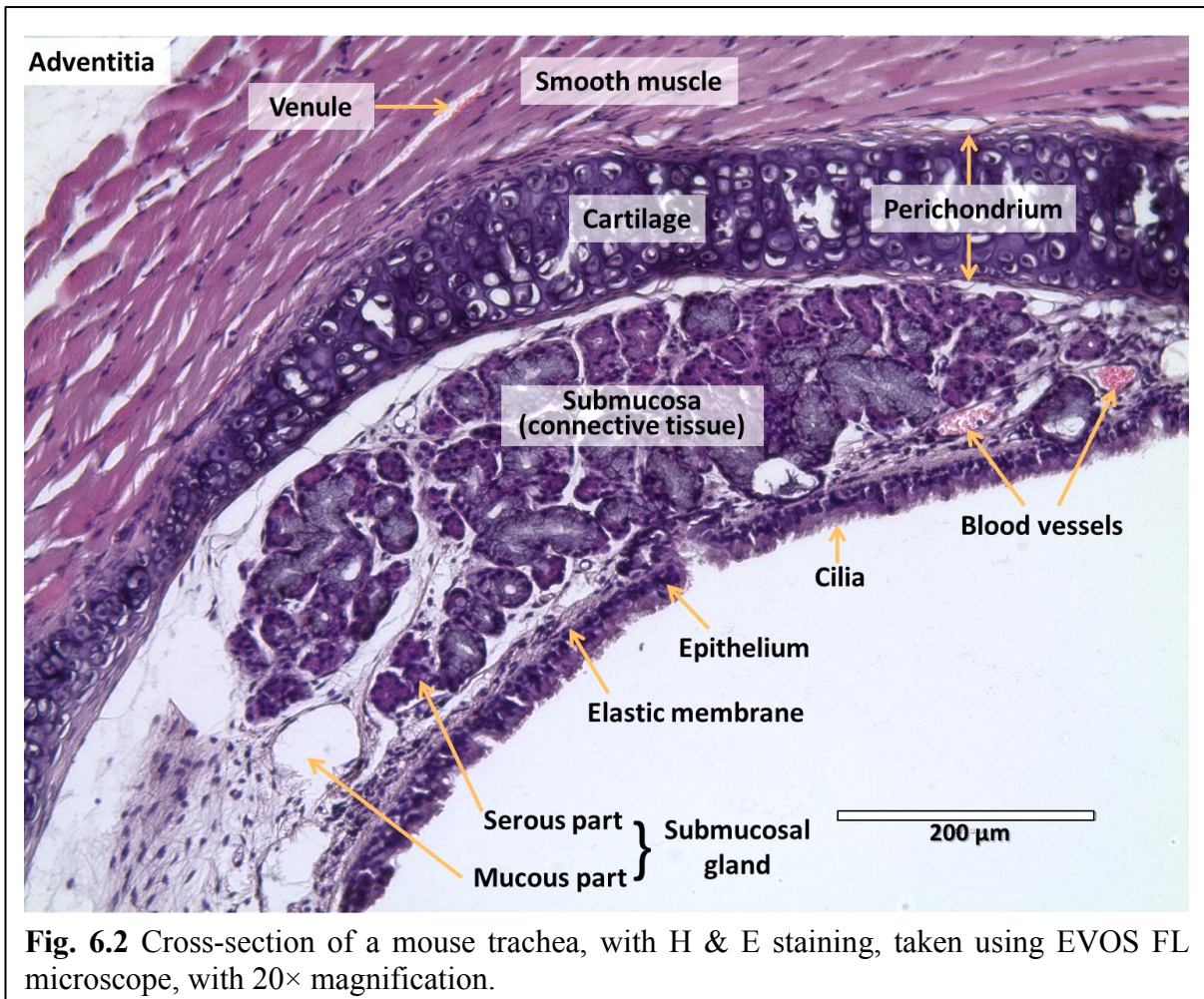


Fig. 6.2 Cross-section of a mouse trachea, with H & E staining, taken using EVOS FL microscope, with 20× magnification.

While the smoke inhalation injury in large animals is produced by directly delivering smoke into the lungs through an endotracheal tube, in smaller animals, they are placed in closed chambers where they spontaneously inhale smoke¹¹. In many studies, investigators have designed self-made smoke generators with some common features. The delivery time of smoke and the material-burning rate can be controlled and the smoke generators can be easily equipped with other devices. Some smoke chambers for rodents possess additional vent which can eject smoke into the lung of large animals and can be used to cause smoke inhalation injury in large animals¹¹.

6.2.2 An overview of currently used smoke inhalation injury models

The clinical manifestations of smoke inhalation injury in small animals differ depending on the animal species. In mice, the absence of bronchial mucus glands limits the amount of mucus in the obstructive material¹². Rats display increased respiratory rate and hyperpnoea immediately after smoke inhalation injury, before gradual reduction in respiratory rate and occurrence of dyspnoea¹³. In late stages, rats present with increased oronasal secretions, mouth breathing, and

wheezing¹³. The main findings of arterial blood gas include decreased pH, partial pressure of oxygen and significantly increased partial pressure of carbon dioxide. Metabolic acidosis occurs in the early stages after smoke inhalation injury, while metabolic acidosis combined with respiratory acidosis occurs in the later stages.

One of the advantages in small animal models is relatively easy histopathological analyses at different time points. Histology of rat lung performed at 6 h post-injury revealed tracheal mucosa with congestion, oedema, necrosis and exfoliation, lung tissues with congestion, swelling and haemorrhages, while the alveolar spaces were filled with oedematous fluid and some red blood cells¹³. The materials that have been used in small animal models of smoke inhalation injury include wood^{14, 15}, sawdust mixed with kerosene¹³, cotton^{12, 16-18} and flexible polyurethane foam¹⁹. High mortality rates are observed in small animals in smoke inhalation due to carbon monoxide poisoning and hypoxia. Since kerosene assists combustion and reduce the concentration of carbon monoxide and aldehydes in smoke, it has been shown to increase survival rates in rat models¹³. Therefore, the addition of kerosene to the combustion materials is recommended for studies designed to observe toxicity caused by smoke compositions other than carbon monoxide.

Since rodents are obligatory nose breathers and they have very complex and highly developed nasal turbinates which are different to human, it is unavoidable to have deposition patterns of smoke different to humans. Animals when exposed to smoke and forced to inhale smoke; it changes their breathing pattern, and avoidance reactions can occur. The shallow breathing patterns in animals are different from the active smoke inhalation by humans, in the case of cigarette smoking. The recurrent exposure of rodents to high doses of cigarette smoke leads to weight loss which can make the interpretation of data complicated. So far, there is no perfect exposure system for laboratory animals. Nose only smoke systems require extensive handling, and it can cause restraint of the animals which leads to stress in the animal. Whole-body exposures to smoke can also cause deposition of smoke particles on the pelt and can induce oral inhalation *via* grooming²⁰.

Methods to assess inhalation injury in small animals

The most common methods used to assess inhalation injury in mice are the analysis of blood gases, bronchoalveolar lavage, histopathology and measurement of lung wet-to-dry weight ratio post injury at different time point, depending on the research questions of the studies. Blood gas analysis is performed by analysing carboxyhemoglobin (COHb), partial pressures

of oxygen (PaO₂), and carbon dioxide (PaCO₂) and pH in the animal blood sample. These parameters are checked after smoke inhalation, and blood gas analysis is performed with the help of blood gas analysers^{12, 21, 22}. Bronchioalveolar lavage fluid (BALF) is usually collected from lung after 48 h of injury by installing cold normal saline intratracheally and withdrawing after 30 s. This procedure is repeated a few times. The collected BALF is then analysed by total cell counts, performed with a hemocytometer. BALF is then centrifuged at 4°C, 1000 rpm for 10 min. The supernatant can be stored at -70°C until use for total protein concentration which can be determined by using Lowry's method. It can also be determined by protein assay kit and bicinchoninic acid method is used to assess lung vascular permeability of lung^{22, 23}. For performing lung histological studies, lung tissues are harvested 48 h after the injury. Firstly, the lungs can be infused through the airway with 1.4 ml of 10% phosphate-buffered formalin, then paraffin-embedded, followed by sectioning (4-6 µm), and finally stained with hematoxylin and eosin for examination under the light microscope. All the samples are then analysed and scored for histological changes by a pathologist^{12, 21-23}. Depending on the aim of the study other assessments including the measurement of lung myeloperoxidase (MPO) activity to quantify of neutrophils in the lungs^{12, 22, 23} and plasma nitric oxide levels in the injured mice lung can be performed¹². Concentrations of interleukin (IL)-8, tumour necrosis factor- α (TNF- α), surfactant protein A, and surfactant protein D in BALF can be detected using ELISA²². For the measurement of lung wet-to-dry weight ratio after the smoke exposure, lung tissues were collected, cleaned to remove other contaminants and weighed. The lungs tissues are then dried at 65-70°C for 48-72 h in an oven, and dry weights are measured to calculate the ratio^{12, 24}.

6.2.3 The development of a smoke inhalation injury model in mice

Selected mouse models for smoke inhalation studies using various smoke inhalation chambers have been summarised in this section (Table 6.2). Matthew *et al.* used a smoke chamber which comprised of an incinerator, a fan for smoke circulation, and an inhalation chamber where mice can be housed for smoke exposure²¹. The amount of heat generated was regulated by the adjustable power supply, and the rate of combustion was monitored. A fan with adjustable speed was connected to the inlet of the incinerator to circulate the smoke through the inhalation chamber in the closed system to adjust the rate of smoke exposure to the animals. Animals were anaesthetised and placed inside the inhalation chamber and exposed to untreated pine lumber smoke and when the incinerator filled with smoke, the fan was turned on to circulate the smoke into the chamber. After 12-15 min exposure the mice were removed, and allowed to awaken from the anaesthesia. This model mimics some features of human smoke inhalation

injury, including cytoplasmic blebbing, cytoplasmic vacuolisation, type II cell hypertrophysloughing, oedema, haemorrhage, lymphocyte infiltration and macrophage infiltration. The BALF of mice with smoke inhalation injuries demonstrated a significant increase in total cell counts compared with those in control mice. The lung tissue response observed in human victims of smoke inhalation are comparable to these findings²¹.

Table 6.2 Summary of selected mouse models used in smoke inhalation injury.

Animal type / strain	Material burnt for creating smoke	Time of exposure to smoke	Assessment of injury after harvesting the injured lung <i>ex vivo</i>	Treatment of smoke inhalation injury (if used)	Ref.
Female C57BL/6 mice	Cool cotton smoke	Two 30 s exposures	<ul style="list-style-type: none"> • Histology • Lung wet/dry ratio • Myeloperoxidase activity • NOS activity • Pulmonary gas exchange 	N/A	12
Male C57BL/6 mice	Cotton smoke	15 min	<ul style="list-style-type: none"> • Assessment of mucus by histology • Quantitative analysis based on the percentage of PAS-positive cells • Pathology scoring • Immunohistochemistry: MUC5AC • qRT-PCR: total RNA • Immunofluorescence pJNK 	After one hour of smoke exposure, animals received an injection of JNK inhibitor subcutaneously	18
Mice Balb/C & C57BL/6	Cooled cotton smoke	4 × 30 s for Balb/C or 2 × 30 s for C57BL/6	<ul style="list-style-type: none"> • Lung wet/dry weight ratio • Lung myeloperoxidase activity using an EIA kit 	N/A	25
Female CD-1 mice	Wood	12 to 20 min exposure	<ul style="list-style-type: none"> • COHb measurements • Lung pathology • Bronchoalveolar lavage (BAL) • TNF-α measurements 	N/A	21
CFW male mice	Flexible polyurethane foam placed into an oven tube preheated to 400°C	Mice were exposed for 30 min	<ul style="list-style-type: none"> • Bronchoalveolar lavage (BAL) • Electron microscopy • Histology 	N/A	19

A custom endotracheal tube was made by Mizutani, *et al.* to deliver smoke directly to the mouse airway upon intubation¹². The aim of this study was to develop a murine model of combined burn and smoke inhalation injury to reveal the exact mechanistic aspects of pathological changes. The in-house smoker device was filled with 20 g of burning cotton towelling, and it was connected to the tubing which provided a constant flow of air. In this model, a condenser coil (copper) was used reduce the temperature of hot smoke to eliminate the possibility of injury

induced by temperature. The intubation process for smoke inhalation offers some advantages to create smoke inhalation injury to animals. Firstly, it reduced the possibility of laryngospasm during the smoke inhalation process in animals. Secondly, it can be assured that the smoke was the primary cause of lung injury; and lastly, the delivery of cooled smoke first into the trachea and then into the lung ensured that pathophysiological changes were caused in response to irritants present in the smoke. This model can be advantageous in exploring various mechanistic aspects underlying cardiopulmonary morbidity in addition to burn trauma with association to smoke inhalation injury.

In a study by Jacob *et al.*, a custom-built miniature smoke generator was used for smoldering cotton toweling and kept burning by a regulated flow of air (1 mL/sec). Smoke was cooled to 25°C from 35°C with the help of copper cooling coil and was conveyed through plastic tubing to the Y-connector attached to the endotracheal tube at near atmospheric pressure. It was attached to the smoke generation chamber with pressurised air and flow meter source to regulate the flow and density of smoke emerging into the Y-tube. Mice were allowed to breathe normally during the smoke exposure. Balb/C mice were exposed to four 30 sec intervals of smoke inhalation initially, but it was observed that the regimen caused an unacceptably high mortality rate due to postexposure apnoea. Therefore, two sets of 30 sec smoke exposure were given to Balb/C and C57BL/6 mice with exposure to ambient air between the smoke exposure intervals. Minute ventilation average was calculated subsequently and the injury was followed by 48 h of reaction and recovery period. These mice showed the features of pulmonary vascular leakage, congestion, oedema and sequestration of neutrophils in the lung. The strength of this study is that it provides a background for studies of the roles of neuropeptides in smoke and burn injury. It has been indicated in this study that the mouse model provides a useful platform for studying pathophysiology of inflammation ARDS as a result of combined smoke and burn injury²⁵.

A mouse model of acute lung injury is well established in combination of burn and smoke inhalation injury, with animals meeting the criteria for diagnosis within 48 h¹².

6.3 Materials and Methods

6.3.1 Designing a smoke inhalation chamber

A 'Single Use Mouse Cage' was purchased from Tecniplast Australia Pty Ltd (Rydalmere NSW Australia) and modified to fit tubes for smoke to go in from the bottom of the cage and out through the top (Fig. 6.3A). The tube drawing smoke out of the chamber was connected to an exhaust pump (Fig. 6.4A) however the vacuum pump was not used after the initial trial

without mice, as it was taking away too much smoke out of the chamber. A snack tin was modified with a mesh to hold the cotton and holes on the side of the tin to ensure oxygen flow to maintain the fire inside the tin, while the lid is kept tightly closed to minimise leakage of smoke (Fig. 6.3B). The tube connecting the tin and the cage was tightly fitted onto using a seal. The smoke chamber was deliberately not sealed completely; no parafilm was used and filter paper was used to cover the hole, in place of a water cup blocking the chamber during its normal use of the cage. Cotton balls were wet in 80% ethanol before ignition of fire and cotton balls were refilled as needed to maintain a constant production of smoke.

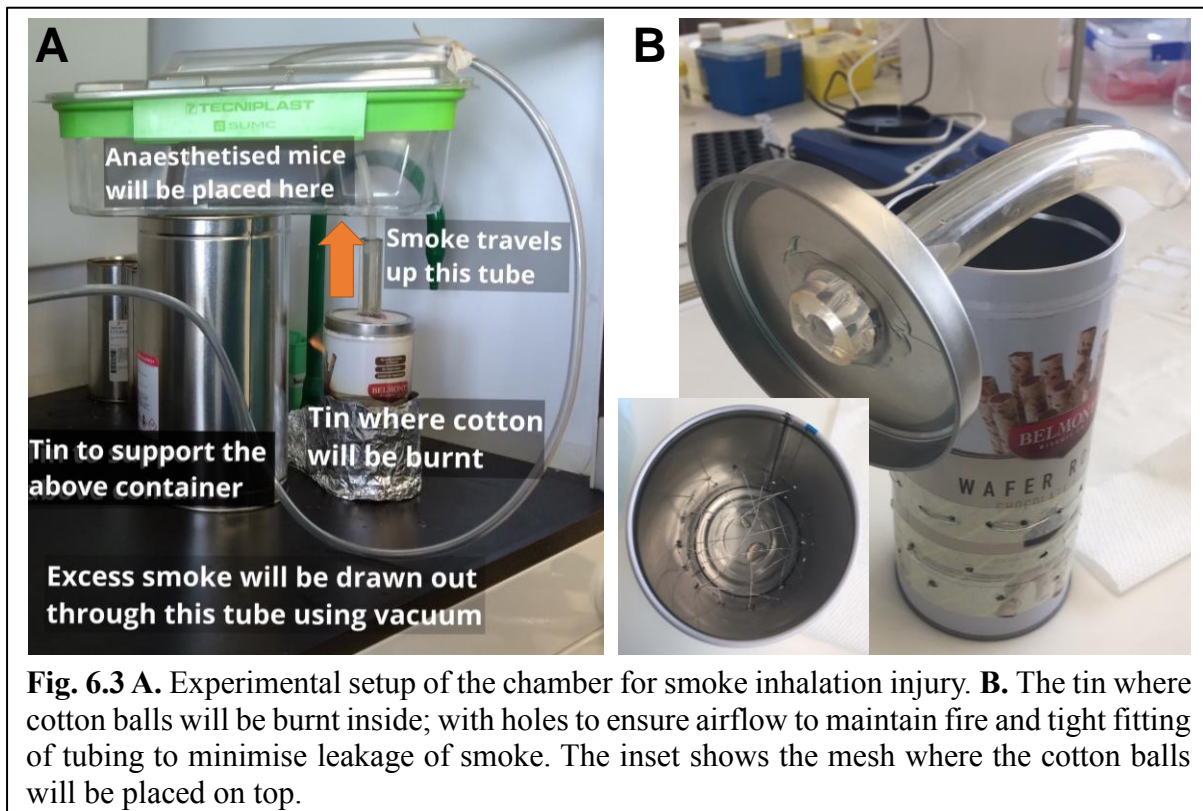


Fig. 6.3 **A.** Experimental setup of the chamber for smoke inhalation injury. **B.** The tin where cotton balls will be burnt inside; with holes to ensure airflow to maintain fire and tight fitting of tubing to minimise leakage of smoke. The inset shows the mesh where the cotton balls will be placed on top.

6.3.2 Smoke inhalation injury regimen in mice

As a pilot study, six Balb/c mice were anaesthetised using ketamine prior to exposure to smoke inhalation using various smoke inhalation regimens as below (n = 1 to 2 per condition). One mouse unfortunately died immediately after anaesthesia, therefore only five mice were used:

- *Mouse 1*: Mild smoke for 1 min (time of exposure started before the chamber is evidently filled with smoke)
- *Mouse 2*: Moderate smoke for 5 min (3 min of smoke actively infusing then 2 min inhalation of pre-filled smoke)
- *Mouse 3*: Moderate smoke for 2 min then rest (out of the smoke chamber) for 10 min then another 2 min of moderate smoke

- *Mouse 4*: Moderate-strong smoke for 2 min with nose right at the tube where smoke was being infused into the chamber
- *Mouse 5*: A repeat of the regimen for Mouse 3

6.3.3 Histology of lung slices

For the assessment of injury, mice were anaesthetised after 24 h and the lungs were harvested and processed for histology, using the previously established methodology described in detail in 2.3.7. Briefly, fixed in 10% formalin was passed through the tissue sample by gravity then incubated in 10% formalin at room temperature for 24 h. Left and right lung lobes to be separated then inserted into tissue processor, for separate paraffin embedding then sectioning by microtome (5 μ m). Standard protocols were used for haematoxylin and eosin staining (section 2.3.7).

6.4 Results and Discussion

The objective of this study was to determine whether our own in-house experimental setup of the smoke inhalation chamber is effective in inducing lung injury detectable by histology. Of the five mice exposed to various degrees of smoke inhalation, Mouse 1 – 4 survived after the smoke inhalation (Fig. 6.4). Mice woke up after the anaesthesia, however breathing looked abnormal, which indicated injury was induced in their lungs or airways. Mouse 5 was a repeat of the regimen used for Mouse 3 but it died without recovering after the second smoke exposure. Nevertheless, Mouse 3 survived until the end of the pilot study. After the smoke inhalation injury, none of the mice appeared to have normal breathing as before the injury. By assessing their breathing pattern, Mouse 2 was chosen to trial histology to assess whether the inhalation injury occurred through the exposure to smoke.

Histology revealed that the smoke inhalation injury (3 min of smoke actively infusing then 2 min inhalation of pre-filled smoke) caused slight broadening of alveolar septa and increased

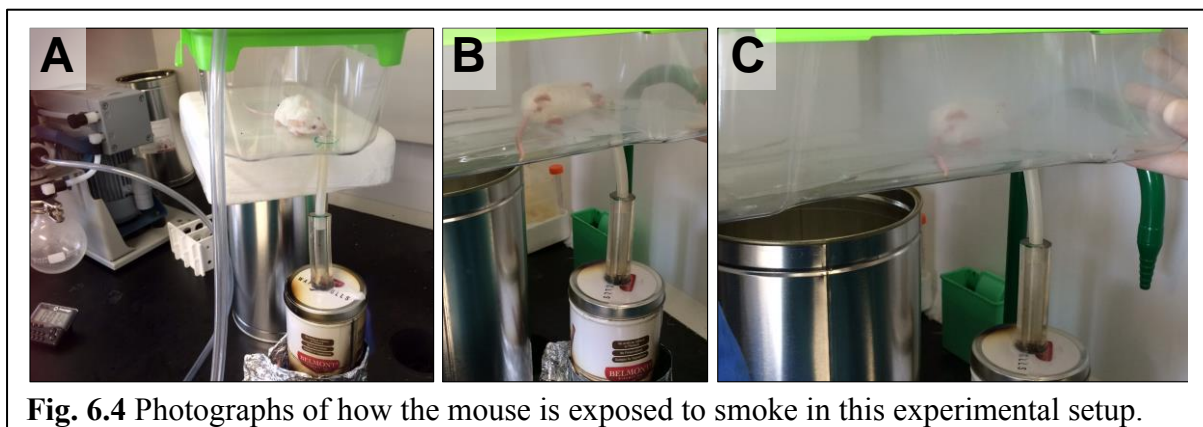
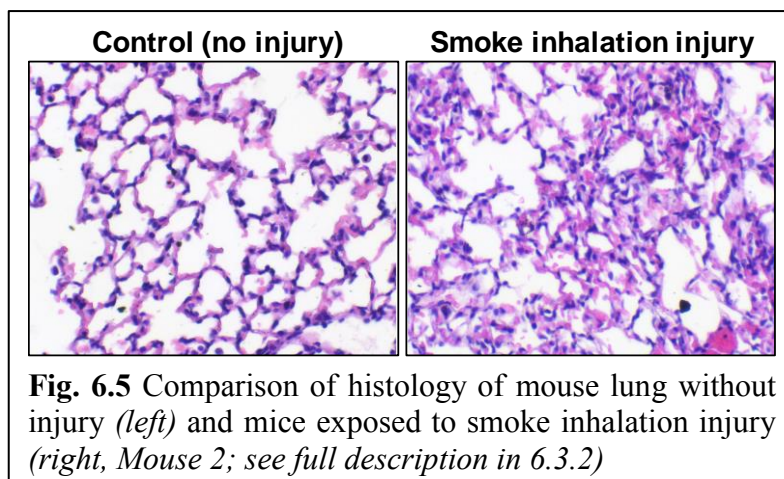


Fig. 6.4 Photographs of how the mouse is exposed to smoke in this experimental setup.

infiltration of inflammatory cells in alveolar cavities (Fig. 6.5). Extensive exudation and shrinking of alveoli were suspected to be caused by pressure. Septa haemorrhage were observed from the enlarged blood vessels and necrotic lesions with ruptured elastic



fibre of alveolar wall were observed. This result confirmed that the smoke inhalation for 5 min in our in-house smoke inhalation chamber evidently caused lung injury in mice.

Advantages of using mouse model of smoke inhalation injury

Mice have many advantages over other laboratory animals. Their genetic material is similar to the human genetic material (99%)²⁶, thus it provides an excellent molecular/genetic toolbox for the pharmaceutical and pharmacological studies²⁷. Their small size makes it manageable to carry out large scale/high throughput studies, and it is also cost-effective. The immune system in the mouse is very well understood. The vast array of species-specific reagents is currently available for mice (i.e. antibodies, siRNA, other genomic probes)²⁷, whereas other laboratory animals lack them to a great extent. They have well-characterised genome and mice have the abundance of genetically modified species that can be used to investigate the physiological function of specific genes. Therefore, robust conclusions can be drawn about the role of specific genes. Moreover, they are cheaper compared to other laboratory animals²⁸. Despite some limitations, the mice model of smoke inhalation injury similarly reflects the overall injury and mortality seen in human patients. It can be useful to explain the mechanisms of smoke inhalation lung injury and for the development of new treatment strategies. The genetically modified mice and the availability of different antibodies enhance the importance of the mice as a model for burn and smoke inhalation injury²¹.

For testing certain treatments to alleviate symptoms after smoke inhalation injury, for example with synthetic peptides or thioaptomers, small animals are the most suitable model because the cost of these interventions becomes prohibitive in large animals²⁵. Mice can be employed for this purpose as they are inexpensive and easy to handle as compared to large animals. It has been demonstrated that there are significant differences in pulmonary responses to noxious chemicals amongst different species and strain differences in mice. The commonly used strain

of genetically modified mice (C57BL/6) is comparatively less sensitive to acute lung injury and non-specific airway stimuli compared with other inbred strains. A study of eight inbred strains including Balb/C and C57BL/6 mice demonstrated the differences in vascular permeability to plasma proteins, indicating the presence of genetic sensitivity to lung injury²⁵. Overall, the mice models of smoke inhalation injury were demonstrated in numerous studies to be beneficial for studying the mechanisms responsible for acute lung injury.

6.5 Limitations and disadvantages

This study was a small pilot study (n = 1) to determine the feasibility of the in-house smoke inhalation chamber to obtain an injury model. The various regimens of smoke inhalation injury were used merely to observe breathing patterns and whether the dosages of smoke were lethal or not. In terms of animal species used, while rodents are the most commonly used model animals in smoke inhalation injury studies, it is well known that they have several limitations over large animals. The main reason for this is because of their differences in lung macrostructure and microstructure to human and strain differences in disease susceptibility as discussed in the introduction section.

Disadvantages of using mouse model of smoke inhalation injury

Mice are obligate nose breathers, but greater proportion of drug/smoke reaches the airways if inhaled through the mouth in humans²⁹. Only a limited volume of blood can be collected at a time due to their small size. The small size can also cause some difficulties with handling and parameters like arterial oxygen tension and mean arterial pressure are relatively difficult to monitor³⁰. It is also hard to do measurements of respiratory signals of flow, volume and trans-pulmonary pressure, unless an animal exposure chamber with plethysmography is used. With the advent of this technique continuous on-line recording of tidal flow patterns during exhalation in conscious mice can be recorded³¹.

One of the prominent features of clinical smoke inhalation injury is widespread obstruction of airways. However, in mice, the presence of obstructive material cannot be considered as a contributing factor since mice do not possess bronchial mucous glands and goblet cells¹². Thus, the amount of mucus in the obstructive material in mice is limited compared to the ovine model of smoke inhalation injury where obstructing material is present. Smoke inhalation injuries increase the risk of pneumonia and ARDS. However, it is very challenging to study pneumonia in mice. In the case of pneumonia caused by bacterial infections, the titration of the bacteria can often be difficult in achieving the desired levels of infection, as it can induce unintended

mortalities during the study. The observed outcomes vary greatly depending on the different strains of bacteria and thus it is difficult to predict the outcomes from other strains. Additionally, the suitability to induce smoke inhalation injury in different strains of mice can vary because of their different genetic components³².

6.6 Conclusions and future work

An in-house smoke inhalation chamber was designed successfully to induce lung injury that mimics the smoke inhalation injury in the literature as observed by histology. The features of the injury induced in our model reflect the injuries that have been observed in human patients. For future work, the following points are recommended:

- Assess the injury using more superior tests in other studies as mentioned in this chapter, such as bronchoalveolar lavage fluid analysis.
- Power calculations and increased number of mice to ensure statistical significance of the results.
- Design studies that enable the development of new improved treatment strategies for smoke inhalation injury, including the testing of cell-based therapy.
- Determine whether continuous exposure of smoke inhalation and/or repeated dosages of treatments to alleviate the injury are more effective in modelling the injury and/or tissue repair.

6.7 References

1. Stec, A.A. and Hull, T.R., Part II: Harmful effects of fire effluents, in *Fire Toxicity*, A.A. Stec and T.R. Hull, Editors. 2010, Elsevier Science.
2. Maynard, R.L., Comparative Biology of the Normal Lung (treatise on pulmonary toxicology, volume 1). *Occupational and Environmental Medicine* 1995, **52**(11):783-783.
3. Phalen, R.F. and Oldham, M.J., Tracheobronchial airway structure as revealed by casting techniques. *Am Rev Respir Dis* 1983, **128**(2 Pt 2):S1-4.
4. Kling, M.A., A Review of Respiratory System Anatomy, Physiology, and Disease in the Mouse, Rat, Hamster, and Gerbil. *Veterinary Clinics of North America: Exotic Animal Practice* 2011, **14**(2):287-337.
5. Parent, R.A., Comparative biology of the normal lung. 2015: Academic Press.
6. Patra, A.L., Comparative anatomy of mammalian respiratory tracts: the nasopharyngeal region and the tracheobronchial region. *Journal of Toxicology and Environmental Health, Part A Current Issues* 1986, **17**(2-3):163-174.
7. Po, J.Y., FitzGerald, J.M., and Carlsten, C., Respiratory disease associated with solid biomass fuel exposure in rural women and children: systematic review and meta-analysis. *Thorax* 2011, **66**(3):232-9.
8. Kurmi, O.P., Semple, S., Simkhada, P., Smith, W.C., and Ayres, J.G., COPD and chronic bronchitis risk of indoor air pollution from solid fuel: a systematic review and meta-analysis. *Thorax* 2010, **65**(3):221-8.
9. Hu, G., Zhou, Y., Tian, J., Yao, W., Li, J., Li, B., and Ran, P., Risk of COPD from exposure to biomass smoke: a metaanalysis. *Chest* 2010, **138**(1):20-31.
10. Shimazu, T., Yukioka, T., Hubbard, G.B., Langlinais, P.C., Mason, A.D., and Pruitt, B.A., A dose-responsive model of smoke inhalation injury. Severity-related alteration in cardiopulmonary function. *Annals of Surgery* 1987, **206**(1):89-98.
11. Zhu, F., Qiu, X., Wang, J., Jin, Y., Sun, Y., Lv, T., and Xia, Z., A rat model of smoke inhalation injury. *Inhal Toxicol* 2012, **24**(6):356-64.
12. Mizutani, A., Enkhbaatar, P., Esehie, A., Traber, L.D., Cox, R.A., Hawkins, H.K., Deyo, D.J., Murakami, K., Noguchi, T., and Traber, D.L., Pulmonary changes in a mouse model of combined burn and smoke inhalation-induced injury. *J Appl Physiol (1985)* 2008, **105**(2):678-84.
13. Xie, E.F., Yang, Z.C., Wang, D., Fu, Q.F., and Wei, J.J., A rat model of smoke inhalation injury. *Annals of Burns and Fire Disasters* 1998, **11**(2).
14. Matthew, E., Warden, G., and Dedman, J., A murine model of smoke inhalation. *American Journal of Physiology - Lung Cellular and Molecular Physiology* 2001, **280**(4):L716-L723.
15. Zhu, F., Qiu, X., Wang, J., Jin, Y., Sun, Y., Lv, T., and Xia, Z., A rat model of smoke inhalation injury. *Inhalation Toxicology* 2012, **24**(6):356-364.
16. Jacob, S., Deyo, D.J., Cox, R.A., Traber, D.L., and Hawkins, H.K., Assessment of lung inflammation in a mouse model of smoke inhalation and burn injury: strain-specific differences. *Toxicol Mech Methods* 2008, **18**(7):551-9.

17. Jacob, S., Deyo, D.J., Cox, R.A., Traber, D.L., Herndon, D.N., and Hawkins, H.K., Mechanisms of toxic smoke inhalation and burn injury: role of neutral endopeptidase and vascular leakage in mice. *Toxicol Mech Methods* 2009, **19**(3):191-6.
18. Choi, W., II, Syrkina, O., Kwon, K.Y., Quinn, D.A., and Hales, C.A., JNK activation is responsible for mucus overproduction in smoke inhalation injury. *Respiratory Research* 2010, **11**(1):172-172.
19. Moores, H.K., Janigan, D.T., and Hajela, R.P., Lung Injury after Experimental Smoke Inhalation: Particle-Associated Changes in Alveolar Macrophages. *Toxicologic Pathology* 1993, **21**(6):521-527.
20. Hecht, S.S., Carcinogenicity studies of inhaled cigarette smoke in laboratory animals: old and new. *Carcinogenesis* 2005, **26**(9):1488-92.
21. Matthew, E., Warden, G., and Dedman, J., A murine model of smoke inhalation. *Am J Physiol Lung Cell Mol Physiol* 2001, **280**(4):L716-23.
22. Sun, Y., Qiu, X., Wu, G., Wang, J., Li, J., Tang, H., and Xia, Z., The effects of porcine pulmonary surfactant on smoke inhalation injury. *Journal of Surgical Research* 2015, **198**(1):200-207.
23. Zhang, F., Wang, Z., Li, M., Lan, Y., Chen, Y., and Wang, C., Puerarin attenuates smoke inhalation injury by regulation of Th1/Th2 expression and inhibition of Th17 cells in rats. *International Immunopharmacology* 2015, **28**(1):546-553.
24. Song, M., Lv, Q., Zhang, X., Cao, J., Sun, S., Xiao, P., Hou, S., Ding, H., Liu, Z., Dong, W., Wang, J., Wang, X., Sun, Z., Tian, M., and Fan, H., Dynamic Tracking Human Mesenchymal Stem Cells Tropism following Smoke Inhalation Injury in NOD/SCID Mice. *Stem Cells International* 2016, **2016**:13.
25. Jacob, S., Deyo, D.J., Cox, R.A., Traber, D.L., and Hawkins, H.K., Assessment of Lung Inflammation in a Mouse Model of Smoke Inhalation and Burn Injury: Strain-Specific Differences. *Toxicology Mechanisms and Methods* 2008, **18**(7):551-559.
26. Peters, L.L., Robledo, R.F., Bult, C.J., Churchill, G.A., Paigen, B.J., and Svenson, K.L., The mouse as a model for human biology: a resource guide for complex trait analysis. *Nat Rev Genet* 2007, **8**(1):58-69.
27. Flint, J. and Eskin, E., Genome-wide association studies in mice. *Nature reviews. Genetics* 2012, **13**(11):807-817.
28. Irvin, C.G. and Bates, J.H.T., Measuring the lung function in the mouse: the challenge of size. *Respiratory Research* 2003, **4**(1):4-4.
29. Meeusen, E.N., Snibson, K.J., Hirst, S.J., and Bischof, R.J., Sheep as a model species for the study and treatment of human asthma and other respiratory diseases. *Drug Discovery Today: Disease Models* 2009, **6**(4):101-106.
30. Matute-Bello, G., Frevert, C.W., and Martin, T.R., Animal models of acute lung injury. *American Journal of Physiology - Lung Cellular and Molecular Physiology* 2008, **295**(3):L379-L399.
31. Lim, R., Zavou, M.J., Milton, P.-L., Chan, S.T., Tan, J.L., Dickinson, H., Murphy, S.V., Jenkin, G., and Wallace, E.M., Measuring Respiratory Function in Mice Using

Unrestrained Whole-body Plethysmography. *Journal of Visualized Experiments : JoVE* 2014(90):51755.

32. Pouwels, S.D., Heijink, I.H., Brouwer, U., Gras, R., den Boef, L.E., Boezen, H.M., Korstanje, R., van Oosterhout, A.J.M., and Nawijn, M.C., Genetic variation associates with susceptibility for cigarette smoke-induced neutrophilia in mice. *American Journal of Physiology - Lung Cellular and Molecular Physiology* 2015, **308**(7):L693-L709.

7 Summary, outcomes and future directions

7.1 Research significance

7.1.1 Summary

My thesis focused on the development of a unique stem cell-based therapy for potential treatment of lung injury using a direct pulmonary delivery. The initial research question was whether it was feasible to atomise stem cells for direct airway delivery to enhance the effectiveness of stem cell therapy for lung injury. Upon successful completion and validation of the **cell spraying technology**, cells were encapsulated in a **bioactive hydrogel platform** which was verified also as being sprayable for direct pulmonary delivery. The focus of the project then moved onto **stem cell-derived extracellular vesicles (EVs)**, as they carry molecular signals for the therapeutic benefits of stem cells. Following isolation and characterisation of EVs from decidual mesenchymal stromal cell line (DMSC23), EVs were atomised for direct pulmonary delivery for the first time. The potential lung repair and regenerative mechanisms were identified by microRNA profiling of stem cells and EVs. An innovative characterisation methodology was developed for the **molecular and structural composition of EVs** using atomic force microscope infrared spectroscopy (AFM-IR). An **in-house smoke inhalation chamber** was designed successfully to establish a mouse model of lung injury.

7.1.2 Key findings and conclusions

- A cell spraying process was established using a commercially available and clinically used atomisation device (LMA MAD780, Teleflex Australia) and uniform cell distribution across the lung was achieved by the atomisation (Chapter 2).
- A ratiometric hypoxia probe synthesised in-house was used to demonstrate that decidual mesenchymal stromal cells are resistant to hypoxic stress, and thus suitable for use in the treatment of lung injury in which the microenvironment may be hypoxic (Chapter 3).
- A bioactive gelatin-based hydrogel was established as a highly compatible and sprayable platform for cell delivery (Chapter 3).
- EVs isolated from DMSC23 was developed for direct pulmonary delivery and have potential therapeutic role in improving the responses to lung injury (Chapter 4).
- An innovative methodology for nanoscale characterisation of EVs was developed using AFM-IR, which enabled single-vesicle analyses at unmatched resolution for interrogating structural and molecular composition (Chapter 5).

- An inhalation injury model is established using an in-house smoke inhalation chamber burning cotton, verified by inflammatory cells assessed using histology (Chapter 6).

7.1.3 New development of research tools and methodologies arising from this thesis

AeroCELL technology (2015)

The AeroCELL technology enabled the successful delivery of stem cells to *ex vivo* lung models. The cell-spraying process was engineered for optimal particle size for cell delivery to the lung while maintaining high cell viability. This technology was using a clinically relevant device and repurposing its use for pulmonary regenerative medicine. The technology was proven versatile as its use was verified also in delivering cells encapsulated in a bioactive hydrogel designed to crosslink *in situ* post-delivery to the lung models.

With further validations that is ongoing, the device has a high potential for commercialisation. This tool has already gained interest from the researchers of regenerative medicine field, to establish collaborations in delivering stem cells and biomolecules using this tool for different conditions of the lung. This technology has the potential to benefit future studies to directly deliver stem cells or biotherapeutics to the lung to accelerate lung tissue repair.

Interrogating the chemical composition of EVs with AFM-IR (2017)

A study of the chemical structure and composition of individual extracellular vesicles (EVs) secreted by stem cells, using resonance enhanced atomic force microscope infrared spectroscopy (AFM-IR) was developed for the first time. The analyses of nanoscale alterations in heterogeneity of EV populations has only recently been recognised as critically important in understanding the mechanism of stem cell therapy and advancing the field for clinical applications. This research tool enables comparison of individual vesicles at a resolution less than 20 nm. Nanoscale examination of individual EVs using AFM-IR will potentially have profound significance in disease diagnostics and in the emerging area of EV-therapies. Further development in these analyses could push the forefront of regenerative medicine closer to the creation of truly bioactive therapies, the demand for which is sharply increasing.

The high-impact publication in *Nanoscale Horizons* arising from this development has led to an ABC radio interview (<http://www.abc.net.au/radionational/programs/breakfast/cell-nanoparticles-could-help-diagnose-and-treat-cancer/9643358>) and media coverages in The Sydney Morning Herald (<https://www.smh.com.au/national/there-s-a-postal-network-running-through-your-veins-can-it-heal-you-20180411-p4z90g.html>) and EurekAlert / American Association for the Advancement of Science (https://www.eurekalert.org/pub_releases/2018-04/uos-sup041118.php).

Hypoxia-responsive ratiometric probe (2017; my role as co-investigator)

High-resolution and real-time sensing of hypoxia is necessary to advance the treatment regimen of disease involving hypoxic microenvironment, for example, cancer. In collaboration, we developed improved probes with ultra-high sensitivity for imaging and monitoring hypoxia, customised for a range of different applications. The innovative bioreductive fluorescent sensors based on a nitro-naphthalimide structure were developed with structural modifications tuned according to toxicity and cellular uptake. It has been verified that the probes had high levels of selectivity and sensitivity using of hypoxia-resistant and non-resistant placenta stem cell lines, which was published in 2018 (Yang *et al*, *Org. Biomol. Chem.* 16:619-624).

7.2 Personal development as a researcher

7.2.1 Research field and skills acquired

I started my M.Phil with research in **biomaterials** and **pharmaceutical science**, where I formulated a naturally-inspired silk-based microparticles for use as a drug carrier for direct pulmonary delivery. I engineered inhalable and biodegradable particles and characterised them thoroughly using a broad range of pharmaceutical assays including drug release, degradation, size and morphology assessment and determination of aerodynamic diameter to optimise the particles to be suitable for pulmonary drug delivery. I was trained in biological assays at a regenerative medicine laboratory in University College London, where I assessed the biocompatibility of the fabricated microparticles. As a result of this experience, I acquired expertise in biological assays and interests in stem cell-based therapy.

Leading on, I pursued my PhD for further research in **stem cell and EV therapy**, focusing on pioneering an innovative technology to deliver stem cells and EVs for accelerated tissue repair. I developed a technology for delivering stem cells and EVs directly to the lung to repair and regenerate injured lungs. I acquired technical skills in **molecular biology** while characterising the molecular composition of EVs and EV-treated cells. I was trained in **tissue engineering** while establishing an advanced *ex vivo* decellularised lung model for testing the stem cell distribution after delivery, learnt from the experts in the Weiss Lab, leading in pulmonary regenerative medicine at the University of Vermont. I continued the biomedical engineering aspect of research by fabricating a hydrogel platform for delivering the stem cells to the lung. I had opportunities to provide trainings to Honours students and students visiting our lab for short-term research on cell culture techniques, hydrogel fabrication and cell-based assays. Through the experience of contributing to supervision and collaboration, I have developed fundamental skills including organisation, communication and problem-solving skills.

7.2.2 Research highlights and collaborations

My publication in *Journal of Aerosol Medicine and Pulmonary Drug Delivery*, reporting the innovative approach of stem cell delivery directly to the lung, was highlighted as a high-impact article by the journal (2016). This was an outcome of an international collaboration I initiated by approaching Prof Daniel Weiss (University of Vermont), a world leader in pulmonary medicine. Following this publication, many experts in the field have conveyed additional benefits of direct airway delivery of stem cells compared to the intravenous route.

Another significant development was a novel silk-based carrier for airway delivery of anti-cancer medication. This work was published in *Scientific Reports* (ranked top 5% of Multidisciplinary field, SJR) and received attention as the Top Story of ‘Pulmonary Cell News’, by Connexion Creative (Aug 2015). This work contributed to the biomaterials field with new possibilities of using bio-inspired materials for pulmonary delivery.

My proactive engagement at conferences initiated collaboration with a stem cell expert Dr Bill Kalionis (Royal Women’s Hospital), which led to the development of an innovative nano-characterisation method for extracellular vesicles using atomic force microscope infrared spectroscopy (manuscript accepted for publication). This innovation has already gained interest from many researchers including Dr Kirsi Rilla (University of Eastern Finland) with whom I will further develop this technology.

7.2.3 Research output and achievements

During the 5 years of research experience (1.5 yr M.Phil and 3.5 yr PhD), I have 10 publications including 9 peer-reviewed journal articles (6 as first-author). Of these, 6 are in journals in the top 15% in their field (SJR), e.g. *Advanced Drug Delivery Review* (ranked 2nd in Pharmaceutical Science), *Scientific Reports* (top 5% of Multidisciplinary). The *Journal of Aerosol Medicine and Pulmonary Drug Delivery* publicised my article on stem cell spraying technology for lung repair as a ‘high-impact article’. The recent innovation on the use of AFM-IR for EV characterisation was published in *Nanoscale Horizons* and received a large volume of public interest as evidenced by numerous media releases in *The Sydney Morning Herald*, *The Age*, *EurekAlert* and ABC radio interview on RN Breakfast (webpage links are available on page 128). My article on silk particles for pulmonary drug delivery published in *Scientific Reports* on was highlighted as the Top Story of *Pulmonary Cell News* (Connexion Creative).

My ability to establish and lead multidisciplinary collaboration was demonstrated by the Sydney Nano Research Collaboration Award for which I was CIA. I am a CI on 4 successful institutional grants (totalling \$78K), including a prestigious University of Sydney–Utrecht

University Partnership Collaboration Award. The outputs during my M.Phil led to an APA for my PhD. Half of the 6 travel awards (totalling \$11.7K) funded trainings at lung/regenerative medicine labs in University College London and University of Vermont, from which I brought back skills to establish new protocols in my home lab. I developed *ex vivo* lung models and nano-bio-characterisation of stem cell-derived vesicles which led to pioneering innovative approaches in tissue regeneration. I presented my work at 7 international and 10 national meetings (3 invited, 7 oral and 7 poster presentations), which earned 7 best presentation awards.

7.3 Perspectives and future directions

7.3.1 Limitations and future directions arising from this thesis

The limitations identified from this thesis provide a strong foundation for the following studies:

- **Chapter 2:** The sprayed cells were cultured on collagen-coated tissue culture plastic yet collagen was not supplemented in media to test the possible benefits. The effects of co-delivery of collagen or other biomolecules (including EVs) with cells or pre-treatment with those prior to delivery of cells (both by atomisation) could be investigated for further benefits in accelerating tissue repair processes. However, due to the possible contribution of collagen to fibrosis or aberrant repair of lung injury, the type and dosage of collagen as well as the risk to benefit ratio should be carefully investigated. The uniformity of cell distribution was assessed using live imaging (IVIS) after spraying cells transfected with luciferase, however these cells were AB12 cells, for proof of concept. There still needs to be some optimisation for optimal cell viability after transfecting stem cells, and this work is ongoing.
- **Chapter 3:** Although thorough cell viability and morphological analyses have been conducted on cells encapsulated in GHPA hydrogel, it is unknown whether the DMSC23 differentiate into lung epithelial or other lineages when cultured in GHPA hydrogel. Differentiation assays to determine whether DMSC23 have an altered differentiation profile after being atomised onto *ex vivo* or *in vivo* lung injury models are necessary.
- **Chapter 4:** The conditioning of cells prior to EV isolation was limited to normoxia and hypoxia so in future studies the range of hypoxic conditions and treatment regimens could be modified to devise a more optimised microRNA composition. The analysis of protein profiles in conditioned DMSC23 EVs using proteomics is also recommended as it is known that proteins also have an important role in the repair mechanism. The effects on DMSC23 EVs on the survival and differentiation profile of the co-delivered cells could be investigated to further conclude the benefits of EVs in lung repair.

- **Chapter 5:** Since the innovative methodology of EV characterisation using AFM-IR focused on identifying the differences between two different stem cell types, the comparison of a broader variety of EV samples from different cell types (e.g. epithelial cells, cancer cells) would unlock the full potential of AFM-IR for future therapeutic or diagnostic applications. Further molecular analyses using proteomics and lipidomics for parallel characterisation of EVs will also be necessary for preclinical studies.
- **Chapter 6:** The inhalation injury established by using an in-house smoke inhalation chamber was only assessed using H & E analyses, therefore more sophisticated analyses such as bronchoalveolar lavage fluid analysis would lead to a more precise and quantitative assessment. Additional validation studies on more smoke inhalation regimens and EV treatment routes (intravenous, traditional instillation and atomisation) and treatment time points would further devise the most appropriate injury and treatment models for preclinical studies. Once a validated injury model is in place, another important investigation would be to determine the minimum required dosage for the treatment of lung injury as a function of changes in the atomisation parameters, for example, particle size.

7.3.2 My next research

My plan for postdoctoral research is at Dr Charlotte Dean's laboratory (National Heart and Lung Institute (NHLI), Imperial College). Dr Dean has supported me in a number of fellowship applications which will help expand my skills in pulmonary regenerative medicine. My expertise in lung models and histology positions me well to develop an innovative pharmacological approach to simulate the protein signals that drive lung tissue repair. The Dean Lab is leading in this field, as they pioneered an important repair mechanism through the Wnt-Planar Cell Polarity pathway and established genetically modified mice to model the injury. I will develop skills in pharmacology and molecular biology while acquiring professional skills through NHLI's well-established career development programs. The proposed outcomes of the planned research places me in a great position to translate this work to the preclinical stage.

7.3.3 Future plans for my research career

The goal of finding an effective approach to treat degenerative lung diseases underpins all my research interests. In the proposed project and my continued research career, I endeavour to progress this goal using a regenerative medicine approach. I will leverage and consolidate learnings and experience in pharmacology, immunology and engineering proposed in this project, with my existing expertise in cell biology and biomaterial science. Taken together, this

collective skill set will contribute to generating new strategies for treating lung diseases. It will further equip me to take on more innovative biomedical projects to address challenging unmet needs revealed in the future. I envisage receiving research fellowships that will help establish me as an internationally-recognised researcher in the field of pulmonary regenerative medicine, and furthermore enable me to develop skills to assist junior researchers pursuing biomedical research. During the postdoctoral research, I will establish collaborations that will be essential for accomplishing my long-term goals of clinical translation. I will take advantage of the opportunities in professional development through the regular courses and support in networking and mentoring offered to postdoctoral researchers.

I have identified commercialisation opportunities for potential tools developed during the proposed projects, where I will be a founder and academic advisor. The skills and strategies gained during the postdoctoral research will enable me to become a leading independent researcher. The high quality of my publications in the short time I have been a researcher is evidence of this potential. Upon completion of research overseas, the experiences will allow me to bring specialised expertise back to Australia, where I aspire to establish my own lab in pulmonary medicine, leading among a strong network of collaboration that will devise effective treatment for lung diseases affecting millions of people around the world.

Appendix A. Protocols for EV characterisation using AFM-IR

(Manuscript to be submitted soon)

High-fidelity probing of the heterogeneity of extracellular vesicles by resonance enhanced atomic force microscopy infrared spectroscopy (AFM-IR)

Sally Yunsun Kim^{1,2*}, Dipesh Khanal^{1,2*}, Bill Kalionis³, Wojciech Chrzanowski^{1,2}

¹Faculty of Pharmacy, The University of Sydney, NSW Australia.

²Australian Institute for Nanoscale Science and Technology, The University of Sydney, NSW Australia.

³Department of Maternal-Fetal Medicine Pregnancy Research Centre and University of Melbourne. Department of Obstetrics and Gynaecology, Royal Women's Hospital, Parkville, Victoria, Australia.

Correspondence should be addressed to W.Ch. (wojciech.chrzanowski@sydney.edu.au)

*Equal contribution

INTRODUCTION

Extracellular vesicles (EVs) are heterogeneous collection of nanoscale messengers that carry biological signals to recipient cells to influence both physiological and pathophysiological processes. EVs have been increasingly investigated for their potential as biomarkers for cancer, cardiovascular and kidney diseases¹⁻⁴, as carriers for drug delivery as well as their intrinsic therapeutic properties. In particular, stem cell-derived EVs deliver biological signals that direct a cascade of protective biological responses that restore cellular function in damaged or diseased tissues and have received immense attention as therapeutics for regenerative medicine⁵⁻⁷.

The therapeutic potential of mesenchymal stem/stromal cells (MSCs) have been confirmed in many studies, including enhancing recovery from cellular injuries caused by myocardial infarction^{8,9}, and they have additional beneficial properties of attenuating inflammation and immune responses¹⁰⁻¹². The therapeutic action of MSCs is primarily through a paracrine mechanism mediated by EVs.

A major problem that besets all EV research is that current isolation methods produce heterogeneous populations of EVs with respect to their size and structure. These problems arise in part due the nanoscale size of EVs and the paucity of specific markers for isolating and identifying the different classes of EVs.

EVs are selectively packaged by the secreting cells and thus the composition of individual EVs are heterogenous. The secreting cell uses a regulated mechanism that responds to various stimuli (e.g. growth conditions such as hypoxia⁵, the cellular microenvironment, and pathological changes within the cell of origin), which determines the final specific composition of EVs.

Methods currently available to interrogate the heterogeneity of EVs restrict the understanding of EV function¹³⁻¹⁵. Conventional technologies to probe individual EVs are limited to determining individual EV particle size, morphology and number. The overall molecular composition of a population of EVs is primarily determined on the entire EV population using protein, lipid or nucleic acids-based analyses. There are no currently available methods for analyzing subpopulations of EVs without isolating them, using capture antibodies for example, from the total population of EVs, and no methods for determining individual EV composition within a population. We present a pioneering approach using AFM-IR spectroscopy, to study the structure, composition and dynamics of whole populations, subpopulations and individual EVs at an ultra-high resolution of less than 20 nm. Gaining a better understanding of EVs assemblies will have profound significance in disease diagnostics and in the emerging area of EV-therapies, pushing the forefront of regenerative medicine closer to the creation of truly bioactive therapies, the demand for which is sharply increasing.

Development of the protocol

Despite the progress in the development of material characterisation methods, many conventional methods have limited resolution and are only suitable for bulk materials. The use of AFM-IR technique was first reported by Hammiche *et al.* for polymeric samples in 1999, using a conventional Fourier transform infrared spectrometer (FTIR) coupled with a thermal source and a temperature sensitive thermal probe¹⁶. The first infrared spectrum obtained using AFM-IR was reported in 2004¹⁷ and since then the technique has been used for various applications in polymers, life sciences, photonics and pharmaceuticals¹⁸. AFM-IR has recently been used for determining conformational changes in intra and extracellular protein structures, which indicate altered biological function¹⁹, and for studying lipid droplets, vesicles and cytoskeletal filaments of cells at the subcellular level²⁰.

AFM-IR for complex biological nanoparticles such as EVs had not been reported. The potential advantages of incorporating AFM-IR for the study of EVs were the ability to profile composition and structure of single EVs within a population as well as for bulk comparison of

EV populations. We believed that the outstanding abilities of AFM-IR for nanoscale structure and composition analysis could be adapted to analyse different EV populations as well as EVs within a population but most importantly the comparisons could also be made between individual EVs. This technique is a label-free method, which is a significant advantage, for mapping IR-absorbing species of individual EVs, enabling comparison of single EVs. With the outstanding resolution of less than 20 nm, we can probe multiple points on single EVs to interrogate differences in composition and structure within single EVs.

Applications of the method

Measuring EV heterogeneity, to determine the uniformity of EV structure and composition, in either the whole EV population or in individual EVs, remains elusive and represents a global challenge. AFM-IR is likely to be a vital tool for understanding EV structure and composition, and to correlate these properties with biological responses/function. AFM-IR will provide basic, essential information on the structure and composition of any EV population, allowing databases of “fingerprint” spectra to be created for EVs from any cell type. The ability to characterise individual EVs, and subpopulations of EVs, will underpin the science that addresses the most important and fundamental biological question of how cells communicate, by determining how EV structure and composition changes during key events in normal and pathological development.

The most immediate practical application of AFM-IR is in testing and optimising methods for the isolation of EVs that have the most uniform structure or desirable composition. Furthermore, changes in EV structure and composition can be determined following changes to growth conditions, or following genetic manipulation of the source cell to change the composition of EVs.

The heterogeneity of EV populations produced by stem cells, and particularly mesenchymal stromal cells, is a significant problem that hinders their therapeutic use and effectiveness. Reproducibility and stringent analyses of the structure and composition of the EV population would assist in meeting regulatory requirements for clinical use. AFM-IR will allow a fast and reliable means of determining the ideal conditioning method to produce the best quality therapeutic EVs, with minimal amounts of samples required for screening.

Recent studies point to EVs as early markers for the diagnosis and progression of various diseases, including cancer^{4,14,21,22}. Alterations in EV numbers, surface proteins and nucleic acid molecular cargos are used as markers of disease prognosis^{4,15,23}. AFM-IR will allow changes

of EV ‘fingerprints’ of molecular compositions to be correlated with diseases, which would facilitate early disease detection. This highly-sensitive method has the potential for a profound impact as a diagnostic and disease prognostic tool. AFM-IR would allow personalized medicine based on EV spectra disease phenotypes, which would benefit individual and overall health outcomes. The AFM-IR spectra of EVs could develop to become the foundation for future biosensors for rapid disease detection. Our new method to characterise EVs using nanoscale AFM-IR may unlock the true potential of EVs in which they can be utilised as clinical tools in both diagnosis and therapy.

Finally, EVs are extensively studied for their potential as natural drug carriers to deliver diverse types of therapeutic drugs. AFM-IR can be used to assess EV structural and compositional changes that follow encapsulation of drug molecules. Such information is likely to enhance our understanding of the relationship between structure/composition and therapeutic efficacy.

Comparison with other methods

Infrared (IR) spectroscopy is an exclusive method for label-free extraction of biochemical information from biological samples²⁴. Fourier transform infrared spectroscopy (FTIR) is one of the most commonly used IR methods²⁴⁻²⁶. However, the main limitation of FTIR is spatial resolution that ranges between 3 and 30 μm depending on the instrumentation used. Thus, the use of FTIR provides microscale, averaged, bulk signal from large sample population (micrograms) and is unsuitable for single EV characterisation²⁷.

Raman spectroscopy is also used to characterise biochemical and structural information for biological samples²⁸. As with FTIR, Raman spectroscopy is only suitable for measuring relatively large sample volumes, lacks sensitivity for individual EVs and provides readout from bulk EV preparations. More recently enhanced Raman spectroscopy techniques such as Raman tweezers microspectroscopy (RTM) and surface-enhanced Raman spectroscopy (SERS) emerged and offer higher sensitivity for biological samples than standard Raman spectroscopy²⁹. However, until now there has been no report that demonstrated that the sensitivity is sufficient to probe individual vesicles. Despite improved sensitivity, both RTM and SERS remain techniques suitable for label-free characterization of larger EVs populations^{30,31}. Another major advantage of our approach is that only a small quantity of EV samples are required for deriving a high-resolution quantitative data about distinct changes in EVs’ composition and structure.

To robustly characterise the elaborate structure of individual EVs, ultra-high resolution (nanoscale) is essential. In general, IR spectroscopy achieves higher resolution because it measures the light absorbance, which is more specific than measuring the light scattering as done in Raman spectroscopy. While ultra-high resolution is offered by combining IR with atomic force microscopy-resonance enhanced atomic force microscopy infrared spectroscopy (AFM-IR). AFM-IR is capable mapping EV surface morphological features (in 3D), physical properties, and chemical composition at nanoscale, simultaneously. A major advantage of this method, not offered by the other techniques, is the connection of all signals by correlative nanospectroscopy. The volume of sample required for AFM-IR is in the range of few microliters (5 μ l volume containing approximately 80 μ g EVs), which is significantly lower than the amount required for Raman-based and conventional FTIR methods.

The analysis of EV composition by attenuated total reflection Fourier-transform infrared spectroscopy (ATR-FTIR) has been recently patented for the application of ‘diagnosing, prognosing and monitoring pathophysiological states for biological samples’³². Although the ATR mode allows for higher sensitivity, resolution remains in microscale, whereas AFM-IR enables characterisation at ultra-high nanoscale resolution (<20 nm). Such ultra-high resolution is attributed to the detection of thermal expansion of the sample using an AFM, tip which measures IR absorption below the diffraction limit²⁷.

AFM-IR is a powerful tool for evaluating the nanoscale composition of individual EVs and can be used to identify physical structures of EVs that have previously been exceptionally difficult to correlatively detect and to analyze. With the capabilities of AFM-IR, we are able to obtain detailed information on EV chemical composition and physical properties at nanoscale.

Level of expertise needed to implement the protocol

The operation of AFM-IR requires training, but the general operation of the nanoIR™ equipment is not overly difficult and does not necessarily require prior experience in AFM and/or IR spectroscopy. Some knowledge in how the AFM-IR works is preferred. Care must be taken when handling the prism to ensure it is correctly placed onto the prism holder. Nevertheless, the loading of the cantilever and sample stage is simpler when compared to other AFM systems.

Sample preparation and the isolation of EVs from cell lines requires cell culture and tissue culture training, including minimization of nuclease contamination. The interpretation of IR spectra requires basic knowledge in spectroscopy and chemistry to correctly analyze the results.

Limitations

The limitations of AFM-IR technique arise from the sample preparation step. The sample must be loaded along the midline of the prism since the sample stage does not allow the laser and the tip to reach the outer regions of the prism. In addition, smaller individual vesicles (20-50 nm) may not provide enough IR signal. Not enough vesicles in a field of view also hinders accurate measurement that represents the overall EVs within the population. Therefore, for smaller vesicles and when the IR signal is not sufficient, concentrating of the sample may be required, which will result in signal increase. Acquired spectra will then represent the chemical composition of only a small selection of EVs.

Outline of the workflow

To demonstrate the ability of AFM-IR to probe differences in molecular composition of vesicles from different cell types, and cell cultured under different conditions (hypoxia and normoxia), we used EVs isolated from two well-characterized, telomerase (hTERT)-transformed human decidual (DMSC23) and chorionic (CMSC29) mesenchymal stromal cell lines^{33,34}. The workflow for performing AFM-IR measurements on EVs isolated from DMSC23 and CMSC29 is outlined in **Fig. 1**. Initially, placenta is obtained, decidual and chorionic mesenchymal stromal cells are isolated respectively from maternal and fetal side of the placenta, then converted into DMSC23 and CMSC29 cell lines^{33,34}. EVs are extracted from the serum-free conditioned media (Steps 1-12). Since the production of EVs is stimulated as a result of the cell's response to changes in the microenvironment³⁵, cells can be cultured in various conditions, for example, in hypoxic conditions which models the stressed environment of tissue injury. Therefore, to demonstrate the capabilities of AFM-IR, we isolated EVs from cells cultured in hypoxic and normoxic conditions.

Sample preparation for AFM-IR can be done by placing a drop of EV sample (dispersed in nuclease-free water) on the zinc selenide (ZnSe) prism and then drying overnight (Step 13-15). Upon initialization of nanoIRTM and collection of background IR spectra (Steps 16-21), the IR laser is aligned and optimized (Steps 22-45). Then AFM-IR spectra are acquired as the AFM tip detects and amplifies the thermal expansion signal (Steps 46-51). The AFM-IR spectra can be acquired from multiple EVs simultaneously or multiple points on single EVs in the 1000 to 1800 cm^{-1} range, and high-resolution spectra can be obtained at 1 cm^{-1} resolution. The AFM tip can map variations in thermal expansion from IR absorption at a slower scan rate of 0.1 Hz (Steps 52-58). These steps can then be repeated on several EVs in other regions of the prism,

or other samples prepared on a different prism. Finally, the data analyses can be processed using the Analysis Studio™ software.

Experimental Design

We present a detailed procedure for the isolation of EVs and their characterization by AFM-IR spectroscopy. We standardized the procedure for obtaining quantitative and reproducible data.

Selection of cells and isolation of EVs. EVs secreted by mesenchymal stromal cells have been extensively researched for their regenerative medicine applications. We isolated EVs from two well characterised, telomerase (hTERT)-transformed human decidual (DMSC23) and chorionic (CMSC29) mesenchymal stromal cell lines^{33,34}. DMSC23 and CMSC29 were used because they retain many of the important characteristics of mesenchymal stromal/stem cells^{33,34}. Moreover, the use of these cell lines ensured reproducibility by avoiding the confounder of patient-to-patient variation between primary mesenchymal stromal cell preparations.

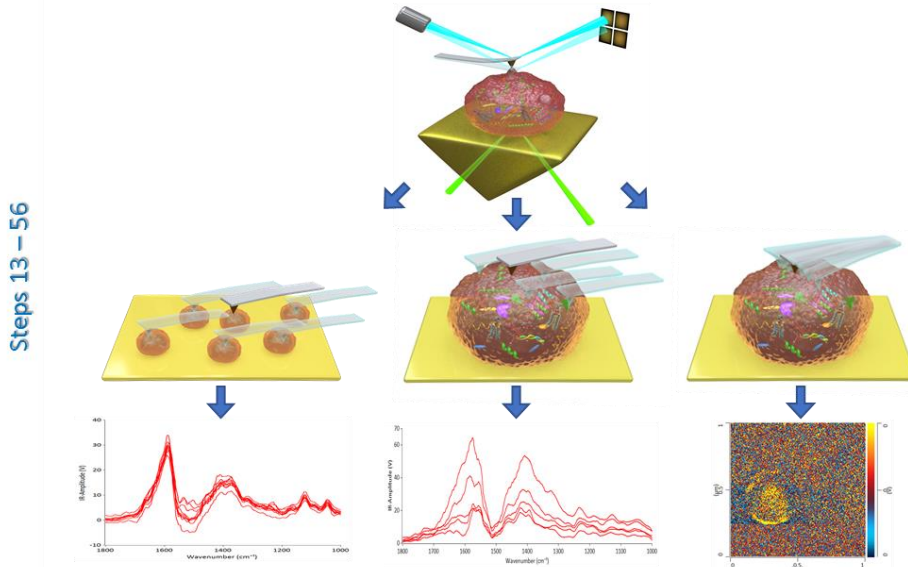
The DMSC23 cell line was of particular interest since the mesenchymal stromal cells used to generate this cell line were isolated from the maternal (*decidua basalis*) component of the placenta. These cells are resistant to the elevated level of oxidative stress, which is characteristic of pregnancy^{33,34}. DMSCs which are conditioned to resist oxidative stress are expected to have a specialised biological cargo packaged in their EVs. CMSC29 cells were chosen for comparison of structure and composition because they are derived mesenchymal stromal cells from the fetal chorionic component of the placenta, which are not as resistant to oxidative stress as DMSC23 cells³⁴. We therefore expected the two cell lines to produce EVs that were different in their structure and composition. Conditioned medium was centrifuged to remove cellular debris and apoptotic bodies, and this was followed by ultracentrifugation to isolate the EVs. Ultracentrifugation remains the method of choice to isolate EVs (Steps 5-12). To avoid PBS crystals interfering the AFM-IR measurement (**Supplementary Fig. 1a**), the EV pellet was dispersed in nuclease-free water before drying on the ZnSe prism (Steps 13-15). In addition, the sample must be properly immobilized, to avoid dragging during imaging (**Supplementary Fig. 1b**).

Appendix A. Protocol for EV characterisation using AFM-IR

Isolation of EVs from human decidual (DMSC23) and chorionic (CMSC29) stem cell lines



AFM-IR spectroscopy: multiple EVs or multiple points on a single EV and IR mapping



Analyses of AFM-IR spectra using the Analysis Studio™ processing software

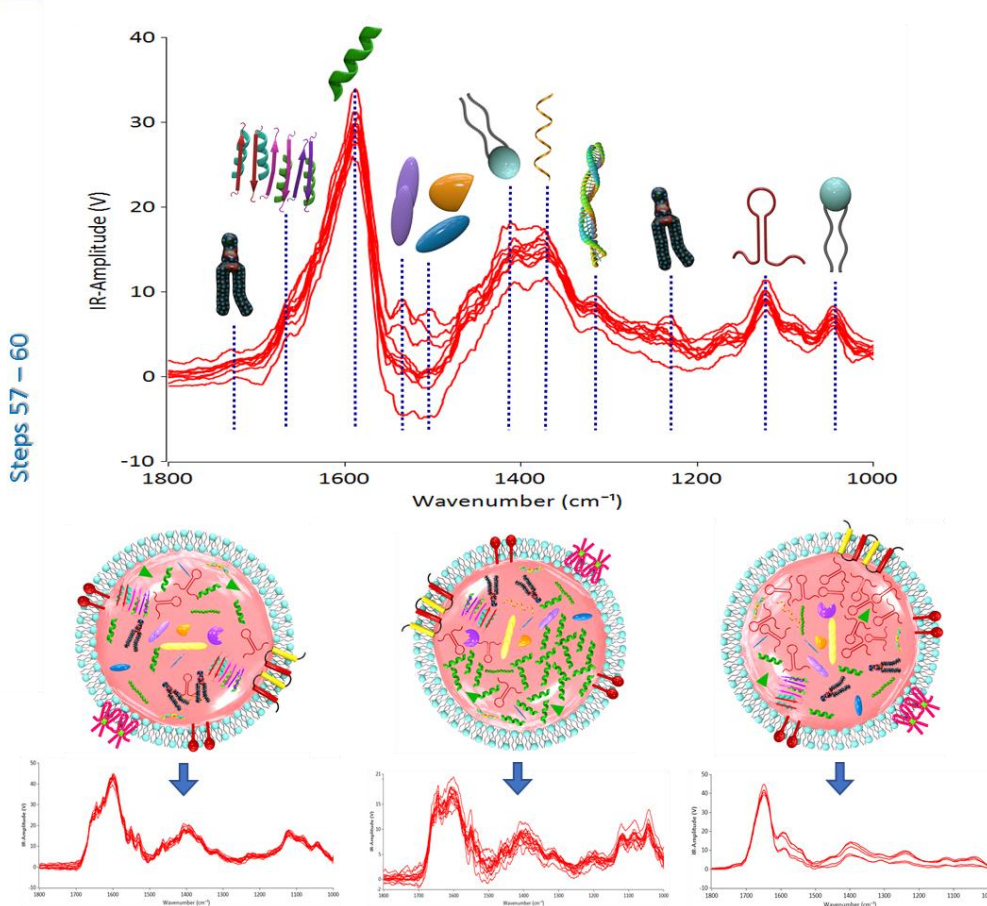


Fig. 1 Workflow of AFM-IR spectroscopy for EVs

Acquiring AFM-IR spectra from individual EVs. Prior to acquiring AFM-IR spectra, proper laser alignment and optimization (Steps 22-45; **Fig. 2a-c**) are crucial for obtaining accurate spectra. When the IR signal is collected without focusing of the IR laser on the cantilever, a number of peaks may be attenuated or not present that produces inaccurate data as those peaks may not be precisely detectable and interpretable (**Supplementary Fig. 1c**).

The properly aligned AFM-IR laser produces spectra such as those presented in **Fig. 4-6**. After obtaining the AFM height image (topography), cursors are placed to indicate regions for AFM-IR measurement. In order to identify differences in composition and structure of individual EVs within the same population, several vesicles are selected and spectra are acquired individually for each vesicle. When comparing between two EV populations, vesicles with similar height and size are selected to be analyzed and cursers are placed on the middle of the vesicle to minimize inconsistency.

For spectral acquisition of several points on single vesicle, there is an option for manual or automated acquisition. For manual acquisition, the region of interest can be selected for spectral acquisition (**Fig. 4c**), while the automated acquisition will allow an array to be placed for collecting spectra across the region of the sample. A line array or grid array option can be used to collect the spectra from the different spatial locations of an individual vesicle. In a $1\ \mu\text{m} \times 1\ \mu\text{m}$ scan size, a grid array can be chosen with 10 to 12 spots on the image for collecting spectra across the sample (**Fig. 5b,c**). The number of selected points controls the resolution of the collected signal.

Collection of nano-infrared image. The nano-infrared image (**Fig. 4e,f**) is an ultra-high resolution map of chemistry at given wavenumber that provides quantitative image of the chemical heterogeneity within a single vesicle. For nano-infrared imaging the scan rate is reduced, so that the update of IR-peak, IR-amplitude and frequency data approximates the pixel rate of the image (Steps 59-62). For example, at a scan rate of 0.1 Hz it takes 10 seconds to scan both trace and retrace lines. With an 'X' resolution of 500 in each scan direction this correlates to a pixel rate of 100 Hz. The repetition rate of IR source is 1 kHz and with the co-averages of $16 \times$, the update rate of the IR peak, amplitude and frequency would be ~ 60 Hz which is similar to the pixel rate. If the co-average value is increased, the scan rate must be decreased to match with the pixel rate and to update all the necessary signals for image acquisition. The mismatch of scan rate and co-average will result in failure of image acquisition.

The nano-infrared image can be collected at various wavenumbers of interest so that the ratio of images can be compared to localize various chemical domains within the sample based on the color intensity (**Fig. 4e,f**). For example, if an Amide I peak of protein is seen at 1640 cm^{-1} and lipid related cholesterol peak is seen at 1730 cm^{-1} , two separate IR image may be collected at these both wavenumbers in order to identify the distribution of lipid and protein across the sample being scanned (**Fig. 4e,f**).

Data analysis using the Analysis Studio™ processing software. When spectra are collected either from multiple EVs, or as an array from single EVs, spectra can be processed for averaging or smoothing using dedicated software (Analysis Studio, Steps 59-62). Smoothing of the spectra can be achieved using a ‘Savitzky-Golay’ function. The choice of polynomial function, and the number of points selected, is crucial. The higher the number of points used for smoothing, greater the risk of losing critical peaks of lower intensity during the smoothing process. From our experience and optimization, ideal smoothing can be achieved by using polynomial function of 2, and 15 number points. When labeling the peaks, the appropriate minimum amplitude value must be specified to minimize the labeling of noise. A minimum amplitude of 5 will result in labeling of peaks associated with noise and therefore higher values should be chosen. The individual peaks in the spectra can be labeled either automatically using a function in the software, or manually by moving the highlighting bar on top of the peak of interest.

Controls. It is essential to include samples of nuclease-free water used to disperse EVs after ultracentrifugation and the medium for EV isolation without exposure to cells. This is to ensure that there are no contaminants in the nuclease-free water used and there is minimal protein contamination in the media used for EV isolation.

MATERIALS

REAGENTS

MesenCult™ Proliferation Kit (Human) (STEMCELL Technologies, cat. no. 05411)

AmnioMAX™ C-100 Basal Media (Life Technologies, cat. no. 17001074)

AmnioMAX™ C-100 supplement (Life Technologies, cat. no. 12556023)

Hanks' Balanced Salts, modified, without Ca/Mg (HBSS(-)) (Sigma-Aldrich, cat. no. H4891-10X1L)

Tryple™ Select (Life Technologies, cat. no. 12563029)

GlutaMAX™-I (Life Technologies, cat. no. 35050061)

Penicillin-Streptomycin (PenStrep; Life Technologies, cat. no. 15140122)

Bovine serum albumin (Sigma-Aldrich, cat. no. A2153)

Molecular biology grade water (Sigma-Aldrich, cat. no. W4502)

REAGENT SETUP

Normal culture medium for DMSC23:

MesenCult™ basal medium supplemented with MesenCult™ supplement 10%, GlutaMAX 1%, PenStrep 1%

Normal culture medium for CMSC29:

AmnioMAX™ basal medium supplemented with AmnioMAX™ supplement 15%

Serum-free medium for EV isolation:

Bovine serum albumin (Sigma-Aldrich) 0.5%, GlutaMAX 1%, PenStrep 1% in MesenCult™ basal media

EQUIPMENT

Beckman Coulter ultracentrifuge Ti70 rotor (Beckman and Coulter)

Ultra-bottle assembly Cat no. PN4416 (Seton Scientific)

nanoIR™ AFM-IR instrument (Anasys Instruments)

Zinc selenide (ZnSe) NIR prism (Anasys Instruments)

Contact-mode AFM probes for nanoIR™ model: EX-C450 (resonance frequency 9-17 kHz, k: 0.07-0.4 N/m)

Tapping-mode AFM probes for nanoIR™ model: EX-T125 (resonance frequency 200-400 kHz, k: 13-77 N/m)

PROCEDURE

Cell culture (TIMING ~3 d)

1. Culture DMSC23 and CMSC29 cells until 80% confluence in normal culture medium.
2. Wash cells twice with HBSS(-).
3. Culture cells in serum-free EV isolation medium, (as detailed above) – 12 ml per T75 flask or 23 ml per T175 flask for 48 h.
4. After 48 h, collect medium and transfer into nuclease-free centrifuge tube.

Isolation of EVs (TIMING ~4 h)

5. Centrifuge medium at 500 g for 5 minutes to remove cells and debris.
6. Centrifuge supernatant at 2,000 g for 20 min to remove apoptotic bodies.
7. Transfer media to thick-wall polycarbonate ultracentrifuge tubes.
8. Centrifuge at 100,000 g for 60 min at 4°C.
9. Remove supernatant and resuspend the pellet in 1 ml nuclease-free PBS.

10. Centrifuge at 100,000 *g* for 60 min at 4°C.
11. Remove supernatant and resuspend the pellet in 100 µl (minimum volume) of nuclease-free PBS.
12. Transfer EV samples to a sterile nuclease-free microcentrifuge tube in -80°C.

PAUSE POINT: Samples can be frozen at -80°C for up to 12 months if handled correctly and by implementing the critical points listed below.

CRITICAL: To prevent RNA degradation, use nuclease-free pipette tips and reagents.

CRITICAL: Minimize repeated freezing and thawing cycles.

Sample incubation on ZnSe prism (TIMING ~18 h)

13. Vortex to evenly mix the EV sample.
14. Remove 5 µl of sample (in nuclease-free water) using a nuclease-free pipette tip and dispense onto a ZnSe prism fitted onto a sample holder, placing the drop on the midline of the prism. 5 µl volume should contain approximately 80 µg EVs.
15. Store overnight at room temperature in a desiccator to dry the sample.

CRITICAL: Wear gloves while handling the ZnSe prism and ensure the prism is correctly fitted onto the sample holder.

CAUTION: Zinc selenide is a skin and eye irritant, and is toxic if inhaled or ingested. Always wear gloves when handling prisms, and wear a face mask to prevent inhalation or ingestion of any dust residue. Read the MSDS available from the supplier.

Set up of nanoIR™ (TIMING ~2 h)

16. Initialize the Analysis Studio™ software and select the AFM-IR mode from the control panel.
17. Load a new AFM cantilever (EXC450 tips, AppNano, CA, USA) with a nominal spring constant of 0.5 Nm⁻¹ into the magnetic probe mount located on the AFM scan head.
18. Switch on the pulse IR laser source and allow the laser to warm up for 30 minutes prior to acquisition of background spectra.
19. Collect IR background spectra from 1000 to 1800 cm⁻¹.

CRITICAL: Loading a clean tip prior to collecting AFM-IR spectra, will minimize erroneous results.

TROUBLESHOOTING (refer to Table 1)

20. Repeat 4 times.
21. Average these background spectra and normalize to calibrate the signal intensity as a function of wavenumber.

CAUTION: Avoid staring directly into the laser beam as it is hazardous to eyes.

Collection of nano-infrared spectra (TIMING ~5 h per sample)

22. Lift up the AFM scanning head, place the ZnSe prism loaded with sample onto the AFM scanning stage.
23. Lower the scan head and focus on the region of interest with the optical microscope.
24. Align the AFM laser onto the end of cantilever to get maximum laser sum of > 3.0 V.
25. Adjust the cantilever deflection value to ~ -1.00 V.

TROUBLESHOOTING (refer to Table 1)

26. Approach the prism surface using the software controls. When the AFM probe is close to the sample, press the “engage” software button to contact the tip with the sample surface.

CRITICAL: The speed of approach of the scanning head for engaging the tip is important. Fast speed while manually lowering the scanning head may result in accidental contact of the tip with the surface, causing damage to the tip.

27. Scan the surface to obtain AFM images in “contact mode”.

CRITICAL: While collecting the image, adjust the speed of the scan ~ 0.3 Hz, set point, integral and proportional gain, so that the trace and retrace graph of cantilever lines are overlapping. EVs are soft samples and these adjustments will prevent vesicle dragging or damage during the scan.

28. Move the cantilever tip to the vesicle of interest. Keep the cantilever in contact with the vesicle.

CRITICAL: Keep the probe engaged on the sample but do not scan for image acquisition.

29. Turn on the green aiming laser and align it onto the end of cantilever.

CRITICAL: Move the green aiming laser to the right and left end of the prism to ensure the proper alignment of the prism onto the prism holder. Ensure that the prism is clean: a focused spot of the green laser indicates that the prism is clean, whereas a more dispersed laser indicates that the prism is not clean.

30. After the alignment of laser, turn off the aiming laser by clicking “Stop Guide Laser” button from the software.
31. Enter the wavenumber into the software where the sample is highly likely to have an absorbance. For example, if the sample contains proteins, enter a wavenumber of 1640 cm^{-1} for optimization of the IR signal.
32. Set the power to 80% and co-averages to $256\times$.

CRITICAL: The selection of laser power is crucial and it depends on the thickness of the sample; for EVs which are typically ~ 100 nm thick, a power of 80% or higher is necessary to get a good absorbance signal.

33. Switch on the ‘IR’ by clicking the ‘Start IR’ software button.

34. Rotate the IR focus wheel to align the IR laser on to the cantilever, keeping an eye on the deflection and Fast Fourier Transformation (FFT) plots to obtain cantilever ringdown signal in a wave form and clear peak in the FFT plot (**Fig. 2a,b**).
35. Disable the band pass filter to observe the ringdown signal and to observe the peaks in the FFT window.
36. Look for a clear peak in the FFT window, choose the second cantilever resonance peak which is typically above 75 kHz as a frequency center, and enter 50 kHz as the frequency window, into the software.
37. Rotate the IR focus wheel to obtain a cantilever deflection reading in the IR meter within ± 1 .
38. After laser optimization, enable the band pass filter, and set the filter strength to 25%.

CRITICAL: A deflection higher than ± 1 value may cause sample damage due to excessive thermal expansion.

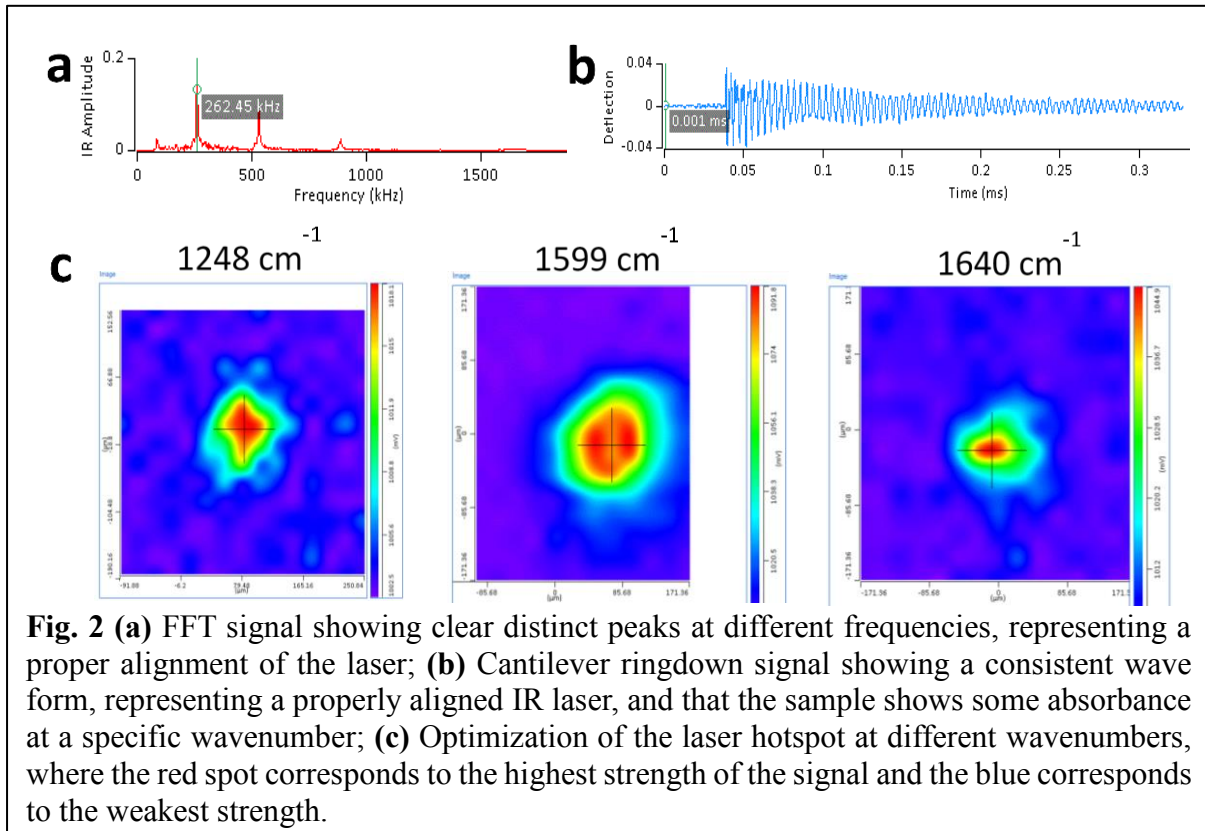
CRITICAL: The band pass filter decreases the signal contribution from frequencies outside the frequency window enhancing the signal to noise ratio. Too large a filter strength can create unwanted artifacts in the FFT.

TROUBLESHOOTING (refer to Table 1)

39. For final fine tuning of the laser position, click on the ‘Optimize’ function in the software.
40. Use the slider bar in the optimize window to select a small search area of $50 \mu\text{m} \times 50 \mu\text{m}$.
41. Enter the wavenumber of interest in the software for optimization of IR laser hot spot. At each particular wavenumber click the ‘Scan’ button in the software.
42. A resulting image of IR-peak signal map at each x and y location across the sample will be obtained. Red zones indicate the strongest signal and blue corresponds to the weakest signal in the sample.
43. Select the region with the strongest IR signal from the image by moving the cross hair and click ‘OK’ to update the optimized spot into the software.
44. Exit the optimize window to update the optimized laser spot for different wavenumbers for each sample.
45. Optimize the laser signal for five to six different wavenumbers. Typically, the wavenumber chosen for biological samples are 1050 cm^{-1} , 1150 cm^{-1} , 1250 cm^{-1} , 1350 cm^{-1} , 1450 cm^{-1} , 1550 cm^{-1} , 1650 cm^{-1} and 1750 cm^{-1} , for the scan range of 1000 to 1800 cm^{-1} (Fig. 2c).

CRITICAL: Once the laser is optimized for different wavenumbers do not rotate the IR focus wheel or change the position of IR laser by moving the IR laser knobs in the AFM-IR system. If the laser position is changed, the entire process of laser optimization and alignment must be repeated.

46. Enter the range of wavenumber in which the spectral acquisition is to be done. For example, from 1000 cm^{-1} to 1800 cm^{-1} .
47. Enter the resolution of spectra to be acquired typically 1 cm^{-1} for high resolution spectra.
48. Enter the co-averages as 256X or higher. The higher the value of co-averages the better the signal to noise ratio of the acquired spectra will be achieved.



49. For spectral acquisition, there are two different options; manual or automated. In manual operation, click on the region of interest where the spectral acquisition is to be done and click ‘Acquire’ from the software to collect the spectra. For automated acquisition, click on the ‘Array’ button from the software, which will open the previously acquired image of the vesicle.

A window will open where the line array or grid array option can be selected to collect the spectra from different spatial locations within the image. For example, in a $1 \mu\text{m} \times 1 \mu\text{m}$ scan size, grid array can be chosen with 10 to 12 spots on the image for collecting spectra across the sample. Higher number of points increases resolution of the data.

CRITICAL: Monitor the spectra as they are collected, as well as the IR deflection window, for the level of IR absorbance signal being collected. If the IR power is higher than ± 1 during the spectral acquisition, stop the scan and reduce the IR laser power to avoid sample damage.

Collection of nano-infrared image (TIMING ~7 h per sample)

50. Tick the ‘IR imaging enabled’ tab on the software.
51. Enter the wavenumber at which IR imaging is to be done.
52. Set the co-average as 16X or below in the general tab of the IR spectra acquisition menu of the software.
53. Set the scan rate at 0.1 Hz and reduce the integral gain to one fifth of the value used for normal AFM image collection.

CRITICAL: A reduction in scan rate is critical to ensure that the IR-peak, IR-amplitude and frequency data approximate the pixel rate of the image.

54. In the AFM image selection channel window, enable IR amplitude, IR peak and contact frequency (provides mechanical information of the sample).
55. Click the ‘Scan’ button on the software to collect the nanochemical map of the vesicle at a desired wavenumber.
56. Collect the image at the various wavenumbers that correspond to different chemical domains of interest within the sample.

Data analysis (TIMING ~3 h)

57. The general steps for data analysis are exemplified in **Fig. 1**, in which the Analysis Studio™ processing software was used to generate averaged or smoothed spectra.
58. All the spectra collected either as an array from a single EV (**Fig. 5**), or spectra collected from multiple EVs (**Fig. 4**) are averaged using the ‘Analysis– Process– Average’ tab from the software.
59. Smoothing of the spectra can be achieved using the ‘Savitzky-Golay’ function from the software. All the individual or averaged spectra to be smoothed must be highlighted and smoothing can be achieved by using polynomial function of 2 and 15 number of points.

CRITICAL: The choice of polynomial function, and number of points selected, is required to smooth the spectra, which depends on the resolution of the spectra (number of points per cm^{-1}) and signal strength obtained during spectral acquisition. Higher the number of points used for smoothing, greater the risk of losing critical peaks of lower intensity.

60. To label the individual peaks in the spectra, use the ‘Analysis– Analyze– Peak find or Show all peak’ function from the software. Peaks can also be identified manually by moving the highlighting bar on top of the peak of interest.

CRITICAL: The appropriate minimum amplitude value must be provided for the software to label the peaks. Choosing the minimum amplitude of 5, makes it highly likely that peaks associated with noise gets labelled.

Table 1: Troubleshooting table.

Step	Problem	Possible reason	Solution
19	Failure to initiate background calibration.	<ul style="list-style-type: none"> • Laser shutter is closed and does not allow the passage of the AFM-IR laser to the cantilever. 	<ul style="list-style-type: none"> • Check the laser shutter knob and ensure that it is open.
19	Failure to pass background calibration due to low signal intensity at specific wavenumber.	<ul style="list-style-type: none"> • Laser source is not properly warmed up prior to collection of background spectra. 	<ul style="list-style-type: none"> • Run the laser for another 15 to 30 minutes and collect the background spectra again. • Increase the number of background spectra to be averaged.
24-25	A sufficient laser sum (~3V) and	<ul style="list-style-type: none"> • Improper alignment of the laser. 	<ul style="list-style-type: none"> • Confirm the alignment of laser at the tip of the cantilever.

Appendix A. Protocol for EV characterisation using AFM-IR

	cantilever deflection (-1V) can't be achieved.	<ul style="list-style-type: none"> • Cantilever not mounted properly. • Defective cantilever reflective coating. 	<ul style="list-style-type: none"> • Check if the cantilever is placed properly onto the probe holder. The cantilever holder must be parallel to the mount. • If these two steps do not solve the problem, replace the cantilever with a new one and repeat the alignment process.
34-36	Failure to achieve a cantilever ringdown and "clean peaks" in the FFT window.	<ul style="list-style-type: none"> • The AFM-IR focus wheel is not aligned properly with reference to the cantilever position. • The AFM-IR laser is not positioned properly on the cantilever. • Insufficient laser power. 	<ul style="list-style-type: none"> • Align the IR focus wheel such that the laser beam is properly focused onto the cantilever, for example, if the center of the prism is well to the right of the probe then rotate the IR focus wheel so that it sits to the right of center in focus wheel housing. • If there is still no signal, adjust the position of the AFM-IR laser with the 'X' and 'Y' knob in the system, and look for any changes in the cantilever deflection signal (ringdown signal plot) and FFT plots. • If the signal is very weak, increase the laser power by another 10% and confirm the magnitude of the signal.

TIMING (summary)

Steps 1-4, cell culture and change to serum-free media: ~3 d

Steps 5-12, isolation of EVs: ~4 h

Steps 13-15, sample incubation on ZnSe prism: ~18 h

Steps 16-21, set up of nanoIR™: ~2 h

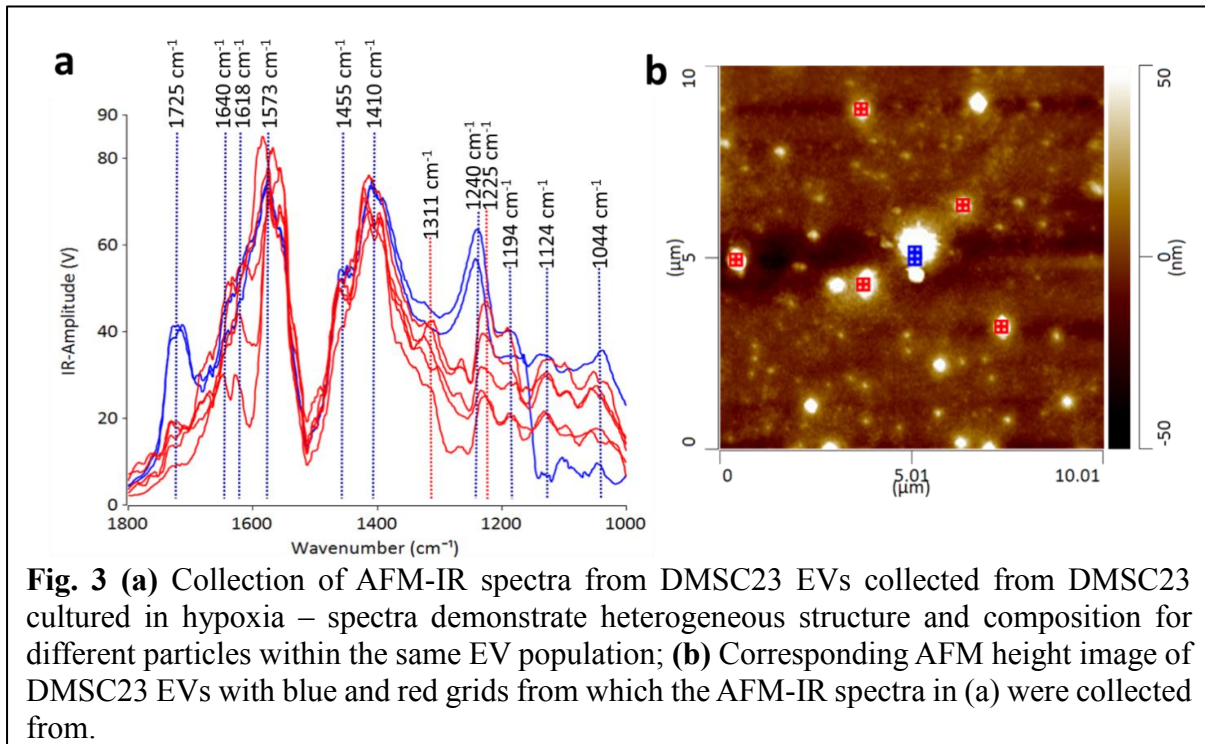
Steps 22-49, collection of nano-infrared spectra: ~5 h per sample

Steps 50-56, collection of nano-infrared image: ~7 h per sample

Steps 57-60, data analysis: ~3 h

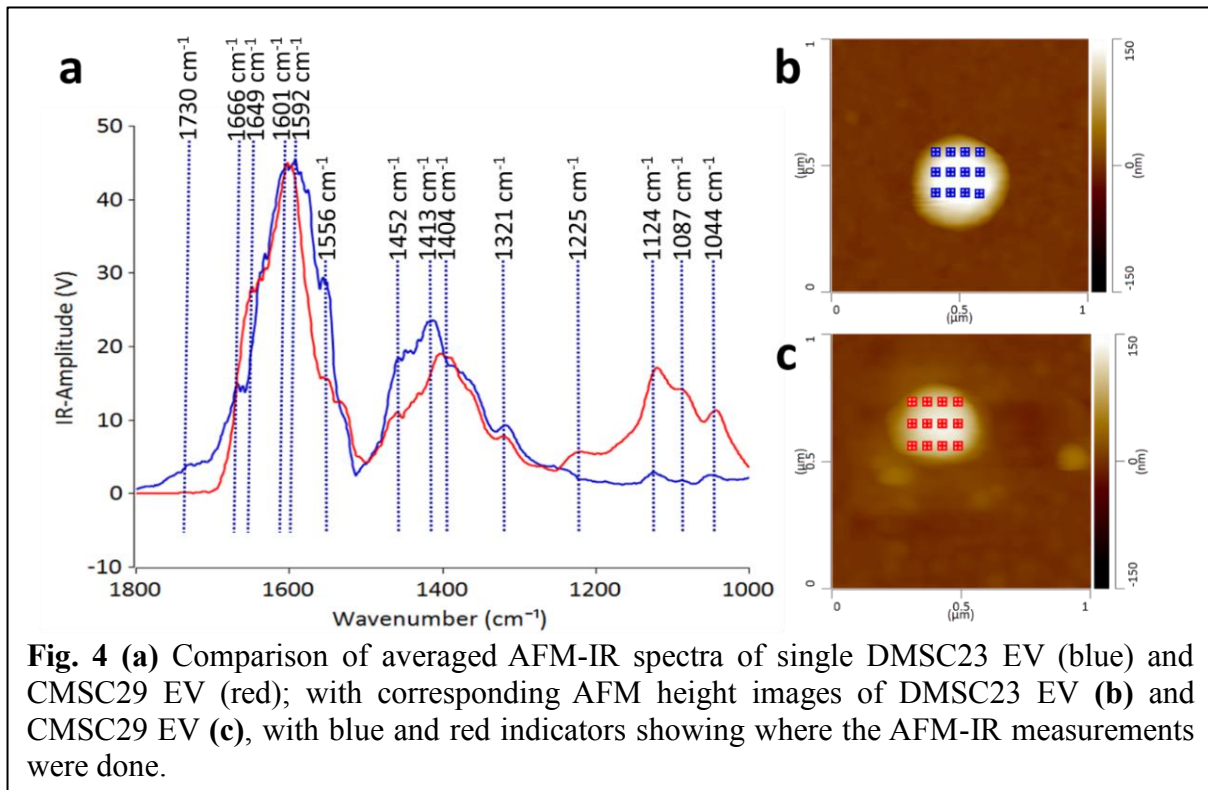
ANTICIPATED RESULTS

The feasibility of identify nanoscale structural and compositional differences within individual EVs of same EV population is demonstrated by using DMSC23 EVs and CMSC29 EVs. **Fig. 3a** shows a collection of AFM-IR spectra from individual EVs in a population of DMSC23 EVs, which were collected from DMSC23 cultured under hypoxia. **Fig. 3b** shows the



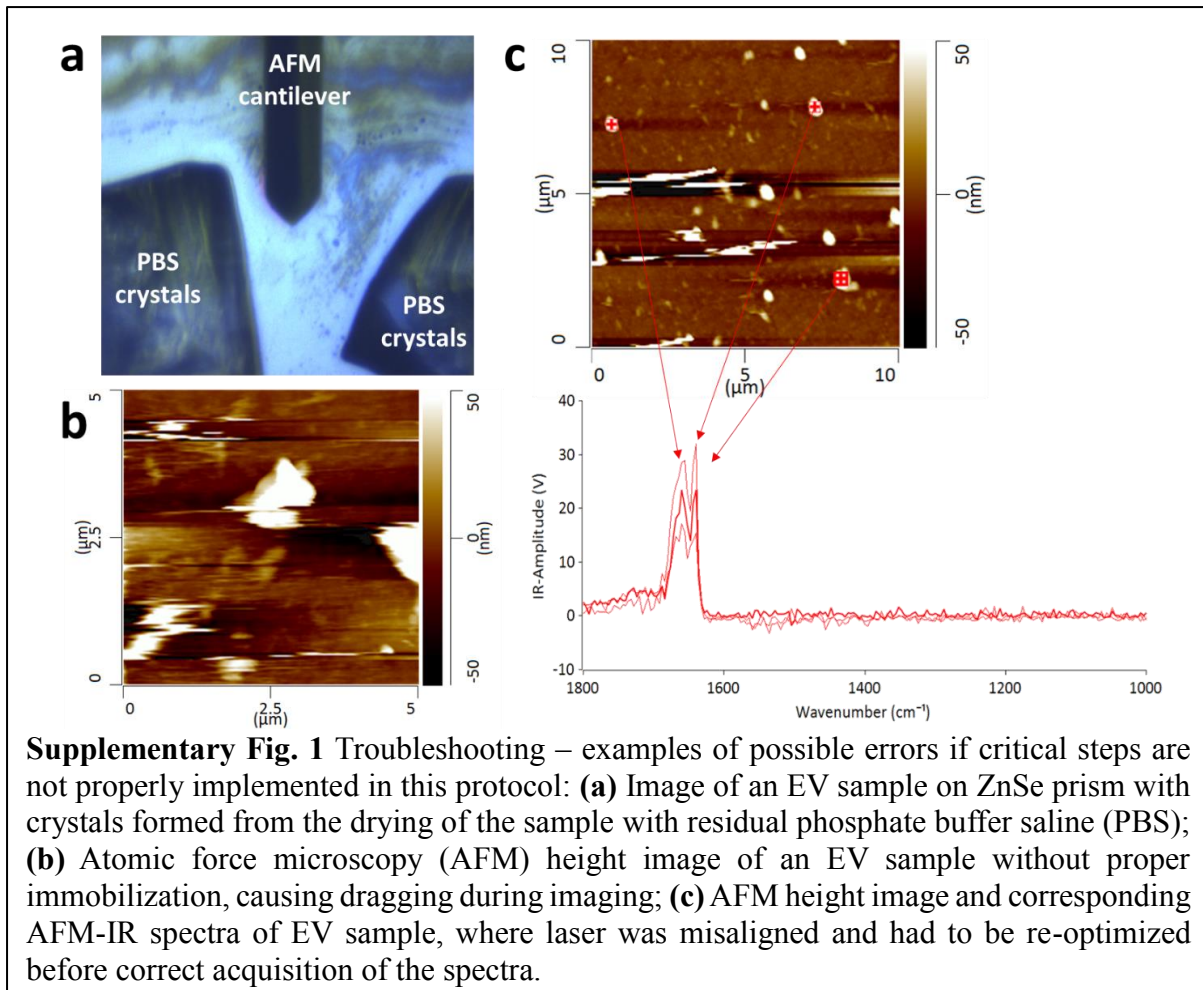
corresponding AFM height image where blue and red grids indicate the areas where spectra were collected. The spectra in blue collected from two points of the same large vesicle show two distinct peaks of increased intensity at 1725 cm^{-1} (fatty acids) and 1240 cm^{-1} (phosphates), which are consistent with increased amounts of lipids and nucleic acids on the surface and inside the vesicle, respectively. The peak corresponding to RNA ribose at 1124 cm^{-1} shows differences in the intensities for each spectrum, which indicates the different amounts of RNA ribose contained in these EVs. These data demonstrate that AFM-IR is a sensitive method to uncover nanoscale differences in molecular composition between individual EVs, and the data highlight the heterogeneity of EV populations.

The ultra-high resolution of AFM-IR is demonstrated by the ability to probe multiple points within an individual EV as well as the ability to identify differences between single EVs, either within the same or different EV populations. An example of this is shown in the averaged AFM-IR spectra of 12 points on a single DMSC23 EV, and a single CMSC29 EV (**Fig. 4**). The stronger intensity of the peaks at 1556 cm^{-1} and 1452 cm^{-1} for DMSC23 EV belongs to amide I and the bending vibration of lipid acyl CH_2 groups, respectively, while the stronger intensity of peaks at 1124 cm^{-1} , 1087 cm^{-1} and 1044 cm^{-1} for the CMSC29 EV is in the region of stretching vibration of phospholipids, triglycerides and cholesterol esters ($950\text{ to }1200\text{ cm}^{-1}$), corresponding to the lipid content of the EV³⁷. The peak at 1124 cm^{-1} in particular, belongs to the RNA ribose as mentioned above.



For both DMSC23 EVs and CMSC29 EVs a low intensity peak at 1730 cm⁻¹ that corresponds to purine base (C=O bond) was observed. However, the intensity of this peak varied across the EV populations, which demonstrated heterogeneity of nucleic acid content in the samples. Overall, this study confirmed differences in protein structure and nucleic acid content between both types of EVs, as well as differences in the composition in single EVs between the two populations.

The data presented above suggest AFM-IR can transform existing protocols for assessing EV purity. The AFM-IR technique can be developed into a screening tool for detecting specific EV “fingerprints” that are associated with a pathology, e.g. multiple sclerosis or cancer. For therapeutic applications AFM-IR will allow researchers to not only assess EV purity but also to define the composition of EV populations. Moreover, AFM-IR has the potential to identify optimal compositions and EV subtypes that initiate tissue repair most efficiently.



ACKNOWLEDGMENTS

The authors acknowledge the University of Sydney for the SOAR Fellowship for W.Ch.

AUTHOR CONTRIBUTIONS

W.Ch. conceived, designed and oversee the project; S.Y.K. design experiments and performed the isolation of EVs; D.K. performed the AFM-IR; BK isolated and developed stem cell lines. S.Y.K., D.K., M.W., B.K., and W.Ch. wrote the manuscript.

COMPETING FINANCIAL INTERESTS

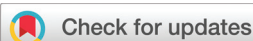
The authors declare no competing financial interests.

REFERENCES

1. Guo, L. & He, B. Extracellular vesicles and their diagnostic and prognostic potential in cancer. *Transl. Cancer Res.* **6**, 599-612 (2017).
2. Zhang, W. *et al.* Extracellular vesicles in diagnosis and therapy of kidney diseases. *Am. J. Physiol. - Renal Physiol.* **311**, F844-F851 (2016).
3. Jansen, F., Nickenig, G. & Werner, N. Extracellular vesicles in cardiovascular disease: Potential applications in diagnosis, prognosis, and epidemiology. *Circ. Res.* **120**, 1649-1657 (2017).
4. Verma, M., Lam, T.K., Hebert, E. & Divi, R.L. Extracellular vesicles: potential applications in cancer diagnosis, prognosis, and epidemiology. *BMC Clin. Pathol.* **15**, 6 (2015).
5. Shurtleff, M.J., Temoche-Diaz, M.M., Karfilis, K.V., Ri, S. & Schekman, R. Y-box protein 1 is required to sort microRNAs into exosomes in cells and in a cell-free reaction. *Elife* **5**, e19276 (2016).
6. van der Pol, E., Böing, A.N., Harrison, P., Sturk, A. & Nieuwland, R. Classification, functions, and clinical relevance of extracellular vesicles. *Pharmacol. Rev.* **64**, 676-705 (2012).
7. Silva, A.M. *et al.* Extracellular Vesicles: Immunomodulatory messengers in the context of tissue repair/regeneration. *Eur. J. Pharm. Sci.* **98**, 86-95 (2017).
8. Bian, S. *et al.* Extracellular vesicles derived from human bone marrow mesenchymal stem cells promote angiogenesis in a rat myocardial infarction model. *J. Mol. Med. (Berl.)* **92**, 387-397 (2014).
9. Arslan, F. *et al.* Mesenchymal stem cell-derived exosomes increase ATP levels, decrease oxidative stress and activate PI3K/Akt pathway to enhance myocardial viability and prevent adverse remodeling after myocardial ischemia/reperfusion injury. *Stem Cell Res.* **10**, 301-312 (2013).
10. Drommelschmidt, K. *et al.* Mesenchymal stem cell-derived extracellular vesicles ameliorate inflammation-induced preterm brain injury. *Brain, Behav. Immun.* **60**, 220-232 (2017).
11. Lo Sicco, C. *et al.* Mesenchymal stem cell-derived extracellular vesicles as mediators of anti-inflammatory effects: endorsement of macrophage polarization. *Stem Cells Transl. Med.* **6**, 1018-1028 (2017).
12. Shigemoto-Kuroda, T. *et al.* MSC-derived extracellular vesicles attenuate immune responses in two autoimmune murine models: Type 1 Diabetes and Uveoretinitis. *Stem Cell Reports* **8**, 1214-1225 (2017).
13. Fatima, F. & Nawaz, M. Nexus between extracellular vesicles, immunomodulation and tissue remodeling: for good or for bad? *Ann. Transl. Med.* **5**, 139 (2017).
14. Giebel, B. On the function and heterogeneity of extracellular vesicles. *Ann. Transl. Med.* **5**, 150 (2017).
15. Willms, E. *et al.* Cells release subpopulations of exosomes with distinct molecular and biological properties. *Sci. Rep.* **6**, 22519 (2016).

16. Hammiche, A. *et al.* Photothermal FT-IR spectroscopy: A step towards FT-IR microscopy at a resolution better than the diffraction limit. *Appl. Spectrosc.* **53**, 810-815 (1999).
17. Hammiche, A., Bozec, L., Pollock, H.M., German, M. & Reading, M. Progress in near-field photothermal infra-red microspectroscopy. *J. Microsc.* **213**, 129-134 (2004).
18. Dazzi, A. & Prater, C.B. AFM-IR: Technology and applications in nanoscale infrared spectroscopy and chemical imaging. *Chem. Rev.* **117**, 5146-5173 (2017).
19. Khanal, D. *et al.* Biospectroscopy of nanodiamond-induced alterations in conformation of intra- and extracellular proteins: a nanoscale IR study. *Anal. Chem.* **88**, 7530-7538 (2016).
20. Quaroni, L., Pogoda, K., Zuber, J.W. & Kwiatek, W. Mid-Infrared spectroscopy and microscopy of subcellular structures in eukaryotic cells with atomic force microscopy-infrared spectroscopy. *arXiv preprint* (2017).
21. Thakur, B.K. *et al.* Double-stranded DNA in exosomes: a novel biomarker in cancer detection. *Cell Res.* **24**, 766-769 (2014).
22. Chen, I.H. *et al.* Phosphoproteins in extracellular vesicles as candidate markers for breast cancer. *Proc. Natl. Acad. Sci. U.S.A.* **114**, 3175-3180 (2017).
23. Revenfeld, A. L. S. *et al.* Diagnostic and prognostic potential of extracellular vesicles in peripheral blood. *Clin. Ther.* **36**, 830-846 (2014).
24. Baker, M.J. *et al.* Using Fourier transform IR spectroscopy to analyze biological materials. *Nat. Protoc.* **9**, 1771-1791 (2014).
25. McCarthy, S.A., Davies, G.L. & Gun'ko, Y.K. Preparation of multifunctional nanoparticles and their assemblies. *Nat. Protoc.* **7**, 1677-1693 (2012).
26. Martin, F.L. *et al.* Distinguishing cell types or populations based on the computational analysis of their infrared spectra. *Nat. Protoc.* **5**, 1748-1760 (2010).
27. Dazzi, A. *et al.* AFM-IR: Combining atomic force microscopy and infrared spectroscopy for nanoscale chemical characterization. *Appl. Spectrosc.* **66**, 1365-1384 (2012).
28. Butler, H.J. *et al.* Using Raman spectroscopy to characterize biological materials. *Nat. Protoc.* **11** (2016).
29. Zhang, Y., Zhao, S., Zheng, J. & He, L. Surface-enhanced Raman spectroscopy (SERS) combined techniques for high-performance detection and characterization. *Trends Analyt. Chem.* **90**, 1-13 (2017).
30. Tatischeff, I., Larquet, E., Falcón-Pérez, J.M., Turpin, P.Y. & Kruglik, S.G. Fast characterisation of cell-derived extracellular vesicles by nanoparticles tracking analysis, cryo-electron microscopy, and Raman tweezers microspectroscopy. *J. Extracell. Vesicles* **1**, 19179 (2012).
31. Park, J. *et al.* Exosome classification by pattern analysis of surface-enhanced Raman spectroscopy data for lung cancer diagnosis. *Anal. Chem.* **89**, 6695-6701 (2017).
32. Grasso, L., Wyss, R. & Vogel, H. Use of fourier transform infrared spectroscopy analysis of extracellular vesicles isolated from body fluids for diagnosing, prognosing and monitoring pathophysiological states and method therfor. *Google Patents* WO 2016097996 A1 (2016).

33. Qin, S.Q. *et al.* Establishment and characterization of fetal and maternal mesenchymal stem/stromal cell lines from the human term placenta. *Placenta* **39**, 134-146 (2016).
34. Kusuma, G.D. *et al.* Mesenchymal stem/stromal cells derived from a reproductive tissue niche under oxidative stress have high aldehyde dehydrogenase activity. *Stem Cell Rev. Rep.* **12**, 285-297 (2016).
35. Borges, F.T., Reis, L.A. & Schor, N. Extracellular vesicles: Structure, function, and potential clinical uses in renal diseases. *Braz. J. Med. Biol. Res.* **46**, 824-830 (2013).
36. Lee, J. *et al.* Infrared spectroscopic characterization of monocytic microvesicles (microparticles) released upon lipopolysaccharide stimulation. *FASEB J.* **31**, 2817-2827 (2017).
37. Mihály, J. *et al.* Characterization of extracellular vesicles by IR spectroscopy: Fast and simple classification based on amide and CH stretching vibrations. *Biochim. Biophys. Acta* **1859**, 459-466 (2017).



Cite this: *Org. Biomol. Chem.*, 2018, **16**, 619

Tailoring the properties of a hypoxia-responsive 1,8-naphthalimide for imaging applications†

Kylie Yang,^a Kathryn G. Leslie,^a Sally Y. Kim,^b Bill Kalionis,^c Wojciech Chrzanowski,^{b,d} Katrina A. Jolliffe[†] and Elizabeth J. New[†]

Received 3rd November 2017,
Accepted 22nd December 2017

DOI: 10.1039/c7ob03164e

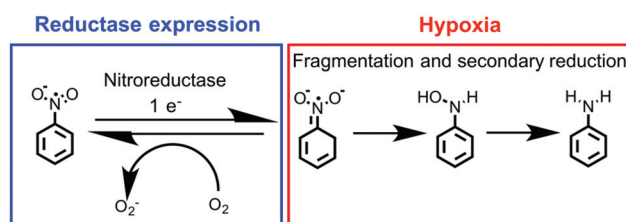
rsc.li/obc

Sensing hypoxia in tissues and cell models can provide insights into its role in disease states and cell development. Fluorescence imaging is a minimally-invasive method of visualising hypoxia in many biological systems. Here we present a series of improved bioreductive fluorescent sensors based on a nitro-naphthalimide structure, in which selectivity, photophysical properties, toxicity and cellular uptake are tuned through structural modifications. This new range of compounds provides improved probes for imaging and monitoring hypoxia, customised for a range of different applications. Studies in monolayers show the different reducing capabilities of hypoxia-resistant and non-resistant cell lines, and studies in tumour models show successful staining of the hypoxic region.

Introduction

Tissue hypoxia (a lack of oxygen) is a hallmark of many diseases, from solid tumours¹ to cardiac ischaemia² to diabetic retinopathy.³ It also plays a pivotal role in development, with the embryo in a state of partial hypoxia during organogenesis.⁴ It is therefore critically important to be able to visualise hypoxic environments to better understand their role in physiology and pathology.

Nitroaromatic compounds undergo hypoxia-induced reduction of the nitro group to an amine *via* a series of intermediates. In biological systems, the first one-electron reduction step is catalysed by the ubiquitous nitroreductase enzyme, but in normoxic tissue this product can be re-oxidised by oxygen. In contrast, this intermediate can undergo further reduction to the aniline group in hypoxic conditions (Scheme 1). This reactivity has been exploited in the development of hypoxia-activated prodrugs, in which the nitroaromatic moiety masks a bioactive molecule, and reduction of the nitro group to an amine then leads to release of the cytotoxic portion.^{5–7} A similar strategy has also been employed for the development of hypoxia-responsive fluorescent sensors, for



Scheme 1 Mechanism of aromatic nitro group reduction in cells.

which reduction leads to a change in fluorescence.⁸ In this manner, sensors based on many fluorophores including acridines,⁹ cyanines^{10,11} and the aggregation-induced emission fluorogen tetraphenylethylene¹² have been reported.

Results and discussion

Sensor design

4-Amino-1,8-naphthalimides have found widespread use in biological sensing for their photostability, large Stokes' shifts, and high quantum yields.¹³ The fluorescence mechanism operates *via* intramolecular charge transfer (ICT), involving electron donation from the 4-amino group to the diimide moiety. The replacement of the 4-amino group with a nitro moiety precludes ICT, and has recently been applied in the development of a lysosomally-targeted hypoxia sensor, where reduction of the nitro to an amine turns on fluorescence.¹⁴ Our interest in the application of naphthalimide-based hypoxia sensors to various biological systems led us to investigate the biological behaviour of the structurally similar probe

^aSchool of Chemistry, The University of Sydney, NSW, 2006 Australia

^bFaculty of Pharmacy, The University of Sydney, NSW, 2006, Australia

^cDepartment of Maternal-Foetal Medicine Pregnancy Research Centre and University of Melbourne. Department of Obstetrics and Gynaecology, Royal Women's Hospital, Parkville, VIC, 3052, Australia

^dThe University of Sydney Nano Institute, NSW 2006, Australia.

E-mail: kate.jolliffe@sydney.edu.au, elizabeth.new@sydney.edu.au

†Electronic supplementary information (ESI) available. See DOI: 10.1039/c7ob03164e

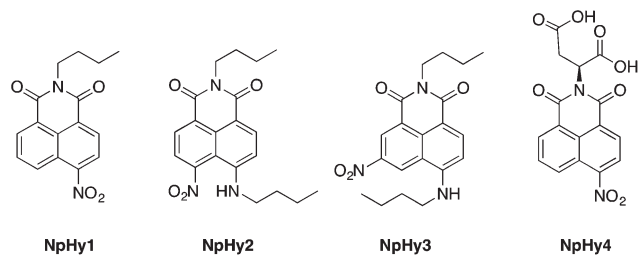


Fig. 1 Structures of **NpHy1** and analogues prepared in this study.

N-butyl-4-nitro-1,8-naphthalimide (**NpHy1** – Fig. 1). We found that this sensor was highly cytotoxic to cultured cells, as the viability of DLD-1 cells was reduced to 50% after a 4 h incubation with 5 μ M of the probe (Fig. S1[†]). We also observed bright fluorescence after just 20 min from cells treated with **NpHy1** under normoxic conditions, indicating poor selectivity for hypoxic cells (Fig. S2[†]). Furthermore, **NpHy1** reports on hypoxia through increased emission intensity, which introduces difficulties in controlling for fluctuations in probe concentration that also cause intensity changes. For data interpretation, ratiometric probes, which undergo emission wavelength changes, are preferable.¹⁵ A notable example of an existing ratiometric hypoxia probe based on a *p*-nitrobenzyl caged 1,3-diaminonaphthalimide has been reported by Xiao and co-workers,¹⁶ but this domain remains largely unexplored.

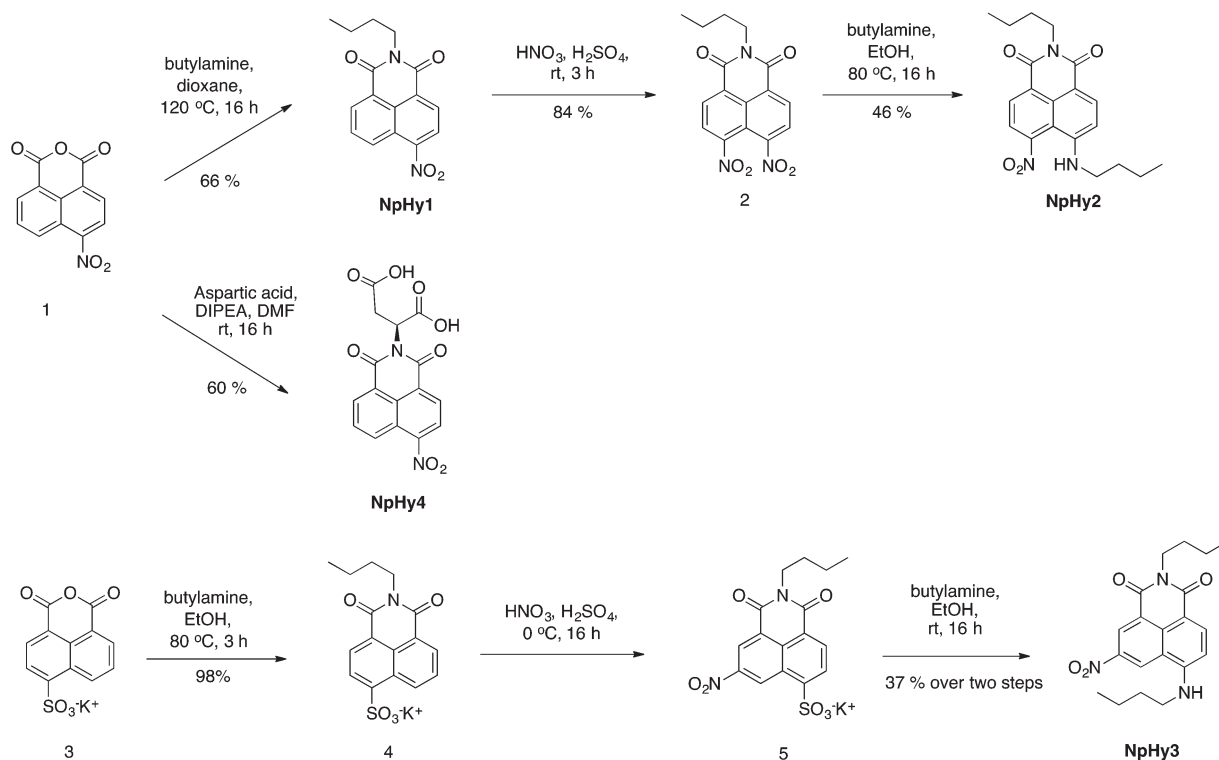
Due to these limitations, we aimed to prepare a set of analogues of **NpHy1** with improved biological properties, and

therefore applicability to a range of experiments. Building on the convenient scaffold of **NpHy1**, we designed three analogues (Fig. 1). In **NpHy2** and **NpHy3** we moved the nitro group to a secondary position on the naphthalene core in order to position an amino group at the 4-position. By installing an electron donor in both the sensor and its product, we hoped to ensure fluorescence emission from both forms, and therefore potentially a ratiometric response. Furthermore, this electron-donating group was expected to increase the reduction potential of the sensor, improving the selectivity for hypoxia over normoxia. **NpHy4** was designed to act as an extra-cellular sensor of hypoxia through the incorporation of an aspartic acid at the imide to prevent cellular uptake.

Synthesis and characterisation

The synthesis of **NpHy2** and **NpHy3** required different synthetic pathways to achieve substitution at the 5- and 6-positions respectively (Scheme 2). **NpHy2** was accessed *via* a nucleophilic aromatic substitution of the 4,5-dinitronaphthalimide that was prepared by nitration of **NpHy1**. The synthesis of **NpHy3** required the nitration of a 4-sulfonaphthalimide in order to nitrate at the 6-position, with subsequent nucleophilic aromatic substitution of the sulfonate. **NpHy4** was readily prepared through the reaction of aspartic acid with 4-nitro-naphthalic anhydride.

We first investigated the fluorescence properties of these molecules through chemical reduction with sodium dithionite (Fig. 2). **NpHy4** showed similar properties to **NpHy1**, with a



Scheme 2 Synthesis of **NpHy** analogues.

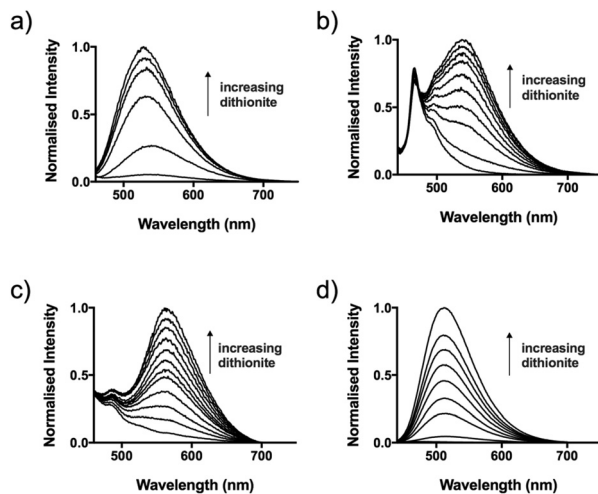


Fig. 2 Fluorescence titrations of (a) **NpHy1** (10 μ M, λ_{ex} = 450 nm), (b) **NpHy2** (10 μ M, λ_{ex} = 420 nm), (c) **NpHy3** (10 μ M, λ_{ex} = 440 nm) and (d) **NpHy4** (20 μ M, λ_{ex} = 450 nm) with increasing sodium dithionite. All spectra collected in PBS, pH 7.4.

single emission peak at approximately 520 nm emerging upon reduction. In contrast, **NpHy2** and **NpHy3** both showed two emission peaks upon reduction. The lower wavelength peak, which is more pronounced for **NpHy2** than **NpHy3**, was observed for the unreacted probes, while a stronger peak at higher wavelengths emerged upon reduction. Interestingly, for both **NpHy2** and **NpHy3** the emission peaks at higher wavelengths were significantly red-shifted (545 and 560 nm respectively) compared to **NpHy1**, potentially due to the presence of two electron donors on the naphthalimide core.

Cyclic voltammetry studies of the naphthalimides revealed that varying the nature of the substituents on the core led to changes in their reduction potentials (Fig. S3†). **NpHy1** was the most easily reduced (E_p = -182 vs. SHE), whereas **NpHy2** and **NpHy3** had more negative reduction potentials (E_p = -226 mV and -458 vs. SHE respectively). It was hoped that these lower reduction potentials could improve the selectivity for hypoxia over normoxia by making the probe more resistant to reduction. With this promising array of fluorescent and electrochemical properties, we then sought to apply these probes for use in biological systems.

Cellular studies

Firstly, we evaluated the cytotoxicity of these probes by measuring their impact on the metabolic activity of cells (Alamar Blue assay) and determined that all the three analogues were significantly less toxic than **NpHy1** (Fig. S1†). Since **NpHy2** showed the most promising ratiometric fluorescence changes, we investigated its response to hypoxia in DLD-1 cells (5 μ M), and were able to see diffuse cytoplasmic fluorescence after 20 min (Fig. S4a†). By collecting the ratio of two emission channels (495–595 nm to 425–485 nm), there was an observable increase in the ratio (Fig. S4b†) within the first five

minutes in 1% oxygen, with the spectral change observed in cells matching that seen in the cuvette (Fig. S4c† and Fig. 2b).

We next investigated whether **NpHy2** was able to respond selectively to intracellular hypoxia, based on its more negative reduction potential compared to **NpHy1**. In particular, we were interested in imaging mesenchymal stem cells that behave differently under hypoxia. DMSC23s and CMSC29s are recently established mesenchymal stromal cell lines, originally isolated from human placenta.¹⁷ DMSC23s originate from tissue exposed to increased inflammation and oxidative stress, and have naturally high resistance to these conditions.¹⁸ CMSC29s originate from the foetal side of the placenta and are non-resistant to hypoxia. We sought to investigate whether the differences between these stem cells could be observed by our probe. The two stem cell lines treated with **NpHy2** were imaged using an IncuCyte (Essen Bioscience) in a hypoxic (1% oxygen) or normoxic (19% oxygen) incubator. The fluorescence intensity of the green channel (504–544 nm) was monitored over time. **NpHy2** showed a rapid turn-on, with complete reduction within 3 h, and there was little difference in intensity between normoxia and hypoxia in both DMSC23 (Fig. 3a) and CMSC29 (Fig. 3c), attributed to the rapid rate of reduction. To address this issue of poor hypoxia selectivity, we investigated the application of **NpHy3**, which had showed a much lower reduction potential. In a similar imaging experiment,

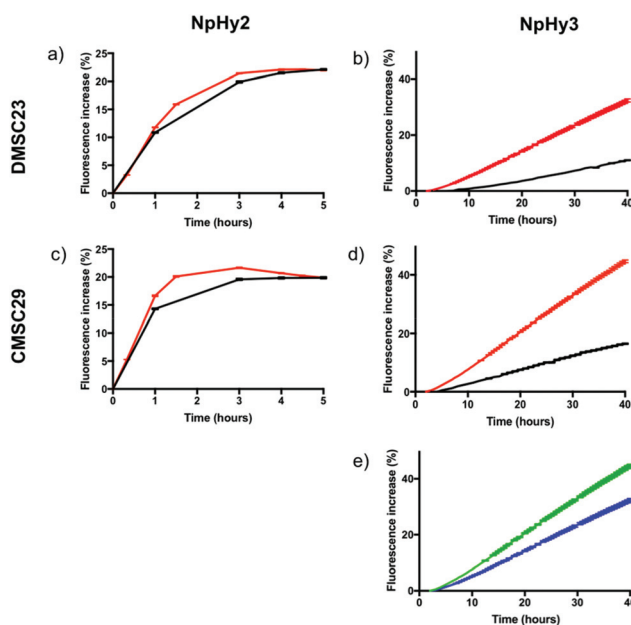


Fig. 3 Imaging of mesenchymal stem cells with **NpHy2** and **NpHy3**. Fluorescence intensity percentage increase of DMSC23s under normoxia (black) and hypoxia (red) treated with (a) **NpHy2** (5 μ M) and (b) **NpHy3** (5 μ M). Fluorescence intensity percentage increase of CMSC29s under normoxia (black) and hypoxia (red) treated with (c) **NpHy2** (5 μ M) and (d) **NpHy3** (5 μ M). (e) Fluorescence intensity percentage increase of DMSC23s (blue) and CMSC29s (green) under hypoxia treated with **NpHy3** (5 μ M). Cells imaged using IncuCyte in hypoxic (1% oxygen) and normoxic (19% oxygen) incubators. Excitation passband = 440–480 nm; emission passband = 504–544 nm.

CMSC29s and DMSC23s were incubated with **NpHy3** under normoxia and hypoxia, and imaged over a period of 40 h. **NpHy3** showed much slower turn-on and greater selectivity for hypoxia in both cell lines (Fig. 3b and d) compared to **NpHy2** (Fig. 3a and c). During incubation with **NpHy3**, the hypoxia-sensitive CMSC29s showed a faster fluorescence increase than the hypoxia-resistant DMSC23s under hypoxic conditions (Fig. 3e and Fig. S5†), which could indicate different nitroreductase activities in these cell lines. Since these imaging experiments were performed over 40 h, we measured the viability of cells incubated over this time period, and confirmed that the probe was not toxic under these conditions (Fig. S6†). These results show that the small chemical modifications of the nitronaphthalimide probes gave rise to an analogue with a reduction potential well suited for intracellular hypoxia sensing.

Having shown the application of nitronaphthalimides to image intracellular hypoxia, we then sought to employ an extracellular probe to monitor hypoxia in tissue models. 3D spheroids are a good model for tumour hypoxia as the low oxygen levels in their core mimic the conditions of tumour cells far from vasculature. The study of tumour spheroids requires probes with poor cell permeability, to prevent sequestration by the outer cell layer and promote diffusion of the probe through the spheroid. The extracellular environment is also less reducing than the intracellular environment, and therefore requires a probe that is more easily reduced in order to sense hypoxia. Although **NpHy1** was too readily reduced inside cells, the environment outside cells is much more oxidising, so reduction of probes is harder to achieve. Consequently, we reasoned that the easily reduced probe **NpHy1** has a sufficiently high reduction potential that would be well-matched to the extracellular redox environment. **NpHy1** was modified with a negatively-charged aspartic acid group to give **NpHy4**, as an analogue with a similar reduction potential but poor cellular uptake, which was confirmed in

DLD-1 cells (Fig. S7†). Despite having a similar structure to the cytotoxic **NpHy1**, **NpHy4** was not toxic to cells, even after 50 h incubation, consistent with its poor cellular uptake (Fig. S6†). **NpHy4** was applied to DLD-1 spheroids of different sizes and imaged with two-photon microscopy (Fig. 4). In both the 2×10^4 and 1×10^4 -cell spheroids, a ring of fluorescence could be observed at a distance of approximately 100 μm from the spheroid surface, which corresponds to the distance oxygen can diffuse through tissues.¹⁹ For smaller spheroid sizes, which do not have a hypoxic region, little fluorescence was observed. These results show that even though the photo-physical and electrochemical properties of **NpHy1** have not been altered, a simple synthetic modification has generated a probe that is useful for biological imaging.

Conclusion

In summary, we have presented a set of three nitronaphthalimide hypoxia probes which exhibit a range of chemical and biological properties. These probes can therefore be used to investigate different biological questions. **NpHy2** showed a promising ratiometric response in spectroscopic studies as well as in live cell experiments, providing a useful lead for future development of ratiometric systems with more finely tuned reduction potentials. The less readily-reduced **NpHy3** showed high selectivity for hypoxia over normoxia and could distinguish differences in hypoxia response between two stem cell types. The extracellular probe **NpHy4** selectively stained hypoxic regions in 3D tumour spheroids. It is clear that small structural modifications can provide a diversity of chemical and biological properties that allow a simple probe design to be tailored to specific imaging applications.

Experimental section

The syntheses of **NpHy1**²⁰ and **NpHy2**²¹ have been reported previously, and details are provided in the ESI.†

Synthesis of **NpHy3**

N-Butyl-4-sulfo-1,8-naphthalimide potassium salt (4). Synthesis was adapted from a published procedure.²² Butylamine (0.17 mL, 1.7 mmol) was added to a suspension of **3** (0.5 g, 1.6 mmol) in ethanol (50 mL), and the mixture was heated at reflux for 16 h. The reaction mixture was then poured onto ice (150 mL), and the resulting precipitate was collected by filtration to give **4** as a white solid (0.58 g, 98%). M.P. 106–108 °C, (lit.²³ 108–110 °C) ¹H NMR (300 MHz, DMSO-*d*₆): δ 9.26 (d, *J* = 8.8, 1H), 8.53–8.43 (m, 2H), 8.22 (d, *J* = 7.6, 1H), 7.93–7.82 (m, 1H), 4.05 (t, *J* = 7.5, 2H), 1.72–1.53 (m, 2H), 1.46–1.25 (m, 2H), 0.92 (t, *J* = 7.2 3H); ESI-MS (*M*)[−] 332.

N-Butyl-4-butylamino-6-nitro-1,8-naphthalimide (NpHy3). Conc. nitric acid (3 mL) was added dropwise to a solution of **4** (70 mg, 0.2 mmol) in conc. sulfuric acid (3 mL) at 0 °C. The reaction mixture was stirred overnight in an ice bath, and then

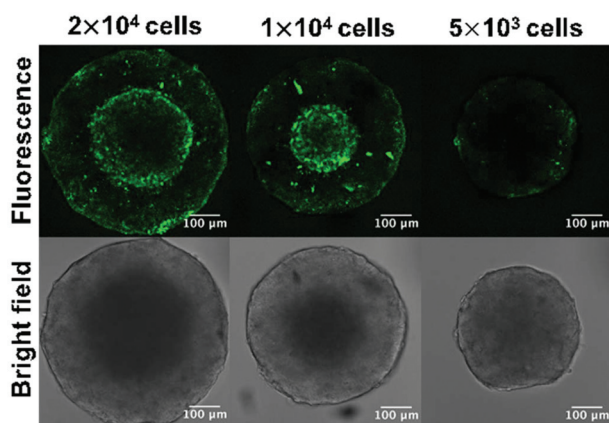


Fig. 4 Two-photon microscopy of **NpHy4** (5 μM , 20 h) in DLD-1 spheroids of different sizes. Brightfield images (acquired with 515 nm laser), fluorescence images (810 nm two-photon excitation, 515–600 nm emission).

poured over ice water and the resulting solution extracted with 1 : 3 CHCl₃ : isopropanol (3 × 30 mL). The combined extracts were dried over sodium sulfate, and then the solvent was removed under reduced pressure to give the crude residue as a yellow oil. Butylamine (15 μL, 0.12 mmol) was added to a solution of crude **5** (20 mg) in ethanol (10 mL) and heated at reflux for 3 h. The reaction mixture was cooled, and the resulting precipitate was filtered and washed with methanol to give **NpHy3** as a bright red solid (26 mg, 37% over two steps). **M.P.** 232–234 °C; ¹H NMR (300 MHz, CDCl₃): δ 9.29 (s, 1H), 9.04 (s, 1H), 8.57 (d, *J* = 8.6, 1H), 6.83 (d, *J* = 8.6, 1H), 5.58 (s, 1H), 4.16 (t, *J* = 7.4, 2H), 3.52–3.42 (m, 2H), 1.92–1.79 (m, 2H), 1.77–1.64 (m, 2H), 1.63–1.36 (m, 4H), 1.05 (t, *J* = 7.4, 3H), 0.97 (t, *J* = 7.4, 3H); ¹³C NMR (75 MHz, CDCl₃): δ 163.2, 163.0, 150.9, 144.2, 137.6, 132.3, 124.7, 124.5, 121.8, 119.3, 110.4, 106.0, 43.7, 40.3, 30.9, 30.2, 20.3, 20.4, 13.8, 13.7; **IR** ν_{max} 3395, 2961, 1695, 1657, 1595, 1555, 1337, 1310; **HR-APCI-MS** [M + Na]⁺ calc. 392.15808, observed 392.15808.

Synthesis of NpHy4

Nitronaphthalimide (**1**) (0.3 g, 1 equiv.) and aspartic acid (1.1 equiv., 0.2 g) was dissolved in DMF, then DIPEA (0.5 mL, 2.2 equiv.) was added and the reaction was stirred overnight at room temperature. The reaction mixture was dissolved in dichloromethane (200 mL) and was washed with 0.5 M HCl (5 × 200 mL). The dichloromethane layer was dried with magnesium sulfate and the solvent was evaporated. The residue was separated using silica flash chromatography (90% CH₂Cl₂, 9% MeOH, 1% acetic acid) to give to product as a yellow solid (260 mg, 60%). **M.P.** 209–211 °C; ¹H NMR (400 MHz, DMSO-d₆): δ 12.9 (s, br, 2H), 8.77 (dd, *J* = 8.7 and 1.0, 1H), 8.70–8.65 (m, 2H), 8.60 (d, *J* = 8.0, 1H), 8.14 (dd, 8.7, 7.4, 1H), 5.99 (dd, *J* = 8.8, 4.2, 1H), 3.30 (dd, *J* = 16.8, 8.8, 1H), 2.78 (dd, *J* = 16.8, 4.2, 1H); ¹³C NMR (300 MHz, DMSO-d₆): δ 171.9, 170.2, 162.6, 161.8, 149.5, 132.3, 130.3, 129.4, 128.4, 126.1, 124.4, 122.8, 122.2, 49.6, 34.2; **IR** ν_{max} 3109 (br), 1712, 1659, 1572, 1346, 1234; **HR-APCI-MS** [M + Na]⁺ calc. 381.03294, observed 381.03350 found.

Fluorescence studies

All fluorescence spectra were recorded on a Varian Cary Eclipse fluorometer in 1 cm pathlength quartz cuvettes. The emission spectra of 10 μM solutions of **NpHy1** (λ_{ex} = 450 nm), **NpHy2** (λ_{ex} = 420 nm), **NpHy3** (λ_{ex} = 440 nm) and **NpHy4** (λ_{ex} = 450 nm) in PBS buffer (pH 7.4) were recorded with 10 μL aliquots of freshly prepared 1 M sodium dithionite in PBS buffer until no further change in fluorescence was observed.

Electrochemical studies

Electrochemical measurements were performed using a BAS 100B/W Electrochemical Analyser. A single compartment cell was used, consisting of a glassy carbon working electrode, a platinum wire auxiliary electrode and an electrolysed Ag/AgCl wire reference electrode. Cyclic voltammograms were performed using a 1 mM solution of the analyte in MeCN, with 0.1 M tetrabutylammonium hexafluorophosphate as a support-

ing electrolyte. Prior to each experiment, the solution was purged with Ar. Uncompensated resistance between the working and the reference electrodes was corrected by using *iR* compensation. Measurements were converted to a standard hydrogen electrode reference (*vs.* SHE) for comparison with the literature.

Biological studies

Cell lines. DLD-1 (colon cancer) cells were maintained in exponential growth as monolayers in Advanced Dulbecco's Modified Eagles Medium (ADMEM) supplemented with 1.25% glutamine (G) and 2% foetal calf serum (FBS). Cells were incubated at 37 °C in 5% v/v CO₂ under humidified conditions. These cell lines were sub-cultured using 0.25% trypsin to facilitate dislodgement of cells from the flask.

Transduced foetal chorionic and maternal mesenchymal stromal cells were used as preferred over primary human placenta cells, for reproducibility of responses to the probes. CMSC29 and DMSC23 cell lines, were cultured in AmnioMAX™ with its supplement (Life Technologies) and Mesencult™ proliferation kit (STEMCELL Technologies) respectively, both supplemented with 1% penicillin-streptomycin and 1% GlutaMAX™ (Life Technologies).¹⁷ Cells were incubated at 37 °C in 5% v/v CO₂ under humidified conditions and were used at passages 25–26.

Other details of biological experiments can be found in the ESI.†

Conflicts of interest

There are no conflicts to declare.

Acknowledgements

The authors acknowledge the support of an Australian Postgraduate Award (KY) and a Research Training Program Scholarship (KGL), a Sydney University SOAR fellowship (WC) and the Westpac Bicentennial Foundation (EJN). We acknowledge the scientific and technical assistance of the Australian Microscopy and Microanalysis Research Facility at the Australian Centre for Microscopy and Microanalysis (ACMM) and the Bosch Institute at the University of Sydney. We thank Kieran Geraghty, Timothy Chisholm and Dr Zelong Lim for assistance with preliminary synthetic studies and A/Prof. Deanna D'Alessandro and Dr Marcello Solomon for access to their electrochemical set-up.

References

- 1 B. Muz, P. de la Puente, F. Azab and A. K. Azab, *Hypoxia*, 2015, **3**, 83–92.
- 2 S. N. Heyman, D. Leibowitz, I. Mor-Yosef Levi, A. Liberman, A. Eisenkraft, R. Alcalai, M. Khamaisi and C. Rosenberger, *Acta Physiol.*, 2016, **216**, 395–406.

- 3 D. J. Ramsey and G. B. Arden, *Curr. Diabetes Rep.*, 2015, **15**, 118.
- 4 W. S. Webster and D. Abela, *Birth Defects Res., Part C*, 2007, **81**, 215–228.
- 5 C. P. Guise, A. M. Mowday, A. Ashoorzadeh, R. Yuan, W.-H. Lin, D.-H. Wu, J. B. Smaill, A. V. Patterson and K. Ding, *Chin. J. Cancer*, 2014, **33**, 80–86.
- 6 F. W. Hunter, B. G. Wouters and W. R. Wilson, *Br. J. Cancer*, 2016, **114**, 1071–1077.
- 7 C. Cazares-Körner, I. M. Pires, I. D. Swallow, S. C. Grayer, L. J. O'Connor, M. M. Olcina, M. Christlieb, S. J. Conway and E. M. Hammond, *ACS Chem. Biol.*, 2013, **8**, 1451–1459.
- 8 R. B. P. Elmes, *Chem. Commun.*, 2016, **52**, 8935–8956.
- 9 A. C. Begg, E. L. Engelhardt, R. J. Hodgkiss, N. J. McNally, N. H. Terry and P. Wardman, *Br. J. Radiol.*, 1983, **56**, 970–973.
- 10 S. Bhaumik, T. V. Sekar, J. Depuy, J. Klimash and R. Paulmurugan, *Gene Ther.*, 2012, **19**, 295–302.
- 11 Y. Li, Y. Sun, J. Li, Q. Su, W. Yuan, Y. Dai, C. Han, Q. Wang, W. Feng and F. Li, *J. Am. Chem. Soc.*, 2015, **137**, 6407–6416.
- 12 X. You, L. H. Li, X. H. Li, H. M. Ma, G. X. Zhang and D. Q. Zhang, *Chem. – Asian J.*, 2016, **11**, 2918–2923.
- 13 R. M. Duke, E. B. Veale, F. M. Pfeffer, P. E. Kruger and T. Gunnlaugsson, *Chem. Soc. Rev.*, 2010, **39**, 3936–3953.
- 14 J. Zhou, W. Shi, L. H. Li, Q. Y. Gong, X. F. Wu, X. H. Li and H. M. Ma, *Chem. – Asian J.*, 2016, **11**, 2719–2724.
- 15 E. J. New, *ACS Sens.*, 2016, **1**, 328–333.
- 16 L. Cui, Y. Zhong, W. Zhu, Y. Xu, Q. Du, X. Wang, X. Qian and Y. Xiao, *Org. Lett.*, 2011, **13**, 928–931.
- 17 S. Q. Qin, G. D. Kusuma, B. Al-Sowayan, R. A. Pace, S. Isenmann, M. D. Pertile, S. Gronthos, M. H. Abumaree, S. P. Brennecke and B. Kalionis, *Placenta*, 2016, **39**, 134–146.
- 18 G. D. Kusuma, M. H. Abumaree, M. D. Pertile, A. V. Perkins, S. P. Brennecke and B. Kalionis, *Stem Cell Rev. Rep.*, 2016, **12**, 285–297.
- 19 A. J. Franko and R. M. Sutherland, *Radiat. Res.*, 1979, **79**, 439–453.
- 20 E. R. Triboni, P. B. Filho, R. G. de Souza Berlinck and M. J. Politi, *Synth. Commun.*, 2004, **34**, 1989–1999.
- 21 M. Alexiou and J. Tyman, *J. Chem. Res.*, 2001, **2001**, 59–61.
- 22 Z. Tian, Y. Liu, B. Tian and J. Zhang, *Res. Chem. Intermed.*, 2015, **41**, 1157–1169.
- 23 V. B. Bojinov, N. I. Georgiev and P. S. Nikolov, *J. Photochem. Photobiol., A*, 2008, **193**, 129–138.

1 **Greater cellular stiffness in fibroblasts from patients with idiopathic pulmonary fibrosis**

2

3 Jade Jaffar^{a,b,c}, Soung-Hee Yang^{d,e}, Sally Yunsun Kim^f, Hae-Won Kim^{d,e}, Alen Faiz^{a,g,h}, Wojciech
4 Chrzanowski^{d,f,*} and Janette K Burgess^{a,g,i,*,#}

5

6 ^a*Woolcock Institute of Medical Research, The University of Sydney, Sydney, AUS*

7 ^b*Dept. of Allergy, Immunology and Respiratory Medicine, The Alfred Hospital, Melbourne, AUS*

8 ^c*Dept. of Immunology and Pathology, Monash University, Melbourne, AUS*

9 ^d*Dept. of Nanobiomedical Science and BK21 PLUS NBM Global Research Center for*

10 *Regenerative Medicine, Dankook University, Cheonan 330-715, Republic of Korea*

11 ^e*Institute of Tissue Regeneration Engineering (ITREN) and College of Dentistry, Dankook*

12 *University, Cheonan 330-715, Republic of Korea*

13 ^f*Faculty of Pharmacy, The University of Sydney Nano Institute, The University of Sydney,*

14 *Sydney, AUS*

15 ^g*University of Groningen, University Medical Center Groningen, Dept. of Pathology and*

16 *Medical Biology, Groningen Research Institute for Asthma and COPD, 9713GZ Groningen,*

17 *The Netherlands*

18 ^h*University of Groningen, University Medical Center Groningen, Dept. of Pulmonology,*

19 *Groningen Research Institute for Asthma and COPD, 9713GZ Groningen, The Netherlands*

20 ⁱ*Discipline of Pharmacology, The University of Sydney, Sydney, AUS*

21

22 *** These authors contributed equally**

23

24 **# corresponding author:**

25 **Prof Janette Burgess j.k.burgess@umcg.nl**

26

27 **RUNNING HEAD**

28

29 IPF fibroblasts have increased cellular stiffness

30

31 **ABBREVIATIONS**

32

33 IPF, idiopathic pulmonary fibrosis; NDC, Non-diseased control; ECM, extracellular matrix,

34 α SMA, alpha-smooth muscle actin

35

36

37 **Abstract 131**

38 **Introduction 265**

39 **Results 470**

40 **Discussion 552**

41 **Methods 960**

42 **References 1191**

43

44 **With legends = 3992 – excluding abstract and title page**

45 **ABSTRACT**

46 Idiopathic pulmonary fibrosis (IPF) is a lethal lung disease involving degenerative breathing
47 capacity. Fibrotic disease is driven by dysregulation in mechanical forces at the organ, tissue
48 and cellular level. While it is known that, in certain pathologies, diseased cells are stiffer than
49 healthy cells, it is not known if fibroblasts derived from patients with IPF are stiffer than their
50 normal counterparts.

51

52 Using IPF patient-derived cell cultures, we measured the stiffness of individual lung fibroblasts
53 via high-resolution force maps using atomic force microscopy. Fibroblasts from patients with IPF
54 were stiffer and had an augmented cytoskeletal response to TGF β 1 compared to fibroblasts
55 from donors without IPF. The results from this novel study indicate that the increased stiffness
56 of lung fibroblasts of IPF patients may contribute to the increased rigidity of fibrotic lung tissue.

57

58

59 **INTRODUCTION**

60

61 Pulmonary fibrosis, a permanent consequence of a range of lung diseases, affects the lung
62 interstitium: the specialized network of tissue that surrounds the air sacs (alveoli) and their
63 corresponding blood vessels. In idiopathic pulmonary fibrosis (IPF) the excessive production of
64 extracellular matrix (ECM) by lung myofibroblasts leads to the progressive stiffening of the
65 tissue (21), resulting in the loss of lung function. However, few studies have investigated the
66 stiffness of the fibroblast's cytoskeleton, which influences the overall stiffness of the tissue (1,
67 10, 19).

68

69 A myofibroblast's ability to contract is a function of its cytoskeleton and these forces are largely
70 generated by α SMA in stress fibres (12). Compared to fibroblasts derived from patients without

71 fibrosis (Non-Diseased Control, NDC, fibroblasts), fibroblasts from patients with IPF (IPF
72 fibroblasts) have increased basal expression of α SMA (27). Therefore, we hypothesized that
73 IPF fibroblasts would also have greater internal cytoskeletal stiffness than NDC fibroblasts.

74
75 TGF β 1 increases α SMA expression in mesenchymal cells (7) and cell stiffness of epithelial cells
76 (31). Lung fibroblasts obtain information about their surrounding physical environment through
77 their cytoskeleton (3), thus a fibrotic ECM potentially activates a continuous loop where the
78 increased stiffness of the fibroblasts' immediate microenvironment causes alterations in cell
79 behavior (20, 24).

80
81 The aim of this study was to measure the nanomechanical properties of primary lung fibroblasts
82 using high-resolution, atomic force microscopy (AFM). To investigate cell cytoskeletal
83 dysregulation in fibrotic disease, primary lung fibroblasts from patients with IPF were compared
84 to fibroblasts from age and sex-matched individuals with no history of fibrotic lung disease. The
85 cytoskeletal rearrangements of α SMA were examined before and after stimulation with TGF β 1.

86

87 **RESULTS**

88 In this study, we demonstrate through molecular force probing that the stiffness of fibroblasts
89 from patients with IPF is greater than those of fibroblasts from NDC donors.

90

91 Due to the prolonged scanning time required (~4 hours) for high-resolution mechanical mapping
92 of cells (23) fixation was necessary. Our preliminary data showed that there was no change in
93 apparent Young's modulus (cellular stiffness) and less variability after fixation (Figure 1A-B).

94

95 For data analysis, the histograms of each force map (Figure 1C-D) were subjected to linear
96 regression analysis (Figure 1E-G). Importantly, quality control measurements (Figure 1H)

97 indicated that there were no differences in the number of force maps or points of stiffness
98 measured between the two disease groups and treatments.

99

100 This study sampled lung tissue from patients with IPF on the severe end of the disease
101 spectrum, reflected in the clinical parameters in Table 1; IPF patients had a diffusion limit of
102 carbon monoxide (DLco) of 21% predicted, consistent with patients with a DLco <35% predicted
103 being considered to have severe, end-stage disease (25).

104

105 Furthermore, because IPF is a disease often associated with smoking (18), it is important that
106 the NDC donors used in the study had a history of smoking. IPF is a disease of primarily older
107 individuals (18) and normal aging-related changes are known to impact on cell stiffness (29). In
108 our study, there was no difference in age between the IPF and NDC donors (Table 1).

109

110 Mechanoperception (cellular sensing of its microenvironment) can dictate cell behavior. We
111 compared cell stiffness on 0.2% gelatin (soft) versus tissue culture plastic (TCP). There was no
112 difference in internal cell stiffness between IPF and NDC fibroblasts on 0.2% gelatin. Strikingly,
113 compared to gelatin, NDC fibroblasts were 115% softer on TCP, while IPF fibroblasts did not
114 respond to the change in surface stiffness (Table 2). Our data show that, the average internal
115 cell cytoskeletons from patients with IPF were stiffer than those from NDC on TCP (Figure 2A).

116

117 The differences in cytoskeletal stiffness were more pronounced after fibroblasts were treated
118 with TGF β 1, a pro-fibrotic cytokine that induces cytoskeletal rearrangement in fibroblasts (7,
119 12). Although both groups became stiffer after stimulation, IPF fibroblasts were nearly 15x stiffer
120 than NDC fibroblasts following TGF β 1 exposure (Figure 2A, Table 2).

121

122 When the topography measurements were combined with the stiffness values, high-resolution,
123 3-dimensional force maps were generated simulating the surface features of the $50\ \mu\text{m}^2$
124 scanned with overlaid colour-scale stiffness information (Figure 2B). Both IPF and NDC
125 fibroblasts changed morphology following TGF β 1 stimulation. Although similar in gross
126 morphology, IPF fibroblasts were significantly stiffer and increases in surface stiffness were
127 seen over the entire $50\ \mu\text{m}^2$ measured.

128

129 Treatment with TGF β 1 induced α SMA expression in both populations although bundles of
130 α SMA+ fibers appeared more prominent in IPF compared to NDC fibroblasts (Figure 2C). At
131 the population level, IPF fibroblasts expressed higher levels of α SMA than NDC fibroblasts
132 (Figure 2D), while TGF β 1 induced upregulated α SMA in both NDC and IPF fibroblasts.

133

134 **DISCUSSION**

135

136 Global mortality from IPF is progressively increasing The mechanisms governing fibroblast
137 behaviour in fibrotic lung disease are not fully understood , consequently current treatments
138 have limited efficacy to prevent, or reverse, the fibrotic process (14, 25, 26). Our study points to
139 an exaggerated physical response of IPF fibroblasts to TGF β 1 as a novel factor driving
140 pathology, potentially resulting in increased tissue stiffening.

141

142 Altered fibroblast behaviour is recognised in the context of IPF (1, 10) making differences in
143 cytoskeletal regulation and mechanoperception rational therapeutic targets (33). The actin
144 cytoskeleton confers important cellular properties, including contractility and motility (13).

145

146 In this study, we show that primary IPF fibroblasts are stiffer than NDC fibroblasts implying that
147 in IPF, the increase in individual fibroblast stiffness may contribute to an increase in overall
148 fibrotic tissue stiffness, not a novel concept in fibrosis pathology (22, 33). In support of this,
149 when normal lungs are decellularized, they maintain 81% of their native stiffness (indicating the
150 cellular contribution is 19% of the native lung stiffness). When IPF lungs are decellularized, they
151 only maintain 44% stiffness (4). Our study presents the possibility that the IPF fibroblasts
152 themselves are stiffer.

153

154 The increase in stiffness we measured on the nanoscale in the IPF fibroblasts, has implications
155 on a tissue level. It is possible that a sustained increased stiffness of a single cell propagates
156 alterations via mechanoperception to other fibroblasts in the immediate microenvironment.
157 Given increased ECM production is one response to a stiffer environment (5), this may generate
158 a pro-fibrotic feedback loop in IPF lung tissue (24). Whether the increased stiffness of the IPF
159 fibroblast is a response to an aberrant wound healing response (ECM deposition) or if the cell is

160 inherently different in an IPF patient is not currently known. The lung is a highly mechanical
161 organ in which the architecture determines its functionality (8). Increased fibroblast stiffness
162 may disrupt the tissue architecture and cause corruption of mechanically-derived signals which
163 normally transmit through the ECM (8).

164
165 The IPF fibroblasts did not exhibit mechanoresponsiveness between a soft and hard surface, a
166 change that was observed with NDC fibroblasts. The IPF fibroblasts showed augmented
167 cytoskeletal responses to TGF β 1, increasing cell stiffness to a greater extent than NDC
168 fibroblasts, indicating that the lack of mechanoresponsiveness in the IPF fibroblasts was not due
169 to defective cytoskeletal machinery. IPF is more prevalent in older individuals (28) and normal
170 aging-related changes share similar mechanisms with lung fibrosis (30). Skin fibroblasts from
171 aged individuals are 60% stiffer than fibroblasts from younger patients (29). However, as there
172 were no age differences between the NDC or IPF fibroblast donors, we can infer that the
173 alterations in cell cytoskeletal response observed were disease related.

174
175 This is the first study to show that cell cytoskeletal regulation in IPF fibroblasts is different to that
176 in NDC fibroblasts, possibly contributing to the increased lung stiffness in IPF. New knowledge
177 about the differences in responses of IPF cells to pro-fibrotic stimuli is critical for understanding
178 underlying mechanisms to prevent or reverse disease development.

179 **METHODS**

180

181 **Primary lung fibroblast culture**

182 Lung tissue was obtained from patients with IPF, or from patients undergoing resection and
183 donors whose lungs were deemed unsuitable for transplantation, and who, or whose next of kin,
184 provided written, informed consent. The University of Sydney Human Research Ethics
185 Committee (#2012/946) and the Alfred Hospital Ethics Committee (#468/14) provided ethical
186 approval. Donor demographical information is in Table 1.

187

188 Fibroblasts were isolated from distal lung parenchyma as previously described (9).

189 All cultures tested negative for mycoplasma before use in experiments and only cell cultures at
190 less than 6 passages were used.

191

192 **Cell Experimentation**

193 Primary fibroblasts were seeded in 5% FBS/1% antibiotics/DMEM for 72 hours and then
194 quiesced in 0.1% FBS/1% Penicillin-Streptomycin/DMEM (quiescing media) for 24 hours. Fresh
195 quiescing media, with or without 10 ng/mL activated TGF β 1 (R&D Systems, USA) was added
196 for 72 hours. Some fibroblasts were seeded on TCP coated with 0.002g/mL gelatin powder
197 (Ajax Chemicals, Australia) in sterile water for 1 hour at room temperature, before rinsing twice
198 with sterile phosphate buffered saline (PBS, Invitrogen, USA) immediately prior to seeding.

199

200 After treatment, cells were rinsed twice with sterile PBS, and fixed in freshly made 4% (v/v)
201 paraformaldehyde (Sigma, Melbourne Australia) in PBS for 15 minutes at room temperature.

202 Cells were rinsed twice with PBS and stored in sterile PBS at 4°C until further experimentation.

203 All samples for nanomechanical experiments were prepared at the same time.

204

205 **Cell Morphology and stiffness measurements**

206 Cell Morphology

207 Detailed 3D morphology of the cells was acquired using molecular force probe microscopy
208 (MFP-3D-Bio, Asylum Research, Santa Barbara, CA, USA). Cells were located using light
209 microscopy and imaged using AFM operating in contact mode using AppNano (HYDRA-ALL)
210 probes with nominal spring constant 0.012 N/m. Sensitivity and spring constant calibrations of
211 the probe were performed immediately prior to indenting cells.

212

213 Nanomechanical analysis of cell stiffness

214 To probe the nanomechanical properties of cells MFP-3D-Bio equipped with HYDRA-ALL probe
215 was used with the probe deflection set to 200 nm. To eliminate dragging effects of, and
216 minimise interaction of fluid on the measurements the approach speed was set at 200 nm/sec.

217 For each sample a minimum of 5 areas (50×50 µm) were scanned each including several cells,
218 for each area 6400 (80×80) force curves were recorded, enabling the creation of force-volumes
219 'maps' for each sample.

220 The elastic properties (Young's modulus) of the cells were determined by fitting each of the
221 6400 force curves to a contact-mechanics model (16). To take into account probe tip-sample
222 adhesion forces (15), the Derjaguin–Muller–Toporov (DMT) model was used (6), with the
223 Poisson ratio of all the samples set to 0.5, the archetypical value for biological samples (2, 11).

224

225 Quantification of stiffness measurements

226 Force maps underwent log transformed regression analysis using the corresponding histogram
227 plot of stiffness measurements (17). Only force maps which obtained a significant Goodness of
228 Fit (R^2) value of greater than or equal to 0.95 ($P < 0.05$) were included.

229

230 **Immunocytochemistry**

231 Fibroblasts were labelled with anti- α SMA (Abcam, UK), detected with a secondary antibody
232 conjugated to AlexaFluor-594 (Abcam, UK), and anti-Vimentin conjugated to AlexaFluor-488
233 (BD Biosciences, USA). Nuclei were labelled with Hoescht 32555 (Invitrogen, USA). Each cell
234 line was imaged 2-3 times in different areas, using the same microscope settings on the same
235 day. Cells were imaged using a Nikon A1r si confocal microscope (Olympus, Japan) in
236 galvanometric scanning mode with a 40x water immersion objective with coverslip correction
237 collar (Nikon CFI Apo Lambda S 40x LWD WI na = 1.15). Z-stack images were combined using
238 Image J software (Version 1.50a, NIH, USA).

239
240 Fibroblasts in 96-well plates were permeabilized with 0.1% (v/v) Triton X-100 (Sigma,
241 Melbourne Australia) before incubation with mouse anti- α SMA and rabbit anti-GAPDH
242 concurrently. Next day anti-mouse IgG-790 fluorochrome and anti-rabbit-680 fluorochrome were
243 added. Plates were imaged using an Odyssey Infrared scanner (Li-cor, USA) and quantification
244 performed by Image Studio (Version 4, Li-cor, USA), with the intensity of the 800 channel set at
245 5 and the 700 channel set to 3. Images were scanned at an offset of 3 mm with a resolution of
246 169 μ m.

247

248 **Quality control and Statistical Analysis**

249 Statistical analysis was performed using SPSS (Version 22, IBM), GraphPad Prism 6
250 (GraphPad, La Jolla, USA) and Microsoft Excel (Microsoft, Redmond USA).

251

252 To account for the intrinsic variability of primary human lung fibroblasts, we performed intra-
253 class correlation coefficient (ICC) analysis on n=10 cells. Using a two-way mixed effects model
254 with experimental error considered consistent and patient variability considered random, the
255 ICC was 0.71 (Degrees of freedom=9, p=0.046), indicating a good degree of reliability within
256 this data set (32).

257

258 To avoid bias in data collection, probing of samples was undertaken in random order by a
259 researcher blinded to disease and treatment. In addition, 2-way repeated measures analysis of
260 variance (ANOVA) was used to ensure there were no differences in the quality of data between
261 groups. In total, 37 force maps, totalling 236800 force measurements, of 50 μm^2 areas across
262 cells from n=3 IPF and n=3 NDC with similar gross morphology were collected for analysis.

263

264 The results in this study were obtained from a total of 102,459 individual force curves, of which
265 72,757 were used to generate linear regression equations with an average R^2 value of 0.98.

266

267 Differences in cell stiffness between NDC and IPF fibroblasts were assessed using unpaired t-
268 tests on the stiffness frequencies calculated from measurements that accounted for the 15th to
269 85th cumulative frequency percentiles. Stiffness frequency was defined as the stiffness
270 (Pascals) multiplied by the number of points measured (counts).

271

272 The effect of TGF β 1 on cell stiffness and α SMA expression were assessed using ratio paired t-
273 tests with the unstimulated condition as control. A P-value of <0.05 was considered significant.

274

275 **ACKNOWLEDGEMENTS**

276 The authors acknowledge Mr. Brock Patton's assistance with research and manuscript
277 preparation and the Monash Micro Imaging platform for technical assistance with confocal
278 microscopy. This study was supported by National Health and Medical Research Council,
279 Australia Fellowship #1032695 (JKB), the University of Groningen and European Union co-
280 funded Rosalind Franklin Fellowship (JKB) and RESPIRE2 fellowship co-funded by the
281 European Respiratory Society and the European Union (AF).

282 REFERENCES

- 283 1. **Alvarez D, Cardenes N, Sellares J, Bueno M, Corey C, Hanumanthu VS, Peng Y, D'Cunha H,**
 284 **Sembrat J, Nourai M, Shanker S, Caufield C, Shiva S, Armanios M, Mora AL, and Rojas M.** IPF lung
 285 fibroblasts have a senescent phenotype. *Am J Physiol Lung Cell Mol Physiol* 313: L1164-L1173, 2017.
- 286 2. **Babahosseini H, Ketene AN, Schmelz EM, Roberts PC, and Agah M.** Biomechanical profile of
 287 cancer stem-like/tumor-initiating cells derived from a progressive ovarian cancer model. *Nanomedicine*
 288 10: 1013-1019, 2014.
- 289 3. **Balestrini JL, Chaudhry S, Sarrazy V, Koehler A, and Hinz B.** The mechanical memory of lung
 290 myofibroblasts. *Integr Biol (Camb)* 4: 410-421, 2012.
- 291 4. **Booth AJ, Hadley R, Cornett AM, Dreffs AA, Matthes SA, Tsui JL, Weiss K, Horowitz JC, Fiore VF,**
 292 **Barker TH, Moore BB, Martinez FJ, Niklason LE, and White ES.** Acellular normal and fibrotic human lung
 293 matrices as a culture system for in vitro investigation. *Am J Respir Crit Care Med* 186: 866-876, 2012.
- 294 5. **Chiquet M, Renedo AS, Huber F, and Fluck M.** How do fibroblasts translate mechanical signals
 295 into changes in extracellular matrix production? *Matrix Biol* 22: 73-80, 2003.
- 296 6. **Derjaguin BVM, V.M; Toporov, Yu. P.** Effect of Contact Deformations on the Adhesion of
 297 Particles. *J Colloid Interface Sci* 53: 314-316, 1975.
- 298 7. **Desmouliere A, Geinoz A, Gabbiani F, and Gabbiani G.** Transforming growth factor-beta 1
 299 induces alpha-smooth muscle actin expression in granulation tissue myofibroblasts and in quiescent and
 300 growing cultured fibroblasts. *Journal of Cell Biology* 122: 103-111, 1993.
- 301 8. **Faffe DS, and Zin WA.** Lung Parenchymal Mechanics in Health and Disease. *Physiological*
 302 *Reviews* 89: 759-775, 2009.
- 303 9. **Ge Q, Chen L, Jaffar J, Argraves WS, Twal WO, Hansbro P, Black JL, Burgess JK, and Oliver B.**
 304 Fibulin1C peptide induces cell attachment and extracellular matrix deposition in lung fibroblasts. *Sci Rep*
 305 5: 9496, 2015.
- 306 10. **Ghavami S, Yeganeh B, Zeki AA, Shojaei S, Kenyon NJ, Ott S, Samali A, Patterson J, Alizadeh J,**
 307 **Moghadam AR, Dixon IMC, Unruh H, Knight DA, Post M, Klonisch T, and Halayko AJ.** Autophagy and
 308 the Unfolded Protein Response Promote Pro-fibrotic Effects of TGFbeta1 in Human Lung Fibroblasts. *Am*
 309 *J Physiol Lung Cell Mol Physiol* ajplung003722017, 2017.
- 310 11. **Haghi M, Traini D, Wood LG, Oliver B, Young PM, and Chrzanowski W.** A 'soft spot' for drug
 311 transport: modulation of cell stiffness using fatty acids and its impact on drug transport in lung model.
 312 *Journal of Materials Chemistry B* 3: 2583-2589, 2015.
- 313 12. **Hinz B, Celetta G, Tomasek JJ, Gabbiani G, and Chaponnier C.** Alpha-Smooth Muscle Actin
 314 Expression Upregulates Fibroblast Contractile Activity. *Molecular Biology of the Cell* 12: 2730-2741,
 315 2001.
- 316 13. **Hwang Y, Gouget CL, and Barakat AI.** Mechanisms of cytoskeleton-mediated mechanical signal
 317 transmission in cells. *Commun Integr Biol* 5: 538-542, 2012.
- 318 14. **King TE, Bradford WZ, Castro-Bernardini S, Fagan EA, Glaspole I, Glassberg MK, Gorina E,**
 319 **Hopkins PM, Kardatzke D, Lancaster L, Lederer DJ, Nathan SD, Pereira CA, Sahn SA, Sussman R, Swigris**
 320 **JJ, and Noble PW.** A Phase 3 Trial of Pirfenidone in Patients with Idiopathic Pulmonary Fibrosis. *New*
 321 *England Journal of Medicine* 370: 2083-2092, 2014.
- 322 15. **Kirmizis D, and Logothetidis S.** Atomic force microscopy probing in the measurement of cell
 323 mechanics. *International Journal of Nanomedicine* 5: 137-145, 2010.
- 324 16. **Kopczynska-Muller M, Geiss RH, and Hurley DC.** Contact mechanics and tip shape in AFM-based
 325 nanomechanical measurements. *Ultramicroscopy* 106: 466-474, 2006.
- 326 17. **Kwok J, Grogan S, Meckes B, Arce F, Lal R, and D'Lima D.** Atomic force microscopy reveals age-
 327 dependent changes in nanomechanical properties of the extracellular matrix of native human menisci:

- 328 implications for joint degeneration and osteoarthritis. *Nanomedicine: Nanotechnology, Biology and*
329 *Medicine* 10: 1777-1785, 2014.
- 330 18. **Ley B, and Collard HR.** Epidemiology of idiopathic pulmonary fibrosis. *Clin Epidemiol* 5: 483-492,
331 2013.
- 332 19. **Liu F, Lagares D, Choi KM, Stopfer L, Marinkovic A, Vrbanac V, Probst CK, Hiemer SE, Sisson TH,**
333 **Horowitz JC, Rosas IO, Fredenburgh LE, Feghali-Bostwick C, Varelas X, Tager AM, and Tschumperlin DJ.**
334 Mechanosignaling through YAP and TAZ drives fibroblast activation and fibrosis. *Am J Physiol Lung Cell*
335 *Mol Physiol* 308: L344-357, 2015.
- 336 20. **Liu F, Mih JD, Shea BS, Kho AT, Sharif AS, Tager AM, and Tschumperlin DJ.** Feedback
337 amplification of fibrosis through matrix stiffening and COX-2 suppression. *J Cell Biol* 190: 693-706, 2010.
- 338 21. **Liu F, and Tschumperlin DJ.** Micro-mechanical characterization of lung tissue using atomic force
339 microscopy. *The Journal of Visualized Experiments* 2011.
- 340 22. **Marinkovic A, Liu F, and Tschumperlin DJ.** Matrices of physiologic stiffness potentially inactivate
341 idiopathic pulmonary fibrosis fibroblasts. *Am J Respir Cell Mol Biol* 48: 422-430, 2013.
- 342 23. **Moreno-Herrero F, Colchero J, Gomez-Herrero J, and Baro AM.** Atomic force microscopy
343 contact, tapping, and jumping modes for imaging biological samples in liquids. *Phys Rev E Stat Nonlin*
344 *Soft Matter Phys* 69: 031915, 2004.
- 345 24. **Parker MW, Rossi D, Peterson M, Smith K, Sikstr, xF, m K, White ES, Connett JE, Henke CA,**
346 **Larsson O, and Bitterman PB.** Fibrotic extracellular matrix activates a profibrotic positive feedback loop.
347 *The Journal of Clinical Investigation* 124: 1622-1635, 2014.
- 348 25. **Raghu G, Collard HR, Egan JJ, Martinez FJ, Behr J, Brown KK, Colby TV, Cordier JF, Flaherty KR,**
349 **Lasky JA, Lynch DA, Ryu JH, Swigris JJ, Wells AU, Ancochea J, Bouros D, Carvalho C, Costabel U, Ebina**
350 **M, Hansell DM, Johkoh T, Kim DS, King TE, Jr., Kondoh Y, Myers J, Muller NL, Nicholson AG, Richeldi L,**
351 **Selman M, Dudden RF, Griss BS, Protzko SL, and Schunemann HJ.** An official ATS/ERS/JRS/ALAT
352 statement: idiopathic pulmonary fibrosis: evidence-based guidelines for diagnosis and management. *Am*
353 *J Respir Crit Care Med* 183: 788-824, 2011.
- 354 26. **Richeldi L, du Bois RM, Raghu G, Azuma A, Brown KK, Costabel U, Cottin V, Flaherty KR,**
355 **Hansell DM, Inoue Y, Kim DS, Kolb M, Nicholson AG, Noble PW, Selman M, Taniguchi H, Brun M, Le**
356 **Maulf F, Girard M, Stowasser S, Schlenker-Herceg R, Disse B, and Collard HR.** Efficacy and safety of
357 nintedanib in idiopathic pulmonary fibrosis. *New England Journal of Medicine* 370: 2071-2082, 2014.
- 358 27. **Roach KM, Wulff H, Feghali-Bostwick C, Amrani Y, and Bradding P.** Increased constitutive
359 alphaSMA and Smad2/3 expression in idiopathic pulmonary fibrosis myofibroblasts is KCa3.1-
360 dependent. *Respir Res* 15: 155, 2014.
- 361 28. **Ryerson CJ, and Collard HR.** Update on the diagnosis and classification of ILD. *Curr Opin Pulm*
362 *Med* 19: 453-459, 2013.
- 363 29. **Schulze C, Wetzel F, Kueper T, Malsen A, Muhr G, Jaspers S, Blatt T, Wittern K-P, Wenck H, and**
364 **Käs JA.** Stiffening of Human Skin Fibroblasts with Age. *Biophysical Journal* 99: 2434-2442, 2010.
- 365 30. **Thannickal V.** Mechanistic links between aging and lung fibrosis. *Biogerontology* 14: 609-615,
366 2013.
- 367 31. **Thoelking G, Reiss B, Wegener J, Oberleithner H, Pavenstaedt H, and Riethmuller C.**
368 Nanotopography follows force in TGF-beta1 stimulated epithelium. *Nanotechnology* 21: 265102, 2010.
- 369 32. **Weir JP.** Quantifying test-retest reliability using the intraclass correlation coefficient and the
370 SEM. *J Strength Cond Res* 19: 231-240, 2005.
- 371 33. **Wells RG.** Tissue mechanics and fibrosis. *Biochim Biophys Acta* 1832: 884-890, 2013.

372

373 **Table 1.** Demographics of patients from whom fibroblasts were derived.

Patient #	Gender	Age **	Diagnosis	History of Smoking?	FEV ₁	FVC	DL _{CO}	CPI
NDC1	n/a	39	Healthy	Yes	n/a	n/a	n/a	n/a
NDC2	Male	69	Healthy	Yes	n/a	n/a	n/a	n/a
NDC3	Female	60	Healthy	Yes	n/a	n/a	n/a	n/a
NDC4	Female	28	Healthy	Yes	n/a	n/a	n/a	n/a
NDC5	n/a	n/a	Healthy	n/a	n/a	n/a	n/a	n/a
NDC6*	Male	66	NSCLC	n/a	n/a	n/a	n/a	n/a
NDC7*	Male	60	NSCLC	Yes	77	97	n/a	n/a
NDC8*	Male	61	NSCLC	Yes	75	77	n/a	n/a
IPF1	Male	65	IPF	Yes	48	43	36	61.1
IPF2	Male	61	IPF	Yes	57	48	47	54.4
IPF3	Male	69	IPF	Yes	86	86	17	63.6
IPF4	Male	63	IPF	Yes	n/a	n/a	19	n/a
IPF5	Female	56	IPF	No	53	47	16	73.7
IPF6*	Male	55	IPF	Yes	52	48	26	66.3
IPF7*	Male	58	IPF	Yes	57	51	18	71.7
IPF8*	Male	58	IPF	Yes	55	46	18	73.6

374

375 Lung function measurements are presented in percent predicted values.

376 FEV₁, forced expiratory volume in 1 second, FVC forced vital capacity, DL_{CO} diffusing capacity

377 of carbon monoxide, CPI composite physiologic index, IPF idiopathic pulmonary fibrosis, NDC

378 Non-diseased control, n/a not available

379

380 * Participants from whom fibroblasts used in the atomic force microscopy experiments were
381 derived

382 ** Unpaired, two-tailed t-test (n=8/group,p=0.3)

383

384

385

386 **Table 2.** Adjusted mean stiffness values of fibroblasts from IPF and NDC under different
387 conditions.

388

389

Surface/ Treatment	NDC		IPF		Adjusted P Value for pairwise comparison
	Adjusted Mean (kPa)	(95% CI)	Adjusted Mean (kPa)	(95% CI)	
Gelatin	1.87	(1.64 - 2.13)	2.16	(1.90 - 2.46)	0.6858
TCP	0.87	(0.74 - 1.02)	1.74	(1.52 - 2.00)	<0.0001
TCP + TGFβ1	2.84	(2.44 - 3.31)	30.95	(27.72 - 34.54)	<0.0001

390

391 Adjusted mean stiffness values calculated as the mean value between log normalised stiffness
392 measurements for the 15th to 85th percentiles of each fibroblast line. Two-way ANOVA was
393 performed and the adjusted p value for the effect of cell disease type on within treatment
394 calculated. $p \leq 0.05$ was considered significant.

395 kPa, kilopascals, TGFβ1 transforming growth factor beta, NDC non-diseased control

396

397 **Figure Legends**

398 **Figure 1.** Quantification of cell cytoskeletal stiffness.

399 Cell stiffness was measured on fixed and live cells. (A) representative plots (B) average data.

400 (C) Representative data of an IPF fibroblast captured using atomic force microscopy (AFM).

401 Points marked in red show where stiffness was not measured. (D) For each $50 \mu\text{m}^2$ area

402 probed, 6400 surface points were measured, generating a force map. Measurements from each

403 force map were quantified on histograms. (E) Histogram analysis of (D) is shown graphically,

404 stiffness values are log normal transformed and plotted against cumulative frequency. (F)

405 Stiffness values between the 15th and 85th percentiles were used in the linear regression

406 model. (G) The calculated linear regression line was overlaid in red. (H) Quality control analysis

407 on the total dataset used in this study.

408 NDC Non-diseased control, IPF idiopathic pulmonary fibrosis, TGF β 1 transforming growth factor

409 beta-1, SD standard deviation

410 P value for repeated measures two-way analysis of variance investigating disease and

411 treatment

412

413 **Figure 2.** IPF fibroblasts are stiffer than NDC fibroblasts. (A) Cell cytoskeletal stiffness

414 frequency of N=3 IPF and N=3 NDC fibroblasts measured before and after TGF β 1 treatment.

415 (B) Representative high-resolution force maps of stiffness of IPF and NDC fibroblasts measured

416 by atomic force microscopy. (C) Representative images and (D) in cell western analysis of

417 α SMA in N=5 IPF and N=4 NDC fibroblasts measured before and after TGF β 1 treatment.

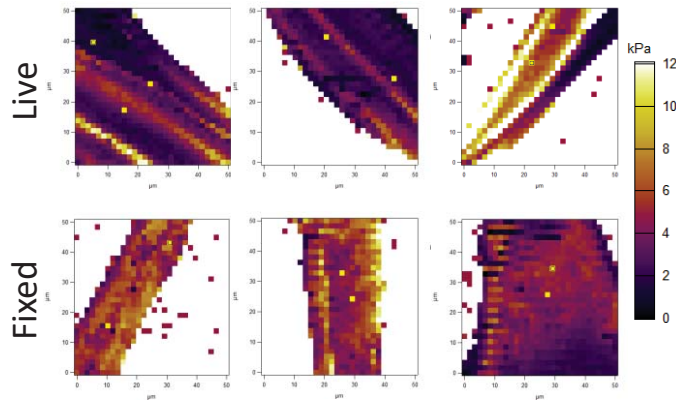
418 IPF idiopathic pulmonary fibrosis, NDC non-diseased control, TGF β 1 transforming growth

419 factor-beta 1

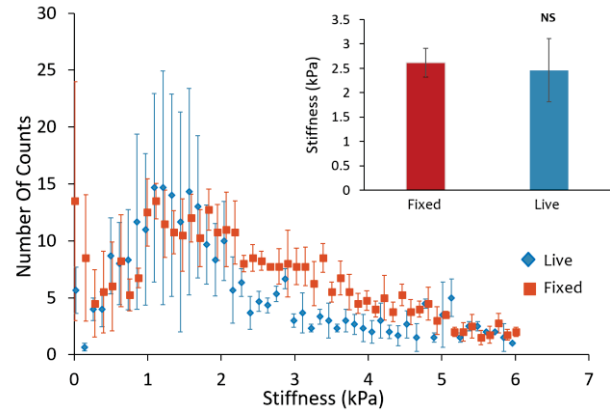
420 P value for repeated measures two-way analysis of variance investigating disease and

421 treatment

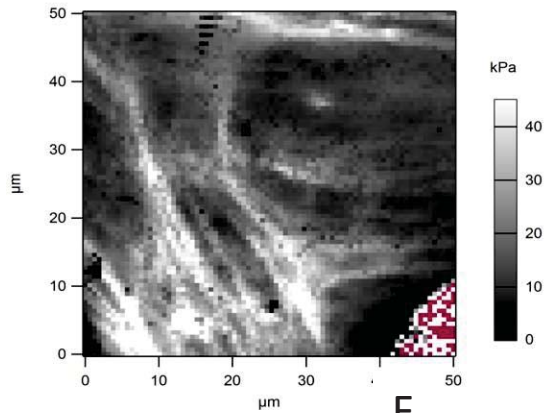
A Maps of Apparent Young's Modulus (kPa) [Cell Stiffness]



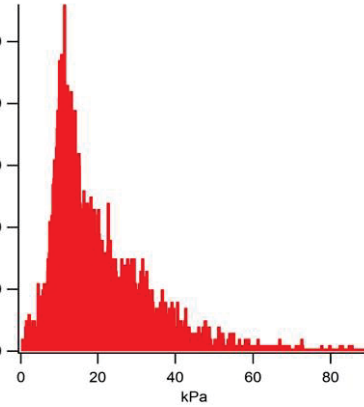
B



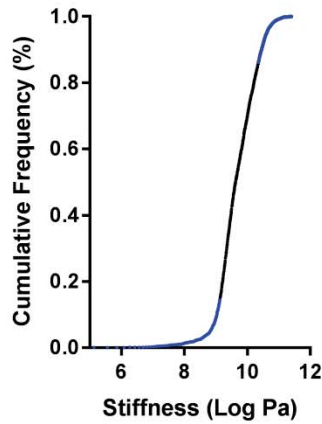
C



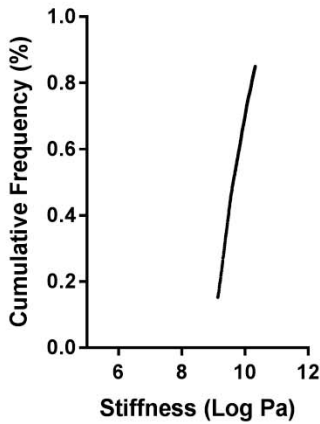
D



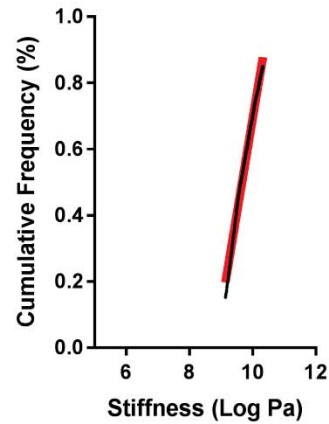
E



F



G



H

	Non-diseased Control (NDC)		Idiopathic Pulmonary Fibrosis (IPF)		
Patient Diagnosis (n=3 each group)	Unstimulated	TGFβ1	Unstimulated	TGFβ1	P Value
Mean (SD) number of force curves generated	3920 (1464)	8661 (5328)	5577 (1272)	4683 (1145)	ns
Mean (SD) number of force curves included in linear regression	2757 (1041)	6136 (3737)	3940 (869)	3385 (733)	ns
Mean (SD) value of linear regression constant (R ²)	0.987 (0.02)	0.981 (0.03)	0.981 (0.03)	0.990 (0.02)	ns

Appendix D. Conference Presentations (presenting author underlined)

- **Kim, S.Y.**, Kalionis, B., Weiss, D., Chrzanowski, W. Aerosolized delivery of mesenchymal stromal cells to the lungs: towards a novel therapy (Oral). *ERS International Congress*, Milan, Italy, 2017.
- **Kim, S.Y.**, Khanal, D., Johnson, J., Kalionis, B., Chrzanowski, W. Probing heterogeneity of stem-cell derived EVs by resonance enhanced AFM-IR (Poster). *Extracellular Vesicles*, Cambridge, UK, 2017.
- **Kim, S.Y.**, Burgess, J.K., Wang, Y., Weiss, D.J., Chan, H.K., Chrzanowski, W. Atomized mesenchymal stromal cells for application in lung diseases (Oral). *Tissue Engineering and Regenerative Medicine International Society – Asia Pacific Conference*, Tamsui, Taiwan, 2016.
- **Kim, S.Y.**, Burgess, J.K., Chan, H.K., Chrzanowski, W. Cell-based therapy for the targeted treatment of lung injury (Poster). *Annual Conference of the European Society of Biomaterials*, Krakow, Poland, 2015.
- **Kim, S.Y.**, Burgess, J.K., Chan, H.K., Chrzanowski, W. Cell-based therapy for targeted treatment of lung injury (Poster). *Stem Cells, Cell Therapies and Bioengineering in Lung Biology and Lung Diseases*, Burlington, VT, USA, 2015.
- **Kim, S.Y.**, Burgess, J.K., Chan, H.K., Chrzanowski, W. Cell-based therapy for the targeted treatment of lung injury” (Oral). *Australasian Society for Biomaterials and Tissue Engineering Conference, joint conference with International Symposium on Surface and Interface of Biomaterials*, Sydney, Australia, 2015.
- **Kim, S.Y.**, Naskar, D., Kundu, S.C., Chan, H.K., Chrzanowski, W., Wall, I. Targeted treatment of lung cancer using silk-based drug carriers (Poster). *Australia and New Zealand Society for Cell and Developmental Biology NSW Meeting*, Sydney, Australia, 2014.
- **Kim, S.Y.**, Naskar, D., Kundu, S.C., Chan, H.K., Chrzanowski, W. Silk-based drug carriers for pulmonary drug delivery (Poster). *Materials Today: Biomaterials Virtual Conference*, 2013.

Appendix E. List of Awards and Achievements

Short-term Intensive Research Trainings

- Kalionis Lab, a stem cell biology laboratory at Royal Women's Hospital, University of Melbourne (*Apr 2016*), learnt harvesting of stress-resistant stem cells from human placenta and assays for stem cell biology.
- Weiss Lab, University of Vermont College of Medicine (*Jul – Dec 2015*), developed skills in lung dissection and establishing mouse, rat, human *ex vivo* lung models for testing direct cell delivery to lungs.
- Wall Lab, a regenerative medicines laboratory in the Biochemical Engineering Department at University College London (*Dec 2014 – Mar 2015*), acquired skills in cell culture and numerous biological assays.

Co-authored Research Grants

- Sydney Nano Research Collaboration Award (\$3,000), **S.Y. Kim**, G. Pinget, C. Limantoro, K. Yang, Dec **2017**.
- University of Sydney – Utrecht University Partnership Collaboration Award (\$30,000), co-written for the project "*Delivery of anti-inflammatory extracellular vesicles via aerosolisation for treatment of inflammatory lung diseases*", W. Chrzanowski, M. Wauben, **S.Y. Kim**, M. van Herwijnen, B. Kalionis, S. Libregtsy, Y. Wang, E. New, H.K. Chan, Aug **2017**.
- DVCR Compact Seed Funding (\$25,000) from the Faculty of Pharmacy, the University of Sydney, co-written for the project titled "*'Firefighters' for Smoke Inhalation Injuries*", W. Chrzanowski, H.K. Chan, Y. Wang, **S.Y. Kim**, May **2016**.
- Innovation Challenge Funding (\$20,000) from the Faculty of Pharmacy, the University of Sydney, co-written for the project titled "*Cell-based therapy for pulmonary injury*", H.K. Chan, W. Chrzanowski, **S.Y. Kim**, Jul **2014**.

Achievements and Honours

- Invited speaker in the research seminar series at ANZAC Research Institute, Sep **2017**.
- Invited to chair the "*Frontier technologies in nano-biomaterials*" session at Summer School in BioNano-Technology and Biomedical Engineering, The University of Sydney, Feb **2017**.
- Publication in *J Aerosol Med Pulm Drug Deliv.* highlighted as a high-impact article, Dec **2016**.
- Invited to co-chair the "*Nanomedicine, drug/gene delivery and RNA therapeutics*" session at *Tissue Engineering and Regenerative Medicine International Society – Asia Pacific (TERMIS-AP) Conference*, Tamsui, Taiwan, Sep **2016**.
- Invited speaker at the *Research Bazaar (ResBaz) Conference "Lightning Talk"* session at the University of Sydney, Feb **2016** and selected to attend the *ResBaz Conference* at the University of Melbourne, Feb **2015**.
- Won the 4th Round of the *Sydney Catalyst Boast and Toast* for "*Novel silk-based drug carriers targeted for lung cancer*" (\$2,500), Sep **2015**.

- Selected as a finalist in Fresh Science NSW Australia, Aug **2015**.
- Publication in *Scientific Reports* selected as the Top Story of Pulmonary Cell News, Aug **2015**.
- Participated in the Three-Minute Thesis competition, Aug **2014**.
- Australian Postgraduate Award Scholarship, the University of Sydney, Jul **2014 – Current**.

Travel Grants / Awards

- Postgraduate Research Support Scheme Award (\$3,000) to attend the *Extracellular Vesicles Conference*, Sep **2017**.
- Postgraduate Research Support Scheme Award (\$2,000) to attend the *TERMIS-AP Conference*, Sep **2016**.
- James Kentley Memorial Scholarship via *Grants-in-Aid*, the University of Sydney (\$2,000), Cancer Research Network Postgraduate Conference Travel Grant Award (\$500) and Postgraduate Research Support Scheme Award (\$3,000) to support extensive laboratory training at a cell therapy laboratory at the University of Vermont College of Medicine and to attend the Vermont Stem Cells Conference (invited), Jul – Nov **2015**.
- Postgraduate Research Support Scheme Award (\$1,200) to visit a regenerative medicines laboratory in Biochemical Engineering Department, University College London, Dec **2013 – Mar 2014**.

Best Presentation Awards

- Best Oral Presentation Award (\$200) at the *American Association of Pharmaceutical Scientists (Australian Chapter) Student Symposium*, Sep **2016**.
- Best Oral Presentation Award (\$500) at the *Postgraduate Conference, Faculty of Pharmacy*, Sep **2016**.
- Winner of poster presentations at *Advances in Biotechnology for Food and Medical Applications*, Oct **2016**.
- Most Outstanding Presentation Award (\$200) for "*Targeted treatment of lung cancer using silk-based drug carriers*" in the Targeted Therapies session, *Postgraduate Cancer Research Symposium*, Nov **2014**.
- Editor's Choice Award for the poster "*Silk-based drug carriers for pulmonary drug delivery*" presented at *Materials Today: Biomaterials* virtual conference, Nov **2013**.
- Poster presentation "*Silk-based drug carriers for pulmonary drug delivery*" warranting opportunity for a podium presentation at *Drug Delivery Australia, CRS Australian Local Chapter*, **2013**.
- The Best Poster Presentation Award at *The University of Sydney Pharmaceutical Student Symposium*, Aug **2013**.